

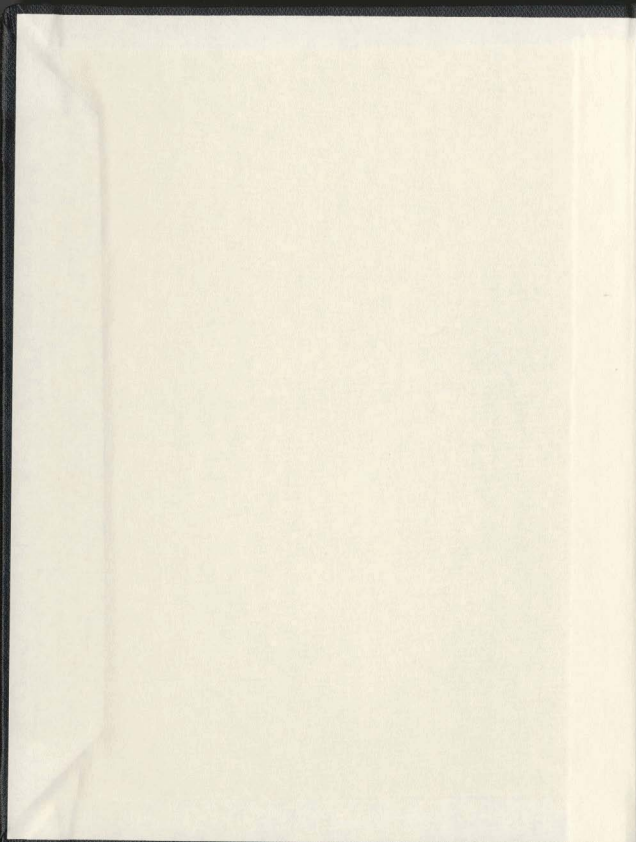
STRUCTURAL INTEGRITY MONITORING OF A
HYDRO-ELASTIC MODEL OF A JACKET PLATFORM

CENTRE FOR NEWFOUNDLAND STUDIES

**TOTAL OF 10 PAGES ONLY
MAY BE XEROXED**

(Without Author's Permission)

MERVIN ALLAN MARSHALL





National Library
of Canada

Acquisitions and
Bibliographic Services Branch

395 Wellington Street
Ottawa, Ontario
K1A 0N4

Bibliothèque nationale
du Canada

Direction des acquisitions et
des services bibliographiques

395, rue Wellington
Ottawa (Ontario)
K1A 0N4

Votre file - Votre référence

Votre file - Votre référence

NOTICE

The quality of this microform is heavily dependent upon the quality of the original thesis submitted for microfilming. Every effort has been made to ensure the highest quality of reproduction possible.

If pages are missing, contact the university which granted the degree.

Some pages may have indistinct print especially if the original pages were typed with a poor typewriter ribbon or if the university sent us an inferior photocopy.

Reproduction in full or in part of this microform is governed by the Canadian Copyright Act, R.S.C. 1970, c. C-30, and subsequent amendments.

AVIS

La qualité de cette microforme dépend grandement de la qualité de la thèse soumise au microfilmage. Nous avons tout fait pour assurer une qualité supérieure de reproduction.

S'il manque des pages, veuillez communiquer avec l'université qui a conféré le grade.

La qualité d'impression de certaines pages peut laisser à désirer, surtout si les pages originales ont été dactylographiées à l'aide d'un ruban usé ou si l'université nous a fait parvenir une photocopie de qualité inférieure.

La reproduction, même partielle, de cette microforme est soumise à la Loi canadienne sur le droit d'auteur, SRC 1970, c. C-30, et ses amendements subséquents.

**STRUCTURAL INTEGRITY MONITORING OF A
HYDRO-ELASTIC MODEL OF A JACKET PLATFORM**

by

© Mervin Allan Marshall, B.Eng., M.Eng.

A thesis submitted to the School of Graduate
Studies in partial fulfillment of the
requirements for the degree of
Doctor of Philosophy

Faculty of Engineering and Applied Science
Memorial University of Newfoundland
September 1990

St. John's

Newfoundland

Canada



National Library
of Canada

Acquisitions and
Bibliographic Services Branch

395 Wellington Street
Ottawa, Ontario
K1A 0N4

Bibliothèque nationale
du Canada

Direction des acquisitions et
des services bibliographiques

395, rue Wellington
Ottawa (Ontario)
K1A 0N4

Your file Votre référence

Our file Notre référence

THE AUTHOR HAS GRANTED AN
IRREVOCABLE NON-EXCLUSIVE
LICENCE ALLOWING THE NATIONAL
LIBRARY OF CANADA TO
REPRODUCE, LOAN, DISTRIBUTE OR
SELL COPIES OF HIS/HER THESIS BY
ANY MEANS AND IN ANY FORM OR
FORMAT, MAKING THIS THESIS
AVAILABLE TO INTERESTED
PERSONS.

L'AUTEUR A ACCORDE UNE LICENCE
IRREVOCABLE ET NON EXCLUSIVE
PERMETTANT A LA BIBLIOTHEQUE
NATIONALE DU CANADA DE
REPRODUIRE, PRETER, DISTRIBUER
OU VENDRE DES COPIES DE SA
THESE DE QUELQUE MANIERE ET
SOUS QUELQUE FORME QUE CE SOIT
POUR METTRE DES EXEMPLAIRES DE
CETTE THESE A LA DISPOSITION DES
PERSONNE INTERESSEES.

THE AUTHOR RETAINS OWNERSHIP
OF THE COPYRIGHT IN HIS/HER
THESIS. NEITHER THE THESIS NOR
SUBSTANTIAL EXTRACTS FROM IT
MAY BE PRINTED OR OTHERWISE
REPRODUCED WITHOUT HIS/HER
PERMISSION.

L'AUTEUR CONSERVE LA PROPRIETE
DU DROIT D'AUTEUR QUI PROTEGE
SA THESE. NI LA THESE NI DES
EXTRAITS SUBSTANTIELS DE CELLE-
CI NE DOIVENT ETRE IMPRIMES OU
AUTREMENT REPRODUITS SANS SON
AUTORISATION.

ISBN 0-315-96053-1

To my wife, daughter and son
Melody, Evannah, and Jonathan ...

Acknowledgements

I should like to thank my advisors for their advice and encouragement, and for allowing me the freedom to pursue my own research interest. Specifically, they are: Dr. Michael Booton, Associate Professor (project supervisor), and Dr. D. B. Muggeridge, Research Professor, and Chairman of Ocean Engineering.

A special word of thanks goes to my friend Dr. Jebaraj Chidambaram for his many helpful suggestions. To Dr. G. Ross Peters, and Dr. T. Ramanuja Chari (Dean and Associate Dean, respectively, of Engineering), I extend sincere gratitude for their helpful suggestions and assistance throughout my years of study at Memorial University.

I am grateful to many people for their help, but I shall only mention a few of them. Mr. Stephen K. Foster and Mrs. Diane Ramsay of Technical Services built the experimental hydro-elastic model; Mr. Terry Dyer and Barry Bowers drew some of the diagrams; Mr. John Bourne, at M.U.N. photography, took and developed all the photographs; the wave tank crew (Mr. Mike Sullivan, Mr. Lloyd Little and Mr. Andrew Kuczora) provided invaluable assistance throughout the experimental investigation; the workers at the Center for Computer Aided Engineering (Mr. David Press, Mr. Mervin Goodyear, Mrs. Ingrid V. Barnes and Mr. Tony Galway) assisted in computer related matters; Mr. Randy Dodge and Mr. Greg Bennett at Computing Services provided many helping suggestions which made my programs more efficient; Dr. J. J. Sharp (Chairman of Civil Engineering) gave many helpful advice regarding the modelling of the hydro-elastic model; Dr. Gary Sabin allowed

me to use his workstation to speed-up some of my analyses, and gave me that special word of encouragement when I needed it most; Mr. Leroy Isidore, my colleague, assisted in the processing of the experimental data; and my fellow graduate students gave incessant support and encouragement.

The funding for the research by the National Research Council of Canada under strategic grant # 330164 is gratefully acknowledged. Also, I am indebted to Dr. F. A. Aldrich (former Dean of Graduate Studies) for the award of a graduate fellowship, and to Dr. Jack Clark at C-CORE for the award of a C-CORE fellowship. Thanks are also expressed to Dr. John Malpas and Dr. C. A. Sharp (Dean and Associate Dean, respectively, of Graduate Studies) for their help.

No amount of gratitude can adequately repay my wife, Melody, and my daughter, Evannah, for their inspiration, support, and sacrifice during my years of study. This thesis truly belongs to them.

Last, but most importantly, I should like to thank the Almighty for making everything possible.

Abstract

As a result of the increasing requirement for structural safety of offshore drilling platforms, the need for monitoring techniques capable of detecting damage of subsurface structural components increases. Since it is not possible, because of limited time constraints, to carry out tests on an actual operating platform in the ocean, an alternative solution is to experiment on a reduced model of an offshore structure. Very few experiments using a truly hydro-elastic model of a jacket platform have been published.

This treatise deals with a detailed design and construction of a hydro-elastic model of a typical four-legged jacket offshore platform to carry out structural integrity monitoring. Both an indepth theoretical and experimental analysis were carried out. Experiments were conducted in a wave tank equipped with a pseudo random wave making facility. To obtain the necessary modal parameters (e.g., resonant frequencies, and damping ratios) from the ambient response data, the recently developed Marple algorithm was used with the very powerful Maximum Entropy Method (MEM). Regarding structural integrity monitoring, structural damage was simulated by saw cutting the member(s) under consideration. In the theoretical analyses, this was done by making the member(s) inactive in the analyses. The detection of damage was based on the changes in resonant frequencies compared with the intact structure.

Resonant frequencies were determined for the intact and damaged structure and the results (i.e., experimental and theoretical) were compared to measure the influence of the damaged member(s) on the resonant frequen-

cies of the structure. By cutting an inclined member in a k-braced panel to simulate damage of the member, a 39% decrease in the resonant frequency of the 2nd flexural mode was measured on the spectral density function of the wave induced vibration from the hydro-elastic model. The theoretical results showed a 29% decrease. (Theoretical results from the prototype structure showed similar trends.)

Based on the reported results and evaluations, it was concluded that the resonant frequency changes clearly indicated the structure had been damaged. Besides, the theoretical analyses showed that the global modes most affected from the damage depended on the location of the damaged member(s).

Contents

Acknowledgements	iii
Abstract	v
List of Figures	xii
List of Tables	xxiii
List of Symbols	xxvi
1 Introduction	1
1.1 Background	2
1.1.1 Possible Causes of Structural Damage	4
1.2 Scope of the Work	6
1.2.1 Modelling the Structure	6
1.2.2 Estimation of Modal Parameters	8
1.2.3 Thesis Outline	8
2 Literature Review	10
2.1 Practical Limitations	21
3 Theoretical Modelling	23
3.1 Wave Forces	23

3.2	Wave Theories	25
3.3	Regular Wave Forces	26
3.3.1	Vertical Cylinder	26
3.3.2	Arbitrarily Oriented Cylinder	34
3.4	Irregular Wave Forces	37
3.5	Mathematical Modelling of the Structure	38
3.5.1	Formulations for the 3-D Model	39
3.5.2	Formulations for the Stick Model	42
3.6	Computer Implementation of Analytical Models	46
3.6.1	Implementation of the 3-D Model	48
3.6.2	Implementation of the Stick Model	53
4	Physical Modelling	57
4.1	Development of Modelling Laws	57
4.2	Wave Modelling	59
4.3	Modelling the Sea Structure Interaction	61
4.4	Modelling the Tower	66
4.5	Difficulties Associated with Hydro-Elastic Modelling	68
4.5.1	Difficulties due to Froude's Law of Similarity	69
4.5.2	Difficulties due to the Interaction between Inertia in the Structure and in the Liquid	70
4.5.3	Difficulties due to Viscosity-Forces and Structural Damp- ing	73
4.6	Model Design and Fabrication	74
4.6.1	Description of the Prototype	74
4.6.2	Design of The Reduced Model	80

4.6.3	Fabrication of the Reduced Model	80
5	Experimental Study	94
5.1	Equipment Installation	94
5.1.1	The Wave Maker System	96
5.1.2	Instrumentation of the Model	101
5.1.3	Instrumentation for Impact Testing	103
5.1.4	Response Circuit	105
5.2	Experimental Procedure	105
5.2.1	Free Vibration Tests	105
5.2.2	Wave Simulation	108
5.2.3	Irregular Wave Simulation	112
5.2.4	Wave Structure Interaction	113
5.2.5	Impact Testing Response	114
6	Analysis of Results	118
6.1	Spectral Estimates Using FFT	120
6.2	Spectral Estimates Using MEM	122
6.2.1	Autoregressive Model of MEM	123
6.2.2	The Determination of AR Coefficients	126
6.2.3	Selection of Optimum Model Order	127
6.3	Estimating Modal Parameters	130
6.3.1	Resonant Frequencies	130
6.3.2	Force Response Damping	131
6.4	Free Oscillation Damping	133
6.5	Impact Testing	137

7	Theoretical and Experimental Results	140
7.1	Theoretical Results	140
7.1.1	Free Vibration Results	141
7.1.2	Dynamic Response to Wave Excitation	149
7.2	Experimental Results	169
7.2.1	Transient Decay Tests to Compute Damping	169
7.2.2	Wave Test Results	179
7.2.3	Impact Test Results	207
8	Discussion of Results	218
8.1	Theoretical Results	218
8.1.1	Free Vibration Results	218
8.1.2	Response to a Train of Regular Waves	224
8.1.3	Response to Irregular Waves	227
8.2	Experimental Results	231
8.2.1	Transient Decay Tests to Compute Damping	231
8.2.2	Wave Probe Results	232
8.2.3	Wave Tests Results	232
8.2.4	Impact Test Results	249
8.3	Comparison Between the Experimental and Theoretical Results	250
9	Concluding Remarks and Recommendations	258
9.1	Concluding Remarks	258
9.2	Recommendations	261
	References	264
	Bibliography	271

A	Selected Algorithms	276
A.1	Diagonalization of a Consistent Mass Matrix Using Cook's Method	277
A.2	Houbolt Algorithm	279
A.3	Longuet-Higgins and Cokelet Smoothing Algorithm	282
B	Sample Calculations	284
B.1	Sample Calculations to Select Member Section Sizes	285
C	Calibration Curve and Instrumentation Settings	287
C.1	Calibration and Instrumentation Settings	288
D	Miscellaneous	290
D.1	Mode Shape (Members 70 and 68 Removed)	291
D.2	Results for an Impact Initiated at I16	301
D.3	MEM Damping Estimates for the Damaged Structure	314

List of Figures

1.1	Important Steps of Structural Integrity Monitoring.	5
3.1	Regions of Applicability for Small and Finite Amplitude Waves.	27
3.2	Notation Used in Connection with Waves.	28
3.3	Incremental Wave Force dF_I on a Vertical Cantilever Cylinder.	29
3.4	Arbitrarily Oriented Cylinder.	35
3.5	Force Components on an Arbitrarily Oriented Cylinder.	35
3.6	Simulated 3-D and Stick Model Representation of the Structure.	47
3.7	Discretization of Members (Prototype).	50
3.8	Discretization of Joints (Prototype).	50
3.9	Discretization of Members (Model).	51
3.10	Discretization of Joints (Model).	51
3.11	Actual and Equivalent Loading for a Concentrated Transverse Force.	52
3.12	Computer Generated Finite Element Method.	54
3.13	Flow chart of the Computer Analyses.	56
4.1	Overall Dimensions of the Prototype Structure.	75
4.2	Member Configuration at Level # 6 and # 7 (Prototype).	76
4.3	3-D View Simulation (Prototype).	77
4.4	Overall Dimensions of the Model Structure.	82

4.5	Member Configuration at Level # 6 and # 7 (Model).	83
4.6	3-D View Simulation (Model).	84
4.7	Jacket Under Construction (A→B).	87
4.8	Deck Under Construction (C→D).	88
4.9	Completed Structure.	89
4.10	Base Connectors Before Attachment to Structure (E→F).	90
4.11	Base Connectors Being Assembled to Structure (G→H).	91
4.12	Weight Holders and Installed Base Connector.	92
5.1	Common Entities of the Experimental and Analytical Investigations.	95
5.2	Dimensions of the Wave Tank Facility.	97
5.3	View of Wave Tank Facility.	98
5.4	Wave Board Characteristics for a Set Span.	99
5.5	Servo Control Loop for the Wave Board.	100
5.6	Instrumentation, Free Vibration and Impact Locations.	102
5.7	Impact Testing in Progress.	104
5.8	Test Apparatus.	106
5.9	Experimental Circuit.	107
5.10	Typical Free Oscillation Response Curves in the X-Direction at A4 (In-Air Tests).	109
5.11	Typical Free Oscillation Response Curves in the Y-Direction at A5 (In-Air Tests).	110
5.12	Wave Tests in Progress.	115
5.13	Severed Member(s) in the Actual and Simulated Model.	116
6.1	Linear or Shaping Filter.	124

6.2	Typical Free Oscillation Response (Spiked and Despiked data —X-Direction, In-Water Tests).	135
6.3	Typical Free Oscillation Response (Spiked and Despiked data —Y-Direction, In-Water Tests).	136
6.4	Typical Windows Used to Process Impact Tests Results.	138
7.1	Dynamic Mode # 1 (Intact Prototype).	144
7.2	Dynamic Mode # 1 (Intact Model).	144
7.3	Dynamic Mode # 2 (Intact Prototype).	145
7.4	Dynamic Mode # 2 (Intact Model).	145
7.5	Dynamic Mode # 3 (Intact Prototype).	146
7.6	Dynamic Mode # 3 (Intact Model).	146
7.7	Dynamic Mode # 4 (Intact Prototype).	147
7.8	Dynamic Mode # 4 (Intact Model).	147
7.9	Dynamic Mode # 5 (Intact Prototype).	148
7.10	Dynamic Mode # 5 (Intact Model).	148
7.11	Dynamic Mode # 1 (Intact Model).	152
7.12	Dynamic Mode # 1 (Member 70 Removed).	152
7.13	Dynamic Mode # 2 (Intact Model).	153
7.14	Dynamic Mode # 2 (Member 70 Removed).	153
7.15	Dynamic Mode # 3 (Intact Model).	154
7.16	Dynamic Mode # 3 (Member 70 Removed).	154
7.17	Dynamic Mode # 4 (Intact Model).	155
7.18	Dynamic Mode # 4 (Member 70 Removed).	155
7.19	Dynamic Mode # 5 (Intact Model).	156
7.20	Dynamic Mode # 5 (member 70 Removed).	156

7.21	Dynamic Mode # 6 (Intact Model).	157
7.22	Dynamic Mode # 6 (Member 70 Removed).	157
7.23	Dynamic Mode # 7 (Intact Model).	158
7.24	Dynamic Mode # 7 (Member 70 Removed).	158
7.25	Dynamic Mode # 8 (Intact Model).	159
7.26	Dynamic Mode # 8 (Member 70 Removed).	159
7.27	Dynamic Mode # 9 (Intact Model).	160
7.28	Dynamic Mode # 9 (Member 70 Removed).	160
7.29	Dynamic Mode # 10 (Intact Model).	161
7.30	Dynamic Mode # 10 (Member 70 Removed).	161
7.31	X-Direction Dynamic Response of the Model and Prototype to Regular Waves (Using the Non-Linear and Linear forms of the Morrison's Wave Force Equation).	163
7.32	X-Direction Dynamic Response of the Model and Prototype to Regular Waves (Non-Dimensionalized displacement vs Non- Dimensionalized Time).	164
7.33	Non-Linear Force Variation Along the Jacket to a Single Wave (Non-Dimensionalized Force vs Non-Dimensionalized Time).	166
7.34	Linear Force Variation Along the Jacket to a Single Wave (Non-Dimensionalized Force vs Non-Dimensionalized Time).	167
7.35	X-direction Dynamic Response of the 3-D and Stick Model at Node 73 (Response of the Hydro-Elastic Model to Regular Waves).	168
7.36	Typical FFT Theoretical Acceleration Spectral Density due to wave Induced Vibration (Intact Structure: Using White Noise Spectrum)	170

7.37	MEM Theoretical Acceleration Spectral Densities due to wave Induced Vibration (Intact Structure: Using White Noise Spec- trum)	171
7.38	MEM Theoretical Acceleration Spectral Densities due to wave Induced Vibration (Damaged Structure: Member 70 Removed— Using White Noise Spectrum)	172
7.39	MEM Theoretical Acceleration Spectral Densities due to wave Induced Vibration (Damaged Structure: Members 70 and 68 Removed—Using White Noise Spectrum)	173
7.40	MEM Theoretical Acceleration Spectral Densities due to wave Induced Vibration (Intact Structure: Using JONSWAP Spec- trum)	174
7.41	MEM Theoretical Acceleration Spectral Densities due to wave Induced Vibration (Damaged Structure: Member 70 Removed— Using JONSWAP Spectrum)	175
7.42	MEM Theoretical Acceleration Spectral Densities due to wave Induced Vibration (Damaged Structure: Members 70 and 68 Removed—Using JONSWAP Spectrum)	176
7.43	Variation of Damping in the X Direction (In-Air Tests).	177
7.44	Variation of Damping in the Y Direction (In-Air Tests).	178
7.45	Average X and Y Direction Damping Ratio Variations (In-Air Tests—Using the Logarithmic Decrement Technique).	180
7.46	Variation of Damping in the X Direction (In-Water Tests).	182
7.47	Variation of Damping in the Y Direction (In-Water Tests).	183
7.48	Average X and Y Direction Damping Ratio Variations (In- Water Tests—Using the Logarithmic Decrement Technique).	184

7.49 Typical Measured Input Wave Spectrum at Wave Probe P1 (Measured White Noise Spectrum: Using Conventional FFT Procedures).	187
7.50 Measured Input Wave Spectra at Wave probes P1, P2 and P3 (Compared to the Theoretical, Target, White Noise Spectrum— Using MEM).	188
7.51 Typical Measured Input Wave Spectrum at Wave Probe P1 (Measured JONSWAP Spectrum: Using Conventional FFT Procedures).	189
7.52 Measured Input Wave Spectra at Wave probes P1, P2 and P3 (Compared to the Theoretical, Target, JONSWAP Spectrum— Using MEM).	190
7.53 Measured Input Wave from P1 and Output Acceleration From P4 (Results from the Regular Wave Tests).	191
7.54 A Comparison Between Experiment and Theory for the Reg- ular Wave Tests (NB: Node 73 on the Theoretical Model Cor- responds to the Position of Accelerometer A4).	193
7.55 Typical Time Domain Accelerations Measured With Accelerom- eters A1 to A4).	194
7.56 Typical FFT Experimental Acceleration Spectral Density due to Wave Induced Vibrations (Intact Structure: Using White Noise Spectrum).	195
7.57 MEM Experimental Acceleration Spectral Densities due to Wave Induced Vibrations (Intact Structure: Using White Noise Spectrum).	196

7.58	MEM Experimental Acceleration Spectral Densities due to Wave Induced Vibrations (Damaged Structure: Member 70 cut Half-Way at Node 18—Using White Noise Spectrum).	197
7.59	MEM Experimental Acceleration Spectral Densities due to Wave Induced Vibrations (Damaged Structure: Member 70 Severed at Node 18—Using White Noise Spectrum).	198
7.60	MEM Experimental Acceleration Spectral Densities due to Wave Induced Vibrations (Damaged Structure: Member 70 Severed and 68 cut-off at Node 16—Using White Noise Spectrum).	199
7.61	FFT Experimental Acceleration Spectral Densities due to Wave Induced Vibrations (Intact Structure: Using JONSWAP Spectrum).	200
7.62	MEM Experimental Acceleration Spectral Densities due to Wave Induced Vibrations (Intact Structure: Using JONSWAP Spectrum).	201
7.63	MEM Experimental Acceleration Spectral Densities due to Wave Induced Vibrations (Damaged Structure: Member 70 cut Half-Way at Node 18—Using JONSWAP Spectrum).	202
7.64	MEM Experimental Acceleration Spectral Densities due to Wave Induced Vibrations (Damaged Structure: Member 70 Severed at Node 18—Using JONSWAP Spectrum).	203
7.65	MEM Experimental Acceleration Spectral Densities due to Wave Induced Vibrations (Damaged Structure: Member 70 Severed and 68 cut-off at Node 16—Using JONSWAP Spectrum).	204

7.66 Results from Accelerometer A2 due to an Impact Initiated at H5 (Intact Structure).	208
7.67 Results from Accelerometer A3 due to an Impact Initiated at H5 (Intact Structure).	209
7.68 Results from Accelerometer A3 due to an Impact Initiated at H5 (Intact Structure).	210
7.69 Results from Accelerometer A4 due to an Impact Initiated at H5 (Intact Structure).	211
7.70 Results from Accelerometer A2 due to an Impact Initiated at H5 (Damaged Structure: Member 70 Severed at Node 18). . .	212
7.71 Results from Accelerometer A3 due to an Impact Initiated at H5 (Damaged Structure: Member 70 Severed at Node 18). . .	213
7.72 Results from Accelerometer A4 due to an Impact Initiated at H5 (Damaged Structure: Member 70 Severed at Node 18). . .	214
7.73 Results from Accelerometer A2 due to an Impact Initiated at H5 (Damaged Structure: Members 70 and 68 Severed at Node 18).	215
7.74 Results from Accelerometer A3 due to an Impact Initiated at H5 (Damaged Structure: Members 70 and 68 Severed at Node 18).	216
7.75 Results from Accelerometer A4 due to an Impact Initiated at H5 (Damaged Structure: Members 70 and 68 Severed at Node 18).	217
8.1 Dynamic Mode # 4 (Member 70 Removed).	222
8.2 Dynamic Mode # 4 (Members 70 and 68 Removed).	222

8.3	The Effect of Member 70 on Mode # 4.	223
8.4	The Effect of Member 68 on Mode # 4.	223
8.5	A Comparison of the Shift in Resonant Frequency at Node 23 Resulting from Damaged (Member 70 Removed—White Noise Test Simulation).	229
8.6	A Comparison of the Shift in Resonant Frequency at Node 23 Resulting from Damaged (Members 70 and 68 Removed— White Noise Test Simulation).	230
8.7	A Comparison of Acceleration Spectral Densities from A3 for the Intact and Damage Structure (Member 70 Severed). . . .	245
8.8	A Comparison of Acceleration Spectral Densities from A3 for the Intact and Damage Structure (Members 70 and 68 Severed). .	246
8.9	A Comparison of Spectral Levels of the White Noise and JON- SWAP Test Results Measured at A3.	247
C.1	Calibration Curve for the Impulse Hammer.	249
D.1	Dynamic Mode # 1 (Intact Model).	292
D.2	Dynamic Mode # 1 (Members 70 and 68 Removed).	292
D.3	Dynamic Mode # 2 (Intact Model).	293
D.4	Dynamic Mode # 2 (Members 70 and 68 Removed).	293
D.5	Dynamic Mode # 3 (Intact Model).	294
D.6	Dynamic Mode # 3 (Members 70 and 68 Removed).	294
D.7	Dynamic Mode # 5 (Intact Model).	295
D.8	Dynamic Mode # 5 (Members 70 and 68 Removed).	295
D.9	Dynamic Mode # 6 (Intact Model).	296
D.10	Dynamic Mode # 6 (Members 70 and 68 Removed).	296

D.11 Dynamic Mode # 7 (Intact Model).	297
D.12 Dynamic Mode # 7 (Members 70 and 68 Removed).	297
D.13 Dynamic Mode # 8 (Intact Model).	298
D.14 Dynamic Mode # 8 (Members 70 and 68 Removed).	298
D.15 Dynamic Mode # 9 (Intact Model).	299
D.16 Dynamic Mode # 9 (Members 70 and 68 Removed).	299
D.17 Dynamic Mode # 10 (Intact Model).	300
D.18 Dynamic Mode # 10 (Members 70 and 68 Removed).	300
D.19 Results from Accelerometer A1 due to an Impact Initiated at H6 (Intact Structure).	302
D.20 Results from Accelerometer A2 due to an Impact Initiated at H6 (Intact Structure).	303
D.21 Results from Accelerometer A3 due to an Impact Initiated at H6 (Intact Structure).	304
D.22 Results from Accelerometer A4 due to an Impact Initiated at H6 (Intact Structure).	305
D.23 Results from Accelerometer A1 due to an Impact Initiated at H6 (Damaged Structure: Member 70 Severed at Node 18). . .	306
D.24 Results from Accelerometer A2 due to an Impact Initiated at H6 (Damaged Structure: Member 70 Severed at Node 18). . .	307
D.25 Results from Accelerometer A3 due to an Impact Initiated at H6 (Damaged Structure: Member 70 Severed at Node 18). . .	308
D.26 Results from Accelerometer A4 due to an Impact Initiated at H6 (Damaged Structure: Member 70 Severed at Node 18). . .	309

D.27 Results from Accelerometer A1 due to an Impact Initiated at II6 (Damaged Structure: Members 70 and 68 Severed at Node 18).	310
D.28 Results from Accelerometer A2 due to an Impact Initiated at II6 (Damaged Structure: Members 70 and 68 Severed at Node 18).	311
D.29 Results from Accelerometer A3 due to an Impact Initiated at II6 (Damaged Structure: Members 70 and 68 Severed at Node 18).	312
D.30 Results from Accelerometer A4 due to an Impact Initiated at II6 (Damaged Structure: Members 70 and 68 Severed at Node 18).	313

List of Tables

4.1	Symbols, Units and Dimensions for Variables Used in Modelling.	64
4.2	Prototype Structural Data (Original Structure).	78
4.3	Prototype Structural Data (Modified Structure).	79
4.4	Model Structural Data (Based on Modified Prototype Structure)	81
4.5	Relevant Material Properties for ABS Plastic.	85
7.1	Natural Frequency Comparison of the 3-D Model and Prototype (Results Obtained from the Free Vibration Computer Analyses).	142
7.2	Natural Frequency Comparison of the 3-D and Stick Model (Results obtained from the Free Vibration Analyses).	143
7.3	Percentage Changes in Natural Frequencies when Certain members were Inactivated (Prototype).	150
7.4	Percentage Changes in Natural Frequencies when Certain members were Inactivated (Model).	151
7.5	X-direction Results From Free Vibration In-Air Tests (Using the Levenberg-Marquardt and Finite Difference Jacobian).	181
7.6	Y-direction Results From Free Vibration In-Air Tests (Using the Levenberg-Marquardt and Finite Difference Jacobian).	181

7.7	X-direction Results From Free Vibration In-Water Tests (Using the Levenberg-Marquardt and Finite Difference Jacobian).	185
7.8	Y-direction Results From Free Vibration In-Water Tests (Using the Levenberg-Marquardt and Finite Difference Jacobian).	185
7.9	MEM Damping Estimates from the Response Measured with Accelerometer A3 (Intact Structure).	205
7.10	MEM Damping Estimates from the Response Measured with Accelerometer A4 (Intact Structure).	206
8.1	Measured Resonant Frequencies from Accelerometer A1 (Results for the Intact and Damaged Structure: White Noise Tests).	234
8.2	Measured Resonant Frequencies from Accelerometer A1 (Results for the Intact and Damaged Structure: JONSWAP Tests).	234
8.3	Measured Resonant Frequencies from Accelerometer A2 (Results for the Intact and Damaged Structure: White Noise Tests).	235
8.4	Measured Resonant Frequencies from Accelerometer A2 (Results for the Intact and Damaged Structure: JONSWAP Tests).	235
8.5	Measured Resonant Frequencies from Accelerometer A3 (Results for the Intact and Damaged Structure: White Noise Tests).	236
8.6	Measured Resonant Frequencies from Accelerometer A3 (Results for the Intact and Damaged Structure: JONSWAP Tests).	236
8.7	Measured Resonant Frequencies from Accelerometer A4 (Results for the Intact and Damaged Structure: White Noise Tests).	237
8.8	Measured Resonant Frequencies from Accelerometer A4 (Results for the Intact and Damaged Structure: JONSWAP Tests).	237

8.9	Percent Changes in Resonant Frequencies Due to Damage (Results from Accelerometer A1: White Noise Tests).	239
8.10	Percent Changes in Resonant Frequencies Due to Damage (Results from Accelerometer A1: JONSWAP Tests).	239
8.11	Percent Changes in Resonant Frequencies Due to Damage (Results from Accelerometer A2: White Noise Tests).	240
8.12	Percent Changes in Resonant Frequencies Due to Damage (Results from Accelerometer A3: JONSWAP Tests).	240
8.13	Percent Changes in Resonant Frequencies Due to Damage (Results from Accelerometer A3: White Noise Tests).	241
8.14	Percent Changes in Resonant Frequencies Due to Damage (Results from Accelerometer A3: JONSWAP Tests).	241
8.15	Percent Changes in Resonant Frequencies Due to Damage (Results from Accelerometer A4: White Noise Tests).	242
8.16	Percent Changes in Resonant Frequencies Due to Damage (Results from Accelerometer A4: JONSWAP Tests).	242
8.17	A Comparison of the Resonant Frequencies obtained from the Experimental and Theoretical Results at Location A1 (White Noise and JONSWAP Tests).	251
8.18	A Comparison of the Resonant Frequencies obtained from the Experimental and Theoretical Results at Location A2 (White Noise and JONSWAP Tests).	252
8.19	A Comparison of the Resonant Frequencies obtained from the Experimental and Theoretical Results at Location A3 (White Noise and JONSWAP Tests).	253

8.20 A Comparison of the Resonant Frequencies obtained from the Experimental and Theoretical Results at Location A4 (White Noise and JONSWAP Tests).	254
D.1 MEM Damping Estimates from the Response Measured with Accelerometer A3 (Damaged Structure: Member 70 Severed).	315
D.2 MEM Damping Estimates from the Response Measured with Accelerometer A4 (Damaged Structure: Member 70 Severed).	316
D.3 MEM Damping Estimates from the Response Measured with Accelerometer A3 (Damaged Structure: Member 70 and 68 Severed).	317
D.4 MEM Damping Estimates from the Response Measured with Accelerometer A4 (Damaged Structure: Member 70 and 68 Severed).	318

List of Symbols

A	wave amplitude of a single wave Airy's wave
A_s	pseudo random infinitesimal amplitude associated with each cosine wave component
$\hat{A}(k)$	autoregressive coefficient for forward prediction of $x(t)$
$\tilde{A}(k)$	autoregressive coefficient for backward prediction of $x(t)$
\underline{A}	vector of autoregressive coefficients
$A(k)$	coefficients of AR model
$[a_{mm}]$	flexibility matrix of master degrees of freedom
$[a_{ss}]$	flexibility matrix of slave degrees of freedom
ABS	Acrylonitrile-Butadiene Styrene
B	maximum frequency content in a discrete time signal
B_s	pseudo random infinitesimal amplitudes associated with each sine wave component
C_i	$\underline{\phi}_i^T [c] \underline{\phi}_i$, modal damping
$[C]$	$[\Phi]^T [c] [\Phi]$, modal damping matrix
C_D	drag coefficient
C_I	inertia or mass coefficient
C	the structural damping constant
C_c	the structural critical damping constant
$C_{xy}(f)$	co-spectrum of $G_{xy}(f)$
D	external diameter of the cylindrical element

D_m	exterior diameter of a member in the model
D_p	exterior diameter of a member in the Prototype
d_m, d_p	wall thickness of the model and prototype, respectively
ds	incremental length of the section
E	modulus of elasticity of the structural material
\hat{e}	forward prediction error of AR model
\tilde{e}	backward prediction error of AR model
$\underline{F}(t)$	$\{\Phi\}^T \underline{f}(t)$, modal force vector
\vec{F}_D	drag component of the wave force
\vec{F}_I	inertia component of the wave force
F_n	force at degree of freedom n
F_t	instantaneous force at time t
\underline{F}^*	equivalently lumped nodal force vector
f_s	sampling frequency
f_{max}	maximum cut-off frequency
f_r	resonant frequency
f_0	peak frequency of JONSWAP spectrum
$\underline{f}(t)$	nodal force vector
$\underline{f}_m(t)$	input force vector at master nodes
$\underline{f}_s(t)$	input force vector at slave nodes
\underline{f}_m	master nodes force vector

$G_{xx}(f)$	autospectral density of $x(t)$
$G_{xy}(f)$	cross-spectral density between $x(t)$ and $y(t)$
g	gravitational acceleration
H_w	wave height
$H(f)$	transfer function
H_s	significant wave height
h_w	mean water depth
$h_{w,m}$	mean water depth for the model
$h_{w,p}$	mean water depth for the prototype
$[I]$	identity matrix
\vec{i}	unit vectors in the x direction
\vec{j}	unit vectors in the y direction
j	$\sqrt{-1}$
$[K]$	$[\Phi]^T[k][\Phi]$, modal stiffness matrix
$[K]^*$	condensed stiffness matrix (i.e., stick model stiffness matrix)
K_i	$\phi_i^T[k]\phi_i$, modal stiffness
k	wave number
$[k_{ss}]$	stiffness matrix of slave variables
$[k_{mm}]$	stiffness matrix of master variables
$[k_{sm}]$	stiffness matrix of slave and master variables
L_s	characteristic length of structural component being investigated

$L_{s,p}$	characteristic length of a structural component in the prototype
L.L.F.	lower limit frequency
$L_{s,m}$	characteristic length of a structural component in the model
M_i	$\phi_i^T[m]\phi_i$, modal mass
M	order of the AR model
$[M]^*$	condensed mass matrix (i.e., stick model mass matrix)
M_{opt}	optimum model order
<i>MEM</i>	Maximum Entropy Method
$[M]$	$[\Phi]^T[m][\Phi]$, modal mass matrix
N	number of samples
n	$1, 2, 3, \dots, N$
$[0]$	null matrix
P_M	output error power
$Q_{xy}(f)$	quad-spectrum of $G_{xy}(f)$
$\underline{q}(t)$	time dependant vector of modal amplitudes
q_i	modal amplitudes
$R_{xx}(\tau)$	autocorrelation function of the input
$R_{yy}(\tau)$	autocorrelation function of the output
$R_{xy}(\tau)$	cross-correlation function between input and output
$S_J(f)$	input JONSWAP wave spectrum
$S_W(f)$	input white noise wave spectrum

s	$0, 1, 2, \dots, N/2$
$[T]$	transformation matrix
T_w	wave period in seconds
T_s	structural period in seconds
$T_{s,p}$	prototype structural period in seconds
$T_{s,m}$	model structural period in seconds
t	time
\vec{U}	instantaneous velocity vector of the water
$\vec{\ddot{U}}$	instantaneous acceleration vector of the water particles normal to the axis of the member
U_0	maximum orbital velocity at the free surface
\dot{U}_0	maximum orbital acceleration at the free surface
u_t	instantaneous displacement at time t
u	water particle velocity component in the x direction
\dot{u}	water particle acceleration component in the x direction
v	water particle velocity component in the y direction
\dot{v}	water particle acceleration component in the y direction
$w(n)$	discrete-time white noise
\vec{X}	instantaneous velocity vector of the structural member
$X^*(f)$	complex conjugate of $X(f)$
$[X]$	Toeplitz autocorrelation matrix of AR model
$\vec{\ddot{X}}$	acceleration vector of the incremental section

$\hat{x}(t)$	forward prediction estimate of $x(t)$
$\tilde{x}(t)$	backward prediction estimate of $x(t)$
x	displacement in the x direction of the incremental section
x_1	x coordinates of a structural joint
\dot{x}	velocity of the incremental section in the x direction
$x(n)$	output of AR filter, true or desired value
\ddot{x}	acceleration of the incremental section in the x direction
$\ddot{\underline{x}}_s$	acceleration vector of slave degrees of freedom
$\ddot{\underline{x}}_m$	acceleration vector of master degrees of freedom
\underline{x}_s	displacement vector of slave degrees of freedom
\underline{x}_m	displacement vector of master degrees of freedom
\underline{Y}	vector of M previous and M future observations of $x(t)$
\ddot{y}	acceleration of the incremental section in the y direction
y	displacement in the y direction of the incremental section
y_1	y coordinate of a structural joint
\dot{y}	velocity of the incremental section in the y direction
z	surface elevation above the mean sea level
z_1	z coordinate of a structural joint
α	arbitrary phase angle
Δt	data sampling interval
Δf	frequency resolution
ϵ	the distortion factor

η	instantaneous water level above the mean sea level
γ	peak enhancement factor for the JONSWAP spectrum
$\gamma_{xy}^2(f)$	coherence function squared
ν	kinematic viscosity of the liquid
ω	circular frequency of the wave
ω_s	wave component circular frequency, $\frac{2\pi s}{N\Delta t}$
$[\Phi]$	mode shape matrix of N modal vectors of length N
ϕ_i	mode shape vector for mode i
ρ_w	density of liquid
ρ_s	density of structural component
$\rho_{s,m}^*$	required material density of the model
$\rho_{s,p}$	material density of the prototype
$\sigma^2(k)$	white noise variance or prediction error
τ	time lag between sample values
θ	angle of propagation of the wave with the +ve x-axis
θ_{xy}	phase angle between input and output
ζ	structural damping ratio (non-dimensional)
ζ_{HP}	half power structural damping estimate
ζ_{LD}	logarithmic decrement structural damping estimate
ζ_m	model structural damping ratio
ζ_p	prototype structural damping ratio

Chapter 1

Introduction

The approach to design in structural engineering could be divided into four categories. Foremost, for small structures, where safety is almost inherent and where ultimate collapse is unlikely, a heuristic approach is common. In the second category, very common for small structures, tables of data and coefficients derived from simplified or semi-empirical theories are used in design. Third, a computer aided approach may be used for larger and more complex structures, where accurate and sophisticated analyses and theories are used. Finally, if the design of an unusual or unique structure is required (or where inaccurate analyses could cause catastrophic consequences), a computer aided design, combined with a model testing and analysis approach, is used.

When little or no experience has been gained from similar existing structures, an assessment of the probable dynamic performance is often made. In such cases, vibration tests on small scale model structures can provide invaluable data. For instance, if no established reliable theoretical approach exists for the analysis of particular structural forms (often the case for recently devised systems), if only a limited number of a particular structural type have been constructed, or if only a short history of the performance has

been recorded, then it is beneficial to compare calculated design quantities, or data from existing structures with results from tests on model structures. Such models can be used to test mathematical models; to find possible effects of structural modifications; or to provide design quantities directly.

Furthermore, since offshore structures are costly and the environmental conditions in which they have to operate are hostile, it is very important that all available knowledge and experience are used in their design. Evidently, computer programs can be written to evaluate stresses in the structure for various conditions of wave and current forces acting on the structure. Still, the vibrational characteristics of the structure are usually difficult to analyze. These vibrations, which can be induced by vortex shedding as the sea flows past structural members, can cause fatigue failure. To gain confidence in a proposed design before fabrication commences, or to gain some understanding of the vibration characteristics of an existing offshore structure, it is, therefore, desirable to build a scale model, and to test it under realistic sea conditions in a tank with a pseudo random wave-making facility. In this treatise, the model testing and analysis approach is adopted.

1.1 Background

Increased activity to explore hydro-carbons in the ocean has resulted in structures being installed in deeper waters and more hostile environments. Thus, unless some cheaper alternative source of energy (not oil or gas) is found, this affinity towards the ocean is expected to increase in the future. Developments in water depths over 300 m are using compliant structural concepts, such as guyed tower platforms, tension leg platforms, or dynamically positioned semi-submersible structures. Future developments may use sub-

mersibles, sea bed, and submarine facilities. Nonetheless, over the past few years, several conventional fixed platforms have been installed in water depths around 300 m. If there is damage to the subsurface structural component(s), the difficulty of inspection to detect the failure increases commensurately with water depth, and the inspection procedure—to detect the damaged component(s)—becomes more expensive and more perilous. Classical techniques, such as ultrasonic measurements or magnetic particle inspection, only give partial results. In addition, they require long diving operations and long periods of good weather. Furthermore, these inspection procedures are usually thwarted by poor visibility, poor lighting and hazardous conditions; for example, very low water temperatures and large water depths. Besides, marine growth and corrosion may conceal structural defects, and the following questions remain unanswered:

- are there any failure on an unexplored part of the structure?
- does the detected crack or failure requires immediate repair?

Cyclic loading, or a very large single load, can damage structures by promoting cracks in certain load carrying member(s). Large stresses occur when a structure vibrates at one of its resonant frequencies. Since each member contributes to the mass, damping and stiffness of the structure, any damage to a member could result in measurable changes in the structural dynamical properties.

Techniques now exist to measure the dynamic properties of a structure, and to represent the structural dynamic behavior in terms of its modes of vibration. Identification of these vibration modes, within a specified frequency range, quantifies the structures over the given frequency spectrum.

Associated with every vibration mode is a mode shape and its corresponding frequency and damping. Therefore, by accurately monitoring these modal parameters and comparing them to a datum, so any changes can be detected, it is possible to detect damage in the structure. The structural integrity method is epitomized, diagrammatically, in Figure 1.1.

1.1.1 Possible Causes of Structural Damage

During severe storms, structural components may be subjected to forces which exceed the designed loads, and could result in damage of the member(s). In addition, damage of offshore structures could be caused by accidents or, at times, sabotage. Some of the causes reported from the field are discussed:

- The chances of mechanical damage resulting from dropped objects or collision by barges and workboats are significant [1]. About 40% of the damage reported were caused by collision with other objects.
- Defects induced during service are another potential cause of failure of large steel structures. The common mechanisms which cause damage are fatigue, corrosion, fretting, stress corrosion, etc. These create surface cracks that can lead to failure on collision.
- Damages caused by explosion are as frequent as collisions and weather damages. It has been shown [2] that columns and beams loaded to normal design units will collapse when the temperature reaches 500–550°C.

The type of damages that could occur are: (i) failure of a single bracing, (ii) deformation of the corner leg, or both. During impact, the steel structure

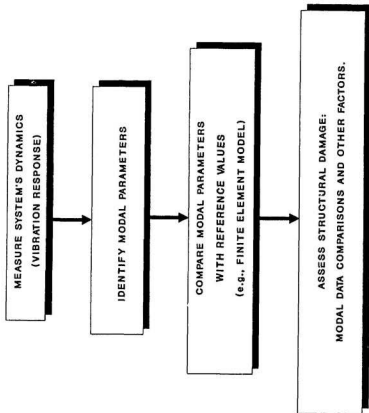


FIG. 1.1 IMPORTANT STEPS OF STRUCTURAL INTEGRITY MONITORING.

absorbs the energy in the following ways:

1. local deformation of the cross section of the bracing or leg,
2. global deformation of adjoining frame, and
3. overall deformation of the platform.

The extent of local damage and energy absorption of the platform members depend on the nature of the impact.

1.2 Scope of the Work

1.2.1 Modelling the Structure

Since it is not possible, as a result of the limited time constraint, to carry out tests on an actual operating structure in the ocean, an alternative solution is to experiment on a reduced model of an offshore tower in a wave tank equipped with a pseudo random wave-making facility.

The most common type of scale models which has been previously built for testing in a wave tank is one which simulates the geometrical outside shape of the structure (i.e., a geometrically similar model). This type of model is usually mounted on a special balance built into the floor of the tank, which measures the forces and moments on the structure resulting from waves and tides. Notwithstanding, the limitation of a geometrically similar model is that only the undistorted non-vibrating shape of the structure is simulated; so any effects resulting from the deflection of the structure or the vibration of its structural components (members) are not reproduced by the model. A much better scale model is one fabricated to deflect in a similar manner, and to exhibit the same vibrational characteristics of the prototype structure.

Such a model is called a dynamically similar or hydro-elastic model. This treatise deals with the design, construction, instrumentation and testing of such a model to carry out *Structural Integrity Monitoring*.

To achieve this objective, a 1/30th scale hydro-elastic model (made from **ABS** plastic) was constructed to simulate the dynamic behavior of a typical 73 m (240 ft), four legged offshore tower. The model was tested in a wave tank equipped with a pseudo random wave making facility. Ocean wave conditions were simulated with regular and irregular waves. For the irregular waves, two different input wave spectra were used: 1) a JONSWAP spectrum, and 2) a white noise spectrum.

A very extensive FORTRAN computer program (using a combination of wave mechanics and structural mechanics) was written to simulate the experimental conditions, and to obtain theoretical estimates of the dynamic behavior of the model structure; so a comparison between experiment and theory could be made.

Regarding integrity monitoring to detect damage of subsurface structural component(s), global monitoring was used.¹ Global Monitoring is based on an accelerometric unit located on the deck of the structure excited by ambient vibration. However, to get a better picture of the global motion, and to increase the sensitivity/resolution in the resonant frequency variations resulting from damaged member(s), three accelerometers were also installed along the jacket. One was placed at the node where the jacket and the deck meet (i.e., at the mean water level), and two were installed (below the water) at the top and bottom of the bay containing the member(s) chosen to simulate

¹An example of permanent global monitoring is on the BARBARA platform in the Adriatic Sea, in 70 m of water. From the analyses of the data collected, four resonant peaks were detected, although they were out of range of the wave frequencies [3].

structural damage. Structural damage was simulated by physically saw-cutting the member(s) under consideration in the experimental model. (In the computer model, damage was simulated by making the member(s) under consideration inactive in the analyses.) Estimates of modal parameters—i.e., resonant frequencies, damping, etc.—from the ambient structural response data were attained using the recently developed Marple algorithm with the Maximum Entropy Method (MEM).

1.2.2 Estimation of Modal Parameters

Estimates of resonant frequencies and damping ratios obtained from the ambient response spectra of a structure by conventional FFT methods (Blackman and Tukey [4]), have been shown to be inherently limited in resolution [18, 72]. This results because of the required truncation of the estimated autocorrelation function, and the implicit extension of the truncation of the function to infinite lag with zeros. However, by applying the recently developed Marple Algorithm for autoregressive spectral analysis, with the (very powerful) Maximum Entropy Method (MEM), the resolution of the autocorrelation function can be improved by analytically extending the function from its truncated point to infinite lag in a more realistic manner. It is this extension of the autocorrelation function which forms the basis of the MEM method.

1.2.3 Thesis Outline

This treatise is divided into nine chapters. The first (Introduction) has already been presented. In Chapter 2, a literature review—which summarizes the results, conclusions and recommendations of previous investigators—is

presented.

Chapter 3 contains the theoretical modelling of the problem at hand. Theoretical formulations based on wave and structural mechanics, applicable to the research, are shown. Besides, a description of the computer implementation to obtain theoretical estimates is given.

Chapter 4 discusses the physical modelling. This includes the development of the modelling laws, difficulties associated with hydro-elastic modelling, and the design and fabrication of the experimental hydro-elastic model.

In Chapter 5, a description of the experimental study is presented. This incorporates a brief description of the instrumentation used in both the in-air tests, to obtain free oscillation damping factors, and in-water tests, to study the dynamic behavior of the structure due to wave action.

Chapter 6 focuses on the analysis of the results. Theory formulations, which include the Maximum Entropy Method (MEM), are explained and their applications (in this dissertation) shown.

The theoretical and experimental results are presented in Chapter 7. An evaluation of these results is given in Chapter 8. And, finally, concluding remarks and recommendations for future research are outlined in Chapter 9.

Chapter 2

Literature Review

Structural integrity monitoring of offshore oil and gas drilling platforms is not without precedence. Loland and Mackenzie [5] experimented on a k-braced offshore model rig from which natural frequencies were computed for the complete structure, and then with a single k-brace in one face removed. Sudden changes in frequencies were observed, particularly the higher ones. Percentage changes as high as 30% were shown; the frequency most affected depended on the location at which the brace was removed. Begg *et al.* [6] dealt with the theoretical ideas and assumptions from which structural integrity monitoring, using vibration analysis, had been developed. At a later symposium (1978), Begg and Mackenzie [7] presented a state-of-the-art discussion of the technique as applied to steel structures and showed possible ways to apply the method to concrete offshore platforms.

Loland and Dodds [8] discussed operating experiences, and presented some of the results obtained from a structural integrity system, which had been used for 6–9 months on three platforms in the North Sea. The objective of that experiment was to extend the laboratory and computational studies of Loland *et al.* [9]. Loland, Mackenzie and Begg (*ibid.*) experimented on a k-braced model of an offshore platform in the laboratory. Changes in natu-



ral frequencies occurred when member(s) in the k-brace was/were removed. They concluded that these changes were large enough to be detected reliably, and that the method should give positive indication of structural failure.

A state-of-the-art discussion (which focussed on possible limitations of the technique in an offshore environment) is presented in Reference [10]. For example, Begg showed that the higher frequencies involved only a small component; so modes involving underwater members cannot be measured, much less identified, from positions above the water line. Begg and Mackenzie [11] showed that under normal circumstances, vibration monitoring provides a back-up assurance of the ability of the platform to withstand major wave loading. As a result, to obtain an assurance of the possible degree of accuracy, it is very necessary that the dynamic characteristics of the platform be completely understood, so a good datum is obtained for later comparisons. Hence, it is necessary to calculate the sensitivity of the platform at various locations in order to provide a basis for identifying the damage from changes in the vibration spectra.

A short study was carried out by Lock and Jones [12] to investigate the feasibility of using vibration monitoring for assessing the structural integrity (stiffness) of oil production platforms, especially those constructed of steel. To achieve this objective, experimental work was done on a space frame model constructed from 3.8 m and 1.9 m 16 gauge steel tubes. The model was 3.8 m long with 0.9 m wide sides and weighed 46.0 kgf. Based on the results obtained, they suggested that monitoring the vibration of an oil production platform would provide information about its condition. Notwithstanding, the major impediment to the success of the method would be estimating the degree of change in the natural frequency of any particular mode, since mode

identification, in these structures, would be difficult (*ibid.*).

Wooton *et al.* [13] discussed the developments that have taken place in using vibration analysis to discern structural failure, and showed the way in which these techniques could be applied more widely. Brown [14] reviewed the various schemes, and outlined the results of recent work in the North Sea. The scope of the work included a theoretical dynamic analysis of the structure, the design, installation and performance of a vibration monitoring system, and the computer analysis of measured vibration spectra to monitor the integrity of the installation. Vandiver *et al.* [15] presented a detailed study of an offshore pile-supported tower. The tower consisted of a welded steel space frame with four primary legs braced with horizontal and diagonal members. It was fixed to driven steel piles and stood 45.72 m above the mud-line in 21.34 m of water, and weighed 5,978.4 kN. Statistical energy analysis was introduced as a method for producing the dynamic response of a wide variety of fixed and floating platforms to random waves. Note that statistical energy analysis provides a means for estimating the maximum energy that a resonant structural mode may have, independent of the structural geometry, and dependent only on the wave height spectrum and frequency (*ibid.*).

In Reference [16], a study of vibration and damping in offshore structures is involved, which includes laboratory measurements made on a model platform (in and out of water), and a full scale platform in the North Sea. The results were used to help in designing vibration analysis monitoring systems.

Experiments were conducted on an operating eight-leg 115 m tall platform in the Gulf of Mexico by Rubin [17]. This was the first part of a pilot study to examine the feasibility of ambient vibration monitoring, so periodic assessment, from a structural integrity viewpoint, could be done. The modes

detected from the data recorded (lateral, vertical and angular sensors) from force transducers at 17 locations above-water on the structure were used to provide a basis for a future analytical phase.

Vandiver and Campbell [18] introduced the Maximum Entropy Method (MEM) of spectral analysis as a powerful technique for estimating the dynamic response properties of offshore platforms. This method was presented in making estimates of natural frequencies and damping ratios for three similar U.S. Navy air combat maneuvering range platforms near Cape Hatteras, North Carolina. Note that MEM has proved the capability of producing smooth high resolution response spectra from short time histories of deck acceleration. Also, this capability to use short record lengths substantially decreases inherent errors arising from the necessary assumption of stationary wave excitation forces (*ibid.*).

Irwin [19] examined the various methods of conducting tests on small scale structures and the details of simple, low cost vibrating systems suitable for tests on stiff models were presented. The analysis and interpretation of the data derived from such experiments were also considered. In reference [20], a rational evaluation of the structural integrity of an offshore structure, using vibration measurements, was done for the USCG Ambrose Tower—a four-legged fixed platform at the entrance to New York harbour. A mathematical model of the structure was analyzed with the SAP IV computer program while considering the effects of mass, entrained water, soil support conditions, equipment, etc. Also, the various parameters affecting the lower-mode vibration characteristics of the structure were examined separately, and their quantitative influence on the structure were investigated. From the results attained, it was verified that the vibration analysis of an offshore

structure, used with on-board vibration measurements, is an efficient method to establish the integrity of the structure. Moreover, they suggested that the determination of the causes for any subsequent frequency changes provides an early warning system to detect potentially hazardous damages, and the technique illustrated for a fixed platform is completely general. Accordingly, it may be extended and applied to other structures such as jack-ups and semi-submersibles.

Vandiver [21] showed that the error involved in estimating the changes in live loads on the structure is one of the main limitations encountered when correlating shifts in natural frequency with structural damage. In particular, the liquids in large storage tanks are identified as serious sources of error. A correlation procedure, which accounts for the sloshing of the liquid, was presented and substantiated by experimental data. It was also proposed that properly designed liquid storage tanks may be useful as dynamic absorbers in suppressing structural response. In a later publication, Vandiver *et al.* [22] presented a detailed analytical procedure to account for the effects due to liquid storage tanks mentioned previously. From the results obtained, they deduced that in particular cases where the lowest mode of the tank is near the flexural fundamental of the structure, a splitting response peak occurs and the nature of the *split peak* varies with small changes in the depth of the water in the tank. It was suggested that, to a lesser extent, similar phenomena could occur if the higher modes are tuned to the structural natural frequencies. Though their analysis had been shown only for the fundamental flexural mode, the authors implicate that similar behavior is expected for torsional and higher-order flexural modes as well.

The scope and results of two joint-industry research projects is discussed

by Duggan *et al.* [23]. This study investigated the feasibility of using ambient surface vibrational measurements to evaluate the integrity of steel template platforms in the Gulf of Mexico. Specifically, the projects sought to establish whether the vibrational behavior of the platform remained stable under varying environmental and operating conditions, but changed because of structural modification. It was acknowledged, based on the results examined from the projects, that the state-of-the-art ambient vibrational monitoring techniques failed to detect the removal of jacket members on the SS274A platform. Yet, at a later symposium (Reference [24]), Duggan *et al.* described further work intended to improve the basis for extrapolation of the project mentioned in the previous publication (i.e., Reference [23]). To achieve this objective, a detailed analysis was carried out on the vibrational data from another platform—Conoco’s Main Pass 296A (MP296A)—in the Gulf of Mexico. The results of the analysis showed excellent frequency and mode shape stability of the first and second order modes of vibration as measured over a six month period. But, the frequencies and mode shapes of the third order modes were not observed to be sufficiently stable for use in integrity monitoring. Moreover, the number of peaks in the response spectra of the platform exceeded the number of identified modes. For instance, several groups of peaks were classified as corresponding to single mode shapes (split peaks). This *split peak* effect was observed consistently for two of the fundamental modes and for the third order modes. The exact cause of the behavior was not identified, but several possible causes were postulated. It was concluded that while it is possible to observe stable vibrational behavior up to, at least, the second order modes on certain Gulf of Mexico platforms, it is unlikely that surface ambient vibrational integrity monitoring would be

a practicable prospect.

Campbell and Vandiver [25] focussed on the estimation of natural frequencies and damping ratios from measured response spectra, with particular emphasis on the dynamic response of offshore structures to wind and wave loading. They showed that present estimate of damping ratios, computed from half-power band width of resonant peaks in the ambient power spectrum of a structure, are highly sensitive to the method employed in estimating the response spectrum. An alternative method, based on the Maximum Entropy Method (MEM), was presented. The technique provided estimates of natural frequencies and modal damping ratios, also approximate statistics of the reliability of the estimates. Coppolino and Rubin [26] studied the Shell platform SP-62C in the Gulf of Mexico. To detect ambient vibration during normal producing operation, the platform was instrumented with sensors at seventeen locations, between the decks and the boat landing level. The purpose of that investigation was to report on the damage sensitivity of the structure. Therefore, a detailed structural dynamic finite-element model of the structure (SP-62C), with adjustments for improved correspondence with the experimental modes, was developed. This mathematical model of the structure was employed to simulate the effect of the severance of a representative set of 32 members. The changes in the natural frequencies of the lowest 25 modes of vibration were predicted. Judgements based upon the field experiments were then made, regarding the likelihood of detection of damage using ambient vibration monitoring. In addition, to broaden the outlook about fracture sensitivity, simplified models of generic jacket-framing configurations were analysed. This approach enabled the determination of the fundamental mode sensitivity for failures of vertical diagonal members. The

validity of the results was compared to known results from actual platforms. It was also possible to determine the maximum increase in member loading resulting from such failure. These results were most helpful in putting the frequencies and load sensitivities into a general perspective.

Reference [27] discussed the main features of a joint research project undertaken in 1980 by Lepert *et al.* about techniques using the dynamic properties of an offshore steel structure to detect structural damage. A relation was established between the occurrence of a failure and the modification of the dynamic properties of the structure. Based on many parts of experiments, using the scale model of a platform, and on modal analysis theory, the investigation showed that such a relation exists which depends on the size and position of the defect. From that investigation, two methods for the mechanical detection of damages were presented and compared, both from the technical and economical viewpoints. A third method, using the adjustment of a theoretical model by the measured modal parameters, was proposed to monitor the residual integrity for a damaged platform. Next vibro-detection was presented as a powerful tool for future offshore surveys, and an efficient complement to the conventional non-destructive testing methods. It was emphasized that the technique can directly relate any structural damage to the resulting loss of integrity of the affected structure.

Burke *et al.* [28] presented a least-squares method for calculating a response shape vector at each discrete frequency of the matrix auto and cross-spectral density functions. The resulting shape vectors provided: (1) a single function of frequency (the squared norm) for displaying peaks in the spectral density function, (2) a quantitative measure of the mode shape associated with the peaks, and (3) a measure of the goodness of fit of the vector data.

These results provided a quantitative and greatly simplified basis for interpretation. Furthermore, a derivation of the method, a description of its design (including a listing of FORTRAN computer code), an example using measured data, and suggestions for further developments were presented (*ibid.*). It should be mentioned that the examples illustrated the capability of the method to quantify mode shapes, difficulties associated with distinguishing between closely spaced modes, and the degree to which the resulting response shapes are stable in time. Additional work was done by Burke and Sosdian [29] in 1982 to define more than one shape vector at a particular frequency, in order to expand the capabilities for quantifying mode shape information. The purpose of this updated development was to reduce the recorded ambient vibration structural data to a form that would allow quantitative evaluation of mode shapes and natural frequencies of the structure. This paper includes: 1) the theoretical model, 2) a derivation of the non-linear, least-squares solution method, and 3) the formulation and implementation of synthetic ambient vibration data reported in the previous paper (i.e., Reference [28]). The results showed the capabilities and limitations of this least-square method for identifying mode shapes.

Two new methods (vibro-detection, and modal analysis) were field tested on a living quarters platform in the Arabian Gulf by Crohas and Lepert (1982). Reference [30] describes the concepts, equipment and operating procedures developed, and the significant results obtained. It was concluded that the full-scale experiments, using vibro-detection and modal analysis, have shown that the techniques have considerable capability for structural integrity monitoring, and potential as design aids and increase efficiency and cost savings in periodic surveys. They also suggested that although the tech-

niques are immediately useful, they are still in their infancy stages and should see substantial developments, in terms of refinement and wider applications. Briggs and Vandiver [31] presented the results of an extension of the single channel Maximum Entropy Method (MEM) to multichannel applications. A transfer function¹ estimate using the multichannel MEM was used in mode shape identification for an Amoco Offshore Caisson platform located in 27 m of water in the Gulf of Mexico. Comparison of these relative acceleration magnitudes to the relative displacements amplitudes, obtained from a finite element model of the Caisson platform, gave reasonable agreement. It was suggested that the MEM technique can be a useful tool (with the cross-spectral estimates of magnitude, phase and coherence) in mode shape identification for offshore platforms. Cook and Vandiver [33] made a detailed investigation of the dynamic response characteristics of an operating single pile platform. Wind, wave and response time histories recorded on the platform formed the basis for comparison of predicted and measured response. In the predictive analysis, the components of the total modal damping were separately computed. These damping components included the steel hysteretic damping, the wave radiation, the viscous hydrodynamic, and the soil damping. Responses in the two fundamental bending modes of the structure were predicted applying the principle of reciprocity for ocean waves. Good agreement between the predicted and measured response levels was attained. Note that the combination of the results of the response prediction method with a dynamic finite element model of the platform lead to a versatile expression for the mean rate of accumulation of fatigue damage.

¹Transfer function estimates, obtained from multichannel spectral analysis, are superior with that obtained using auto-spectral methods in their relative insensitivity to input and output noise [32].

In 1983, Nataraja [34] carried out a program of structural integrity monitoring through vibration measurements of three fixed steel platforms in the North Sea. His objectives were to develop monitoring systems to operate continuously over a period of two years and to prove the feasibility of such systems to detect structural damage. The results showed that only the lowest natural frequencies could be identified without ambiguity, and these frequencies were stable throughout the monitoring period. Temporary reduction of these frequencies, caused by an increase in deck mass associated with drilling activity, was detected. It was suggested that deck mass should be monitored to distinguish the frequency variation associated with primary structural damage and foundation stiffness reduction. It was acknowledged that the vibration monitoring systems consisting of accelerometers at the water surface and deck of the structure can only detect global changes. Nevertheless, ambient monitoring systems were recommended for continuous monitoring of the global condition of an offshore platform (*ibid.*).

Jones *et al.* [35] described the latest safety and performance monitoring techniques that are employed on structures and vessels engaged in Canadian offshore oil and gas exploration projects. The results of several monitoring programs were discussed. In reference [36], a system identification technique which uses a state space equation was used. It was proposed that once the eigenvalues and eigenvectors of the system are determined, the mass, stiffness and damping can be obtained. Hence changes of the matrix elements will provide the identification of the location and severance of the structural damage. Moan *et al.* [37] presented a brief description of the likely conditions for offshore steel platforms. The theoretical basis for two finite element methods for non-linear collapse analysis was presented, followed by a brief outline of

the system behavior of trusswork platforms. Shahrivar *et al.* [38] applied the structural integrity monitoring technique to a 1/50th scale plastic model representing the structural system of a typical full-scale tower in 66 m of water. The effect of severance of diagonal bracing members on selected frequencies and mode shape parameters, measured at the deck, were presented.

In 1988, Tsai *et al.* [39] presented a system identification technique for detecting and characterizing the existence and location of crack damages in offshore structures. Numerical and experimental tests were carried out on a 1/14th scale model of an offshore platform in the Gulf of Mexico. Significant changes in both the mass and flexibility of the identified system mathematical model were found after a through-cut damage was created on one horizontal bracing. These results were consistent to that obtained experimentally. Based on the results obtained, they concluded that the technique was useful in identifying, localizing and, also, evaluating the damage for an offshore platform.

2.1 Practical Limitations

There are limitations to the *Structural Integrity Method* in its practical applications. Some of these are discussed and, where possible, solutions are suggested. Resonant Frequency changes may occur due to reasons other than primary structural damage—e.g., soil foundation failure and changes in deck mass.

Soil Foundation Failure. A possible solution is to use a computer model with two or three resonant frequencies. The type of failure may be deduced by examining the relative shifts in frequency. For instance, if the

elastic properties of the soil change, they will influence the flexural resonant frequencies in both the x and y directional modes. Whereas, a damaged member may often contribute principally to stiffness in one direction only. Computer models present the means for drawing the correct conclusions from experimental evidence.

Changes in Deck Mass. Changes in live loads on the deck of the structure is one of the main limitations encountered when correlating shifts in resonant frequencies with structural damage. The addition of significant mass of drilling equipment and consumables may cause shifts in certain resonant frequencies (particularly the fundamental sway and torsional modes). However, the frequencies that are affected will return to their original values once the extra mass is removed. To detect whether those frequency shifts mentioned above were attributable to the extra masses, strain gauges could be mounted near the top of the main legs to detect changes in topside mass.

Besides these periodic deck mass changes discussed above, liquid in large storage tanks has been identified as serious sources of error [21]. This results if there is a coupling between the platform resonant frequencies and the sloshing liquid in the storage tanks. These effects on resonant frequencies are exhibited as split peaks in the mode(s) affected (*ibid.*). Such changes could give erroneous indications that the structure had been damaged, when, in fact, it has not. To eliminate the problem, measures should be taken to isolate the sloshing problem mentioned above. A possible solution is to use computer models with the measured data from the actual structure. Vandiver (*ibid.*) has developed an analytical method which could be used to isolate the influence of the sloshing liquid on the resonant frequencies.

Chapter 3

Theoretical Modelling

This chapter presents the mathematical modelling of the problem. The theoretical formulations based on wave and structural mechanics, applicable to the investigation, are given. In addition, a description of the computer implementation (to obtain theoretical estimates of the dynamic behavior of the structure) is presented.

3.1 Wave Forces

Wave forces on offshore structures are commonly computed using linearized wave theory. Generally, three different methods are used: 1) Morrison-O'Brien's theory, 2) Froude-Krylov Hypothesis and 3) Linear Diffraction theory. The Morrison-O'Brien's theory considers the force as being composed of an inertia and drag component linearly added. This method is usually applicable to smaller objects (i.e., smaller compared with the wave length). If the inertia forces predominate, but the object is still not very small, the Froude-Krylov approach (F-K theory), using pressure-area method on the surface of the object, is used. However, a force coefficient dependent on experimental data is required to include the effects of added mass and

wave diffraction. For larger objects (i.e., larger compared with the wave length) linear diffraction theory, using numerical techniques, is used. Here, the Laplace's equation is solved with appropriate boundary conditions in terms of a total potential which is the sum of an incident and reflected potential. This method may be mathematically more pleasing and desirable, but, the first two methods, mentioned previously, are more readily used.

In this treatise, the wave forces on the structure are calculated using the Morrison-O'Brien's equation. The inertia term includes an inertia coefficient, C_M ; the drag term involves a drag coefficient, C_D . Morrison *et al.* [74] first used the equation to calculate the forces on a vertical cylinder subjected to waves. Since then it has been applied to other orientations of a cylinder besides other submerged shapes. Usually, the expression is applied to small objects where diffraction and added mass effects are synonymous. (Applications to larger objects are not unusual.)

The inertia force is proportional to the water particle acceleration, and the drag force to the square of the water particle velocity. These are taken in the direction of the wave force. For instance, on a vertical cylinder the horizontal force is composed of the horizontal water particle velocity and acceleration. (This is similar for a horizontal cylinder normal to the wave propagation.) For an inclined cylinder, the velocity and acceleration are resolved into their normal and tangential components. The normal velocity component causes both viscous and pressure forces, while the tangential component causes only a shear force—i.e., skin friction—tangential to the axis of the cylinder which, often, is ignored in computations [40]. Normal components are then resolved in their horizontal and vertical directions. These components are then used to compute forces in the respective directions in the usual way.

3.2 Wave Theories

Works by earlier investigators (Laplace, Gerstner, Airy, Stokes *et al.*) are deterministic. For example, in Airy's small amplitude irrotational wave theory [41], the basic hydrodynamic (i.e., Euler's) equations for an incompressible, frictionless fluid, with irrotational fluid motion, are employed. When a velocity potential ϕ is incorporated into the continuity equation (i.e., conditions of zero curl prevail, $\vec{\nabla} \times \vec{U} = 0$), the Laplace's equation becomes:

$$\sum_{i=1}^3 \frac{\partial^2 \phi}{\partial x_i^2} = 0. \quad (3.1)$$

If the momentum equation—Euler's equation of motion—combined with conditions of irrotationality are integrated, the Bernoulli's equation is obtained.

That is:

$$-\frac{\partial^2 \phi}{\partial t^2} + \frac{1}{2} \sum_{i=1}^3 u_i^2 + \frac{p}{\rho} + gZ = 0, \quad (3.2)$$

where $u_i = -\frac{\partial \phi}{\partial x_i}$.

These equations are solved subject to the appropriate boundary conditions. Since the boundary condition $Z = \eta$ (free surface) appears as an unknown, the general solution for the wave motions is complex. But by assuming various boundary conditions, different solutions for the above equations result. For instance, the assumption of small amplitude and zero pressures on the boundary leads to Airy's solution for two dimensional motion. Also, using perturbation techniques, the solutions to the above equations in the form of series expansion in ascending powers of $\frac{H_w}{L_w}$ for very deep water and in terms $\frac{H_w}{h_w}$ lead to sinusoidal—i.e., Stokes'—and Cnoidal wave forms, respectively [42, 43]. (H_w is the wave height, L_w the wave length and h_w the water depth.)

Stokes' waves exhibit vertical symmetry, sharper crests and flatter troughs; whereas Airy's waves are sinusoidal. The kinematics of Stokes' waves are described in terms of circular functions. Cnoidal waves, attributable to Korteweg and de-Vries [43], are developed in terms of elliptical functions. Besides the above waves, there are solitary waves [44]. These waves rise entirely above the still water level and result in mass transport in the direction of wave advance. Such waves are generated by displacing a mass of water (e.g., due to seismic movements). Regions of applicability—i.e., small amplitude (Airy's wave), and finite amplitude (Stokean, Cnoidal and Solitary waves) theories—are depicted in terms of the relative depth, $\frac{h_w}{L_w}$, in Figure 3.1. The notations used in connections with waves are shown in Figure 3.2.

In the following sections, the mathematical formulations used to calculate the wave forces on a structure, subjected to regular and irregular waves, are presented.

3.3 Regular Wave Forces

3.3.1 Vertical Cylinder

Based on the linearized Morrison's wave equation, the incremental wave force, $d\vec{F}_T$, on a cylindrical element of length, ds , of a vertical cantilever cylinder (see Figure 3.3) is expressed as:

$$d\vec{F}_T = d\vec{F}_D + d\vec{F}_I, \quad (3.3)$$

where

$$d\vec{F}_D = \frac{1}{2}\rho C_D D |\vec{U} - \vec{X}| (\vec{U} - \vec{X}) ds, \text{ and}$$

$$d\vec{F}_I = \rho C_I \frac{\pi D^2}{4} (\vec{U} - \vec{X}) ds.$$

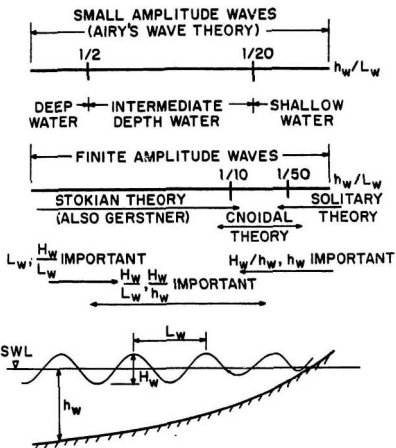


FIG. 3.1 REGIONS OF APPLICABILITY FOR SMALL AND FINITE AMPLITUDE WAVES.

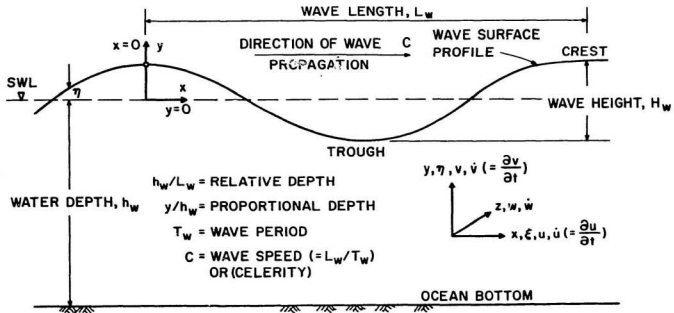


FIG. 3.2 NOTATION USED IN CONNECTION WITH WAVES.

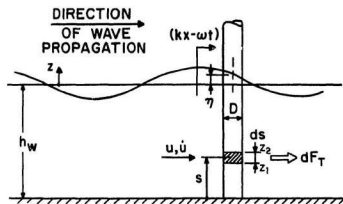


FIG. 3.3 INCREMENTAL WAVE FORCE dF_T ON A VERTICAL CANTILEVER CYLINDER.

Therefore, the total force \vec{F}_T on the cylinder is given by:

$$\vec{F}_T = \int_{-h_w}^{\eta} (\vec{F}_D + \vec{F}_I) ds, \quad (3.4)$$

where

\vec{F}_D = drag component of the force,

\vec{F}_I = inertia component of the force,

C_D = drag coefficient,

C_I = inertia or mass coefficient,

D = external diameter of the cylindrical element,

\vec{U} = instantaneous velocity vector of the water particle normal to the member (i.e., $\vec{U} = u\vec{i} + v\vec{j}$),

$\vec{\dot{U}}$ = instantaneous acceleration vector of the water particles normal to the axis of the member (i.e., $\vec{\dot{U}} = \dot{u}\vec{i} + \dot{v}\vec{j}$),

\vec{i}, \vec{j} = unit vectors in the x and y directions, respectively,

u, v = water particle velocity components in the x and y directions, respectively,

\dot{u}, \dot{v} = water particle acceleration components in the x and y directions, respectively,

\vec{X} = instantaneous velocity vector of the structural member (i.e., $\vec{X} = \dot{x}\vec{i} + \dot{y}\vec{j}$),

x, y = displacement components in the x and y directions of the incremental section, respectively,

$\vec{\ddot{X}}$ = instantaneous acceleration vector of the incremental section of the member (i.e., $\vec{\ddot{X}} = \ddot{x}\vec{i} + \ddot{y}\vec{j}$),

$\dot{x}, \dot{y}, \ddot{x}, \ddot{y}$ = instantaneous velocity and acceleration of the incremental section in the x and y directions, respectively,

ds = incremental length of the section, and

η = instantaneous water level above the mean sea level.

Here, \vec{U} and its velocity component \vec{U}_n normal to the axis of the cantilever cylinder are synonymous. If $\dot{x}, \ddot{x} \ll u, \dot{u}$, and $\dot{y}, \ddot{y} \ll v, \dot{v}$ equation (3.4) reduces to:

$$\vec{F}_T = \int_{-h}^h \left(\frac{1}{2} \rho C_D D |\vec{U}| \vec{U} + \rho C_I \frac{\pi D^2}{4} \ddot{\vec{U}} \right) ds. \quad (3.5)$$

The drag term in the above expression has the non-linear quantity $|\vec{U}| \vec{U}$ which, for many calculations, particularly in spectral methods, makes the solution difficult. (Note that the absolute value sign preserves the direction of the force.) Furthermore, since frequency domain analysis requires linear systems, the drag term must be linearized. This is done by using the method of equivalent linearization [75]. The mean square error introduced by replacing the nonlinear term $|\vec{U}| \vec{U}$ with $\vec{U} \bar{U}$ is minimized [76]. It should be emphasized that \vec{U} is time dependent and \bar{U} is a constant having directional components:

$$\bar{u} = \frac{E[|u|u^2]}{E[u^2]}, \quad (3.6)$$

and

$$\bar{v} = \frac{E[|v|v^2]}{E[v^2]}, \quad (3.7)$$

where the operator $E[\dots]$ represents the ensemble average.

Since the input process (water particle motion) is assumed to be a zero mean ergodic Gaussian process, the linearized output process is a zero mean ergodic Gaussian process. So the probability density function for the water velocity is:

$$p(u) = \frac{1}{\sqrt{2\pi}\sigma_u} \exp\left(-\frac{u^2}{2\sigma_u^2}\right), \quad (3.8)$$

and

$$p(v) = \frac{1}{\sqrt{2\pi}\sigma_v} \exp\left(-\frac{v^2}{2\sigma_v^2}\right), \quad (3.9)$$

where σ_u , and σ_v are the standard deviation of the water particle velocity components which, here, are equal to the root mean square of the velocity components (i.e., u_{rms} and v_{rms}). By substituting equations (3.8) and (3.9) into equations (3.6) and (3.7), respectively, the linearization drag factors for the velocity components (u,v) become:

$$\bar{u} = \sqrt{\frac{8}{\pi}} u_{rms}, \quad (3.10)$$

and

$$\bar{v} = \sqrt{\frac{8}{\pi}} v_{rms}; \quad (3.11)$$

therefore,

$$\bar{U}\bar{U} = \bar{U}\sqrt{\bar{u}^2 + \bar{v}^2}. \quad (3.12)$$

Assuming a single right moving Airy wave propagating in a constant density, irrotational and ideal fluid, the wave potential, ϕ , is expressed as:

$$\phi = \frac{\omega A \cosh[k(z + h_w)]}{k \sinh(kh_w)} \cos(kx \cos \theta + ky \sin \theta - \omega t + \alpha), \quad (3.13)$$

where

k = wave number,

A = wave amplitude,

z = surface elevation above the mean sea level,

θ = angle of propagation of the wave with the +ve x-axis,

α = arbitrary phase angle, and

ω = radian frequency of the wave.

But $\vec{U} = u\vec{i} + v\vec{j}$, where:

$$u = \frac{\partial \phi}{\partial x},$$

and

$$v = \frac{\partial \phi}{\partial y}.$$

Therefore,

$$u = \cos \theta \frac{\omega A \cosh[k(z + h_w)]}{\sinh(kh_w)} \sin(kx \cos \theta + ky \sin \theta - \omega t + \alpha), \quad (3.14)$$

$$v = \sin \theta \frac{\omega A \sinh[k(z + h_w)]}{\sinh(kh_w)} \sin(kx \cos \theta + ky \sin \theta - \omega t + \alpha), \quad (3.15)$$

and

$$|\vec{U}| = \sqrt{u^2 + v^2}. \quad (3.16)$$

At a point (x, y) —arbitrarily chosen to be $(0, 0)$ on the cantilever cylinder—for a wave propagating at $\theta = 0^\circ$ with the +ve x axis, the velocity¹ of the water particles is:

$$u = \frac{\omega A \cosh[k(z + h_w)]}{\sinh(kh_w)} \sin(-\omega t + \alpha). \quad (3.17)$$

The root mean square of this velocity is given by:

$$u_{rms} = \frac{\omega A \cosh[k(z + h_w)]}{\sinh(kh_w)} \frac{1}{\sqrt{2}}. \quad (3.18)$$

Then the linearization drag factor (i.e., equation (3.10)) is written as:

$$\bar{u} = \frac{\omega A \cosh[k(z + h_w)]}{\sinh(kh_w)} \sqrt{\frac{8}{2\pi}}. \quad (3.19)$$

¹NB: The velocity in the vertical or z direction is tangential to the axis of the cylinder and is, therefore, ignored for reasons mentioned earlier in section 3.1, page 24.

So $\vec{U}\vec{U}$ becomes:

$$\vec{U}\vec{U} = \sqrt{\frac{8}{2\pi}} \frac{\omega^2 A^2 \cosh[k(z + h_w)]}{\sinh^2(kh_w)} \sin(-\omega t + \alpha) \vec{i}. \quad (3.20)$$

Finally, for a single Airy wave represented by:

$$\eta = A \sin(-\omega t + \alpha), \quad (3.21)$$

the total force on a cylindrical element located between z_1 and z_2 (refer to Figure 3.3) is expressed as (α is assumed equal to 90°):

$$\vec{F}_T = [C_1 \cos(\omega t) - C_2 \sin(\omega t)] \vec{i}, \quad (3.22)$$

where

$$\begin{aligned} C_1 &= \frac{\gamma C_D D A^2}{2\sqrt{\pi} \sinh(2kh_w)} [\sinh(2kh_w - 2kz_1) - \sinh(2kh_w - 2kh_w z_2) \\ &\quad + 2k(z_2 - z_1)]; \\ C_2 &= \frac{\gamma C_I \pi D^2 A}{4 \cosh(kh_w)} [\sinh(kh_w - kz_1) - \sinh(kh_w - kz_2)]; \text{ and} \\ \gamma &= \text{specific density of the water.} \end{aligned}$$

3.3.2 Arbitrarily Oriented Cylinder

For an arbitrarily oriented cylinder, the velocity and acceleration of the incident wave are resolved into their normal and tangential components. (Here \vec{U} and \vec{U}_n are not synonymous.) Then wave forces are computed in the same way as for the vertical cylinder discussed earlier (i.e., in section 3.3.1). This section presents the formulations used to obtain the resolved components of velocity and acceleration.

Consider the arbitrarily oriented cylinder shown in Figure 3.4. Defining the orientation of the cylinder in polar coordinates, the position vector of the cylinder is:

$$\vec{A} = x\vec{i} + y\vec{j} + z\vec{k}. \quad (3.23)$$

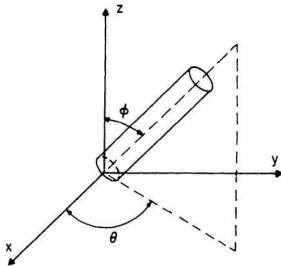
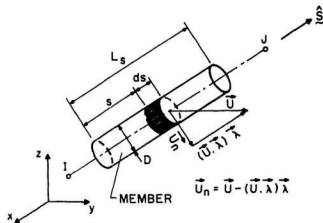


FIG.3.4 ARBITRARILY ORIENTED CYLINDER.



GLOBAL CO-ORDINATE SYSTEM

FIG.3.5 FORCE COMPONENTS ON AN ARBITRARILY ORIENTED CYLINDER.

Therefore, the unit vector $\vec{\lambda}_A$ is:

$$\vec{\lambda}_A = \frac{\vec{A}}{|\vec{A}|}; \quad (3.24)$$

i.e.,

$$\vec{\lambda}_A = c_x \vec{i} + c_y \vec{j} + c_z \vec{k}, \quad (3.25)$$

where

$$c_x = \sin \phi \cos \theta,$$

$$c_y = \sin \phi \sin \theta, \text{ and}$$

$$c_z = \cos \phi.$$

Defining the velocity of the wave in its more general form as:

$$\vec{U} = u\vec{i} + v\vec{j} + w\vec{k}, \quad (3.26)$$

where w and \vec{k} are the velocity component and unit vector in the z direction, respectively—the other variables have been previously defined—the projection of $\vec{U}_{on\vec{A}}$ is:

$$\vec{U}_{on\vec{A}} = \vec{U} \cdot \frac{\vec{A}}{|\vec{A}|}. \quad (3.27)$$

Since $\frac{\vec{A}}{|\vec{A}|} = \vec{\lambda}_A$, then the vector parallel to \vec{A} shown in Figure 3.5 (i.e., it lies on \vec{A}) is $(\vec{U} \cdot \vec{A})\vec{\lambda}_A$.

Thus, the normal velocity vector to \vec{A} (i.e., U_n) is:

$$\vec{U}_n = \vec{U} - (\vec{U} \cdot \vec{\lambda}_A)\vec{\lambda}_A. \quad (3.28)$$

Taking the components separately:

$$u_n = u - c_x(uc_x + vc_y + wc_z), \quad (3.29)$$

$$v_n = v - c_y(u c_x + v c_y + w c_z), \quad (3.30)$$

and

$$w_n = w - c_z(u c_x + v c_y + w c_z). \quad (3.31)$$

If a long crested wave is being considered, $w = 0$ (i.e., $\frac{\partial \eta}{\partial z} = 0$); so the above expressions will be reduced. Similarly, the normal components of the acceleration are given by:

$$a_{nx} = u - c_x(a_x c_x + a_y c_y), \quad (3.32)$$

$$a_{ny} = v - c_y(a_x c_x + a_y c_y), \quad (3.33)$$

and

$$a_{nz} = -c_z(a_x c_x + a_y c_y). \quad (3.34)$$

3.4 Irregular Wave Forces

For a train of irregular waves, the wave profile is decomposed into a series of sine and cosine components. This is achieved by first digitizing the wave profile into N discrete points, spaced at an interval of Δt seconds. The discrete signal is then transformed into a series of $N/2 + 1$ cosine and $N/2$ sine waves, using an FFT algorithm as:

$$\eta(t) = \sum_{s=0}^{N/2} A_s \cos(\omega_s t) + \sum_{s=1}^{N/2} B_s \sin(\omega_s t), \quad (3.35)$$

where

$$\begin{aligned} \omega_s &= \frac{2\pi s}{N\Delta t}, \\ A_s &= \frac{2}{N} \sum_{j=0}^{N-1} \eta_{j+1} \cos(\omega_s t), \\ B_s &= \frac{2}{N} \sum_{j=0}^{N-1} \eta_{j+1} \sin(\omega_s t), \\ s &= 0, 1, 2, \dots, N/2, \text{ and} \end{aligned}$$

A_s, B_s = pseudo random infinitesimal amplitudes associated with each wave component.

Based on equation (3.22) and applying the superposition principle (a linear system is assumed), the force on the cylindrical element due to a train of irregular waves is represented by:

$$F_T(t) = \sum_{s=0}^{N/2} [C_{1s} \cos(\omega_s t) - C_{2s} \sin(\omega_s t)] + \sum_{s=0}^{N/2} [C_{1s} \sin(\omega_s t) + C_{2s} \cos(\omega_s t)]. \quad (3.36)$$

In contrast to equation (3.22), the force coefficients C_1 and C_2 are computed for each wave component represented by $s = 0, 1, 2, \dots, N/2$. (Hence, the new notations C_{1s} and C_{2s} are introduced.)

As a result, the theoretical response of the structure is obtained by using the force computed with the above expression as the input forcing function on the finite element (FEM) model of the structure.

3.5 Mathematical Modelling of the Structure

Two methods were used to obtain a mathematical model of the structure: 1) a 3-D model, and 2) a stick model. In the 3-D model, all the DOF of the structure are considered. This model requires a large computer core storage and is very CPU intensive. The stick model, on the other hand, originates from an eigenvalue economizer which eliminates secondary DOF from the analysis. (It requires less CPU time and core storage.) A common technique used to economize the analysis of large structures is the **method of sub-structures** [45]. Leung [46] has presented a sub-structure procedure whereby the sub-structure DOF are used as *master* DOF. This method along with the economizer procedure outlined by Zienkiewicz [47] is discussed and extended

further. Ultimately, the resulting consistent mass matrix is diagonalized—using a method recommended by Cook [48]—to construct the stick model.

3.5.1 Formulations for the 3-D Model

Consider a linear multiple degrees of freedom (MDOF) system with mass lumped at N degrees of freedom subjected to the loading function $f_j(t)$, where $f_j(t)$ is the force applied at DOF j at time t . The equation of motion in the time domain may be expressed as:

$$[m]\ddot{\underline{x}} + [c]\dot{\underline{x}} + [k]\underline{x} = \underline{f}(t), \quad (3.37)$$

where

$[m]$, $[c]$ and $[k]$ = $N \times N$ mass (added mass + structural mass), damping (viscous damping, radiation or wave making damping), stiffness (structural + hydrostatic) matrices, respectively; and

\underline{x} , $\dot{\underline{x}}$, $\ddot{\underline{x}}$ and $\underline{f}(t)$ = $N \times 1$ displacement, velocity, acceleration and load vectors, respectively.

The above expression is coupled, and, as it stands, difficult to solve. To simplify the analysis, the equation is uncoupled using the normal mode method (Clough and Penzien [49]). This is done by representing the displacement vector $\underline{x}(t)$ as a sum of orthogonal mode shapes² multiplied by modal amplitudes. Hence:

$$\underline{x}(t) = \sum_{j=1}^N \phi_j q_j(t), \quad (3.38)$$

or

$$\underline{x}(t) = [\Phi] \underline{q}(t), \quad (3.39)$$

²The total vibration of the structure is considered as a linear combination of the characteristic harmonic mode shape denoted by ϕ_j .

where

$[\Phi]$ = mode shape matrix of N mode vectors of length N , and

$\underline{q}(t)$ = time dependant vector of modal amplitudes.

However, the dynamic analysis of the structural system using normal mode method requires, as a first step, the solution of the general eigenvalue problem; thus:

$$[m]\ddot{\underline{x}} + [c]\dot{\underline{x}} + [k]\underline{x} = \underline{0}. \quad (3.40)$$

If the displacement and acceleration of any characteristic mode of vibration, j , is expressed as:

$$\underline{x}_j = \underline{\phi}_j \sin \omega_j t, \quad (3.41)$$

and

$$\ddot{\underline{x}}_j = -\underline{\phi}_j \omega_j^2 \sin \omega_j t, \quad (3.42)$$

(where ω_j is the frequency of vibration of the j th mode, and $\underline{\phi}_j$ is the mode shape or normalized eigenvector³), the undamped equation for free vibration is:

$$[k]\underline{x} = -[m]\ddot{\underline{x}}. \quad (3.43)$$

Substituting equations (3.41) and (3.42) into equation (3.43) yields:

$$[k]\underline{\phi}_j = \omega_j^2 [m]\underline{\phi}_j. \quad (3.44)$$

Equation (3.44) is an eigenvalue problem in non-standard form, where the eigenvalues are the squares of the frequencies and eigenvectors are the vibrational mode shape associated with the frequencies. Considering all possible

³NB: The amplitudes of vibration in the normalized eigenvector are only relative values and may be scaled or normalized, to some extent, as a matter of choice.

frequencies and mode shapes, equation (3.44) may be written as:

$$[k][\Phi] = [\Omega][m][\Phi], \quad (3.45)$$

where $[\Omega]$ is diagonal matrix containing the eigenvalues in order of increasing magnitudes. The matrix $[\Phi]$ contains the eigenvectors stored columnwise in an order corresponding to the eigenvalues in $[\Omega]$. Often, the matrix $[\Omega]$ is called the spectral matrix while $[\Phi]$ is called the mode shape matrix.

Since the mode shape matrix is available, a set of N normal mode equations for the structure is attained by substituting equations (3.39) into equation (3.37), and pre-multiplying by the transpose of the mode shape matrix (i.e., $[\Phi]$). Therefore,

$$[M]\ddot{\underline{q}} + [C]\dot{\underline{q}} + [K]\underline{q} = \underline{E}(t), \quad (3.46)$$

where

$[M] = [\Phi]^T[m][\Phi]$, modal mass matrix,

$[C] = [\Phi]^T[c][\Phi]$, modal damping matrix,

$[K] = [\Phi]^T[k][\Phi]$, modal stiffness matrix, and

$\underline{E}(t) = [\Phi]^T \underline{f}(t)$, modal force vector.

Assuming Rayleigh damping of the form:

$$[c] = [m] \sum_b a_b [[m]^{-1}[k]]^b \quad (3.47)$$

(where a_b is an arbitrary constant), then the normal uncoupled modal equations may be written as N independent single degree of freedom (SDOF) equations. As a result for the i th mode, the equation of motion becomes:

$$M_i \ddot{q}_i + C_i \dot{q}_i + K_i q_i = \phi_{i1} F_1 + \phi_{i2} F_2 + \cdots + \phi_{iN} F_N, \quad (3.48)$$

where

$M_i = \phi_i^T [m] \phi_i$, modal mass,

$C_i = \phi_i^T [c] \phi_i$, modal damping,

$K_i = \phi_i^T [k] \phi_i$, modal stiffness,

q_i = modal amplitudes,

ϕ_i = mode shape vector for mode i , and

F_1, F_2, \dots, F_N = forces at degrees of freedom 1, 2, \dots , N , respectively.

Having solved each modal equation for the number of structural modes being investigated, the modal response ($q(t)$) is then transformed back to the original co-ordinates using 3.39) (i.e., $\mathbf{x}(t) = \sum_{j=1}^N \phi_j q_j(t)$).

3.5.2 Formulations for the Stick Model

If damping is neglected, the equation of motion for the structure (i.e., equation (3.37) presented earlier in section 3.5.1) can be written as:

$$\begin{bmatrix} [m_{ss}] & [0] \\ [0] & [m_{mm}] \end{bmatrix} \begin{Bmatrix} \ddot{\mathbf{x}}_s \\ \ddot{\mathbf{x}}_m \end{Bmatrix} + \begin{bmatrix} [k_{ss}] & [k_{sm}] \\ [k_{ms}] & [k_{mm}] \end{bmatrix} \begin{Bmatrix} \mathbf{x}_s \\ \mathbf{x}_m \end{Bmatrix} = \begin{Bmatrix} \mathbf{L}_s(t) \\ \mathbf{L}_m(t) \end{Bmatrix}, \quad (3.49)$$

where the column vectors \mathbf{x} and $\ddot{\mathbf{x}}$ have been partitioned into two parts:

$$\mathbf{x} = \begin{Bmatrix} \mathbf{x}_s \\ \mathbf{x}_m \end{Bmatrix},$$

and

$$\ddot{\mathbf{x}} = \begin{Bmatrix} \ddot{\mathbf{x}}_s \\ \ddot{\mathbf{x}}_m \end{Bmatrix}.$$

Here, the displacement \mathbf{x}_s is assumed to depend, in a unique way, on the displacement \mathbf{x}_m . Therefore, \mathbf{x}_s is called the vector of slave variables. (For simplicity, assume the mass matrix is diagonal.) Usually, \mathbf{x}_s and \mathbf{x}_m are chosen, so the number of slave DOF, \mathbf{x}_s , will be much greater than the master DOF, \mathbf{x}_m .

To establish the relationship between master and slave DOF, the following transformation is introduced:

$$\begin{Bmatrix} \underline{x}_s \\ \underline{x}_m \end{Bmatrix} = [\alpha] \underline{x}_m, \quad (3.50)$$

where

$$[\alpha] = \begin{Bmatrix} [T] \\ [I] \end{Bmatrix}.$$

Moreover, to obtain $[\alpha]$, the general deformation of the structure is assumed to follow a configuration attainable by imposing displacements \underline{x}_m on an, otherwise, unloaded structure in static condition. (NB: $[T]$ and $[I]$ are the transformation and identity matrices, respectively.) If equation (3.49) is partitioned with $\underline{\ddot{x}} = \underline{0}$, and since the slave nodes are unloaded, the following expression is obtained:

$$\begin{bmatrix} [k_{ss}] & [k_{sm}] \\ [k_{ms}] & [k_{mm}] \end{bmatrix} \begin{Bmatrix} \underline{x}_s \\ \underline{x}_m \end{Bmatrix} = \begin{Bmatrix} \underline{0} \\ \underline{f}_m(t) \end{Bmatrix}. \quad (3.51)$$

Therefore:

$$[k_{ss}]\underline{x}_s + [k_{sm}]\underline{x}_m = \underline{0},$$

and

$$\underline{x}_s = -[k_{ss}]^{-1}[k_{sm}]\underline{x}_m. \quad (3.52)$$

Thus,

$$[T] = -[k_{ss}]^{-1}[k_{sm}]. \quad (3.53)$$

The above expression is the Guyan transformation [50]. Substituting equation (3.52) into (3.49) and pre-multiplying by $[T]^T$, to preserve symmetry, yields the following condensed equation of motion:

$$[M]^* \ddot{\underline{x}}_m + [K]^* \underline{x}_m = \underline{F}^*, \quad (3.54)$$

where

$$\begin{aligned} [M]^* &= [m_m] + [T]^T [m_{ss}] [T], \\ [K]^* &= [k_{mm}] - [k_{ms}] [k_{ss}]^{-1} [k_{sm}], \text{ and} \\ F^* &= f_m + [T]^T f_s(t). \end{aligned}$$

Here, $[M]^*$ and $[K]^*$ are the condensed mass and stiffness matrices, respectively; F^* is the equivalently lumped nodal force vector; while x_m is a column vector involving fewer variables than the original force vector in equation (3.49). Since it requires less CPU time and core storage, the solution of equation (3.54) is relatively simple.

Implementation: Because the slave DOF vastly outnumber the master DOF, inverting $[k_{ss}]$ is CPU intensive. This problem could be overcome by applying the following suggestion to the flexibility matrix—i.e., from the output of the static analysis:

$$\begin{bmatrix} [k_{ss}] & [k_{sm}] \\ [k_{ms}] & [k_{mm}] \end{bmatrix}^{-1} = \begin{bmatrix} [a_{ss}] & [a_{sm}] \\ [a_{ms}] & [a_{mm}] \end{bmatrix}; \quad (3.55)$$

the right hand side matrix in the above expression is the familiar global flexibility matrix. As a result:

$$\begin{bmatrix} [k_{ss}] & [k_{sm}] \\ [k_{ms}] & [k_{mm}] \end{bmatrix} \begin{bmatrix} [a_{ss}] & [a_{sm}] \\ [a_{ms}] & [a_{mm}] \end{bmatrix} = \begin{bmatrix} [I] & [0] \\ [0] & [I] \end{bmatrix}. \quad (3.56)$$

Based on the above expression,

$$[k_{ss}][a_{sm}] + [k_{sm}][a_{mm}] = [0];$$

so

$$[a_{sm}] = -[k_{ss}]^{-1} [k_{sm}][a_{mm}], \quad (3.57)$$

and

$$-[k_{ss}]^{-1} [k_{sm}] = [a_{mm}]^{-1} [a_{sm}] = [T]. \quad (3.58)$$

Furthermore, from equation (3.56), the following relationship is obtained:

$$[k_{ms}][a_{sm}] + [k_{mm}][a_{mm}] = [I]. \quad (3.59)$$

Substituting equation (3.57) into the above expression leads to:

$$[[k_{mm}] - [k_{ms}][k_{ss}]^{-1}[k_{sm}]][a_{mm}] = [I],$$

or

$$[[k_{mm}] - [k_{ms}][k_{ss}]^{-1}[k_{sm}]] = [a_{mm}]^{-1} = [K]^*. \quad (3.60)$$

Hence, it is correct to write:

$$[K]^* = [a_{mm}]^{-1}, \quad (3.61)$$

and

$$[T] = [a_{mm}]^{-1}[a_{sm}], \quad (3.62)$$

where $[a_{mm}]$ is the flexibility matrix of the master DOF and the inversion will give the transformation matrix. (The inversion of $[a_{mm}]$ is less expensive, since it is of a low order.) It may be recalled that $[T]$ is the matrix which relates the displacements of the slave nodes to those of the master nodes.

Existing FEM programs such as *SAP IV*, *GTSTRUDL*, etc., could be used to compute $[a_{mm}]$ and $[a_{sm}]$. The following steps are suggested:

- (a) ... first, identify the master DOF;
- (b) find the corresponding deflection along all the master DOF and arrange them as the 1st column of matrix $[a_{mm}]$; and
- (c) choose the corresponding deflection along all the slave DOF and arrange them as the 1st column of the matrix $[a_{sm}]$.

Each step is repeated for the remaining master DOF, while the corresponding deflections are positioned columnwise in their appropriate locations. Having obtained $[a_{mm}]$ and $[a_{sm}]$, the matrix $[T]$ can be formed. Subsequently, the condensed mass and stiffness matrices, and the load vector are computed. (Refer to equation (3.54), section 3.5.2.) To construct a stick model of the structure, the reduced consistent mass matrix is diagonalized using Cook's method. (A summary of the method is presented in section A.1, Appendix A.) Consequently, the condensed form of the equation of motion is solved using the Houbolt recurrence procedure [51]. This numerical scheme incorporates a finite difference and step by step integration procedure—a synopsis of the algorithm is presented in section A.2, Appendix A. At this stage in the analysis, the responses computed are only at the master DOF selected initially. Therefore, to compute the responses at the slave DOF, the responses at the master DOF should be multiplied by the Transformation matrix $[T]$.

3.6 Computer Implementation of Analytical Models

Two analytical models were used to analyse the structure: 1) a 3-D model, and 2) a stick model. In this section, the computer implementation of each analytical model is summarized. Figure 3.6 shows the simulated 3-D and stick model.

ORIENTATION

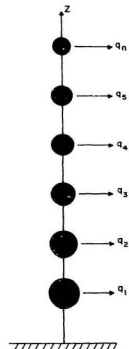
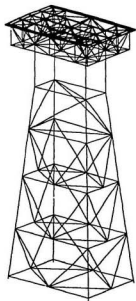


FIG. 3.6 SIMULATED 3-D AND STICK MODEL REPRESENTATION OF THE STRUCTURE .

3.6.1 Implementation of the 3-D Model

A finite element approach was used to analyse the structure. The method is epitomized as:

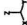
- *discretize* the structure (i.e., sub-divide the structure into components);
- select a interpolation function which represents the assumed number of degrees of freedom;
- select the element properties;
- assemble the element properties to obtain system properties;
- solve the system equations; and
- interpret the results by making additional calculations if necessary.

For analyses (i.e., computations to estimate natural frequencies, mode shapes, etc.), a computer generated Finite Element Analysis (FEM) *discretization* was generated. In the model and prototype there were 85 nodes or joints and 278 beam elements. These are shown in Figures 3.7 and 3.8 for the prototype. The corresponding diagrams for the model are depicted in Figures 3.9 and 3.10. All the tubular members of the frame structure were modelled using 2-D beam elements, while the deck was modelled using 36 eight noded 3-D solid elements. Finite element analyses were done based on the following assumptions:

1. rigid connections at the joints,
2. lumped masses at nodes,
3. rigid deck,

4. prismatic beam members,
5. six degrees of freedom per node for each beam element (three translational and three rotational),
6. three degrees of freedom per node for each 3-D solid element which forms the deck (three translational—a total of 24 degrees of freedom), and
7. the mass distribution throughout the structure is fixed.

Natural frequencies and mode shapes were computed using the *subspace iteration* technique. For the submerged members, the hydrodynamic added mass was assumed equal to the mass of water displaced by the member [52, 53]. The inertial resistance due to the added mass of water was assumed to apply to components of acceleration normal to the member axis for such members [55, 54]. To compute the nodal wave forces, resulting from wave action, a structural mechanics approach was used: Each element was subdivided into n sub-sections (here, $n = 10$), and the wave forces at each section were computed using the linearized Morrison's equation presented earlier in section 3.3.1 The force at each section was then transferred to the joints as nodal forces and fixed-end moments, as is usually done in structural mechanics. (This operation is shown diagrammatically in Figure 3.11.) Thus, the nodal forces and moments at each node were computed as the algebraic sum of all the forces and moments resulting from each point load on the member, respectively. Finally, the total force and moment were computed as the algebraic sum of all the nodal forces and moments sharing the same joint. As the waves propagated through the structure, the above numerical scheme was repeated for each time step (Δt).

ORIENTATION 

HORIZONTAL SCALE = 70,000 FEET PER INCH
 VERTICAL SCALE = 70,000 FEET PER INCH
 EQUIVALENT ROTATION X 0.0 Y 20.0 Z -40.0

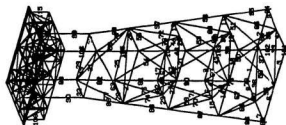
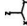


FIG.3.7 DISCRETIZATION OF MEMBERS (PROTOTYPE).

ORIENTATION 

HORIZONTAL SCALE = 70,000 FEET PER INCH
 VERTICAL SCALE = 70,000 FEET PER INCH
 EQUIVALENT ROTATION X 0.0 Y 20.0 Z -40.0

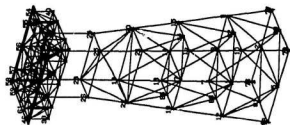


FIG.3.8 DISCRETIZATION OF JOINTS (PROTOTYPE).

ORIENTATION  HORIZONTAL SCALE = 2.8460 FEET PER INCH
VERTICAL SCALE = 2.8460 FEET PER INCH
EQUILIBRIUM NOTATION X 0.0 Y 20.0 Z -40.0

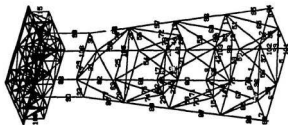
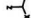


FIG.3.9 DISCRETIZATION OF MEMBERS (MODEL).

ORIENTATION  HORIZONTAL SCALE = 2.8460 FEET PER INCH
VERTICAL SCALE = 2.8460 FEET PER INCH
EQUILIBRIUM NOTATION X 0.0 Y 20.0 Z -40.0

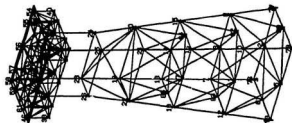


FIG.3.10 DISCRETIZATION OF JOINTS (MODEL).

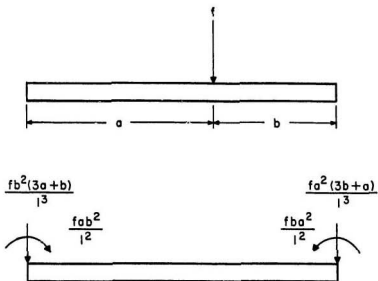


FIG. 3.11 ACTUAL AND EQUIVALENT LOADING FOR A CONCENTRATED TRANSVERSE FORCE (NB: $l = a + b$).

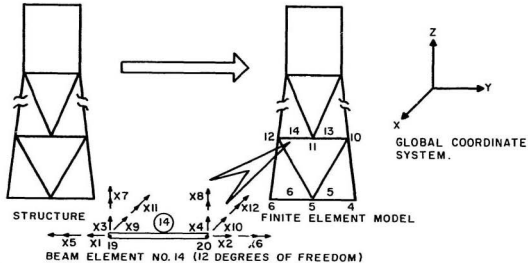
The equation of motion for each element plus all the boundary points at connecting nodes between each element were computer generated from the geometrical and physical properties of the input data for each element or member as depicted in Figure 3.12. Ultimately, the equations of motion were assembled by the computer into one equation representing the structure, and the analyses were done. (All analyses were carried out with a special purpose program compiled by the author.)

It should be emphasized that since it would be difficult and very time consuming to obtain exact analytical solutions for the structure considered, numerical analyses of the physical model, based on certain approximations, are incorporated in the computer approach.

3.6.2 Implementation of the Stick Model

To obtain a stick model of the structure, it was first necessary to select the master DOF, so the nodes chosen represented the expected global motion of the structure. Since the structure did not have any central nodes at each horizontal level on the jacket (the most suitable position for a master node), one corner node was chosen from each level on the broad side of the structure; that is, starting from level # 1 and proceeding in a zigzag manner to level # 7. Therefore, the flexibility matrices of the master and slave nodes were obtained by applying unit loads at the corresponding master DOF, successively, in the global x direction, and static analyses were carried out to compute static displacements. There were as many load cases as master DOF. The above procedure was accomplished with the same computer program used to analyse the 3-D model of the structure.

1. STRUCTURE IS REPRESENTED BY A COMBINATION OF SMALL ELEMENTS.



2. EQUATIONS OF MOTION ARE COMPUTER GENERATED FROM PHYSICAL PROPERTIES OF STRUCTURE :

$$\underbrace{\begin{bmatrix} m_{11} & m_{12} & \dots \\ m_{21} & & \end{bmatrix}}_{\text{MASS MATRIX}} \underbrace{\begin{bmatrix} \ddot{x}_1(t) \\ \ddot{x}_2(t) \\ \vdots \end{bmatrix}}_{\text{INERTIAL FORCES}} + \underbrace{\begin{bmatrix} c_{11} & c_{12} & \dots \\ c_{21} & c_{22} & \end{bmatrix}}_{\text{DAMPING MATRIX}} \underbrace{\begin{bmatrix} \dot{x}_1(t) \\ \dot{x}_2(t) \\ \vdots \end{bmatrix}}_{\text{DISSIPATIVE FORCES}} + \underbrace{\begin{bmatrix} k_{11} & k_{12} & \dots \\ k_{21} & k_{22} & \end{bmatrix}}_{\text{STIFFNESS MATRIX}} \underbrace{\begin{bmatrix} x_1(t) \\ x_2(t) \\ \vdots \end{bmatrix}}_{\text{RESTORING FORCES}} = \underbrace{\begin{bmatrix} p_1(t) \\ p_2(t) \\ \vdots \end{bmatrix}}_{\text{EXTERNAL FORCES (FREE VIBRATION = 0)}}$$

FIG. 3.12 COMPUTER GENERATED FINITE ELEMENT METHOD.

From the static displacement results, the master flexibility matrix, $[a_{mm}]$, and the slave flexibility matrix, $[a_{sm}]$, were formed. Similarly, the master mass matrix, $[m_{mm}]$, and slave mass matrix, $[m_{ss}]$, were also computed. By applying equation (3.61), the condensed master stiffness matrix, $[K]^*$, and from equation (3.62), the transformation matrix, $[T]$, were determined. Then the condensed mass matrix, $[M]^*$, was obtained (i.e., $[M]^* = [m_{mm}] + [T]^T[m_{ss}][T]$). Likewise, knowing the forces at the various slave and master DOF, the condensed master force vector, \underline{F}^* , is computed with the expression $\underline{F}^* = \underline{f}_m + [T]^T \underline{f}_s(t)$. Since the resulting mass matrix, $[M]^*$, is a consistent matrix, it was diagonalized to form the stick model, using the method recommended by Cook referenced earlier in Appendix A. Thus, equation (3.54) was established.

Natural frequencies of the system were solved (i.e., setting $\underline{f}_m(t) = 0$) using Cholesky's procedure and the response was computed using the Houbolt algorithm referenced earlier in Appendix A. The wave force vector at each master node was generated with the same program used to solve the 3-D structure discussed in the previous section.

Damage Simulation: Structural damage or failure in the 3-D and stick model was simulated by making the member(s) inactive in the analyses. This was accomplished by removing the member(s) and the associated properties from the computations. Since the flexibility matrix used to generate the stick model was obtained from the 3-D model program, the influence of member removal was present in the flexibility analysis attained from the unit load(s) static displacement analyses. (A summary of the computer analyses is presented in flow chart form in Figure 3.13.)

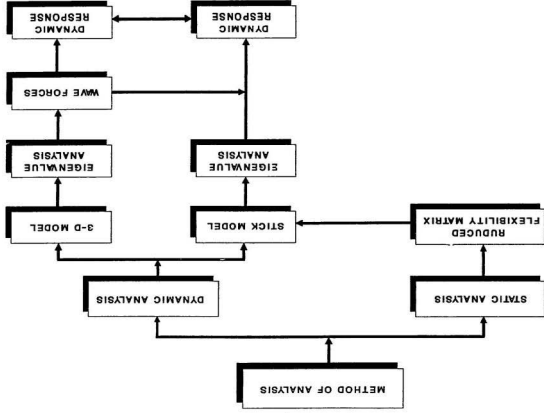


FIG. 3.13 FLOW CHART OF THE COMPUTER ANALYSES.

Chapter 4

Physical Modelling

In this chapter, the physical modelling of the problem is discussed. It includes the development of the modelling laws, difficulties associated with hydro-elastic modelling, and a description of the design and fabrication of the experimental hydro-elastic model.

4.1 Development of Modelling Laws

Three basic methods of partial analysis are commonly in use: 1) dimensional analysis, 2) the method of force ratios and 3) the method of governing equations. Each aims at sorting out the relevant variables of a system in such a way, so a better understanding of the physical phenomenon is obtained. The Method of Synthesis (due to Barr [56]) is the most modern and powerful method of partial analysis, because it guides the analysis to a convenient, rather than a merely correct solution [57]. This results because the method permits considerable choice and redundancy not directly available with other methods. Any non-dimensional equation in n terms can be considered to have originated from an $(n + 1)$ term dimensionally homogeneous equation. For

instance, the non-dimensional equations:

$$\Phi \left(\frac{X_1}{X_2}, \frac{X_3}{X_2}, \frac{X_4}{X_2}, \frac{X_5}{X_2} \right) = 0, \quad (4.1)$$

$$\Phi \left(\frac{X_1}{X_3}, \frac{X_3}{X_4}, \frac{X_5}{X_1}, \frac{X_2}{X_3} \right) = 0, \quad (4.2)$$

or

$$\Phi \left(\frac{X_1}{X_3}, \frac{X_4}{X_2}, \frac{X_2}{X_1}, \frac{X_5}{X_4} \right) = 0, \quad (4.3)$$

could have originated from the dimensionally homogeneous equation,

$$\Phi(X_1, X_2, X_3, X_4, X_5) = 0 \quad (4.4)$$

(where X_1, X_2, X_3, X_4 , and X_5 have the same dimension), provided the following rules are applied:

1. the terms in equations (4.1) to (4.3) must contain all the terms of equation (4.4),
2. the terms of equations (4.1) to (4.3) must be linked by the terms of equation (4.4), and
3. the number of terms in each of the equations—i.e., (4.1) to (4.3)—must contain one term fewer than equation (4.4).

From equation (4.4), many forms of non-dimensional equations, other than the ones given in equations (4.1) to (4.3), may be derived.

An examination of equations (4.1) to (4.3) suggests that if the dimensionally homogeneous equation (i.e., equation (4.4)) is available, rather than the non-dimensional equation, some choice is readily available. The additional choice results because of redundancy. This is the primary objective of

the *Method of Synthesis*, which uses dimensional reasoning to form combinations of variables having dimensions of length rather than to develop non-dimensional groups, directly, as is more usual. The combinations are made by combining each variable not having length dimensions (e.g., V, g, ν, t , etc.) with each other variable, two at a time. Any relevant density is excluded, except where necessary, to eliminate a mass dimension. These combinations have been called linear proportionalities. Usually, if there are m variables available to combine—i.e., all variables excluding density (used to eliminate mass densities), temperature difference, and relevant lengths of the system being investigated—it is theoretically possible to form ${}^m C_2$ linear proportionalities (i.e., $(m-1) + (m-2) + \dots + 1$). Only $m-1$ of these are required in any correct dimensionally homogeneous equation [57, 58]. For completeness, this equation must include all the original variables together with any actual lengths of the system. The following section summarizes the development of the modelling laws necessary to design the *hydro-elastic model*, using the Method of Synthesis.

4.2 Wave Modelling

Before a dimensional analysis can be carried out, the characteristic variables of the wave(s) should be first defined. There are only five variables¹ involved: L_w (wave length), H_w (wave height), h_w (water depth), g (gravitational acceleration), and T_w (wave period). Only four of these are necessary and sufficient to characterize the wave, because three are interdependent. A

¹For the case of deep water or intermediate and short waves, the effects of water viscosity—present in the oscillatory boundary layer—and the roughness of the seabed can be disregarded.

functional relationship relating these variables can be written as:

$$\Phi(T_w, g, L_w, h_w, H_w) = 0. \quad (4.5)$$

By the method of synthesis, the variables are combined in such a way, so each has dimension of length. Therefore,

$$\Phi\left(T_w^2 g, L_w, h_w, H_w\right) = 0. \quad (4.6)$$

Using L_w as the repeating variable to non-dimensionalize the above expression, the following expression results:

$$\Phi\left(\frac{T_w^2 g}{L_w}, \frac{h_w}{L_w}, \frac{H_w}{L_w}\right) = 0, \quad (4.7)$$

or

$$\frac{T_w^2 g}{L_w} = \Phi\left(\frac{h_w}{L_w}, \frac{H_w}{L_w}\right). \quad (4.8)$$

After compounding the above expression, the following equation is obtained:

$$T_w \sqrt{\frac{g}{L_w}} = \Phi\left(\frac{h_w}{L_w}, \frac{H_w}{L_w}\right). \quad (4.9)$$

The function Φ may be obtained from a convenient wave theory (e.g., Airy's small amplitude wave theory, Stokes' 3rd or 5th order wave theories, etc.) depending on the application. For instance, if small amplitude waves are being considered (the wave steepness $\frac{H_w}{L_w}$ is irrelevant), equation (4.9) reduces to:

$$T_w \sqrt{\frac{g}{L_w}} = \Phi\left(\frac{h_w}{L_w}\right). \quad (4.10)$$

For deep water and small amplitude waves (since h_w is no longer relevant), the equation is further reduced to simply:

$$T_w \sqrt{\frac{g}{L_w}} = \sqrt{2\pi}. \quad (4.11)$$

The ratio $\frac{h_w}{L_w}$ characterizes the still water depth. Since three variables L_w , H_w , and T_w are interdependent, only two can be used to define the wave. Often the variables² H_w and T_w are chosen, and L_w is determined as a function of them in addition to the ratio $\frac{h_w}{H_w}$. The following section is concerned with a fixed but flexible structure in deep or intermediate depth water, and is subjected to progressive gravity waves (classified as short waves).

4.3 Modelling the Sea Structure Interaction

The variables involved are:

(a) **structural variables**

L_s, ρ_s, E, ζ , and

shape ratios of the type $\frac{D}{L_s}$, and $\frac{d}{L_s}$ (where D and d represent the exterior diameter and wall thickness of a member, respectively), $\frac{x_1}{L_s}$, $\frac{y_1}{L_s}$, and $\frac{z_1}{L_s}$ (coordinates of the structural joints), relative roughness, etc. ...;

(b) **sea variables**

$H_w, T_w, l, \rho_w, \nu, g$, and

shape ratio $\frac{h_w}{H_w}$;

(c) **response or dependent variables**

F_t (instantaneous force due to wave action),

or

u_z (instantaneous displacement due to wave action);

²For an irregular sea state, described by a spectrum, the variables adopted are: H , (significant wave height), T_z (mean zero crossing period) [59, 60].

where

F_t = instantaneous force at time t ,

u_t = instantaneous displacement at time t ,

E = modulus of elasticity of the structural material,

g = gravitational acceleration,

ν = kinematic viscosity of the liquid,

H_w = wave height,

T_w = wave period in seconds,

t = time,

ρ_w = density of liquid,

L_s = characteristic length of structural component being investigated,

ρ_s = density of structural component, and

ζ = structural damping ratio (non-dimensional).

Besides the shape ratios, there are eleven variables from which the functional relationship can be formed:

$$F_t = \Phi(E, g, \nu, H_w, T_w, t, \rho_w, L_s, \rho_s, \zeta, \text{shape ratios}). \quad (4.12)$$

or alternatively,

$$u_t = \Phi(E, g, \nu, H_w, T_w, t, \rho_w, L_s, \rho_s, \zeta, \text{shape ratios}). \quad (4.13)$$

The homogeneous equation is given as:

$$\Phi(F_t, E, g, \nu, H_w, T_w, t, \rho_w, L_s, \rho_s, \zeta, \text{shape ratios}) = 0. \quad (4.14)$$

Since ζ and the shape ratios are dimensionless, they are ignored from the dimensional analysis, with the understanding that they will reappear after the above equation has been non-dimensionalized.

Using the method of synthesis,³ there are six terms available to form linear proportionalities—i.e., F_t, E, g, ν, T_w and t . Applying the rules presented earlier in section 4.1, page 58, it is possible to form 15 (i.e., 6C_2) linear proportionalities using each of the densities (ρ_s, ρ_w), independently, with the six available terms. But since F_t and ν , and t and T_w cannot combine to form linear proportionalities, only 13 of the 15, mentioned above, are formable. This yields a total of 26 linear proportionalities. Still, six combinations (i.e., $\underbrace{F_t, E}_{\rho_s}, \underbrace{\nu, T_w}_{\rho_s}, \underbrace{\nu, g}_{\rho_s}, \underbrace{T_w, g}_{\rho_s}$ and $\underbrace{t, g}_{\rho_w}$) will not need either of the densities to form linear proportionalities; so each of these combinations will appear twice. As a result, six of them should be excluded, so none is repeated. This yields the following set of linear proportionalities:

$$\begin{aligned} & \sqrt{\frac{F_t}{E}}, \frac{E}{\rho_s g}, \frac{E}{\rho_w g}, \frac{\nu^{2/3}}{g^{1/3}}, \sqrt{\nu T_w}, \sqrt{\nu t}, \sqrt[3]{\frac{F_t}{\rho_w g}}, \sqrt[3]{\frac{F_t}{\rho_s g}}, \\ & \sqrt{\frac{F_t T_w^2}{\rho_s}}, \sqrt{\frac{F_t T_w^2}{\rho_w}}, \sqrt{\frac{F_t t^2}{\rho_s}}, \sqrt{\frac{F_t t^2}{\rho_w}}, \sqrt{\frac{E T_w^2}{\rho_s}}, \sqrt{\frac{E T_w^2}{\rho_w}}, \\ & \sqrt{\frac{E t^2}{\rho_s}}, \sqrt{\frac{E t^2}{\rho_w}}, \sqrt{\frac{\rho_w \nu^2}{E}}, \sqrt{\frac{\rho_s \nu^2}{E}}, T_w^2 g, t^2 g. \end{aligned} \quad (4.15)$$

Not all the above proportionalities⁴ are required; there are redundancies. Using the rules of the method of synthesis, five linear proportionalities should be selected, from the above set, to include F_t, E, g, ν, T_w and t . But, since there are two densities (i.e., ρ_s and ρ_w), an extra linear proportionality is required because these densities can be combined to form a dimensionless ratio. Hence six linear proportionalities should be chosen from equation (4.15) to include $F_t, E, g, \nu, T_w, t, \rho_s$ and ρ_w . Thus, using these terms and

³A table of dimensions in terms of M, L, t and T , for all the variables used, in equation (4.14), is presented in Table 4.1.

⁴These linear proportionalities can be easily formed by using Table 4.1 in Sharp [58].

Table 4.1 Symbols, Units and Dimensions for Variables used in Modelling.

	Units and Dimensions	
	Units	Mass, Length, Time Dimensions
Instantaneous force, F_t	$N(\text{kg.m/s}^2)$	ML/T^2
Instantaneous displacement, u_t	m	L
Modulus of elasticity, E	$\text{Pa}(\text{N/m}^2)$	M/LT^2
Gravitational acceleration, g	m/s^2	L/T^2
Kinematic viscosity, ν	m^2/s	L^2/T
Wave height, H_w	m	L
Wave Period, T_w	s	T
Time, t	s	T
Density of water, ρ_w	kg/m^3	M/L^3
Characteristic length, L_s	m	L
Material density, ρ_s	kg/m^3	M/L^3
Still water depth, h_w	l	L

NB: M = mass, L = length, and T = time.

actual lengths of the systems:

$$\Phi \left(\underbrace{\sqrt[3]{\frac{F_t}{\rho_w g}}, \sqrt{\nu T_w}, \sqrt{\nu t}, T_w^2 g, \frac{E}{\rho_s g}, \frac{E}{\rho_w g}}_6, H_w, L_s \right) = 0. \quad (4.16)$$

The above equation is one of the many expressions that can be obtained from equation (4.14). The important feature is that each term in equation (4.14), except for the non-dimensional terms and shape ratios, is included. Variables of interest are included only once if possible.

Each term in equation (4.16) has dimension of length. Therefore, using L_s as the repeating variable to non-dimensionalize the expression, the following expression results:

$$\Phi \left(\frac{1}{L_s} \sqrt[3]{\frac{F_t}{\rho_w g}}, \frac{\sqrt{\nu T_w}}{L_s}, \frac{\sqrt{\nu t}}{L_s}, \frac{T_w^2 g}{L_s}, \frac{E}{L_s \rho_s g}, \frac{E}{L_s \rho_w g}, \frac{H_w}{L_s} \right) = 0. \quad (4.17)$$

Linking the terms of the above non-dimensional equation throughout by one or more terms results in:

$$\Phi \left(\frac{F_t}{\rho_w g L_s^3}, \frac{t}{T_w}, \frac{T_w}{L_s} \sqrt{\frac{E}{\rho_s}}, \frac{H_w L_s}{T_w \nu}, \frac{\rho_s}{\rho_w}, \frac{H_w}{L_s}, T_w \sqrt{\frac{g}{H_w}} \right) = 0. \quad (4.18)$$

Subsequently, dimensionless ratios (including ζ and the shape ratios) for the fluid structure interaction may be expressed in an explicit form as:

$$\frac{F_t}{\rho_w g L_s^3} = \Phi \left(T_w \sqrt{\frac{g}{H_w}}, \frac{\rho_s}{\rho_w}, \frac{H_w}{L_s}, \frac{T_w}{L_s} \sqrt{\frac{E}{\rho_s}}, \frac{H_w L_s}{T_w \nu}, \frac{t}{T_w}, \zeta, \text{shape ratios} \right), \quad (4.19)$$

or alternatively,

$$\frac{u_t}{L_s} = f \left(T_w \sqrt{\frac{g}{H_w}}, \frac{\rho_s}{\rho_w}, \frac{H_w}{L_s}, \frac{T_w}{L_s} \sqrt{\frac{E}{\rho_s}}, \frac{H_w L_s}{T_w \nu}, \frac{t}{T_w}, \zeta, \text{shape ratios} \right). \quad (4.20)$$

The functions $\Phi(\dots)$ and $f(\dots)$ may be obtained from any of the wave theories mentioned earlier in section 4.2. Observe that the final equation satisfies

the Buckingham π -Theorem (i.e., 12 terms – 3 dimensions = 9 π terms). Since 20 linear proportionalities are available in equation (4.15), at least $^{20}C_6 \times 8$ (i.e., 310,080) non-dimensional equations can be formed. It is not suggested that these could not be obtained by other methods of partial analysis. Notwithstanding, dimensional or similitude analysis starts with equation (4.14) and would lead directly to one dimensionless equation, probably of the form given in equation (4.19) or (4.20). Other solutions would then be attained by compounding. The method of synthesis, on the other hand, develops equation (4.15) as a first step in the analysis, but proceeds directly from that to any of the at least 310,080 possible results.

An examination of equations (4.19) or (4.20) shows the dimensionless ratio $\frac{H_w L_s}{T_w \nu}$ is an alternative way of accounting for viscous action; it might be termed an alternative form of Reynolds number (i.e., $R_e = \frac{U_o L_s}{\nu}$). Also, the dimensionless ratio $\frac{H_w}{L_s}$ is an alternative form of the Keulegan-Carpenter number (i.e., $K = \frac{U_o T_w}{L_s}$); it corresponds to the oscillatory motion of the waves. These alternative forms result because the maximum orbital velocity U_o at the free surface of the ocean can be substituted, in any dimensionless ratio where they appear, by the ratios $\frac{H_w}{T_w}$. Further examination of the equations mentioned above also reveals the dimensionless ratio $\frac{T_w}{L_s} \sqrt{\frac{E}{\rho_s}}$ expresses the ratio of the wave period to the natural representative period of the structure.

4.4 Modelling the Tower

Earlier, the non-dimensional products necessary to model the structure, for the *fluid-structure-interaction*, were presented. To interpret the results ob-

tained from the scaled model of the structure, it is necessary that these non-dimensional ratios presented in equations (4.19) and (4.20) have the same (or approximately the same) value in both the model and the prototype. This means that (subscripts m and p refer to model and prototype, respectively) :

$$\left[T_w \sqrt{\frac{g}{H_w}} \right]_m = \left[T_w \sqrt{\frac{g}{H_w}} \right]_p, \quad (4.21)$$

$$\left[\frac{\rho_s}{\rho_w} \right]_m = \left[\frac{\rho_s}{\rho_w} \right]_p, \quad (4.22)$$

$$\left[\frac{H_w}{L_s} \right]_m = \left[\frac{H_w}{L_s} \right]_p, \quad (4.23)$$

$$\left[\frac{T_w}{L_s} \sqrt{\frac{E}{\rho_s}} \right]_m = \left[\frac{T_w}{L_s} \sqrt{\frac{E}{\rho_s}} \right]_p, \quad (4.24)$$

$$\left[\frac{H_w L_s}{T_w \nu} \right]_m = \left[\frac{H_w L_s}{T_w \nu} \right]_p, \quad (4.25)$$

$$[\zeta]_m = [\zeta]_p, \quad (4.26)$$

$$\left[\frac{t}{T_w} \right]_m = \left[\frac{t}{T_w} \right]_p, \quad (4.27)$$

in order for

$$\left[\frac{F_t}{\rho_w g L_s^3} \right]_m = \left[\frac{F_t}{\rho_w g L_s^3} \right]_p, \quad (4.28)$$

and

$$\left[\frac{u_t}{L_s} \right]_m = \left[\frac{u_t}{L_s} \right]_p. \quad (4.29)$$

That is, equations (4.28) and (4.29) are truly justified if and only if equations (4.22) to (4.27) are satisfied simultaneously⁵. On many occasions, however, it may not be possible to satisfy this condition. A summary of the difficulties involved in attempting to satisfy the above requirements is presented in the following section.

4.5 Difficulties Associated with Hydro-Elastic Modelling

Difficulties arise when attempting to model the soil-structure interaction. These are related, fundamentally, to the practical impossibility of using any liquid other than water in the model, and to the problem that gravitational acceleration is the same in both the model and prototype. These difficulties⁶ may be described as:

1. the different relations between **period** and **geometry** due to periodic motions governed by gravity and inertia forces and with that governed by elastic and inertia forces (i.e., $C_g = T_w \sqrt{\frac{g}{L_w}}$, and $C_e = \frac{T_s}{L_s} \sqrt{\frac{E}{\rho_s}}$). T_w and T_s represent the period of the wave and structure, respectively, while C_g (i.e., *Froude's Law*) and C_e are arbitrary constants⁷ chosen to represent the dimensionless products—the other variables have been previously defined;

⁵If the maximum value of F_t or u_t is desired instead of the instantaneous values, equation (4.27) should be excluded—i.e., the *dimensionless time* ratio.

⁶The *soil-structure interaction*, which also causes serious problems in modelling, is not considered in this treatise.

⁷For the elastic and inertia forces (e.g., free vibration of elastic structures in air), the variables involved (L_s, ρ_s, E , and T_s) combine to give the dimensionless product C_e .

2. the interaction between inertia forces in the liquid and those in the structure; and
3. the presence of viscous forces in the liquid and of damping in the structure.

In the following sub-sections, those difficulties are explained in more details.

4.5.1 Difficulties due to Froude's Law of Similarity

Based on Froude's law (i.e., C_g), it can be shown that the time scale factor is equal to the square root of the geometric scale factor; that is:

$$\begin{aligned} \left[T_w \sqrt{\frac{g}{L_s}} \right]_m &= \left[T_w \sqrt{\frac{g}{L_s}} \right]_p, \\ \Rightarrow \frac{T_{w,m}}{T_{w,p}} &= \sqrt{\frac{L_{s,m}}{L_{s,p}}}. \end{aligned}$$

However, if the model were fabricated with the same material as the prototype, the time scale factor, resulting from the constant C_e , would be equal to the geometric scale factor, and not with the square root. More explicitly:

$$\begin{aligned} \left[\frac{T_s}{L_s} \sqrt{\frac{E}{\rho_s}} \right]_m &= \left[\frac{T_s}{L_s} \sqrt{\frac{E}{\rho_s}} \right]_p, \\ \Rightarrow \frac{T_{s,m}}{T_{s,p}} &= \frac{L_{s,m}}{L_{s,p}} \sqrt{\left(\frac{E_p}{\rho_p} \right) \left(\frac{\rho_m}{E_m} \right)}; \end{aligned}$$

therefore, if the material in the model and prototype is the same, then:

$$\frac{T_{s,m}}{T_{s,p}} = \frac{L_{s,m}}{L_{s,p}}.$$

Assuming the prototype experiences resonance at a certain wave frequency and wave length, the natural frequency of the reduced model would be greater than the frequency of the corresponding wave(s) as seen by the constant

C_d . Hence, if the dynamic amplification in the response of the prototype is significant, this discrepancy should not be accepted, even in the presence of structural damping.

To avoid this problem, it will be necessary to modify $\frac{E}{\rho_s}$, so the time scale factor resulting from Froude's law (valid for waves) is also valid for the structure. This objective can be achieved if the material of the model is different from the material of the prototype. As a result, the scale factor for $\frac{E}{\rho_s}$ must be equal to the geometric scale factor (i.e., $\frac{L_m}{L_p}$). Therefore,

$$\frac{T_{s,m}}{T_{s,p}} = \frac{\frac{L_m}{L_p}}{\sqrt{\left[\frac{E}{\rho_s}\right]_m \left[\frac{E}{\rho_s}\right]_p^{-1}}}; \quad (4.30)$$

so

$$T_{s,m} = T_{s,p} \sqrt{\frac{L_m}{L_p}}, \quad (4.31)$$

where $T_{s,m}$ and $T_{s,p}$ are the period of the model and prototype, respectively.

4.5.2 Difficulties due to the Interaction between Inertia in the Structure and in the Liquid

From a practical viewpoint, equation (4.31) can only be justified if a material which has a smaller modulus of elasticity, a greater density, or both is used. Nonetheless, the adoption of this solution will be restricted, because as a fully or partially submerged structural component vibrates, inertia forces will be produced in the liquid. (The effect is sometimes described, in a manner conceptually not rigorous, as the *added mass* of the liquid.) This new impediment would, therefore, satisfy equation (4.22); that is, $\left(\frac{\rho_w}{\rho_s}\right)_m = \left(\frac{\rho_w}{\rho_s}\right)_p$. From the viewpoint of the fluid structure interaction, this could be achieved by using a material in the model with the same density as the prototype

(i.e., $\rho_{s,m} = \rho_{s,p}$), but with a modulus of elasticity reduced to the general geometric or model scale ratio (i.e., $\frac{E_m}{E_p} = \frac{L_m}{L_p}$), which is applied to the external dimension(s). Practically, it may be impossible to construct such a model, since the material may be difficult to obtain. A possible solution to this dilemma would be to resort to a distorted model.

Distorted Model: To avoid having a linear scale ratio equal to the moduli scale ratio, a certain geometric distortion can be used, since both the model and prototype will be composed of thin walled section members. This distortion can be achieved by applying a geometric scale factor to the wall thickness of the model. Yet, to reproduce the hydrodynamic wave forces in the model⁸, the external dimension of the model member(s) must be maintained at the model scale ratio (i.e., $\frac{D_m}{D_p} = \frac{L_m}{L_p}$).

For this reason, the distortion should occur in the wall thickness of the structural member(s), such that:

$$\left(\frac{d_m}{d_p}\right) = \frac{1}{\epsilon} \left(\frac{D_m}{D_p}\right), \quad (4.32)$$

where

ϵ = the distortion,

d_m, d_p = wall thickness of the model and prototype, respectively, and

D_m, D_p = exterior diameter of the model and prototype, respectively.

Based on the foregoing, the ratio of the modulus of elasticity should be:

$$\left(\frac{E_m}{E_p}\right) = \epsilon \left(\frac{L_m}{L_p}\right). \quad (4.33)$$

Making use of the above expressions, equation (4.32) now becomes:

$$\left(\frac{d_m}{d_p}\right) = \left(\frac{D_m}{D_p}\right) \left(\frac{E_p}{E_m}\right) \left(\frac{L_m}{L_p}\right), \quad (4.34)$$

⁸As shown in equation (3.3), Chapter 3, the wave force is a function of the external dimension(s) of the structural members.

where $\left(\frac{L_m}{L_p}\right)$ is the general geometric or model scale; it is different from $\left(\frac{d_m}{d_p}\right)$, the member(s) wall thickness scale. Since $\left(\frac{D_m}{D_p}\right) = \left(\frac{L_m}{L_p}\right)$, then equation (4.34) can be reduced to the following expression:

$$\left(\frac{d_m}{d_p}\right) = \left(\frac{L_m}{L_p}\right)^2 \left(\frac{E_p}{E_m}\right). \quad (4.35)$$

To satisfy the above expression, it will be necessary for the material of the model to have a density $\rho_{s,m}^*$, so:

$$\rho_{s,m}^* \frac{D_m d_m}{D_m^2} = \rho_{s,p} \frac{D_p d_p}{D_p^2}, \quad (4.36)$$

where $\rho_{s,m}^*$ and $\rho_{s,p}$ are the material densities of the model and prototype, respectively—the other variables have been previously defined. Observe that the products $D_m d_m$ and $D_p d_p$ are proportional to the cross sectional areas of the structural component(s) of the model and prototype, respectively. The above expression results because the submerged weight to the hydrodynamic force ratio⁹ should be held constant [59]. Rearranging equation (4.36) results in the following expression:

$$\rho_{s,m}^* = \rho_{s,p} \left(\frac{L_m}{L_p}\right) \left(\frac{d_p}{d_m}\right). \quad (4.37)$$

Since models constructed of a material having a low modulus of elasticity (e.g., plastic) often have a lower density than $\rho_{s,m}^*$, then it will be necessary to add flexibility and conveniently distribute extra masses to compensate for the difference¹⁰; that is:

$$\Delta \rho_{s,m} = \rho_{s,m}^* - \rho_{s,m}. \quad (4.38)$$

⁹... i.e., $(F_{submerge} \propto \rho_{s,m} D_m d_m \text{ or } \rho_{s,p} D_p d_p) :: (F_{hydrodynamic} \propto D_m^2 \text{ or } D_p^2)$.

¹⁰... e.g., for the model being investigated in this treatise, $\rho_{s,m}^*$ is $2.087 \times 10^{-3} \text{ kg/cm}^3$; while $\rho_{s,m}$ for ABS plastic is $1.107 \times 10^{-3} \text{ kg/cm}^3$.

4.5.3 Difficulties due to Viscosity-Forces and Structural Damping

Viscous forces, due to the liquid, and structural damping create problems in modelling. Viscous forces are important if the external diameter (D) of the structural component is small compared with the wave height, H_w [59, 60]. The variables which are important are: 1) U_0 (maximum orbital velocity at the free surface), 2) D (external diameter of the member(s)), and 3) ν (kinematic viscosity of the liquid). These variables can be combined to produce a Reynolds number.

The conclusion is that the similitude condition corresponding to equality of Reynolds number cannot be satisfied in both model and prototype [60]. Since this problem cannot be eliminated, a reasonable possibility is to accept this limitation, and to assess its consequences.

On many occasions, the influences of variation in Reynolds number are not so critical; for example, member(s) having large external diameter(s), and member(s) having rough surface(s). Conversely, for member(s) with smooth surfaces and small external diameter(s) compared with the wave height, H_w , the effects of variation in Reynolds number should not be ignored. This is mainly because the prototype is, often, in a supercritical, and the model in a subcritical regime.

Thus, if the prototype has a certain roughness, then the model should present the same relative roughness. It is not always possible to satisfy this condition.

Structural damping creates a problem in hydro-elastic modelling, because it is not always easy to reproduce the same damping in the model as that in

the prototype. Damping is defined by the damping ratio:

$$\zeta = \frac{C}{C_c}, \quad (4.39)$$

where

C = the structural damping constant, and

C_c = the structural critical damping constant.

The condition $\zeta_m = \zeta_p$ should be at least approximately satisfied.

4.6 Model Design and Fabrication

The reduced model, fabricated to observe the dynamic behavior in air and in water, was designed to be hydro-elastically similar to the main structural system of a typical full-scale four-legged tower prototype. For practical reasons, an exact reduced scale replica of the prototype was not possible. Nevertheless, the modelled tower was designed to have the following salient features.

4.6.1 Description of the Prototype

The prototype structure is a 73 m tall *conventional* steel jacket platform (i.e., a combination of k-bracing and diagonal bracing) operating in 50 m of water, and has overall structural external dimensions depicted in Figure 4.1–4.2. A 3-D view simulation is shown in Figure 4.3. Tables 4.2 and 4.3 depict the member sections and material properties. (The geometrical configuration and member section properties of the structure were obtained from Ref. [61, 62].) In table 4.3, modified refers to the material and section properties of a modified version of the prototype. This modification in certain member section properties was carried out to simplify the design of the reduced model, and

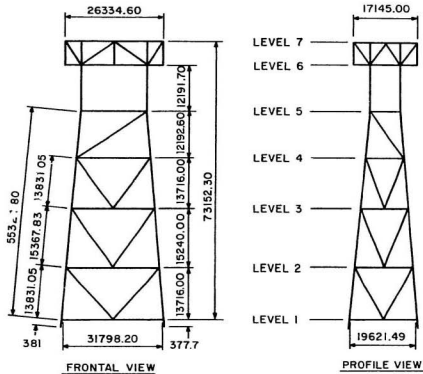


FIG. 4.1 OVERALL DIMENSIONS OF THE PROTOTYPE STRUCTURE.

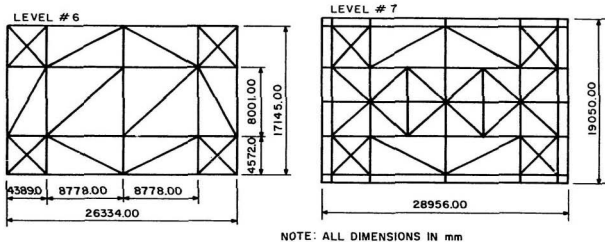


FIG. 4.2 MEMBER CONFIGURATION AT LEVEL #6 AND #7 (PROTOTYPE)

ORIENTATION



HORIZONTAL SCALE =
VERTICAL SCALE =
EQUIVALENT ROTATION

43.9890 FEET PER INCH
43.9890 FEET PER INCH
X 0.0 Y 20.0 Z -40.0

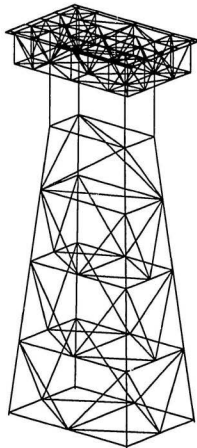


FIG.4.3 3-D VIEW SIMULATION (PROTOTYPE).

Table 4.2 Prototype Structural Data (Original Structure).

	Prototype (Prismatic Member Properties)				
	Cross-sectional Area A [mm ²]	Outer Diameter D [mm]	Wall Thickness d [mm]	Moment of Inertia	
				I_{yy} [mm ⁴]	I_{zz} [mm ⁴]
Horizontal Jacket Bracings Members 1-49	1,367.74	355.60	12.70	2.01×10^8	2.01×10^8
Diagonal Jacket Bracings Members 50-77	1,774.19	457.20	12.70	4.38×10^8	4.38×10^8
Horizontal Deck Beams Members 122-193 (36WF194)	36,836.64	—	—	5.04×10^9	1.48×10^8
Deck Column Members 83, 84, 90, 92, 93, 100 & 107	1,548.38	406.40	25.40	4.38×10^8	4.38×10^8
Jacket Column Members 78-82, 85-89, 94-98 & 101-105	123,161.04	1,066.80	38.10	1.63×10^{10}	1.63×10^{10}
Deck Bracings Members 108-121, & 194-278	1,548.38	406.40	12.70	4.38×10^8	4.38×10^8

Material = Structural Steel,

$E = 206.89$ [kN/mm²],

$\rho_s = 7.85 \times 10^{-6}$ [kg/mm³].

Table 4.3 Prototype Structural Data (Modified Structure).

	Prototype (Prismatic Member Properties)				
	Cross-sectional Area A [mm ²]	Outer Diameter D [mm]	Wall Thickness d [mm]	Moment of Inertia I_{yy} [mm ⁴]	Moment of Inertia I_{zz} [mm ⁴]
Horizontal Jacket Bracings Members 1-49	1,367.74	355.60	12.70	2.01×10^8	2.01×10^8
Diagonal Jacket Bracings Members 50-77	1,548.38	406.40	12.70	4.38×10^8	4.38×10^8
Main Columns Members 78-107	2,989.57	762.00	25.40	2.09×10^9	2.09×10^9
Horizontal Deck Beams Members 122-193	1,774.19	457.20	12.70	4.38×10^8	4.38×10^8
Deck Bracings Members 108-121, 194-278	1,548.38	406.40	12.70	4.38×10^8	4.38×10^8

Material: Structural Steel,
 $E = 206.89 \text{ [kN/mm}^2\text{]},$
 $\rho_s = 7.85 \times 10^{-6} \text{ [kg/mm}^3\text{]}.$

to obtain a model which has its dominant frequencies within the frequency range of the wave maker in the wave tank facility.

4.6.2 Design of The Reduced Model

In Table 4.4 the model structural data—scaled from the modified version of the prototype—are shown. These values were computed using the modelling laws presented earlier in equations (4.35) to (4.38), section 4.4. Sample calculations are presented in Appendix B. Figures 4.4–4.5 depict the overall external dimensions. The corresponding 3-D view simulation is shown in Figure 4.6.

The geometric scale of the model to that of the prototype was computed by using the ratio of the mean water depth of the model to that of the prototype—i.e., $\frac{h_{w,m}}{h_{w,p}}$ or 1:30. Since the experimental model was being tested in the wave tank facility at Memorial University of Newfoundland, the mean water depth was chosen as 1.6 m. This value was selected, because previous research by other experimentalists (e.g., Ref. [63]) suggests that at 1.6 m, the influences of wave reflection from the mechanical beach of the wave tank facility will be minimized.

4.6.3 Fabrication of the Reduced Model

The experimental model was fabricated using Acrylonitrile-Butadiene Styrene (ABS) plastic tubing. This material was selected because of its material properties (i.e., low modulus of elasticity, low density and low material damping ratio). Table 4.5 summarizes the appropriate material property values.

Table 4.4 Model Structural Data (Based on Modified Prototype Structure).

	Model (Prismatic Member Properties)				
	Cross-sectional Area A [mm ²]	Outer Diameter D [mm]	Wall Thickness d [mm]	Moment of Inertia	
				I_{yy} [mm ⁴]	I_{zz} [mm ⁴]
Horizontal Jacket Bracings Members 1-49	47.50	11.11	1.59	553.67	553.67
Diagonal Jacket Bracings Members 50-77	55.42	12.50	1.59	872.92	872.92
Main Columns Members 78-107	118.77	25.40	1.59	8,454.91	8,454.91
Horizontal Deck Beams Members 122-193	71.23	15.88	1.59	1,840.57	1,840.57
Deck Bracings Members 108-121, & 194-278	55.42	12.50	1.59	872.92	872.92

Material: ABS Plastic,
 $E = 1.83$ [kN/mm²],
 $\rho_s = 1.11 \times 10^{-6}$ [kg/mm³].

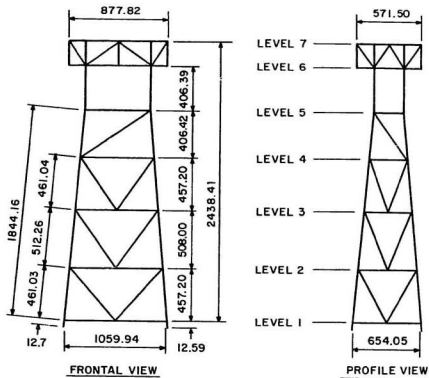


FIG.4.4 OVERALL DIMENSIONS OF THE MODEL STRUCTURE.

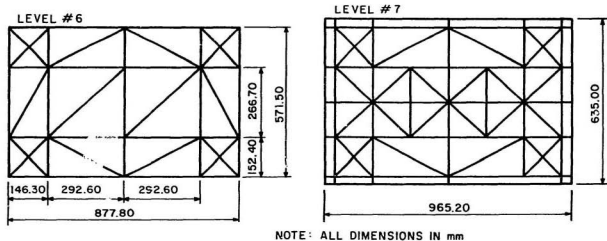


FIG. 4.5 MEMBER CONFIGURATION AT LEVEL #6 AND #7 (MODEL)

ORIENTATION



HORIZONTAL SCALE =
VERTICAL SCALE =
EQUIVALENT ROTATION

1.4663 FEET PER INCH
1.4663 FEET PER INCH
X 0.0 Y 20.0 Z -10.0

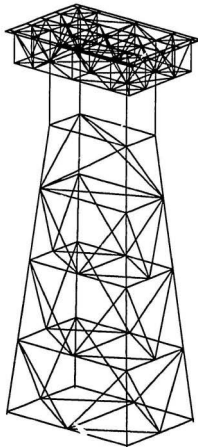


FIG.4.6 3-D VIEW SIMULATION (MODEL).

Table 4.5 Relevant Material Properties for ABS Plastic.

	ABS Plastic Properties Chart	
	A.S.T.M. Test Method	Impact Acrylic Molding Compound
Tensile Strength, p.s.i.	D1708	5000.-9000.
Elongation, %	D1708	20.0-70.0
Tensile Modulus $\times 10^5$, p.s.i.	D1708	2.0-4.0
Compressive Strength, p.s.i.	D695	4000.-14000.
flexural Yield Strength, p.s.i.	D790-66	7000.-13000.
Hardness, Rockwell	D785	R105-R120
flexural Modulus $\times 10^5$, p.s.i.	D790	2.4-3.8
Compressive Modulus $\times 10^5$, p.s.i.	D695	2.4-3.7

Excerpt from 1971-1972 Plastics Encyclopedia [73].

Each member of the model was fastened at the joints with **ABS** solvent glue. Glueing was chosen over welding, because of the size of the wall thickness (1.586 mm) of the members. Had welding been used, the joints might have been damaged by the amount of heat and weld necessary to provide an appropriate bond; besides, welding is more time consuming. Preliminary tests on sample joints—to assess the bonding strength of the glue—showed that the glued joints are capable of withstanding over two times the load(s) that would be experienced by the model during testing. In the prototype structure, the joints are welded to provide rigid moment resisting connections. From the preliminary tests on the glued specimens, it was concluded that the joints (as used in the model) would be capable of providing similar connections.

The deck of the model consisted of a 965.2 mm × 635 mm × 4.76 mm **ABS** plastic plate. It was fastened to the trusswork structure, composed of tubular members, also with **ABS** solvent glue. Figures 4.7–4.9 epitomize the various stages of fabrication. To simulate a rigid base connection, the legs of the tower at the base were attached to four specially designed connectors bolted unto a circular plywood plate. One advantage of the base connectors is that they can be rotated; so the structure can be easily levelled in place. Figures 4.10–4.11 show the various stages of the installation.

At all the nodes along the main columns below the mean water level, **ABS** weight holders were attached. (See Figure 4.12.) These were installed because, as discussed previously, extra weights were needed to compensate for the difference between the density of the material required ($\rho_{s,m}^*$), and the actual density ($\rho_{s,m}$) of the **ABS** material—refer to equation (4.38), section 4.5.2, and Appendix B for sample calculations.

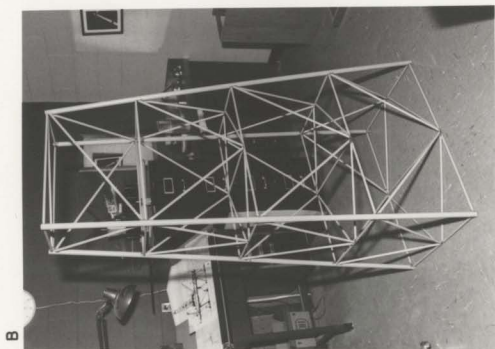
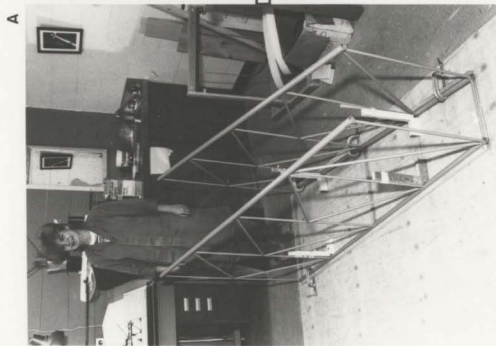
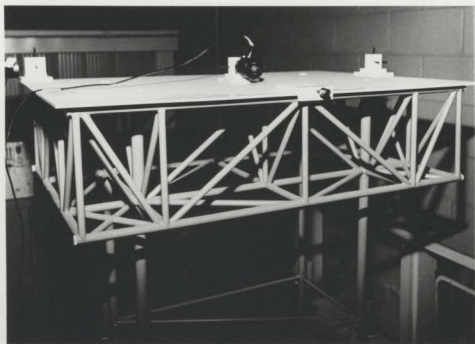
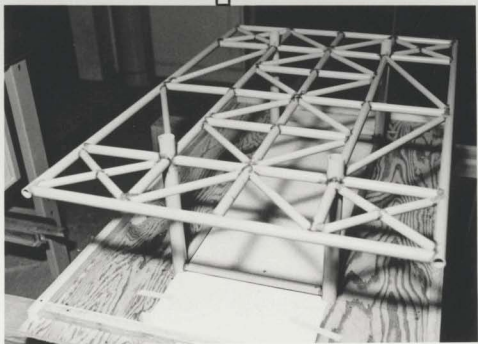


FIG. 4.7 JACKET UNDER CONSTRUCTION (A→B).



D



C

FIG. 4.8 DECK UNDER CONSTRUCTION (C → D)

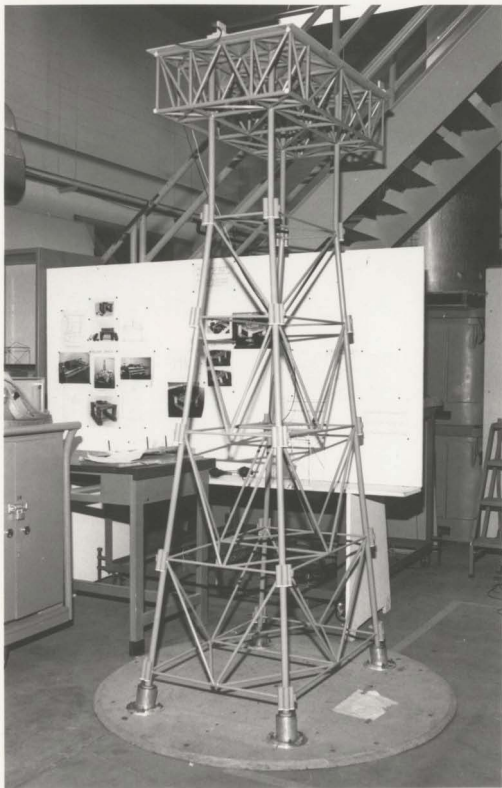
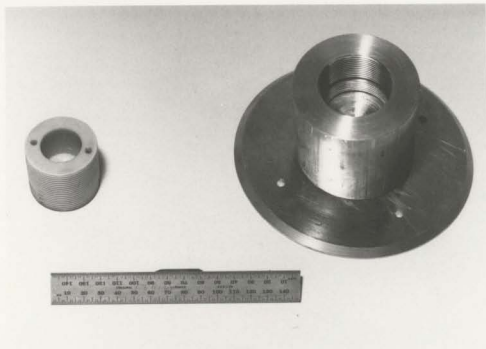
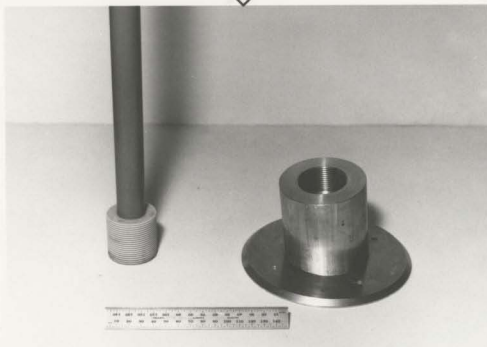


FIG. 4.9 COMPLETED STRUCTURE.



E



F

FIG. 4.10 BASE CONNECTORS BEFORE ATTACHMENT TO STRUCTURE (E→F).

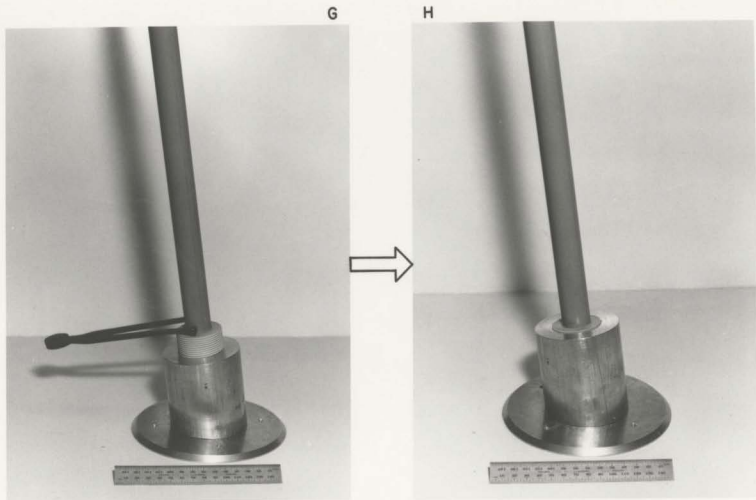


FIG. 4.11 BASE CONNECTOR BEING ASSEMBLED TO STRUCTURE (G→H).

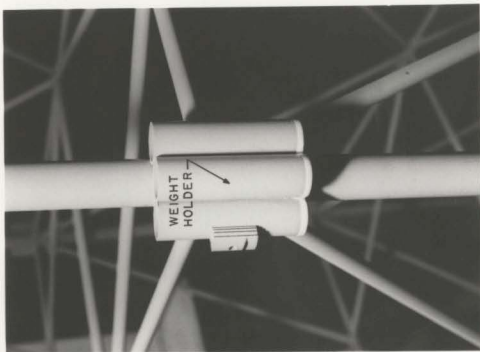


FIG. 4.12 WEIGHT HOLDERS AND INSTALLED BASE CONNECTOR .

Since the deck section of the structure (because of its geometrical configuration) is inherently more flexible than the jacket (i.e., the section below the water level), it was considered that the extra lumped masses should be distributed in the region where more flexibility was required. Hence, the locations of the weight holders were selected at the nodes along the main columns of the jacket, into which the extra lumped masses were inserted.

Chapter 5

Experimental Study

This chapter deals with the dynamical testing of the experimental model. Dynamic testing is very advantageous, because it can be used to:

- (i) verify the analytical model,
- (ii) diagnose (trouble-shoot) the vibration problem,
- (iii) assess design changes in the structure, and
- (iv) devise a dynamic model for parts of the structure too complicated to model analytically.

For all these cases, the objective of the dynamic testing procedure was to excite and identify the modes of vibration of structure and to determine the dynamic response. In both the analytical and experimental phases of this investigation, the common entity was the set of modal parameters. The relationship is summarized diagrammatically in Figure 5.1.

5.1 Equipment Installation

A brief description of the equipment used in the experiments is presented in this section. First the wave maker system is described, followed by the

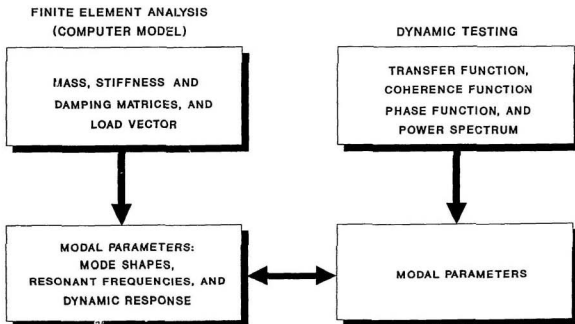


FIG. 5.1 COMMON ENTITIES OF THE ANALYTICAL AND EXPERIMENTAL INVESTIGATIONS.

instrumentation of the model structure, then the equipment used for the impact tests, and, finally, the response circuit.

5.1.1 The Wave Maker System

The wave tank facility at Memorial University is 58.27 m in length, 4.57 m in width and 3.04 m in depth (see Figure 5.2). However, the hydraulically operated piston type wave generator also shown in Figure 5.2, installed behind the wave board at one end of the tank, restricts the actual operating length to approximately 54.74 m. The walls of the tank are of reinforced concrete construction, while the wave board is fabricated from aluminum with a water tight teflon seal along its sides and bottom. Several large viewing windows are conveniently located in one of the tank's walls, enabling visual and photographic analysis of a model's response at surface and sub-surface elevations.

Both regular and irregular wave spectra can be generated by the translatory motion of the wave board. The force capability of the hydraulic actuator shown in Figure 5.3 (it drives the board over a 0.5 m stroke) is specified at 48.8 kN and limits the actual operating depth to about 2.13 m or less. As shown in Figure 5.4, wave heights and frequencies are governed by the motions of this actuator. Electronic control for the board is provided from the control room through an MTS closed-loop servo-controlled system with error detection and compensation applied through an LVDT feedback loop. (Refer to Figure 5.5.)

Located at the far end of the tank is a parabolic beach consisting of an aluminum frame covered by wooden slats and layers of nylon net. This device is intended to absorb and dissipate the energy contained in the incident wave

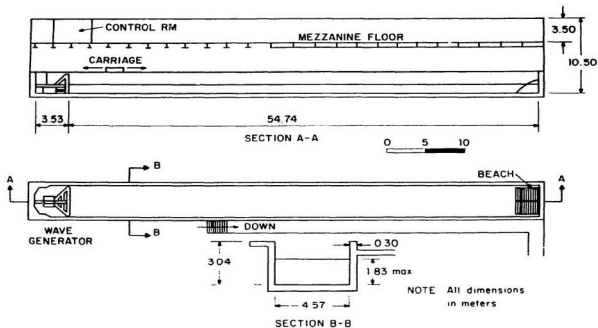


FIG.5.2 DIMENSIONS OF WAVE TANK FACILITY.

LOCATION OF EXPERIMENT

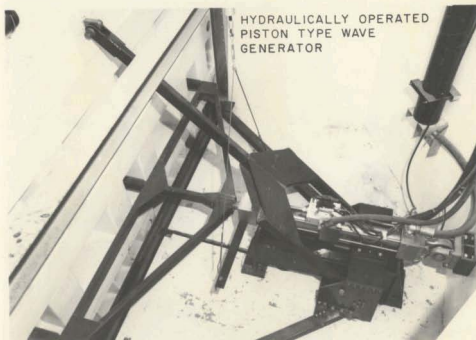


FIG. 5.3 VIEW OF WAVE TANK FACILITY

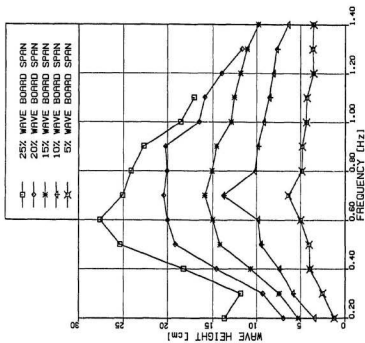


FIG. 5.4 WAVE BOARD CHARACTERISTICS FOR A SET OF SPAN.

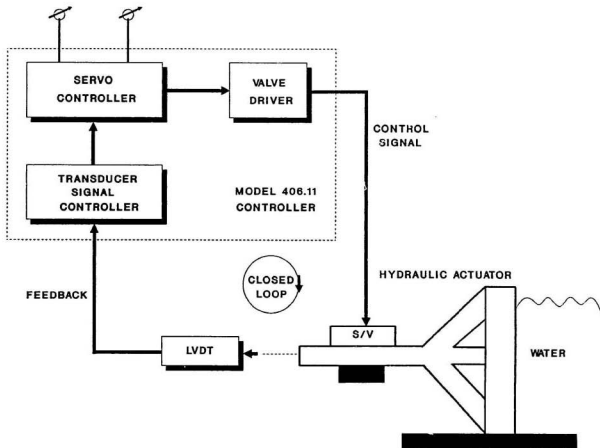


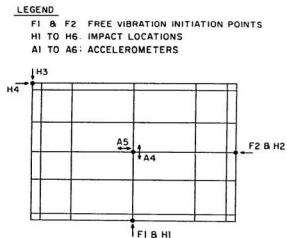
FIG. 5.5 SERVO CONTROL LOOP FOR THE WAVE BOARD.

and maintain a minimum reflection coefficient. Wave filter plates affixed directly to the front of the wave generator are used to reduce the presence of cross tank oscillation in the tank.

5.1.2 Instrumentation of the Model

The experimental model was bolted onto a 152.4 cm diameter, 2.54 cm thick, circular water-proofed plywood plate—which in turn was bolted to the bottom of the wave tank—and levelled in place by the specially designed base connectors mentioned earlier in section 1.1; refer to Figure 4.9. The model was installed at a distance of about 12.8 m from the zero position of the wave board. Three capacitance type wave probes were used to measure the incoming waves; these were designated P1 to P3 for ease of reference. Each probe is equipped with a capacitance meter to convert the change in capacitance (resulting as the waves interact with the probe) to a d.c. voltage. The probes were calibrated in units of distance in centimeters per volt. Therefore, the changes in wave elevation above or below the mean water level could be computed. Probe P1 was located about 1 m in front of the model; that is, along the centerline of the broad side of the structure. Probes P2 and P3 were installed adjacent to the narrow side at distances 0.6 and 1.2 m, respectively, from the wall of the tank shown earlier in Figure 5.3. These two probes were used to determine if there were any cross-tank oscillation effects. This would be shown by any major dissimilarities between the signals measured with the first probe and with those measured with the second and third probes.

Five accelerometers were used to measure the acceleration of the structure. These were designated A1 to A5 for ease of reference; refer to Figure 5.6. (Specifications and calibration settings for the tests are presented in



ORIENTATION

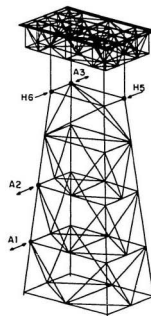


FIG. 5.6 INSTRUMENTATION, FREE VIBRATION AND IMPACT LOCATIONS.

section C.1, Appendix C.) Accelerometers A1 and A2 were submerged,¹ and A3 was placed at the mean water level, and A4 and A5 were installed at the center of the deck of the model structure. Accelerometers A1 to A4 were used to measure the acceleration of the structure in the direction of the incoming waves—i.e., the designated x-direction of the global xyz system of the structure). The accelerometer designated A5 was used to measure the acceleration at 90° to accelerometer A4 (i.e., in the designated global y-direction).

To keep the deck weights of the structure in place, six aluminum weight holders were riveted onto the deck in a rectangular configuration. Each weight holder held 19.16 kg—a total deck mass of 114.59 kg.

5.1.3 Instrumentation for Impact Testing

To carry out impact tests on the model, six impact locations (designated H1 to H6 in Figure 5.6) were selected. At each of these locations a metal attachment was fitted as shown in Figure 5.7. These were used as impact points to transmit the pulse (resulting from the impact) through the structure. Figure 5.7 also shows the modally tuned impact hammer, the power unit, and accelerometers A1 to A5 before they were made water-tight. The response of the structure to the impact tests were also measured with these accelerometers. A calibration curve for the impact hammer is depicted in Figure C.1, Appendix C. As will be explained later, in more detail in section 5.2.5, impact tests were necessary to validate the results obtained from the wave excitation experiments.

¹ Accelerometers A1, A2 and A3 were made water-tight by coating them with an inner layer of silicon, and an outer layer of heavy duty wax seal.

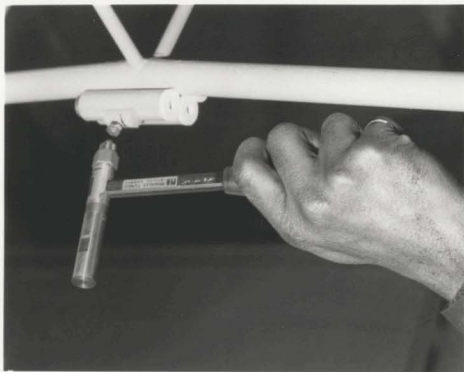


FIG. 5.7 IMPACT TESTING IN PROGRESS.



5.1.4 Response Circuit

Data acquisition and much of the subsequent analyses were carried out in the control room of the wave tank facility, with some on-line equipment producing real time analyses. Each acceleration signal was passed through a charge amplifier where it was calibrated and then through a low pass filter to remove extraneous noise occurring above the maximum cut-off frequency desired. Voltage measurements from the probe meters were filtered in a similar manner. (Data from the accelerometers and wave probes were in an analog format.) Subsequently, all data were digitized with an analog to digital converter. Then the digitized data were transmitted via an Ethernet link system to the Faculty's VAX 8530 computer for storage. The VAX computer provided additional analysis packages, decreased computation times and increased mass storage capability in a universal format. For diagrams showing the entire experimental equipment installation, refer to Figure 5.8 and 5.9.

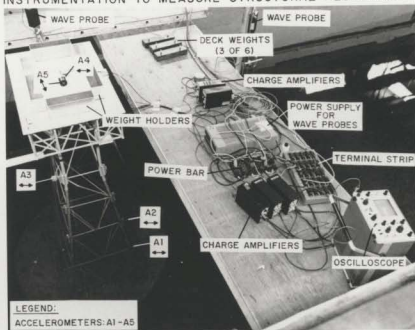
5.2 Experimental Procedure

Three modes of testing were used: 1) free vibration testing in air and in water to determine the free oscillation damping coefficient of the model structure, 2) wave testing to determine the dynamic response to compute the modal parameters (i.e., resonant frequencies, and wave induced damping coefficients) and 3) impact testing to validate the values obtained for the resonant frequencies in the wave tests.

5.2.1 Free Vibration Tests

Before the structure was placed in the wave tank, free vibration tests were carried out in air. These experiments were done to determine the damping

INSTRUMENTATION TO MEASURE STRUCTURAL RESPONSE



COMPUTER CONTROL ROOM



FIG. 5.8 TEST APPARATUS

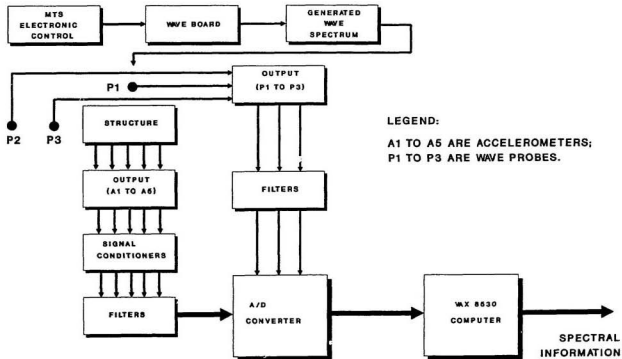


FIG. 5.9 EXPERIMENTAL CIRCUIT

coefficient (i.e., ζ_{air}) of the model structure in air. Two locations, designated F1 and F2 on the deck of the structure (refer to Figure 5.7), were selected. First, free vibration was initiated at location F1 by giving the structure an initial displacement and then releasing it to obtain a record of the oscillatory motion such as those shown in Figure 5.10–5.11, and to measure the rate of decay of amplitude of motion. The procedure was repeated ten times, and each time the oscillatory motion (in the direction of the initial displacement—the global x-direction) was measured with an accelerometer located at the center of the deck. Second, the procedure was repeated at location F2, and the motion was recorded in like manner in the direction of the initial displacement (i.e., the global y-direction).

After the structure had been installed in the wave tank, free vibration tests were accomplished in the same manner as the *in-air* tests. These tests were carried out to compute the free vibration damping coefficient of the structure in water (i.e., ζ_{water}), so the effect of the fluid on the free vibration of the structure could be investigated.

5.2.2 Wave Simulation

Since a true sea state is a random phenomena, where waves are continually changing in height, length and breadth, it is impossible to characterize or define it exactly in terms of its pattern or shape. It is possible, however, to define the sea in terms of the total energy it contains. Furthermore, it is also possible to define the contributions made to its total energy by each of its components. That is, for any given sea state, a wave energy spectrum may be developed which expresses the wave energy density distribution of the sea as a function of wave frequency or as a function of wave number. This is

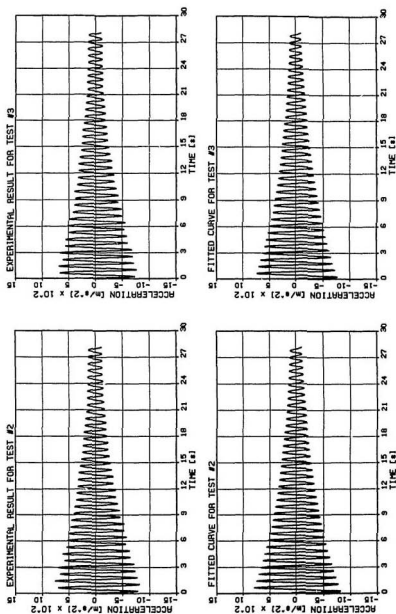


FIG. 5.10 TYPICAL FREE OSCILLATION RESPONSE CURVES IN THE X-DIRECTION AT R4 (IN-AIR TESTS).

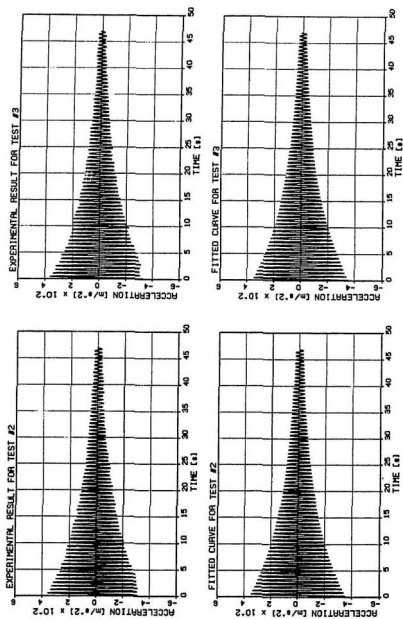


FIG. 5.11 TYPICAL FREE OSCILLATION RESPONSE CURVES IN THE Y-DIRECTION AT A5 (IN-AIR TESTS).

the basis upon which the irregular wave spectra were simulated by the wave maker system.

Two different spectra were used in the tests: 1) a white noise spectrum, and 2) a JONSWAP spectrum. The spectral density equations used to define these respective spectra are:

$$S_W(f) = \begin{cases} \left(\frac{H_s}{4\sqrt{f_{max}}} \right)^2, & \Delta f < f \leq f_{max} \\ 0, & \text{otherwise} \end{cases} \quad (5.1)$$

for the white noise spectrum, where: H_s is the significant wave height, Δf is the frequency resolution of the signal, and f_{max} is the maximum cut-off frequency. (In the experiment, H_s was set equal to 16 cm and f_{max} , 1.2 Hz.) For the JONSWAP spectrum,

$$S_J(f) = \frac{A}{f^5} \exp\left(-\frac{B}{f^4}\right) \gamma^a, \quad (5.2)$$

where

$$\begin{aligned} a &= \exp\left[\frac{-(f - f_0)^2}{2\sigma^2 f_0^2}\right], \\ \sigma &= 0.07 \text{ for } f \leq f_0, \\ \sigma &= 0.09 \text{ for } f > f_0, \\ A &= \frac{5H_s^2 f_0^4}{16\gamma^{\frac{1}{3}}} \text{ for } 1 < \gamma < 4, \\ B &= 5\frac{f_0^4}{4}; \end{aligned} \quad (5.3)$$

and where: f_0 is the peak frequency; H_s is the significant wave height; and γ is a peak enhancement factor.² (The values used for H_s , γ , and f_0 in the experiments are: 10 cm, 1.0, and 0.6 Hz, respectively.)

Two different spectra were used for the following reasons:

²If $\gamma = 1$, equation (5.2) is reduced to a Pierson Moskowitz spectrum.

- (a) Because the objective was to excite the higher modes of the model structure, it was decided that if a flat spectrum (i.e., white noise) were used, it might have been possible to excite the higher modes more easily over a specified frequency range.
- (b) The JONSWAP spectrum was used to examine the behavior of structure under realistic sea conditions.

5.2.3 Irregular Wave Simulation

To simulate each irregular wave spectrum, the following five steps were carried out:

1. Having defined the desired wave spectrum, the spectral density curve was calculated using either equation (5.1) or (5.2), depending on which spectrum was being simulated. For the white noise spectrum, inputs to the equation included: the significant wave, H_s , the frequency resolution, Δf , and the maximum frequency, f_{max} ; while for the JONSWAP, the inputs included: the peak frequency, f_0 , the significant wave height, H_s , and the peak enhancement factor, γ .
2. An initial digitized time-history drive signal was calculated by the computer. This signal was subsequently converted to its analog form to drive the wave board and create an irregular sea state in the wave tank.
3. Then an achieved wave spectrum was calculated from the waves generated by the initial drive signal. This was achieved by recording the time history data with a wave probe located about one metre in front of the broad side of the model structure (i.e., probe P1). The data were

then manipulated by the computer software to create an achieved wave spectrum.

4. Any discrepancies between the desired wave spectrum and the achieved wave spectrum was corrected via an iterative process. Variations between the two were determined by the computer, and additional drive signals were created until the differences between the desired and the achieved were within acceptable limits.
5. The corrected time history drive signal was applied to the wave board to create irregular waves for model testing. Collected data were finally manipulated by the system application software to create spectral density information.

Approximately four hours were required to complete the wave simulation process for each spectrum. (All computations for the above steps were accomplished with a special purpose program (**SPECGEN**) developed by Mr. Lloyd Little, project engineer at the wave tank facility.)

5.2.4 Wave Structure Interaction

As a result of the frequency resolution desired, and the memory limitation of the data acquisition computer at the wave tank facility, the duration for the wave test was set at three minutes. Therefore, to collect sufficient data to allow transfer function analyses, ten separate runs, for each test, were carried out. (A set of ten runs lasted approximately eight hours.) This was accomplished by running a test for three minutes (while collecting data), then stopping the test and allowing the water in the tank to settle. The water was considered settled, when the wave probe readings showed a particular

pre-determined value. Figure 5.12 shows the structure in still water, and as it is acted upon by waves. For each spectrum, the stopping and starting procedure was repeated.

Wave tests were carried out for both the intact and damaged structure. For the damaged case, the member under consideration (member 70, see Figure 5.13) was severed in three stages. Initially, an incision was made halfway through the member at node 18, by saw cutting, to investigate if there would be any noticeable changes in the frequency response of the structure. Second, the member was cut-off at the joint (i.e., node 83). In so doing, the stiffness of the structure was reduced appreciably, but the mass remained virtually unchanged. Finally, the member was removed. Thus, the mass of the structure was reduced by the mass of the severed member. At each stage, the acceleration of the structure was measured with accelerometers A1 to A5.

After the first member was removed, a similar member (member 68), located in the plane parallel to the previously severed member, was cut-off at node 16 and the essential measurements were repeated.

Since the structural response for two separate wave spectra was needed, the structure was excited with irregular waves generated with the white noise spectrum and, following, with the JONSWAP spectrum. Thus, after each set of ten tests with the white noise spectrum, similar tests were carried out for the JONSWAP spectrum, and the necessary measurements taken.

5.2.5 Impact Testing Response

As the response of the structure at resonance was a major concern, impact tests were carried out to test the validity of the location of the resonant peaks that would have been obtained from the irregular waves tests. Therefore,

STRUCTURE IN STILL WATER



STRUCTURE ACTED UPON BY WAVES

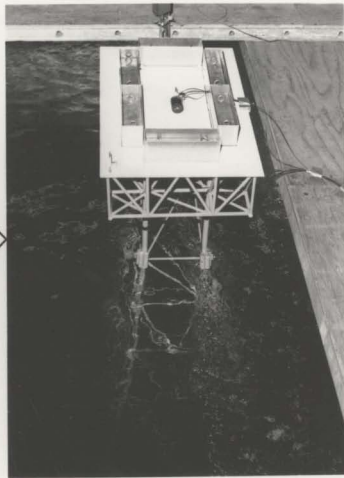


FIG. 5.12 WAVE TESTS IN PROGRESS.

ACTUAL MODEL



COMPUTER SIMULATED MODEL

ORIENTATION

LEGEND:

① DAMAGED MEMBERS

● DAMAGED JOINTS

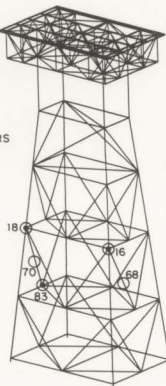


FIG. 5.13 SEVERED MEMBER(S) IN THE ACTUAL AND SIMULATED MODEL.

after every set of ten wave excitation tests, impact testing were carried out for the corresponding structural configuration—i.e., intact and damaged.

•

Chapter 6

Analysis of Results

Time signals obtained (in an analog format) from the experimental investigation, described in chapter 5, were analysed to extract relevant information. Two types of analyses were used: 1) the conventional Fast Fourier Transform (FFT) algorithm, and 2) the recently developed Marple algorithm for autoregressive spectral analysis, with the Maximum Entropy Method. The conventional FFT method was used to obtain an overview of the response in the frequency domain (i.e., transfer function, phase function and power spectrum); while the MEM was used to compute the modal parameters (i.e., resonant frequencies, and damping ratios), because the method is capable of producing higher resolution spectra.

Computations for the undistorted spectrum related to the aperiodic signal $x(t)$ with maximum frequency content B Hertz and duration T seconds were accomplished using the following signal processing method:

- (i) a sample frequency $f_s \leq 2B$ is selected ($\Delta t = \frac{1}{f_s}$),
- (ii) an appropriate data block length is selected so:

$$T = N\Delta t$$

$$\begin{aligned}
&= N \frac{1}{f_s} > t \\
\Rightarrow \Delta f &= \frac{1}{T} \\
&= \frac{1}{N \Delta t} \\
&= \frac{f_s}{N}.
\end{aligned}$$

To gather spectral information from the input and output signal to and from the structure, the transfer function, coherence function, phase function and power spectrum are necessary. The mathematical formulations used to define these functions are presented, here, without justification.

Transfer Function: The transfer function (frequency response function) may be computed directly as the ratio of the Fourier transform of the output to the input signal. But better results are obtained, in practice, by computing the frequency response of the cross-spectrum between input and output to the power spectrum of the input. Thus:

$$H(f) = \frac{G_{xy}(f)}{G_{xx}(f)}, \quad (6.1)$$

where

$$\begin{aligned}
G_{xy}(f) &= \text{cross-spectral density between } x(t) \text{ and } y(t), \\
G_{xx}(f) &= \text{autospectral density of } x(t), \text{ and} \\
X^*(f) &= \text{complex conjugate of } X(f).
\end{aligned} \quad (6.2)$$

Coherence Function: Coherence is a measure of causality between any two signals. When a transfer function is computed, extraneous inputs or whether the system is linear may not be too evident. The coherence ranges between 0 and 1. Zero means no coherence between input and output or, in other words, extraneous inputs and/or the system is non-linear. One means

a complete coherence between input and output or, stated differently, only one input and a linear system. In mathematical terms, the coherence is:

$$\gamma_{xy}^2(f) = \frac{|G_{xy}(f)|^2}{G_{xx}(f)G_{yy}(f)}. \quad (6.3)$$

Phase Function: The phase function is used to determine the phase shift or angle between an input and output signal. This function has useful applications, because as the structure passes through resonance, a 180° phase shift develops between the input and output signal. Normally, this rule is used as an indicator to establish if a peak (i.e., relative maxima) on the frequency response or power spectrum results because of resonance in the system (i.e., conditions of low dynamic stiffness in a structure). The phase angle between an input and output signal is:

$$\theta_{xy}(f) = \tan^{-1} \left[\frac{Q_{xy}(f)}{C_{xy}(f)} \right], \quad (6.4)$$

where $C_{xy}(f)$ and $Q_{xy}(f)$ are the co and quad-spectrum, respectively, of $G_{xy}(f)$.

6.1 Spectral Estimates Using FFT

The Fourier Transform relationship between the autocorrelation function $R_{xx}(\tau)$ and the power spectrum is given by:

$$G_{xx}(f) = \int_{-\infty}^{\infty} R_{xx}(\tau) e^{-j2\pi f\tau} d\tau, \quad (6.5)$$

where

$$R_{xx}(\tau) = \lim_{T \rightarrow \infty} \frac{1}{T} \int_{-\frac{T}{2}}^{\frac{T}{2}} x(t)x(t+\tau)dt, \text{ and} \quad (6.6)$$

τ is the time lag between sample values. Nevertheless, for numerical purposes, the auto and cross-correlation functions can be estimated at discrete lags as:

$$R_{xx}(\tau = n\Delta t) = \frac{1}{N} \sum_{n=-\infty}^{\infty} x(t)x(t + n\Delta t), \quad (6.7)$$

$$R_{yy}(\tau = n\Delta t) = \frac{1}{N} \sum_{n=-\infty}^{\infty} y(t)y(t + n\Delta t), \quad (6.8)$$

and

$$R_{xy}(\tau = n\Delta t) = \frac{1}{N} \sum_{n=-\infty}^{\infty} x(t)y(t + n\Delta t), \quad (6.9)$$

where

$$x(t) = \begin{cases} x(t), & 0 \leq t \leq (N-1)\Delta t \\ 0, & t > (N-1)\Delta t. \end{cases} \quad (6.10)$$

As a result, the auto and cross-spectral density functions can be estimated for the first $n = 1, 2, \dots, N$ lags as:

$$G_{xx}(f) = \Delta t \sum_{n=-\infty}^{\infty} R_{xx}(\tau = n\Delta t)e^{(-j2\pi f n\Delta t)}, \quad (6.11)$$

$$G_{yy}(f) = \Delta t \sum_{n=-\infty}^{\infty} R_{yy}(\tau = n\Delta t)e^{(-j2\pi f n\Delta t)}, \quad (6.12)$$

and

$$G_{xy}(f) = \Delta t \sum_{n=-\infty}^{\infty} R_{xy}(\tau = n\Delta t)e^{(-j2\pi f n\Delta t)}. \quad (6.13)$$

Thus, using equations (6.1) to (6.3) while making the appropriate substitutions for $G_{xx}(f)$, $G_{yy}(f)$ and $G_{xy}(f)$, estimates for $H(f)$, $\gamma^2(f)$ and $G_{xy}(f)$ can be obtained.

As seen in equation (6.10), estimates for the autocorrelation function have been implicitly extended to infinite lag with zero (i.e., $x(t) = 0$ for $t \geq N\Delta t$). An estimated spectrum computed using conventional FFT procedures is limited in resolution [72, 32, 64]. This fundamental limit in resolution results

because the estimated autocorrelation function is assumed zero for time lags $n \geq N$. Furthermore, FFT procedures have the inherent problem of generating spurious peaks, because of the limit placed on the resolution. Also, smoothing of the resulting spectra using window functions (e.g., Hanning window) can distort the shapes of peaks and significantly influence inferred damping. Unlike the conventional FFT methods of spectral analysis, the Maximum Entropy Method (MEM) does not require the use of a window function. For this reason, the Maximum Entropy Method was used to obtain estimates of resonant frequencies and damping ratios from the spectral density function of the wave induced response of the model structure. This is because the MEM extends the autocorrelation function in a more realistic manner. The method provides the analytical means of extrapolating from $N + 1$ samples of the known autocorrelation function, $R_{xx}(\tau)$, for example, $\tau = 0\Delta t, 1\Delta t, \dots, (N - 1)\Delta t$, to compute the remaining values of $R_{xx}(\tau)$ for $\tau = (N)\Delta t, (N + 1)\Delta t, \dots, \infty$.

6.2 Spectral Estimates Using MEM

To obtain estimates of resonant frequencies and damping ratios from the wave induced response of the model structure, the Maximum Entropy Method was used. Entropy is a measure of the average information content contained in a signal. Maximizing entropy, therefore, maximizes the information transmitted in a signal. This method, whose development is due to Burg [64], has been used extensively in the fields of geophysics, speech communication, and neurophysics to list a few. Through these applications, MEM has been accepted as a method to produce smooth highly resolved spectra from short duration time histories. Nonetheless, its application in structural dynam-

ics, with a few notable exceptions, remains untried. Therefore, to facilitate understanding of the MEM concept, a discussion of the technique as an autoregressive (AR) model is given. For clarity, the presentation will attempt to obviate an extensive background in time series analyses and signal processing. As such, the development favours intuitive arguments over mathematical rigor. However, for completeness, a list of references is included, so the interested reader may draw from the rich background material available to build a working knowledge of the technique.

6.2.1 Autoregressive Model of MEM

A simple model used by time series analysts to explain the Maximum Entropy Method is the autoregressive (AR) model proposed by Van den Bos [65]. This model states that if a white noise with unit variance discrete signal $w(n)$ is input into a linear or shaping filter $H(f)$ (refer to Figure 6.1) the corresponding output $x(n)$ (true or desired value) is given in the time domain as :

$$x(n) = - \sum_{k=1}^M A(k)x(n-k) + w(n), \quad (6.14)$$

where

$x(n)$ = output of AR filter, true or desired value,

A = coefficients of AR model,

M = order of the AR model,

n = 1, 2, 3, ..., N ,

N = number of samples, and

$w(n)$ = discrete-time white noise.

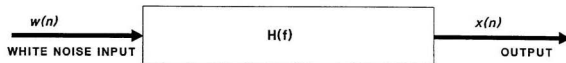


FIG. 6.1 LINEAR OR SHAPING FILTER.

If both sides of the above equation are multiplied by the z operator (i.e., $z = e^{(-j2\pi f\Delta t)}$, Δt is the time increments between sampled data points), and the corresponding z or Fourier Transform is taken, the frequency domain equivalent of equation (6.14) is:

$$X(f) = - \sum_{k=1}^M A(k) e^{(-2j\pi f k \Delta t)} X(f) + W(f). \quad (6.15)$$

Thus:

$$X(f) \left\{ 1 + \sum_{k=1}^M A(k) e^{(-2j\pi f k \Delta t)} \right\} = W(f),$$

$$\Rightarrow X(f) = \frac{W(f)}{\left\{ 1 + \sum_{k=1}^M A(k) e^{(-2j\pi f k \Delta t)} \right\}},$$

or

$$X(f) = H(f)W(f), \quad (6.16)$$

where $H(f) = \left\{ 1 + \sum_{k=1}^M A(k) e^{(-2j\pi f k \Delta t)} \right\}^{-1}$ is the transfer function of the system.

So, the power spectral density estimate between the Nyquist frequency, f_{ny} , is given by:

$$X(f)X^*(f) = H(f)H^*(f)W(f)W^*(f), \quad -f_{ny} \leq f \leq f_{ny}. \quad (6.17)$$

Therefore,

$$\begin{aligned} G_{xx}(f) &= |H(f)|^2 G_{ww}(f), \\ &= \frac{G_{ww}(f)}{\left| 1 + \sum_{k=1}^M A(k) e^{(-2j\pi f k \Delta t)} \right|^2}, \\ &= \frac{2\sigma^2(M)\Delta t}{\left| 1 + \sum_{k=1}^M A(k) e^{(-2j\pi f k \Delta t)} \right|^2}, \end{aligned} \quad (6.18)$$

where $\sigma^2(M)$ or $G_{ww}(f)/2\Delta t$ is the white noise variance or prediction error. The 1 in the denominator is $A(0)$.

To obtain an MEM spectral estimate of a time series, the following steps are taken:

- calculate the AR filter coefficients to the desired filter order;
- compute the prediction error due to a white noise signal at filter order;
- take the magnitude squared of the Fourier Transform of the AR coefficient; and
- do the operations shown in equation (6.18).

6.2.2 The Determination of AR Coefficients

Autoregressive coefficients (AR) are obtained via a forward and backward linear prediction algorithm. For a time series $x(t_1), x(t_2), \dots, x(t_N)$, assume $x(t)$ can be estimated by:

$$\hat{x}(t) = \sum_{k=1}^M \hat{A}(k)x(t-k) \quad \text{for } t = M+1, M+2, \dots, N. \quad (6.19)$$

For given values of the parameter $\hat{A}(k)$, equation (6.19) provides a forward prediction of $\hat{x}(t)$. Letting $\hat{e}(t) = x(t) - \hat{x}(t)$, and adopting the least square (LS) criterion, $\hat{A}(j)$ can be determined by minimizing the residual sum of the squares (i.e., $\sum_{t=M+1}^N \hat{e}^2(t)$).

Equivalently, a LS solution is sought for the AR scheme of order M defined by:

$$x(t) = \sum_{k=1}^M \hat{A}(k)x(t-k) + \hat{e}(t) \quad \text{for } t = M+1, M+2, \dots, N. \quad (6.20)$$

Conversely, $x(t)$ can be estimated by $\tilde{x}(t)$, where:

$$\tilde{x}(t) = \sum_{k=1}^M \tilde{A}(k)x(t+k) \quad \text{for } t = 1, 2, \dots, N-M. \quad (6.21)$$

Then equation (6.21) provides a backward prediction of $x(t)$, and its parameters $\tilde{A}(k)$ can be computed by minimizing $\sum_{t=1}^{N-M} \tilde{e}^2(t)$, where $\tilde{e}(t) = x(t) - \tilde{x}(t)$.

In the Maximum Entropy Method, it is assumed $x(t)$ can be estimated by a weighted sum of M previous observations and a sum of M future observations (refer to equation (6.21), using the same weights $A(k)$ in both directions. As a result, the MEM coefficients $A(k)$ of order M may be computed as the LS solution to the forward and backward linear prediction model defined by the $2(N-M) \times M$ matrix equation:

$$[X]A = Y, \quad (6.22)$$

where

$$[X] = \begin{bmatrix} x(M) & x(M-1) & \dots & x(1) \\ x(M+1) & x(M) & \dots & x(2) \\ \vdots & \vdots & \dots & \vdots \\ \vdots & \vdots & \dots & \vdots \\ \vdots & \vdots & \dots & \vdots \\ x(N-1) & x(N-2) & \dots & x(N-M) \\ x(2) & x(3) & \dots & x(M+1) \\ x(3) & x(4) & \dots & x(M+2) \\ \vdots & \vdots & \dots & \vdots \\ \vdots & \vdots & \dots & \vdots \\ \vdots & \vdots & \dots & \vdots \\ x(N-M-1) & x(N-M+2) & \dots & x(N) \end{bmatrix}, \quad (6.23)$$

$$\underline{A} = \begin{Bmatrix} A(1) \\ A(2) \\ A(3) \\ \vdots \\ \vdots \\ \vdots \\ A(M) \end{Bmatrix}, \quad (6.24)$$

and

$$\underline{Y} = \begin{Bmatrix} x(M+1) \\ x(M+2) \\ \vdots \\ \vdots \\ \vdots \\ x(N) \\ x(1) \\ x(2) \\ \vdots \\ \vdots \\ \vdots \\ x(N-M) \end{Bmatrix}. \quad (6.25)$$

It turns out that the matrix $[X]$ exhibits Toeplitz symmetry; that is, a symmetric matrix with all the diagonal elements equal. The LS solution \underline{A} to equation (6.22) satisfies the $M \times M$ system of normal equations:

$$[X]^T[X]\underline{A} = [X]^T\underline{Y}. \quad (6.26)$$

The Marple algorithm is designed specifically for the forward and backward linear prediction problem discussed earlier [66]. Unlike other algorithms, all components of equation (6.22) are assumed to be complex numbers¹, and the vector \underline{Y} is replaced by $-\underline{Y}$. Furthermore, the computational efficiency of the Marple algorithm is very impressive. Marple's algorithm re-

¹NB: For complex data the backward AR coefficients are the conjugate of the forward AR coefficients.

quires about $N(M + 1) + 9M^2$ arithmetic operations (1 operation = 1 multiplication + 1 addition), and about $N + 4M$ memory locations to solve the forward and backward problem of N data points for all $k = 1, 2, \dots, M$. The mathematical formulations and derivations of the Marple algorithm is beyond the scope of this thesis. Therefore, the reader is referred to the original paper by Marple [67], and a supplementary paper by Vetter and Porsani [68].

6.2.3 Selection of Optimum Model Order

In the previous discussion on MEM, the question regarding the most appropriate order of M had not been discussed. Generally, it has been observed that, for a given value of record length N , small values of M yield spectral estimates with insufficient resolution, whereas—for large values of M —the estimates are statistically unstable, and result in spurious details [69]. For these reasons, various model order selection criteria have been derived. Each, though different in approach, leads to the same result.

The most popular criteria are: 1) Akaike's Final Prediction Error (FPE), and 2) Akaike's Information Theoretic Criterion (AIC) [32, 69]. Mathematically, these criteria² are expressed as:

$$FPE(M) = \frac{N + M + 1}{N - M - 1} P_M, \text{ and} \quad (6.27)$$

$$AIC(M) = \ln(P_M) + \frac{2M}{N}, \quad (6.28)$$

where M is the model order, P_M is the output error power, and N is the number of samples.

Selecting the value of M which results in an optimum order (i.e., M_{opt}) is obtained via an iterative process. An optimum model order is attained when

²NB: $FPE(M)$ and $AIC(M)$ are asymptotically equivalent; that is, $\lim_{T \rightarrow \infty} \{\ln[FPE(M)]\} = AIC(M)$ [69].

a new value of $FPE(M)$ or $AIC(M)$ exceeds the previous one; the iteration is then terminated. (Both criteria are used in this treatise.)

6.3 Estimating Modal Parameters

Estimating resonant frequency and damping ratios from the MEM spectral estimate (i.e. equation (6.22) does not immediately appear to have any great advantage over conventional methods (FFT). But when the expression is re-examined, it is observed that the spectral estimate is actually a closed-form equation for the response spectrum. This unique feature of the MEM spectral estimate provides the key to formulating the modal parameter estimators and their statistics.

6.3.1 Resonant Frequencies

Resonant frequencies can be estimated as the selection of frequencies corresponding to relative maximum of the corresponding spectrum. This search for maxima can be expressed in a mathematical form using the result of differential calculations which states: the derivative of a function is zero at an extrema. Thus, as the spectrum is available in the functional form, the relative extrema of the spectral density spectrum can be obtained as the solution of:

$$\frac{dG_{xx}}{df} = 0. \quad (6.29)$$

To obtain an expression which satisfies equation (6.29), the following steps are taken:

Let

$$z = \sum_{k=0}^M A(k) e^{(-j2\pi k \Delta t)J}, \text{ and}$$

$$(6.30)$$

$$\bar{z} = \sum_{k=0}^M A(k) e^{(j2\pi k \Delta t) f}.$$

So equation (6.18) becomes:

$$G_{xx}(f) = \frac{2\sigma^2(k)\Delta t}{z\bar{z}}. \quad (6.31)$$

Since $\frac{dG_{xx}}{df} = 0$, then $\frac{d(z\bar{z})}{df} = 0$. Hence, setting $F(f) = z\bar{z}$:

$$\begin{aligned} \frac{dF}{df} &= z \frac{d\bar{z}}{df} + \bar{z} \frac{dz}{df} \\ &= \sum_{k=0}^M A(k) e^{-j(2\pi k \Delta t) f} \cdot \sum_{l=0}^M A(l) e^{j(2\pi l \Delta t) f} \cdot (j2\pi k \Delta t) \\ &\quad + \sum_{k=0}^M A(k) e^{k(2\pi l \Delta t) f} \cdot \sum_{l=0}^M A(l) e^{-j(2\pi l \Delta t) f} \cdot (-j2\pi k \Delta t), \\ &= j2\pi \Delta t \sum_{k=0}^M \sum_{l=0}^M k A(k) A(l) \left[e^{(j2\pi \Delta t l(l-k))} - e^{(-j2\pi \Delta t l(l-k))} \right], \quad (6.32) \end{aligned}$$

where k and l are dummy variables. Using Euler's theorem: $e^{j\theta} - e^{-j\theta} = 2j \sin \theta$, equation (6.32) becomes:

$$\frac{dF}{df} = -4\pi \Delta t \sum_{k=0}^M \sum_{l=0}^M k A(k) A(l) \sin(2\pi \Delta t f(l-k)). \quad (6.33)$$

So the computation of resonant frequencies can be estimated as values of $f = f_r$ which satisfy the following expression :

$$\sum_{k=0}^M \sum_{l=0}^M k A(k) A(l) \sin(2\pi \Delta t f_r(l-k)) = 0, \quad (6.34)$$

where f_r is the resonant frequency of the system.

6.3.2 Force Response Damping

Force response damping is usually obtained using the half-power band width method. This method is based on the characteristics of a single degree-of-freedom system and incorporates some assumptions, which restricts the

method to lightly damped systems [72]. The half-power frequencies are defined, here, as a pair of frequencies bracketing the natural frequencies corresponding to spectral ordinates 3 dB down from the peak frequency. More explicitly, the half power frequencies are the solutions of:

$$G_{xx}(f) = \frac{1}{2} G_{xx}(f_r). \quad (6.35)$$

To obtain an expression for estimating the half-power frequencies which satisfies equation (6.35), the following steps are taken:

After substituting equation (6.18) in equation (6.35), and cancelling the numerators on both sides of equation, the following equality results:

$$\left| \sum_{k=0}^M A(k) e^{-j2\pi f k \Delta t} \right|^2 = 2 \left| \sum_{k=0}^M A(k) e^{-j2\pi f_r k \Delta t} \right|^2. \quad (6.36)$$

Thus:

$$\sum_{k=0}^M \sum_{l=0}^M A(k) A(l) e^{-j2\pi f \Delta t (k-l)} = 2 \sum_{k=0}^M \sum_{l=0}^M A(k) A(l) e^{-j2\pi f_r \Delta t (k-l)}.$$

Using Euler's theorem again, the above expression is rewritten as:

$$\begin{aligned} & \sum_{k=0}^M \sum_{l=0}^M A(k) A(l) \{ \cos[2\pi f \Delta t (k-l)] - 2 \cos[2\pi f_r \Delta t (k-l)] \} \\ &= -j \underbrace{\sum_{k=0}^M \sum_{l=0}^M A(k) A(l) \sin[2\pi f_r \Delta t (k-l)]}_0. \end{aligned}$$

It may be recalled that the R.H.S. of the above is the result of equation (6.34). Thus, estimates of frequencies, f , corresponding to half-power values at a given resonant frequency, f_r , are computed as the roots to the following expression:

$$\sum_{k=0}^M \sum_{l=0}^M A(k) A(l) \{ \cos[2\pi f \Delta t (k-l)] - 2 \cos[2\pi f_r \Delta t (k-l)] \} = 0. \quad (6.37)$$

At each resonant frequency, the half-power damping is estimated as:

$$\zeta_{HP} = \frac{f_2 - f_1}{2f_r}, \quad (6.38)$$

where ζ_{HP} is the half-power estimated damping factor, f_2 and f_1 are the roots of equation (6.37) to the right and left of the estimated value of f_r .

Resonant and half-power frequencies estimates, respectively, using equation (6.34) and (6.37) can be accomplished with many of the available numerical schemes. In this treatise, Muller's method is used.³ The algorithm is fast and easy to use. Since in the programming mode, it may not be always possible to ascertain whether a value of f_r —obtained from the solution of equation (6.34)—corresponds to a relative maxima or minima, the second derivation is taken to estimate the curvature of the spectral density function at the computed value (a method used often in differential calculus). The following expressions⁴ is used:

$$-\sum_{k=0}^M \sum_{l=0}^M k(l-k)A(k)A(l) \cos[2\pi(l-k)f_r \Delta t] \begin{cases} < 0, & \text{relative maximum @ } f_r \\ = 0, & \text{indeterminate @ } f_r \\ > 0, & \text{relative minimum @ } f_r. \end{cases} \quad (6.39)$$

6.4 Free Oscillation Damping

Two methods were used to estimate the damping from the free oscillation test data: 1) the logarithmic decrement method, and 2) a curve fitting technique. The second method was used to test the validity of the results obtained with the first method.

³This algorithm is available in the IMSL library as *ZREAL*.

⁴A derivation analogous to the one used for equation (6.34), on page 131, is applied.

Logarithmic Decrement. By the logarithmic decrement method, damping is estimated from the free oscillation vibration as:

$$\zeta_{LD} = \frac{1}{2\pi k} \ln \frac{x_n}{x_{n+k}}, \quad (6.40)$$

where ζ_{LD} is the logarithmic decrement estimated damping factor, x_n is the amplitude of the n^{th} peak and x_{n+k} is the amplitude of the peak k cycles later.

Since in the digitized-time test data there were spikes at some amplitudes, the Longuet-Higgins and Cokelet smoothing algorithm (refer to section A.3, Appendix A) was used to remove (chop-off) any spikes that would give erroneous results when extracting peak values. (See Figure 6.2–6.3) Depending on the level of the spike at a peak value, the data were reprocessed several times until the spike disappeared or reached an acceptable limit. The nature of the smoothing algorithm is to remove any spikes, while leaving the rest of the data virtually intact. Peak values were extracted by processing the data with a sorting program to obtain all the maximum positive and negative peaks within a specified duration, independently.

Curve Fitting. The data were curve fitted using a numerical scheme which incorporates the modified Levenberg-Marquardt algorithm and a finite difference Jacobian. Bass and Haddara [70] have shown this method to be an effective way of predicting damping from free oscillation response data. This algorithm is available in the IMSL library as *UNLSF*. Unlike the logarithmic decrement method (capable of providing several values of damping per number of cycles), the curve fitting method provides only one value.

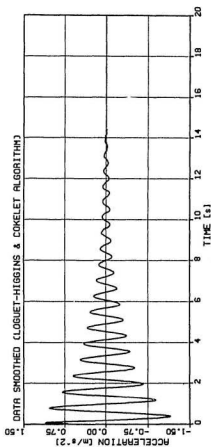
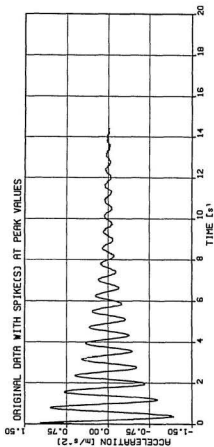


FIG. 6.2 TYPICAL FREE OSCILLATION RESPONSE (SPIKED & DE-SPIKED DATA)
CX-DIRECTION, IN-WATER TESTS).

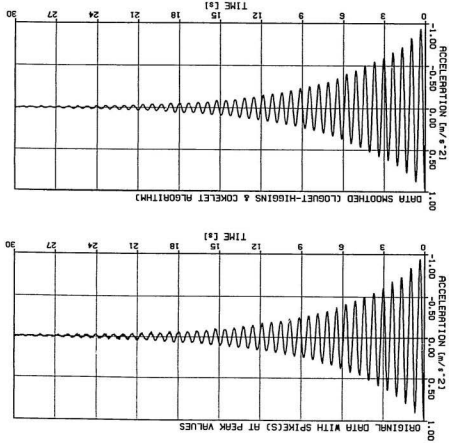


FIG. 6.3 TYPICAL FREE OSCILLATION RESPONSE (SPIKED & DE-SPIKED DATA) (Y-DIRECTION, IN-WATER TESTS).

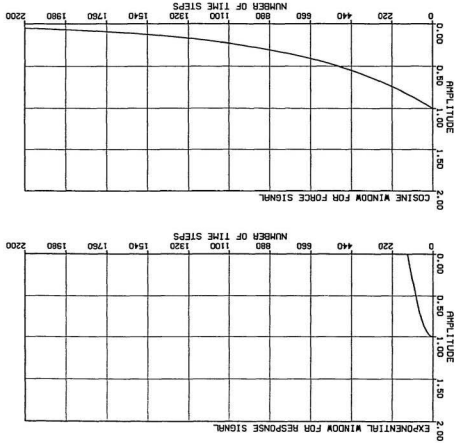
6.5 Impact Testing

Impact tests were carried out to test the validity of the resonant peaks on the output power spectrum from the wave induced vibrations of the model structure. This mode of testing was chosen, because it is a quick way to analyse the dynamic characteristics of a structure. Besides, the method uses short duration broadband spectra inputs that excite all frequencies within the useful frequency range. The usable frequency range of an impulse depends on the shape and time duration of the impulse. As a result, to ensure there was sufficient force over the frequency range of interest, the first zero crossing of the Fourier Transform of the impulse was well above the maximum frequency range of interest for each pulse. (In cases where this objective was not satisfied, the results were discarded.) The first zero crossing occurs at the lowest frequency (i.e, the inverse of the time duration of the pulse). This was achieved by ensuring the duration of the pulse was $2\Delta t$ —a generally accepted rule of thumb used by time series analysts [71].

Since the duration of impulse is very short compared with the sample length, the total energy of noise represented in the time-sample can be of the order of the energy of the impulse, even for high signal-to-noise ratios. The noise problem can be made worse when using the zoom transform to yield increased resolution in a given frequency range by effectively increasing the sample length.

To alleviate these problems, special time windows were employed. Two windows (a cosine for the impulse force and an exponential for the response) were used; these windows are depicted in Figure 6.4. The cosine window is one with unity amplitude for the duration of the impulse and a cosine taper

FIG. 6.4 TYPICAL WINDOWS USED TO PROCESS IMPACT TESTS RESULTS.



with duration $1/16$ of the sample time from unity to zero. While, in the exponential window the amplitude decays exponentially from 1 to a value of 0.05 of the sample time. An exponential window does change the resulting frequency response function, but its only effect is to increase the apparent damping in the resonances [71]. It does not change the resonant frequencies, since the influence of the exponential window is the same on all frequency response measurements; it will not alter the measured mode shape if applied to all measured frequency response functions (*ibid.*). However, because the exponential window increases the apparent damping in the resonant modes, the window tends to couple closely spaced resonant modes. This impediment could be alleviated with the MEM technique. Since the objective of the impact tests was to validate the wave test results, detailed analyses with the MEM were not done on the results from the impact tests. These were done using conventional FFT procedures.

Chapter 7

Theoretical and Experimental Results

In this chapter, the theoretical and experimental results are presented. As noted earlier in Chapter 5, section 5.2.4, only two members were severed in the experimental investigation; because, once a member was cut-off at one or two joints, it could not be easily repaired or replaced in the water. But, in the computer analyses, many members were made inactive to simulate damage of those inactivated members. This approach was taken to suggest the most suitable member(s) to be severed in the experimental hydro-elastic model, so the effect of the structural integrity technique could be optimized. (An evaluation of all the results is given Chapter 8.)

7.1 Theoretical Results

This section is sub-divided into two sub-sections: 1) free vibration analyses (both 3-D and stick model) to obtain natural frequencies of the intact and damaged model and prototype structure, and 2) force response analyses to obtain the dynamic response of the structure to wave excitation.

7.1.1 Free Vibration Results

Computed natural frequency comparisons of the model and prototype (obtained from the free vibration analyses of the 3-D and stick model) are presented in Table 7.1 and 7.2, respectively. Table 7.1 shows the error encountered when scaling up the prototype values from the model values. Twelve frequencies were computed for the idealized 3-D cases, but only the modes associated with the ten frequencies were used in the dynamic response analyses. Because, it was considered that it might not have been possible to excite more resonant frequencies, experimentally, in the wave tank facility at Memorial University. For the idealized stick models, it was only possible to extract seven frequencies, because the structure was idealized as a seven lumped mass system—i.e., one mass at each level.

To ascertain the type of mode(s) (i.e., global bending, twisting, etc.) associated with a particular resonant frequency, mode shapes were theoretically computed. Figures 7.1–7.10 show five typical modes for the idealized 3-D hydro-elastic model and prototype.¹ It was from the computer generated mode shapes that the type of mode associated with a particular frequency—shown in Tables 7.1 and 7.2—was labelled. The mode shapes were also used to identify the type of mode(s) associated with the resonant peaks on the experimentally measured spectral density functions from the wave and impact tests.

As has already been stated, various members were made inactive to simulate damage, and to select the most suitable member(s) that would optimize the structural integrity method in the experimental phase of this study.

¹NB: The corresponding frequency for each mode is also shown with each mode shape.

Table 7.1 Natural Frequency Comparison of the Model and Prototype
(Results obtained from Free Vibration Computer Analyses).

	Computed Natural Frequency			
	Prototype f_p [Hz]	Model f_m [Hz]	$f_p^* = f_m \sqrt{K_L}$ f_p^* [Hz]	% Error $\frac{f_p - f_p^*}{f_p} \cdot 100\%$
Mode 1 (1st Flexure, M_y)	0.2258	1.2022	0.2195	2.79
Mode 2 (1st Flexure, M_z)	0.2565	1.3547	0.2473	3.58
Mode 3 (1st Torsion, M_z)	0.2780	1.4343	0.2619	5.79
Mode 4 (2nd Flexure, M_y)	2.0328	11.4325	2.0872	-2.67
Mode 5 (1st Axial, M_z)	2.1836	11.0482	2.1996	-0.73
Mode 6 (2nd Flexure, M_z)	2.3583	13.1699	2.4044	-1.95
Mode 7 (3rd Flexure, M_y)	2.4099	13.4405	2.4538	-2.00
Mode 8 (3rd Flexure, M_z)	2.8865	16.1227	2.9435	-1.93
Mode 9 (2nd Torsion, M_z)	3.0482	17.3015	3.1588	-3.62
Mode 10 (4th Flexure, M_z)	5.1830	29.7538	5.4322	-4.80
Mode 11 (2nd Axial, M_z)	6.1275	33.1737	6.0566	1.15
Mode 12 (4th Flexure, M_y)	6.4377	36.4737	6.6591	-3.43

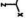
Where $K_L = \frac{L_m}{L_p}$.

Table 7.2 Natural Frequency Comparison of the Model and Prototype
(Results from the 3-D and Stick Model Idealizations).

	3-D Model		Stick Model	
	Prototype f_p [Hz]	Model f_m [Hz]	Model \bar{f}_m [Hz]	Prototype \bar{f}_p [Hz]
Mode 1 (1st Flexure, M_y)	0.2258	1.2022	1.0234	0.1920
Mode 2 (1st Flexure, M_x)	0.2565	1.3547	1.4296	0.2702
Mode 3 (1st Torsion, M_z)	0.2780	1.4343	†	†
Mode 4 (2nd Flexure, M_y)	2.0328	11.4325	11.2105	1.9920
Mode 5 (1st Axial, M_z)	2.1836	12.0482	†	†
Mode 6 (2nd Flexure, M_x)	2.3583	13.1699	13.5489	2.4253
Mode 7 (3rd Flexure, M_y)	2.4099	13.4405	21.5067	3.8479
Mode 8 (3rd Flexure, M_x)	2.8865	16.1227	†	†
Mode 9 (2nd Torsion, M_z)	3.0482	17.3015	†	†
Mode 10 (4th Flexure, M_x)	5.1830	29.7538	43.1896	7.5068
Mode 11 (2nd Axial, M_z)	6.1275	33.1737	†	†
Mode 12 (4th Flexure, M_y)	6.4377	36.4737	54.7232	9.6483

† indicates natural frequency was not excited.

ORIENTATION



HORIZONTAL SCALE = 19.1096 UNITS PER INCH
 VERTICAL SCALE = 19.1096 UNITS PER INCH
 EQUIVALENT ROTATION X 0.0 Y 20.0 Z -40.0
 MODE 1 FREQ 0.2088 CYC /SEC

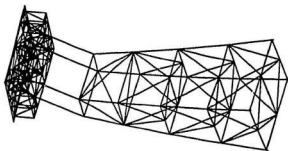


FIG.7.1 DYNAMIC MODE # 1 (CONTACT PROTOTYPE).

ORIENTATION



HORIZONTAL SCALE = 0.0997 UNITS PER INCH
 VERTICAL SCALE = 0.0997 UNITS PER INCH
 EQUIVALENT ROTATION X 0.0 Y 20.0 Z -40.0
 MODE 1 FREQ 1.2023 CYC /SEC

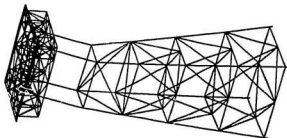


FIG.7.2 DYNAMIC MODE # 1 (CONTACT MODEL).

ORIENTATION



HORIZONTAL SCALE = 18.0130 UNITS PER INCH
 VERTICAL SCALE = 18.0130 UNITS PER INCH
 EQUIVALENT ROTATION X 0.0 Y 20.0 Z -40.0
 MODE 2 FREQ 0.2586 CYC /SEC

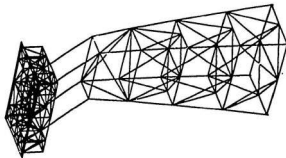
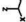


FIG.7.3 DYNAMIC MODE # 2 (CONTACT PROTOTYPE).

ORIENTATION



HORIZONTAL SCALE = 0.2586 UNITS PER INCH
 VERTICAL SCALE = 0.2586 UNITS PER INCH
 EQUIVALENT ROTATION X 0.0 Y 20.0 Z -40.0
 MODE 2 FREQ 1.2547 CYC /SEC

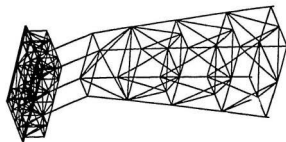


FIG.7.4 DYNAMIC MODE # 2 (CONTACT MODEL).

FIG.7.5 DYNAMIC MODE # 3 (INTACT PROTOTYPE).

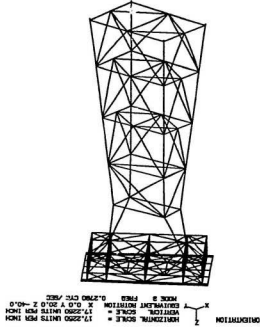
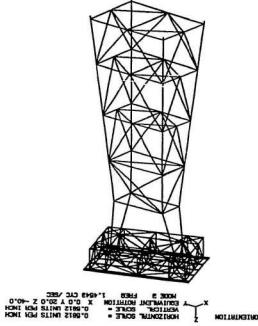


FIG.7.6 DYNAMIC MODE # 3 (INTACT MODEL).



ORIENTATION 

HORIZONTAL SCALE = 17.7620 UNITS PER INCH
 VERTICAL SCALE = 17.7620 UNITS PER INCH
 EQUIVALENT ROTATION X 0.0 Y 20.0 Z -40.0
 MODE 4 FREZ 2.0258 CVC /SEC



FIG. 7.7 DYNAMIC MODE # 4 (INTACT PROTOTYPE).

ORIENTATION 

HORIZONTAL SCALE = 0.8580 UNITS PER INCH
 VERTICAL SCALE = 0.8580 UNITS PER INCH
 EQUIVALENT ROTATION X 0.0 Y 20.0 Z -40.0
 MODE 4 FREZ 11.4225 CVC /SEC

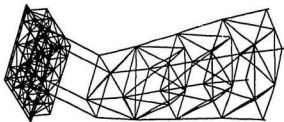


FIG. 7.8 DYNAMIC MODE # 4 (INTACT MODEL).

ORIENTATION



HORIZONTAL SCALE = 18.7064 UNITS PER INCH
 VERTICAL SCALE = 18.7064 UNITS PER INCH
 EQUIVALENT ROTATION X 0.0 Y 20.0 Z -40.0
 MODE B FINES 2.1866 CTC /SEC

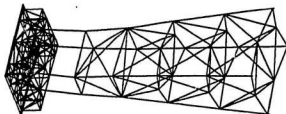


FIG.7.9 DYNAMIC MODE # 5 (CINTRACT PROTOTYPE).

ORIENTATION



HORIZONTAL SCALE = 2.4680 FEET PER INCH
 VERTICAL SCALE = 2.4680 FEET PER INCH
 EQUIVALENT ROTATION X 0.0 Y 20.0 Z -40.0
 MODE B FINES 12.0483 CTC /SEC

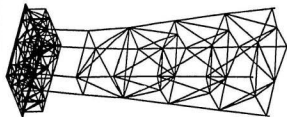


FIG.7.10 DYNAMIC MODE # 5 (CINTRACT MODEL).

Therefore, with the natural frequencies of the intact structure as a base line (reference point), the percentage changes in natural frequencies resulting from the effects of damaged (inactive) members were computed for each mode, and the results tabulated. Tables 7.3 and 7.4 show the results for the 3-D model and prototype, respectively.

To illustrate the influence of member severance of the selected members (i.e., member 70, and members 70 and 68—refer to Figure 5.13) on the free vibration response of the model structure, mode shapes for both the intact and damaged structure were computed. Figures 7.11–7.30 compare the influence on each mode, when member 70 was made inactive. The corresponding case for two members (70 and 68) is presented in Appendix D.

7.1.2 Dynamic Response to Wave Excitation

In the preceeding sections, the results from the free vibration analyses were presented. This section presents the dynamic response results. The section is sub-divided into two sub-sections: 1) dynamic response to a train of regular waves for both the 3-D and stick model (model and prototype); 2) dynamic response to irregular waves; that is, the response of the computer generated 3-D idealization of the hydro-elastic model to the irregular waves measured from the experimental wave tank tests.

Response to a Train of Regular Waves

Having completed the free vibration analyses, the dynamic response of the structure to a train of regular waves was investigated. Preliminary analyses were carried out to compare the performance of the hydro-elastic model to that of the prototype. For these analyses, the following wave parameters,

Table 7.3 Percentage Changes in Natural Frequencies when Certain Members were Inactivated (Prototype).

Modes of Vibration	Inactive Member(s)											
	6	22	48	58	61	63	70	68	101	59 & 60	59 & 70	70 & 68 & 74
Mode 1 (1st Flexure, M_y)	0.00	-0.39	0.00	0.00	0.00	-0.04	-0.74	-0.86	-16.02	0.00	-5.54	-5.71 -3.41
Mode 2 (1st Flexure, M_z)	-0.03	-1.04	-0.01	-0.73	-1.52	-5.96	0.00	0.00	-2.56	-1.67	-7.92	-0.02 -0.02
Mode 3 (1st torsion, M_z)	-0.02	1.73	-0.04	-0.76	-2.43	-2.17	-1.45	-1.32	-0.10	-1.87	-6.28	-1.65 -1.52
Mode 4 (2nd Flexure, M_y)	0.00	-1.04	0.67	-6.24	0.39	0.82	-28.42	-27.79	-28.56	-9.83	-54.59	-61.27 -48.91
Mode 5 (1st Axial M_z)	0.00	-6.57	-0.16	-6.89	-4.42	-0.61	0.00	0.01	-3.40	-15.25	-10.88	-0.16 0.04
Mode 6 (2nd Flexure, M_y)	-0.40	-7.73	0.42	-7.40	-7.38	0.35	-3.67	-3.34	-2.85	-13.50	-7.39	-6.74 -5.10
Mode 7 (3rd Flexure, M_y)	-0.03	-0.82	0.05	-0.21	-0.25	0.06	-1.86	-2.04	-0.22	-9.31	-4.45	-5.28 -2.36
Mode 8 (3rd Flexure, M_z)	-1.19	-11.26	0.21	-12.32	-12.82	-6.42	-6.60	-5.29	-1.36	-16.67	-14.68	-17.74 -14.63
Mode 9 (2nd torsion, M_z)	-0.10	-0.57	-0.14	-0.77	-0.91	0.34	-4.32	-5.08	-1.73	-17.38	-5.63	-5.06 -4.79
Mode 10 (4th Flexure, M_z)	-0.03	-20.20	0.04	-4.05	-4.86	-6.26	-6.19	-9.56	-2.22	-41.73	-6.01	-19.28 -27.81

ORIENTATION 

HORIZONTAL SCALE = 2.3648 FEET PER INCH
 VERTICAL SCALE = 2.3648 FEET PER INCH
 EQUIVALENT MOTION X 0.0 Y 20.0 Z -40.0
 MODE 1 FREQ 1.2029 CYC /SEC

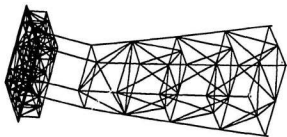


FIG. 7.11 DYNAMIC MODE # 1 (CONTRACT MODEL).

ORIENTATION 

HORIZONTAL SCALE = 2.2932 FEET PER INCH
 VERTICAL SCALE = 2.2932 FEET PER INCH
 EQUIVALENT MOTION X 0.0 Y 20.0 Z -40.0
 MODE 1 FREQ 1.1336 CYC /SEC

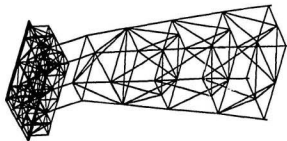
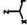


FIG. 7.12 DYNAMIC MODE # 1 (MEMBER 70 REMOVED).

ORIENTATION

 HORIZONTAL SCALE = 2.8672 FEET PER INCH
 VERTICAL SCALE = 2.8672 FEET PER INCH
 EQUIVALENT ROTATION X 0.0 Y 20.0 Z -40.0
 MODE 2 FREQ 1.2647 CYC /SEC

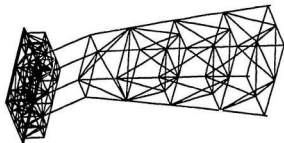


FIG. 7.13 DYNAMIC MODE # 2 (INTRACT MODEL).

ORIENTATION

 HORIZONTAL SCALE = 2.8648 FEET PER INCH
 VERTICAL SCALE = 2.8648 FEET PER INCH
 EQUIVALENT ROTATION X 0.0 Y 20.0 Z -40.0
 MODE 2 FREQ 1.2648 CYC /SEC

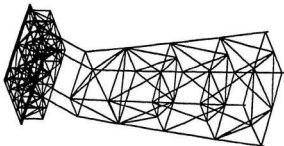


FIG. 7.14 DYNAMIC MODE # 2 (MEMBER 70 REMOVED).

ORIENTATION 

HORIZONTAL SCALE = 2.3248 FEET PER INCH
 VERTICAL SCALE = 2.3248 FEET PER INCH
 EQUILIBRIUM POSITION 1.000 Y 20.0 Z -40.0
 MODE 3 FREQ 1.4543 CTC /SEC

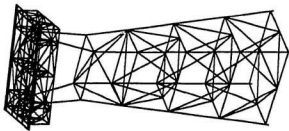


FIG. 7.15 DYNAMIC MODE # 3 (CONTACT MODEL).

ORIENTATION 

HORIZONTAL SCALE = 2.3672 FEET PER INCH
 VERTICAL SCALE = 2.3672 FEET PER INCH
 EQUILIBRIUM POSITION 1.000 Y 20.0 Z -40.0
 MODE 3 FREQ 1.4340 CTC /SEC

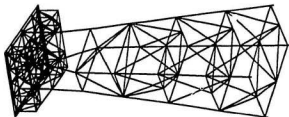


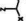
FIG. 7.16 DYNAMIC MODE # 3 (MEMBER 70 REMOVED).

ORIENTATION 

HORIZONTAL SCALE = 2.3640 FEET PER INCH
 VERTICAL SCALE = 2.3640 FEET PER INCH
 EQUIVALENT ROTATION X 0.0 Y 25.0 Z -40.0
 MODE 4 FREQ 111.4858 C/C /SEC



FIG. 7.17 DYNAMIC MODE # 4 (INTRACT MODEL).

ORIENTATION 

HORIZONTAL SCALE = 2.3112 FEET PER INCH
 VERTICAL SCALE = 2.3112 FEET PER INCH
 EQUIVALENT ROTATION X 0.0 Y 25.0 Z -40.0
 MODE 4 FREQ 8.1047 C/C /SEC

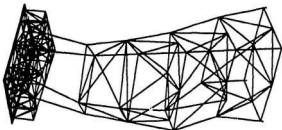


FIG. 7.18 DYNAMIC MODE # 4 (MEMBER 70 REMOVED).

ORIENTATION 

HORIZONTAL SCALE = 2.4950 FEET PER INCH
 VERTICAL SCALE = 2.4950 FEET PER INCH
 EQUIVALENT NOTATION X 0.0 Y 20.0 Z -40.0
 MODE 6 FREQ 11.0486 CYC /SEC

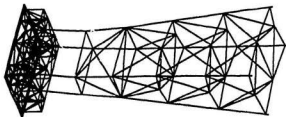
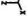


FIG.7.19 DYNAMIC MODE # 5 (INTRACT MODEL).

ORIENTATION 

HORIZONTAL SCALE = 2.2438 FEET PER INCH
 VERTICAL SCALE = 2.2438 FEET PER INCH
 EQUIVALENT NOTATION X 0.0 Y 20.0 Z -40.0
 MODE 6 FREQ 11.0479 CYC /SEC

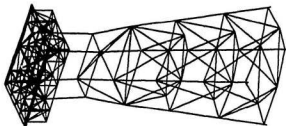


FIG.7.20 DYNAMIC MODE # 5 (MEMBER 70 REMOVED).

ORIENTATION

 HORIZONTAL SCALE = 2-2148 FEET PER INCH
 VERTICAL SCALE = 2-2148 FEET PER INCH
 EQUIVALENT ROTATION X 0.0 Y 20.0 Z -40.0
 MODE 6 FREQ 13.1588 CYC /SEC

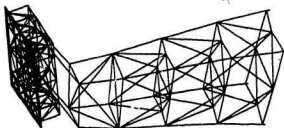


FIG. 7.21 DYNAMIC MODE # 6 (CONTRACT MODEL).

ORIENTATION

 HORIZONTAL SCALE = 2-2672 FEET PER INCH
 VERTICAL SCALE = 2-2672 FEET PER INCH
 EQUIVALENT ROTATION X 0.0 Y 20.0 Z -40.0
 MODE 6 FREQ 12.5438 CYC /SEC

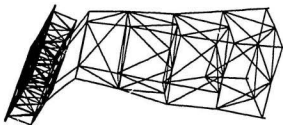


FIG. 7.22 DYNAMIC MODE # 6 (MEMBER 70 REMOVED).

ORIENTATION 

HORIZONTAL SCALE = 2.5176 FEET PER INCH
 VERTICAL SCALE = 2.5176 FEET PER INCH
 EQUIVALENT ROTATION X 0.0 Y 20.0 Z -60.0
 MODE 7 FINI 13.448 CTS /SEC

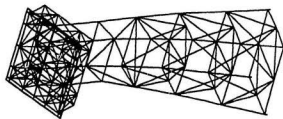


FIG. 7.23 DYNAMIC MODE # 7 (INTRACT MODEL).

ORIENTATION 

HORIZONTAL SCALE = 2.2560 FEET PER INCH
 VERTICAL SCALE = 2.2560 FEET PER INCH
 EQUIVALENT ROTATION X 0.0 Y 20.0 Z -60.0
 MODE 7 FINI 13.208 CTS /SEC

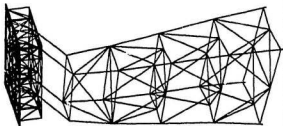


FIG. 7.24 DYNAMIC MODE # 7 (MEMBER 70 REMOVED).

ORIENTATION 

HORIZONTAL SCALE = 2.8188 FEET PER INCH
 VERTICAL SCALE = 2.2188 FEET PER INCH
 EQUILIBRIUM POSITION X 0.0 Y 20.0 Z -40.0
 MODE 8 FREQ 14.1258 CYC/SEC

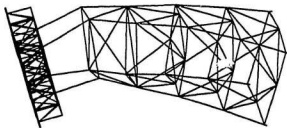


FIG. 7.25 DYNAMIC MODE # 8 (INTACT MODEL).

ORIENTATION 

HORIZONTAL SCALE = 2.3680 FEET PER INCH
 VERTICAL SCALE = 2.3680 FEET PER INCH
 EQUILIBRIUM POSITION X 0.0 Y 20.0 Z -40.0
 MODE 8 FREQ 16.1879 CYC/SEC

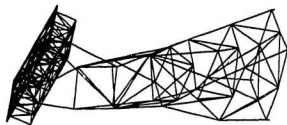


FIG. 7.26 DYNAMIC MODE # 8 (MEMBER 70 REMOVED).

ORIENTATION 

HORIZONTAL SCALE = 2.3174 FEET PER INCH
 VERTICAL SCALE = 2.3174 FEET PER INCH
 EQUIVALENT ROTATION X 0.0 Y 20.0 Z -40.0
 MODE 8 FREQ 17.3018 CYC /SEC

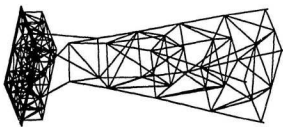


FIG.7.27 DYNAMIC MODE # 9 (INTERACT MODEL).

ORIENTATION 

HORIZONTAL SCALE = 2.3424 FEET PER INCH
 VERTICAL SCALE = 2.3424 FEET PER INCH
 EQUIVALENT ROTATION X 0.0 Y 20.0 Z -40.0
 MODE 8 FREQ 16.3479 CYC /SEC

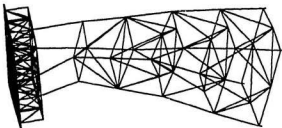


FIG.7.28 DYNAMIC MODE # 9 (MEMBER 70 REMOVED).

ORIENTATION  HORIZONTAL SCALE = 2.5000 FEET PER INCH
VERTICAL SCALE = 2.5000 FEET PER INCH
UNIT WEIGHT = 1.0000 POUNDS PER CUBIC FOOT
MODE IS FINO 20.7600 CYS /SEC.

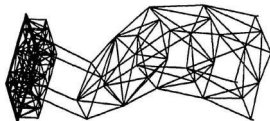


FIG. 7.29 DYNAMIC MODE # 10 (INTRACT MODEL).

ORIENTATION  HORIZONTAL SCALE = 2.0652 FEET PER INCH
VERTICAL SCALE = 2.0652 FEET PER INCH
UNIT WEIGHT = 1.0000 POUNDS PER CUBIC FOOT
MODE IS FINO 271.8000 CYS /SEC.

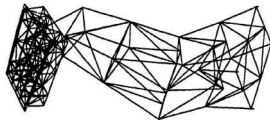


FIG. 7.30 DYNAMIC MODE # 10 (MEMBER 70 REMOVED).

obtained from [62], were used:

Prototype Wave Data
(Hurricane Condition)

Wave Height = 17.6 m

Wave Period = 16.0 seconds

mean Water Depth = 48.8 m

Model Wave Data
(Hurricane Condition)

Wave Height = 0.6 m

Wave Period = 2.92 seconds

mean Water Depth = 1.6 m

Note that the wave data, shown above, for the model were computed using the wave modelling laws developed in Chapter 4 (i.e., equations 4.21 and 4.23).

The dynamic response at an arbitrarily chosen location (node 73, the central node on the deck of the structure) was computed, and the results were plotted, so a visual comparison could be made between the model and prototype. Displacement results using the non-linearized and linearized form of the drag component in Morrison's equation (i.e., equations (3.3) and (3.20), respectively) are depicted in Figures 7.31. In all the analyses, the inertia and drag components were chosen as: $C_M = 2.0$ and $C_D = 1.2$, individually in their given order. Using equation (4.29), these displacement responses were non-dimensionalized as shown in Figures 7.32. The non-dimensionalized global x-direction dynamic forces along one of the main columns of the jacket

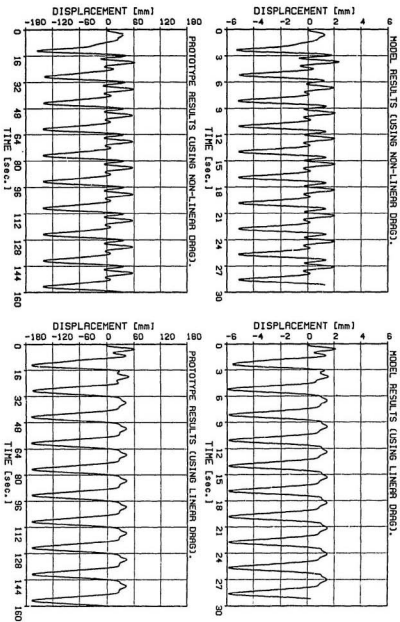


FIG. 7.31 X-DIRECTION DYNAMIC RESPONSE OF THE MODEL AND PROTOTYPE TO REGULAR WAVES USING THE NON-LINEAR AND LINEAR FORMS OF THE MORRISON'S WAVE FORCE EQUATION).

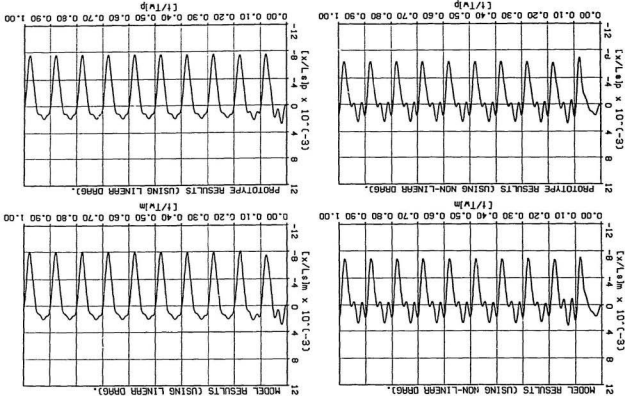


FIG. 7.32 X-DIRECTION DYNAMIC RESPONSE OF THE MODEL AND PROTOTYPE TO REGULAR WAVES (NON-DIMENSIONALIZED DISPLACEMENT & NON-DIMENSIONALIZED TIME).

(i.e., at nodes 6, 12, 18, 22 and 23 shown in Figures 3.8 and 3.10 for the model and prototype, respectively) are presented in Figures 7.33 and 7.34. To compare the dynamic performance of the stick model to that of the 3-D model, the dynamic response at node 73 of the stick model was compared to that of the 3-D idealization of the hydro-elastic model—using the linear form of Morrison's wave force equation. The results are shown in Figure 7.35. In all the computations, the nodes at the base were assumed rigid.

Response to Irregular Waves

To simulate the experimental investigation theoretically, the wave spectrum of the irregular waves (measured in the wave tank) was used as the input in the computer model. The theoretical justification for this approach has already been discussed in Chapter 3, section 3.4. In the experimental investigation, accelerometers were installed to measure the dynamic response of the model structure. So, instead of computing displacements in the dynamic response computer analyses, and then numerically differentiating the results to compute accelerations (a method which could introduce numerical errors), the acceleration response of the structure was computed directly. Since the objective was to compare the spectral density functions of the dynamic responses, the approach noted above is justified.

It may be recalled from Chapter 6, that a complete test for a particular structural configuration (intact or damaged) consisted of a set of ten runs for each wave spectrum in the wave tank. This was done to collect enough data to carry out spectral averaging using FFT procedures. Therefore, rather than repeat the above procedure in the computer simulation studies, the average spectral density function, for the set of ten runs, was used. The resulting

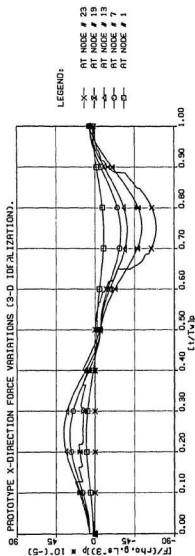
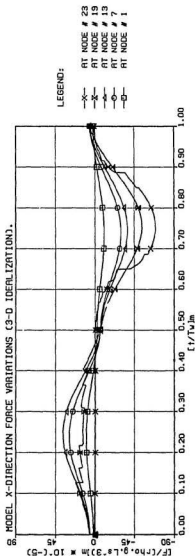


FIG. 7.33 NON-LINEAR FORCE VARIATION ALONG THE JACKET TO A SINGLE WAVE
[NB: NON-DIMENSIONALIZED FORCE vs NON-DIMENSIONALIZED TIME].

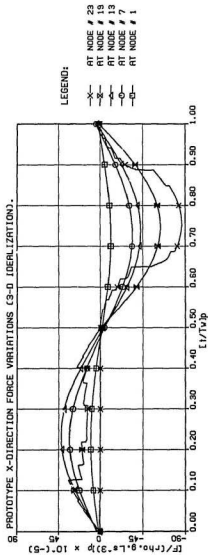
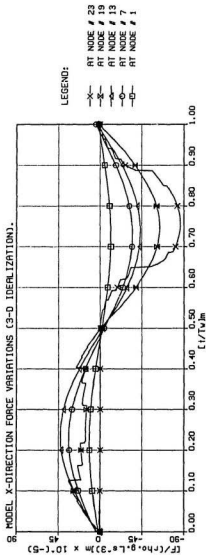


FIG. 7.34 LINEAR FORCE VARIATION ALONG THE JACKET TO A SINGLE WAVE
 (NB: NON-DIMENSIONALIZED FORCE vs NON-DIMENSIONALIZED TIME).

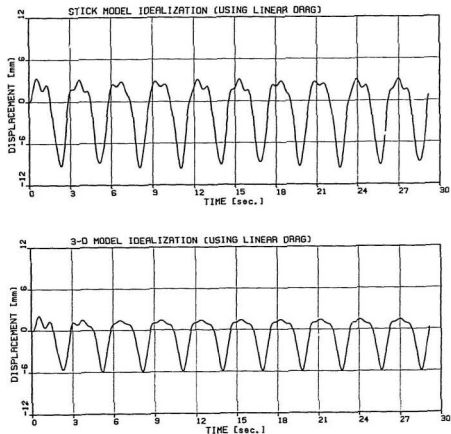


FIG. 7.35 X-DIRECTION DYNAMIC RESPONSE OF THE 3-D AND STICK MODEL AT NODE 73
(RESPONSE OF THE HYDRO-ELASTIC MODEL TO REGULAR WAVES).

time domain representation of the irregular wave was attained by taking the inverse FFT of the average wave spectrum from the wave tests. Note that this time domain representation has the same energy as the average wave spectrum, but the phase is random. However, since the comparison between experiment and theory would be done in the frequency domain (e.g., spectral density functions of the dynamic responses), the approach taken is, again, justified.

For easy comparison between the theoretical and experimental results, the dynamic responses of the 3-D model were computed at the nodes corresponding to the locations and directions where the accelerometers A1 to A5 were installed in the experimental model. As a result, dynamic responses were computed at nodes 12, 18, 23 and 73 in the same directions. Figures 7.36–7.42 show the spectral density functions of the results from the intact and damaged structure to irregular waves. (Notice the difference in smoothness and resolution with the functions attained using MEM and with that computed using the FFT method.)

7.2 Experimental Results

7.2.1 Transient Decay Tests to Compute Damping

In-Air Tests. The results from the in-air tests to compute the free oscillation damping factor—using the logarithmic decrement method—are presented in Figures 7.43 and 7.44. These graphs represent the results for the x and y directions, respectively.² The variation of the damping factor, ζ_{Air} , over various oscillation cycles was computed by taking the average variation of

²Typical free oscillation plots for the in-air tests have already been shown in Figures 5.1–5.2.

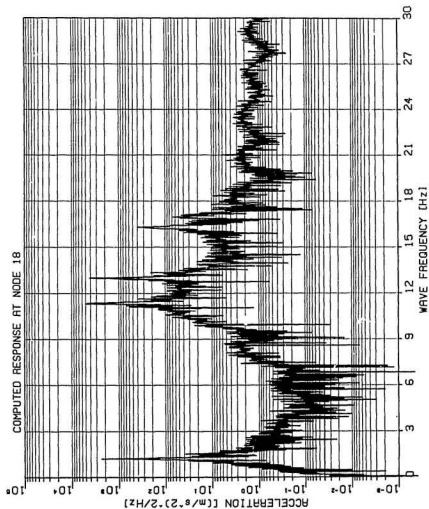
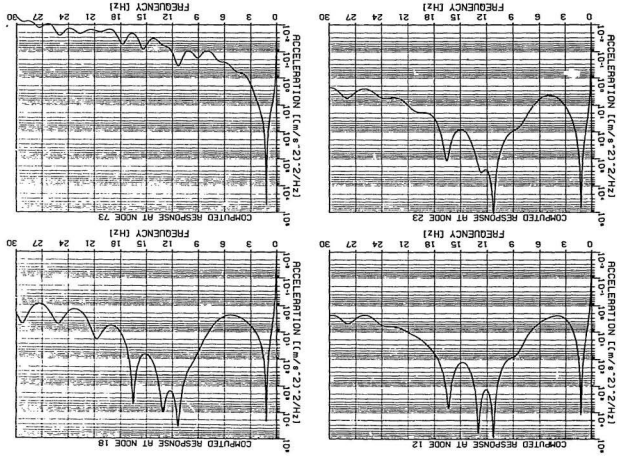


FIG. 7.36 TYPICAL FFT THEORETICAL ACCELERATION SPECTRAL DENSITY DUE TO WAVE ACTION
(INTACT STRUCTURE: USING WHITE NOISE INPUT WAVE SPECTRUM).

FIG. 7.37 NEW THEORETICAL ACCELERATION SPECTRAL DENSITIES DUE TO WAVE INDUCED VIBRATION (INTEGRAL STRUCTURE, USING WHITE NOISE SPECTRUM).



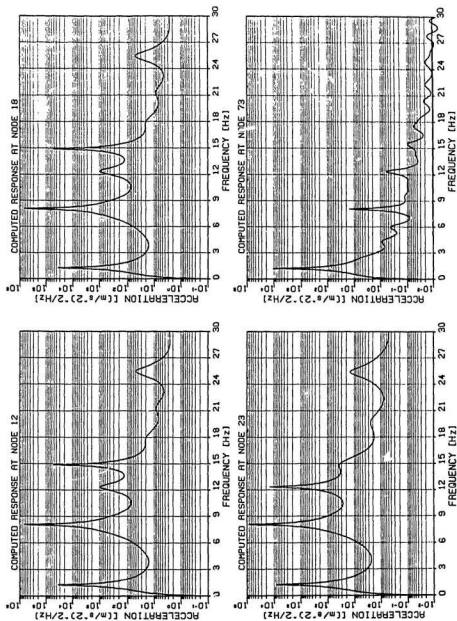


FIG. 7.38 MEM THEORETICAL ACCELERATION SPECTRAL DENSITIES DUE TO WAVE INDUCED VIBRATION (DAMAGED STRUCTURE; MEMBER 70 REMOVED—USING WHITE NOISE SPECTRUM).

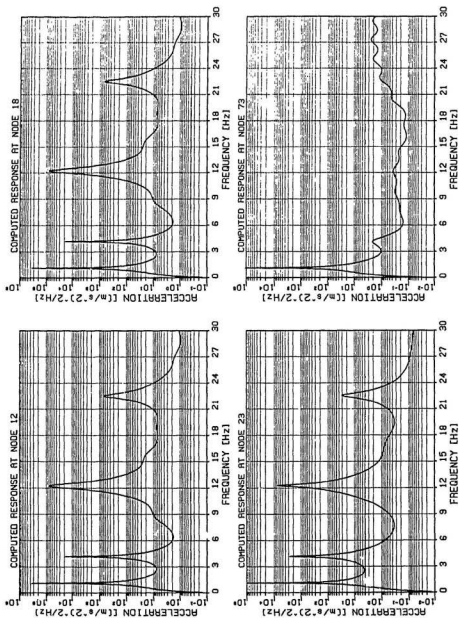


FIG. 7.39 THEORETICAL ACCELERATION SPECTRAL DENSITIES DUE TO WAVE INDUCED VIBRATION (DAMAGED STRUCTURE: MEMBERS 70 AND 68 REMOVED—USING WHITE NOISE SPECTRUM).

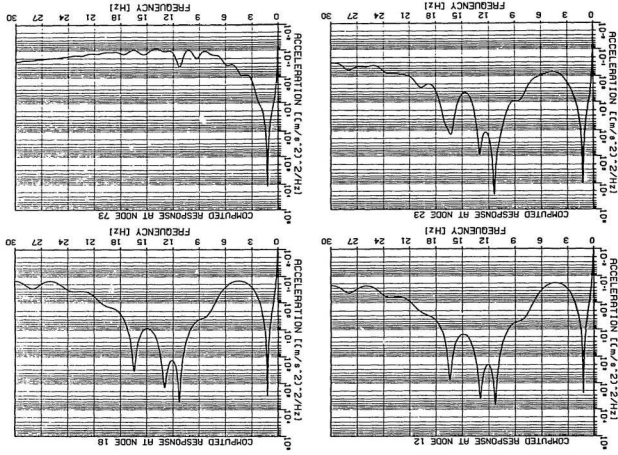
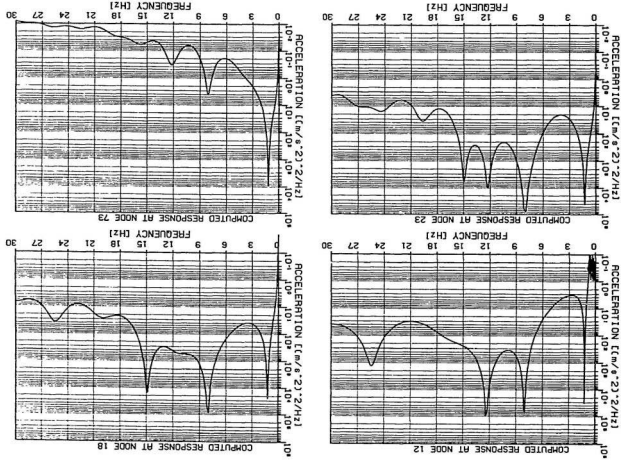


FIG. 7.40 MEM THEORETICAL ACCELERATION SPECTRAL DENSITIES DUE TO WAVE INDUCED VIBRATION (INTEGRAL STRUCTURE; USING JONSWAP SPECTRUM).

FIG. 7.41 MEM THEORETICAL ACCELERATION SPECTRAL DENSITIES DUE TO WAVE INDUCED VIBRATION
(DAMAGED STRUCTURE: MEMBER 70 REMOVED--USING JONSWAP SPECTRUM).



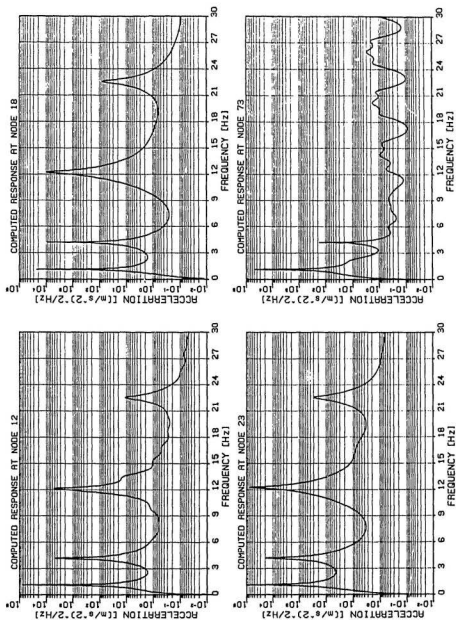


FIG. 7.42 MEM THEORETICAL ACCELERATION SPECTRAL DENSITIES DUE TO WAVE INDUCED VIBRATION (DAMAGED STRUCTURE: MEMBERS 70 AND 68 REMOVED—USING JONSWAP SPECTRUM).

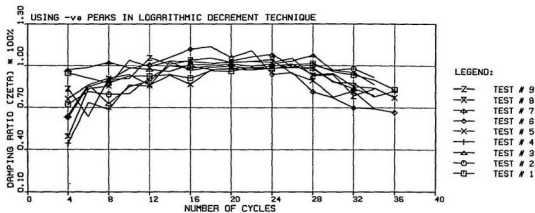
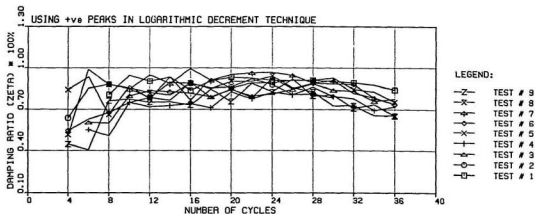


FIG. 7.43 VARIATION OF DAMPING IN THE X DIRECTION
(IN-AIR TESTS).

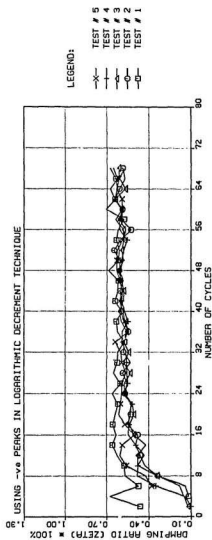
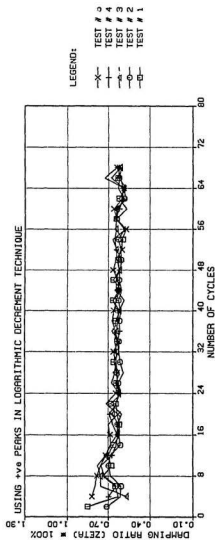


FIG. 7.44 VARIATION OF DAMPING IN THE Y DIRECTION
(IN-AIR TESTS).

the positive and negative peaks. Results for both the x and y directions are shown in Figure 7.45. It may be recalled, from Chapter 6, section 6.4, that the results from the free oscillation tests were curve fitted (using the Levenberg-Marquardt and Finite Difference Jacobian), to test the validity of the results obtained with the logarithmic decrement method; and to provide an alternative damping estimator. These results are tabulated in Tables 7.5 and 7.6 for the global x and y directions, respectively.

In-Water Tests. After the hydro-elastic model was installed in the wave tank facility, similar tests, as noted earlier, were carried out to determine the free oscillation damping factor of the structure in water. The variation, using the logarithmic decrement method, for the global x and y directions are presented in Figures 7.46 and 7.47. Average variations are depicted in Figure 7.48. Using the curve fitting technique, the corresponding results are presented in Tables 7.7 and 7.8.

7.2.2 Wave Test Results

Graphical outputs of the experimental results are presented for:

- (i) spectral density functions of the signals measured with the wave probes,
- (ii) response of the hydro-elastic model to a train of regular waves, and
- (iii) response of the model to irregular waves (i.e., the white noise and JONSWAP spectrum, independently).

Wave Probe Signals

As discussed in Chapter 5, section 5.2.2, five steps were necessary to achieve the desired wave spectra (i.e., the white noise and JONSWAP) from the

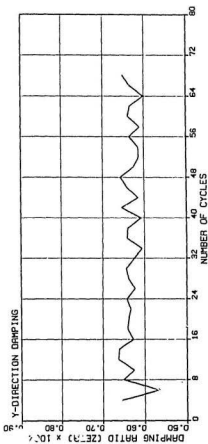
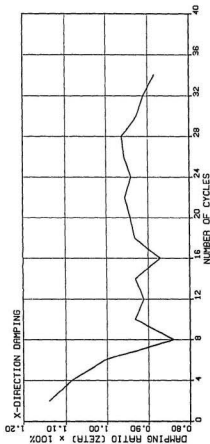


FIG. 7.45 AVERAGE X & Y DIRECTION DAMPING RATIO VARIATIONS
(IN-AIR TESTS--USING LOGARITHMIC DECREMENT TECHNIQUE).

**Table 7.5 X-Direction Results From Free Vibration In-Air Tests
(Using the Levenberg-Marquardt and Finite Difference Jacobian).**

	X-Direction Results	
	Damping Ratio % ζ	Resonant Frequency $f_{1,x}$ [Hz]
Test # 1	0.9345	1.2906
Test # 2	0.9117	1.2905
Test # 3	0.9034	1.2902
Test # 4	0.8875	1.2899
Test # 5	0.9222	1.2903
Test # 6	0.8916	1.2887
Test # 7	0.9429	1.2901
Test # 8	0.8927	1.2892
Test # 9	0.9144	1.2896
Average Values	0.9112	1.2899

**Table 7.6 Y-Direction Results From Free Vibration In-Air Tests
(Using the Levenberg-Marquardt and Finite Difference Jacobian).**

	Y-Direction Results	
	Damping Ratio % ζ	Resonant Frequency $f_{1,y}$ [Hz]
Test # 1	0.6310	1.4731
Test # 2	0.6206	1.4735
Test # 3	0.6283	1.4729
Test # 4	0.6270	1.4726
Test # 5	0.6317	1.4734
Average Values	0.6277	1.4731

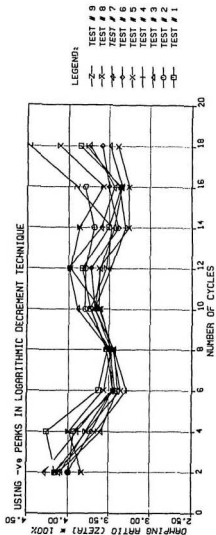
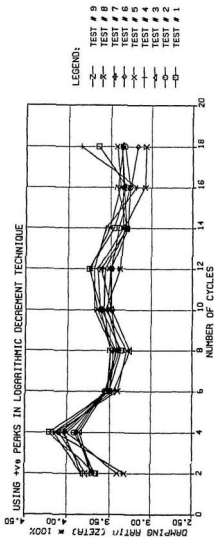


FIG. 7.46 VARIATION OF DAMPING IN THE X DIRECTION
(IN-WATER TESTS).

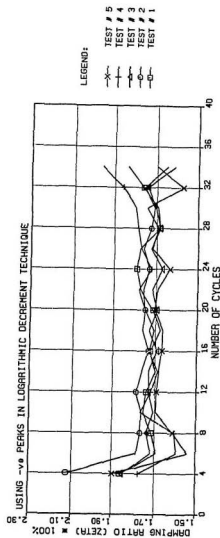
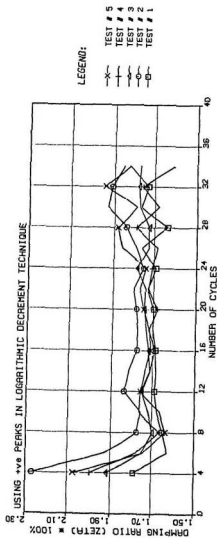


FIG. 7.47 VARIATION OF DAMPING IN THE Y DIRECTION
(IN-WATER TESTS).

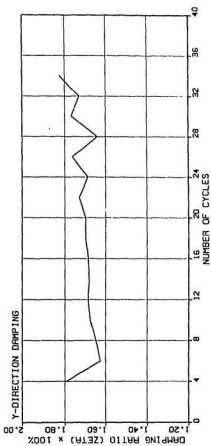
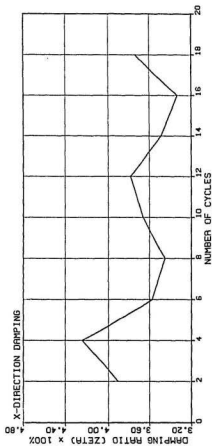


FIG. 7.48 AVERAGE X & Y DIRECTION DAMPING RATIO VARIATIONS (IN-WATER TESTS---USING LOGARITHMIC DECREMENT TECHNIQUE).

**Table 7.7 X-Direction Results From Free Vibration In-Water Tests
(Using the Levenberg-Marquardt and Finite Difference Jacobian).**

	X-Direction Results	
	Damping Ratio % ζ	Resonant Frequency $f_{1,x}$ [Hz]
Test # 1	3.6268	1.2792
Test # 2	3.6102	1.2817
Test # 3	3.6074	1.2817
Test # 4	3.6388	1.2770
Test # 5	3.6817	1.2799
Test # 6	3.7154	1.2784
Test # 7	3.7138	1.2815
Test # 8	3.6682	1.2779
Test # 9	3.6562	1.2760
Average Values	3.6576	1.2792

**Table 7.8 Y-Direction Results From Free Vibration In-Water Tests
(Using the Levenberg-Marquardt and Finite Difference Jacobian).**

	Y-Direction Results	
	Damping Ratio % ζ	Resonant Frequency $f_{1,y}$ [Hz]
Test # 1	1.7135	1.4592
Test # 2	1.7439	1.4589
Test # 3	1.7257	1.4589
Test # 4	1.7301	1.4590
Test # 5	1.6971	1.4594
Average Values	1.7221	1.4591

target or theoretical wave spectra. Figures 7.49–7.52 show the measured spectra at wave probes P1, P2 and P3 compared to the target spectrum, for both input wave spectra. A typical result for the white noise spectrum, using FFT procedures, is depicted in Figure 7.49, while those using the MEM technique are shown in Figure 7.50. (Observe the difference in smoothness and resolution of the MEM graphs.)

Structural Response to a Train of Regular Waves

Before the irregular wave tests were carried out, it was necessary to examine the behavior of the structure to a train of regular waves. These tests were desirable to test the workability of the instrumentation, and the Finite Element program written to simulate the experimental investigations. Besides, since the motion of the hydro-elastic model to regular waves is not as complex as that due to irregular waves, these tests were done, bearing in mind the shape of the response curve(s) that should be expected. Figure 7.53 shows the input wave signals measured with the wave probe designated P1 (refer to Figure 5.9, Chapter 5), and the corresponding x-direction response from the accelerometer designated A4, located at the center of the deck of the hydro-elastic model.

To compare the output acceleration from A4 and with that predicted from theory (i.e., FEM analyses), the measured input waves and the output acceleration signals were centered by subtracting their means. In the computer analyses used to simulate the experimental tests, computations were carried out—using both the non-linear and linear form of the Morrison’s wave force equation, independently—to calculate the required nodal wave forces from the measured input wave signals. A comparison between the experimental

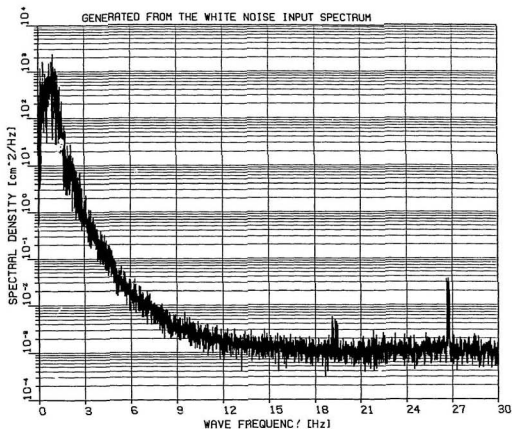
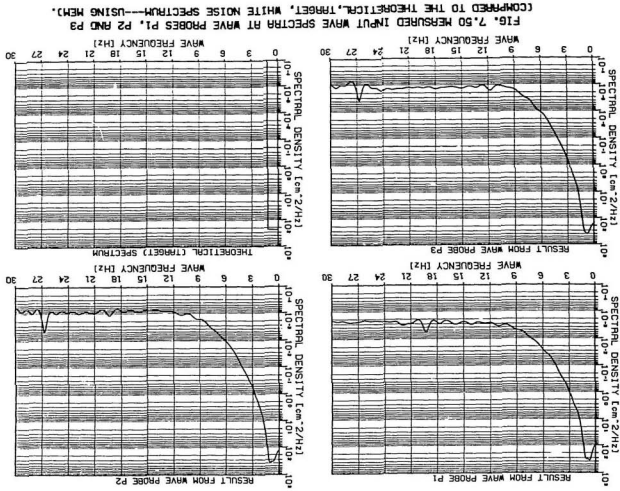


FIG. 7.49 TYPICAL MEASURED INPUT WAVE SPECTRUM AT WAVE PROBE P1
(USING CONVENTIONAL FFT PROCEDURES).



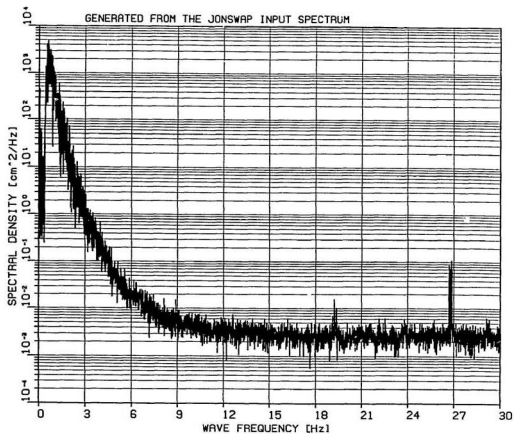


FIG. 7.51 TYPICAL MEASURED INPUT WAVE SPECTRUM AT WAVE PROBE P1
(USING CONVENTIONAL FFT PROCEDURES).

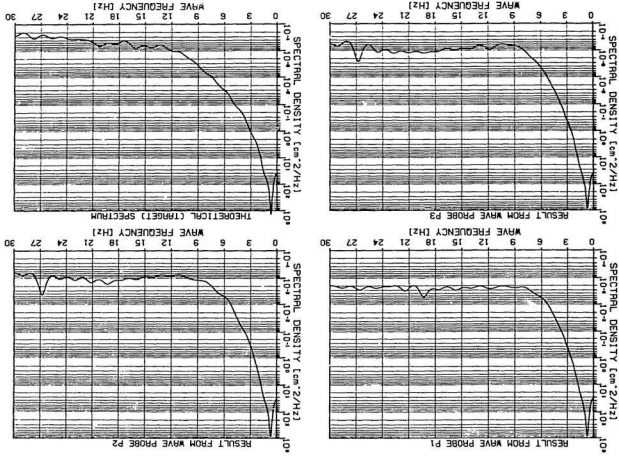


FIG. 7.52 MEASURED INPUT WAVE SPECTRA AT WAVE PROBES P1, P2 AND P3
 (COMPARED TO THE THEORETICAL, TARGET, JONSWAP SPECTRUM—USING MEM).

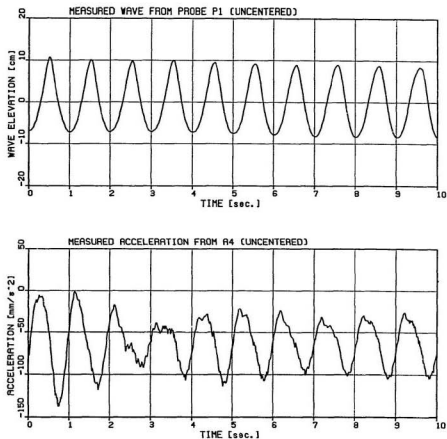


FIG. 7.53 MEASURED INPUT WAVE FROM P1 AND OUTPUT ACCELERATION FROM A4
(RESULTS FROM REGULAR WAVE TESTS).

and theoretical results is shown in Figure 7.54.

Structural Response To Irregular Waves

Using the White Noise Input Wave Spectrum. Typical time domain accelerations measured with accelerometers A1 to A4, for the intact structure, are depicted in Figure 7.55. A typical spectral density function of the acceleration measured with A4, using FFT, is illustrated in Figure 7.56. Figure 7.57 shows the corresponding functions using the MEM technique. (Note the difference in smoothness and resolution of the graphs obtained using both methods.) Results for the damaged structure—i.e., member 70, and members 70 and 68—are given in Figures 7.58–7.60.

Using the JONSWAP Input Wave Spectrum. The spectral density functions for the intact and damaged structure, using the JONSWAP spectrum, are presented in Figures 7.61–7.65. Like the white noise case, Figure 7.61 was plotted to further emphasize the difference in resolution and smoothness between the spectra obtained using FFT procedures, and with that using the MEM technique (i.e., Figure 7.62).

Estimating Damping from the Forced Response Data

Computed damping estimates based on the global x-direction motion of the structure, using the half-power bandwidth method, are summarized in Tables 7.9–7.10, for the white noise and JONSWAP input wave spectra, respectively. These values were computed based on the MEM formulations presented in section 6.3.2., Chapter 6. (Damping estimates from the response of the damaged Structure are presented in Appendix D.)

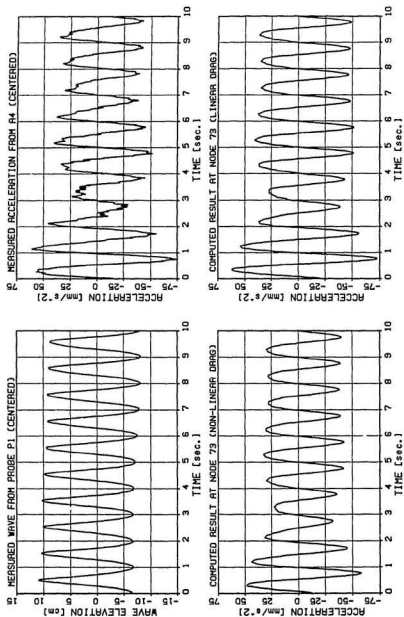


FIG. 7.54 A COMPARISON BETWEEN EXPERIMENT AND THEORY FOR THE REGULAR WAVES TESTS (NB: NODE 73 ON THE THEORETICAL MODEL CORRESPONDS TO THE POSITION OF ACCELEROMETER A4).

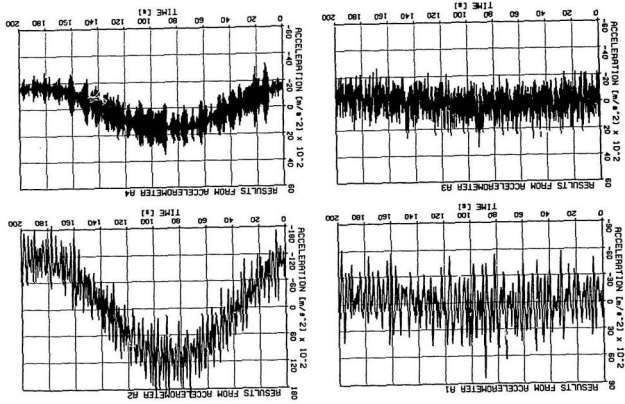


FIG. 7.55 1/PICRL TIME DOMAIN ACCELERATIONS MEASURED WITH ACCELEROMETERS A1 TO A4.

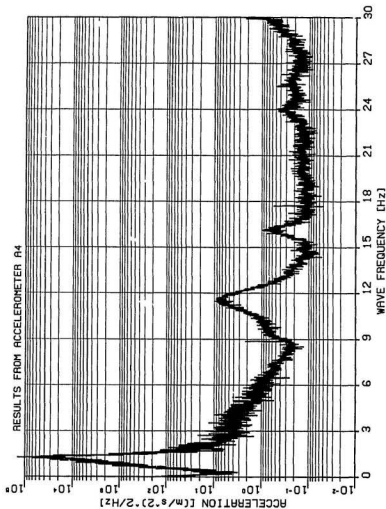


FIG. 7.56 TYPICAL FFT EXPERIMENTAL ACCELERATION SPECTRAL DENSITY DUE TO WAVE ACTION (INTACT STRUCTURE: USING WHITE NOISE INPUT WAVE SPECTRUM).

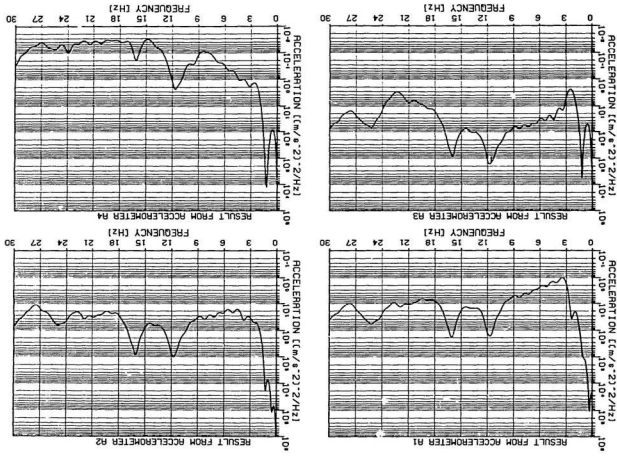


FIG. 7.57 MEM EXPERIMENTAL ACCELERATION SPECTRAL DENSITIES DUE TO WAVE INDUCED VIBRATION (INTACT STRUCTURE, USING WHITE NOISE SPECTRUM).

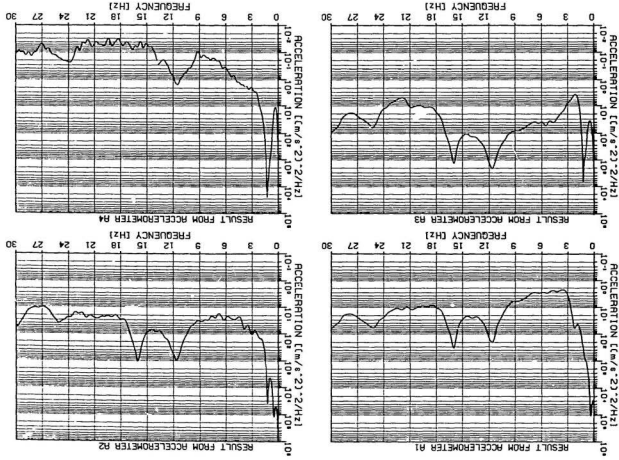


FIG. 7.58 MEM EXPERIMENTAL ACCELERATION SPECTRAL DENSITIES DUE TO WAVE INDUCED VIBRATION (DAMAGED STRUCTURE: MEMBER 70 CUT HALF-WAY AT NODE 16--USING WHITE NOISE SPECTRUM).

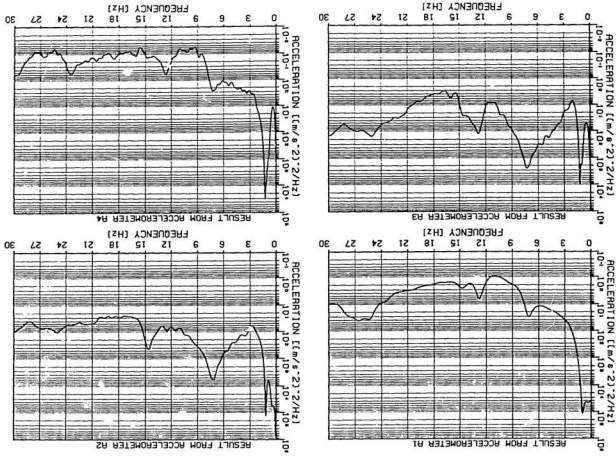


FIG. 7. S9 NEW EXPERIMENTAL ACCELERATION SPECTRAL DENSITIES DUE TO WAVE INDUCED VIBRATION (DAMAGED STRUCTURE; MEMBER 70 SEVERED AT NODE 18--USING WHITE NOISE SPECTRUM).

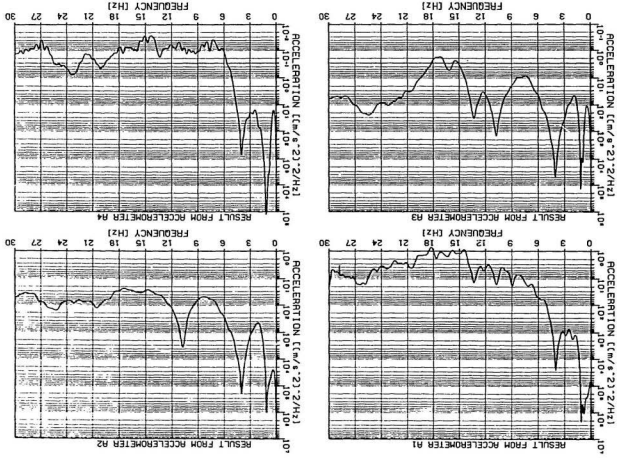


FIG. 7.60 MEM EXPERIMENTAL ACCELERATION SPECTRAL DENSITIES DUE TO WAVE INDUCED VIBRATION (DAMAGED STRUCTURE: MEMBER 70 SEVERED, AND 68 CUT-OFF AT NODE 16—USING WHITE NOISE SPECTRUM).

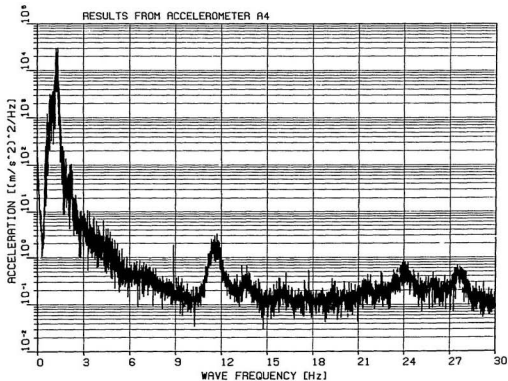


FIG. 7.61 TYPICAL FFT EXPERIMENTAL ACCELERATION SPECTRAL DENSITY DUE TO WAVE ACTION
(INTACT STRUCTURE: USING JONSWAP INPUT WAVE SPECTRUM).

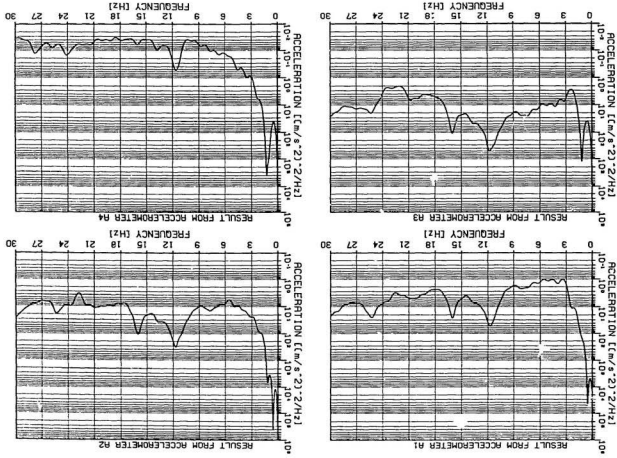


FIG. 7.62 MEM EXPERIMENTAL ACCELERATION SPECTRAL DENSITIES DUE TO WAVE INDUCED VIBRATION (INTEGRATED STRUCTURE; USING JONSWAP SPECTRUM).

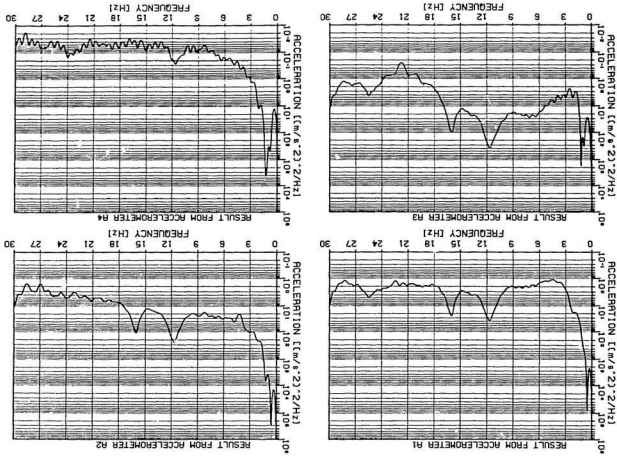


FIG. 7.63 MEM EXPERIMENTAL ACCELERATION SPECTRAL DENSITIES DUE TO WAVE INDUCED VIBRATION (DAMAGED STRUCTURE: MEMBER 70 CUT HALF-WAY AT NODE USING JONSWAP SPECTRUM).

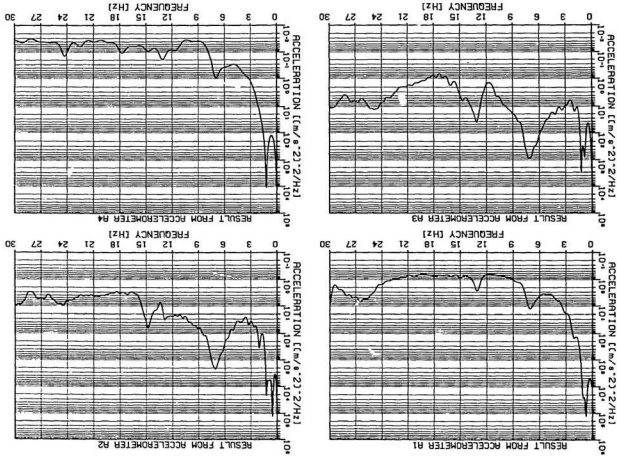


FIG. 7.64 MEM EXPERIMENTAL ACCELERATION SPECTRAL DENSITIES DUE TO WAVE INDUCED VIBRATION (DAMAGED STRUCTURE: MEMBER 70 SEVERED AT NODE 18—USING JONSWAP SPECTRUM).

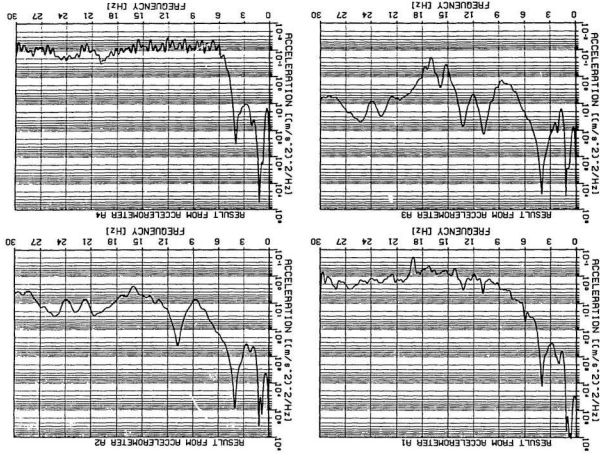


FIG. 7.65 MEM EXPERIMENTAL ACCELERATION SPECTRAL DENSITIES DUE TO WAVE INDUCED VIBRATION (DAMAGED STRUCTURE: MEMBER 70 SEVERED, AND 68 SEVERED AT NODE 16—USING JONSWAP SPECTRUM).

Table 7.9 MEM Damping Estimates from the Response Measured with Accelerometer A3 (Intact Structure).

	Modal Damping Ratios at each Resonant Frequency			
	White Noise Tests		JONSWAP Tests	
	Frequency [Hz]	Damping Ratio, ζ	Frequency [Hz]	Damping Ratio, ζ
Mode 1 (1st Flexure, M_y)	1.2669	0.0202	1.2752	0.0362
Mode 4 (2nd Flexure, M_y)	11.7228	0.0348	11.7395	0.0350
Mode 8 (3rd Flexure, M_z)	16.0102	0.0207	15.9904	0.0169
Mode 10 (4th Flexure, M_y)	25.4543	0.0385	25.3107	†

† indicates resonant peak not well defined.

Table 7.10 MEM Damping Estimates from the Response Measured with Accelerometer A4 (Intact Structure).

	Modal Damping Ratios at each Resonant Frequency			
	White Noise Tests		JONSWAP Tests	
	Frequency [Hz]	Damping Ratio, ζ	Frequency [Hz]	Damping Ratio, ζ
Mode 1 (1st Flexure, M_y)	1.2757	0.0202	1.2718	0.0241
Mode 4 (2nd Flexure, M_y)	11.7332	0.0405	11.7350	0.0336
Mode 8 (3rd Flexure, M_x)	16.1025	0.0241	†	‡
Mode 10 (4th Flexure, M_y)	25.7214	‡	†	‡

† indicates levels too low to be measured.

‡ indicates resonant peak not well defined.

7.2.3 Impact Test Results

In Chapter 5, section 5.2.5, it was noted that impact tests were carried out to test the validity of the wave test results. More explicitly, to verify the location of the resonant peaks, particularly the higher ones, obtained from the spectral density functions of the wave induced vibration of the structure. For each impact location, a set of ten tests were done. This was necessary to carry out spectral averaging (a form of filtering), and also to compute the transfer, phase, coherence, and spectral density functions of the time domain signals recorded with accelerometers A1 to A5. The complete set of results for the response measured with accelerometers A2, A3 and A4 from an impact initiated at location H5 (refer to Figure 5.6) are shown in Figures 7.66–7.75. Similar results were attained when the impact was initiated at the other designated impact locations. (For the case when the impact was initiated at location H6, refer to Figures D.19–D.30, Appendix D.)

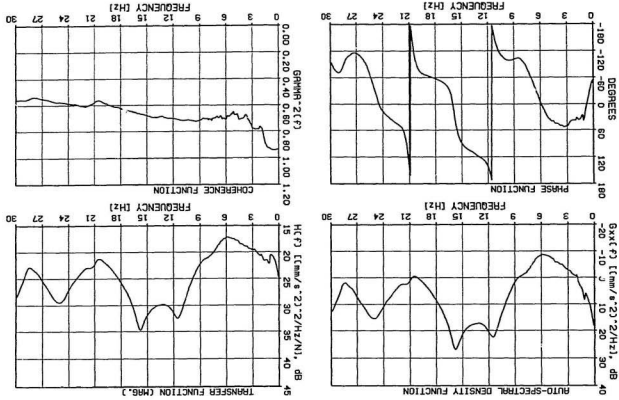


FIG. 7.66 RESULTS FROM ACCELEROMETER A2 DUE TO AN IMPACT INITIATED AT H5 (INTRACT STRUCTURE).

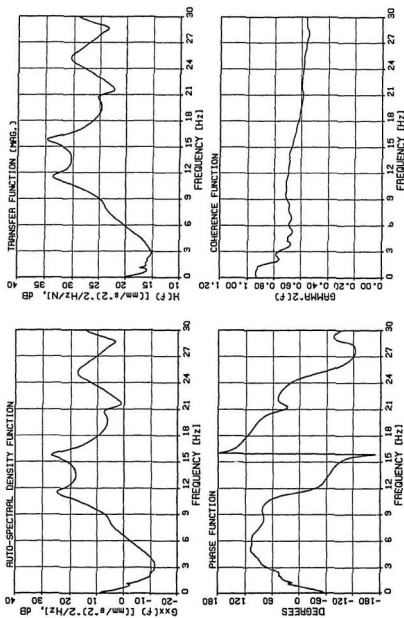


FIG. 7.67 RESULTS FROM ACCELEROMETER A3 DUE TO AN IMPACT INITIATED AT H5
(INTACT STRUCTURE).

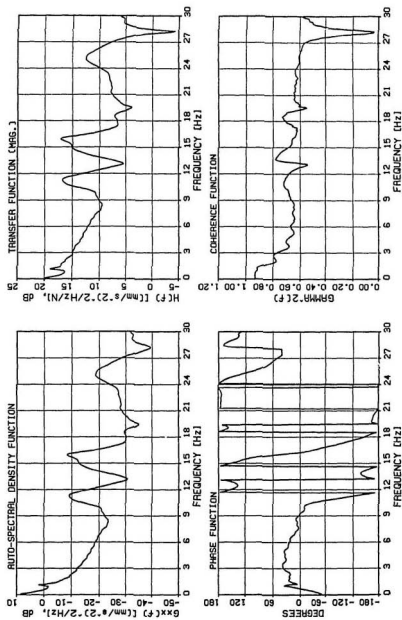


FIG. 7.68 RESULTS FROM ACCELEROMETER A4 DUE TO AN IMPACT INITIATED AT H5
(INTACT STRUCTURE).

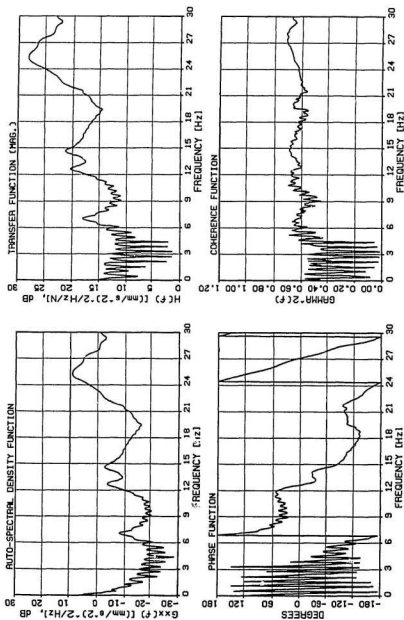


FIG. 7.69 RESULTS FROM ACCELEROMETER A1 DUE TO AN IMPACT INITIATED AT H5
(DAMAGED STRUCTURE; MEMBER 70 SEVERED AT NODE 18).

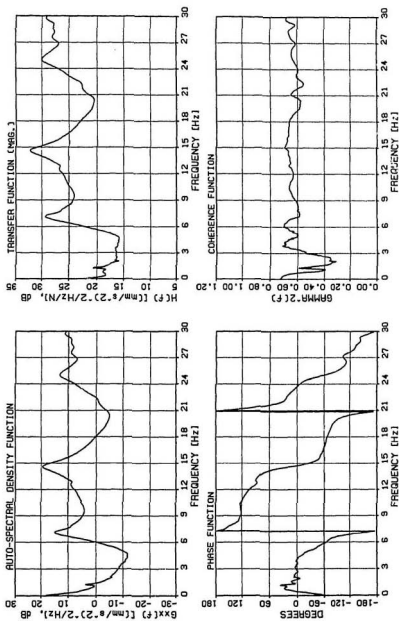


FIG. 7.70 RESULTS FROM ACCELEROMETER A2 DUE TO AN IMPACT INITIATED AT H5
(DAMAGED STRUCTURE; MEMBER 70 SEVERED AT NODE 18).

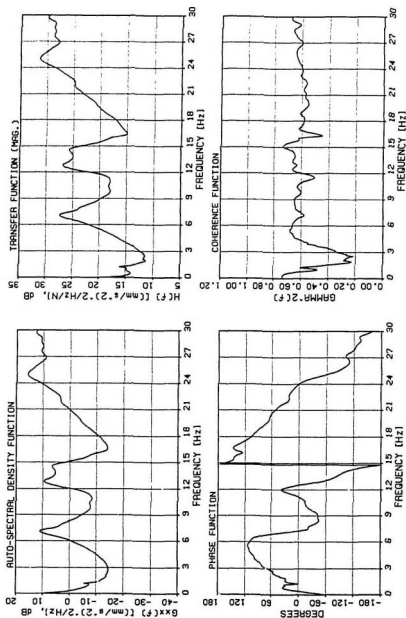


FIG. 7.71 RESULTS FROM ACCELEROMETER A3 DUE TO AN IMPACT INITIATED AT H5
(DAMAGED STRUCTURE: MEMBER 70 SEVERED AT NODE 18).

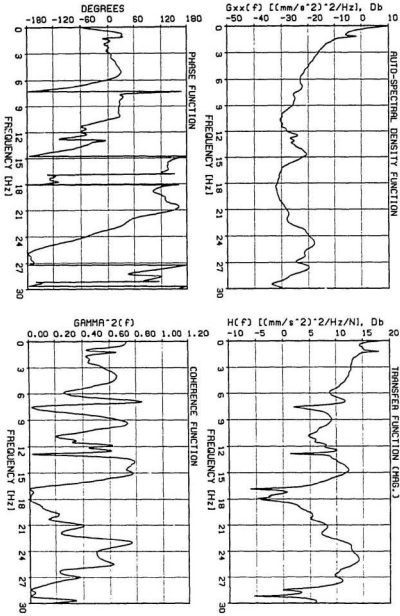


FIG. 7.72 RESULTS FROM ACCELEROMETER A4 DUE TO AN IMPACT INITIATED AT H5
(DAMAGED STRUCTURE: MEMBER 70 SEVERED AT NODE 183.)

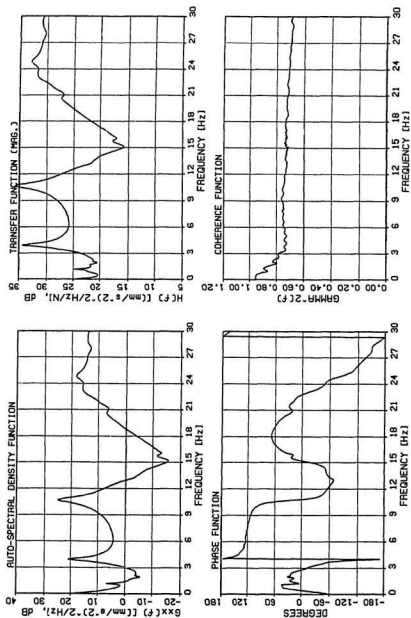


FIG. 7.73 RESULTS FROM ACCELEROMETER A2 DUE TO AN IMPACT INITIATED AT H5 (DAMAGED STRUCTURE: MEMBER 70 SEVERED, AND MEMBER 69 CUT-OFF AT NODE 18).

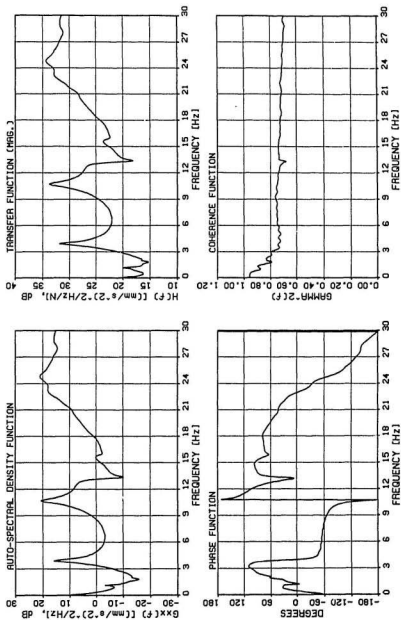


FIG. 7.74 RESULTS FROM ACCELEROMETER A3 DUE TO AN IMPACT INITIATED AT H5 (DAMAGED STRUCTURE: MEMBER 70 SEVERED, AND MEMBER 68 CUT-OFF AT NODE 18).

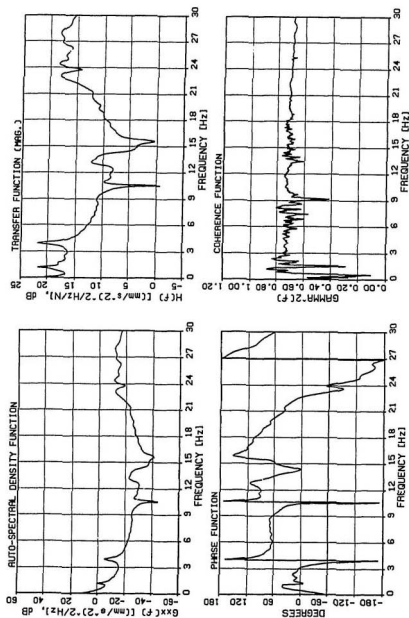


FIG. 7.75 RESULTS FROM ACCELEROMETER A4 DUE TO AN IMPACT INITIATED AT H5 (DAMAGED STRUCTURE: MEMBER 70 SEVERED, AND MEMBER 68 CUT-OFF AT NODE 18).

Chapter 8

Discussion of Results

In the preceding chapter, the theoretical and experimental results were presented. This chapter deals with the evaluation of those results.

8.1 Theoretical Results

8.1.1 Free Vibration Results

An examination of the computed free vibration natural frequencies tabulated in Table 7.1 shows good agreement between the hydro-elastic model and prototype frequencies, for the 3-D idealization. This statement is verified, because the percentage differences between the scaled-up frequencies, f_p^* , and the original prototype values, f_p , are less than 6%. These percentage differences could have resulted, because a distorted model¹ was used. (An exact reduced scale replica is not always possible.) For example, it was possible to model the external dimensions from the linear scale ratio (i.e., $\frac{L_m}{L_p}$), but it was not possible to model the wall thickness of the members likewise. The global influence of the distortion is most pronounced on the 1st torsional mode (i.e., mode 3), where a percentage difference of 5.79%

¹The theoretical justification for using a distorted model has already been discussed in section 4.5.2, Chapter 4.

was computed. This may have resulted, because the global influence of the distortion on the wall thickness of the members may have decreased the overall moment of inertia in the direction affecting global torsion. On the other hand, for those modes where the percentage differences are negative (e.g., modes 4 to 10), the effect is reversed. (That is, the global influence of the distortion may have increased the moment of inertia in the directions influencing these modes.)

In Table 7.2, the computed natural frequencies of the model and prototype for the stick model idealization of the hydro-elastic model and prototype are presented. Similar trends to that of the 3-D model idealization are observed. By comparing these results with those for the 3-D cases, it is observed that not all the frequencies were extracted with the stick model idealization of the structures. The global bending modes were computed, but the torsional and axial modes were not. This resulted, because the flexibility matrix of the stick model was obtained by applying unit loads only in the direction of global bending. Therefore, this structural idealization should be conceptualized as an approximate method.

Computed Mode Shapes. From the computed mode shapes of the idealized 3-D models of the prototype and hydro-elastic model (Figures 7.1-7.10), it is seen that the free vibration dynamic behavior of the prototype and model is similar. This is observed from the geometrical configuration of the computer generated mode shapes. From these mode shapes and the computed natural frequencies, it is concluded that the hydro-elastic model deflects in a similar manner, and exhibits the same vibrational characteristics as the prototype structure during free vibration.

Damage Simulation. An examination of the results tabulated in Tables

7.3 and 7.4 for the idealized 3-D prototype and model, respectively, reveals that the modes most affected when member 70 was inactivated (removed from the analyses) was the 2nd flexural mode, M_y . When member 70 was removed, a decrease of 28.42% resulted for the prototype; that is, a change from 2.03 to 1.45 Hz. Similarly, a decrease of 29.11% resulted for the hydro-elastic model—a change from 11.43 to 8.08 Hz. Furthermore, when two members were removed, the mode most affected was, again, the 2nd flexural mode, M_y (i.e., mode 4). The removal of two members on the prototype (i.e., members 70 and 68) resulted in a 61.27% change in the natural frequency of the 2nd flexural mode; while for the hydro-elastic model, a 63.55% change resulted. Observe that the modes least affected by the removal of members 70, and 70 and 68 are: mode 1 (1st flexural mode, M_y), mode 2 (1st flexural mode, M_x), mode 3 (1st torsional mode, M_z), and mode 5 (1st axial mode, M_z). This results because the damaged members do not occur in the panels along the global direction in which modes 1, 2, 3 and 5 occur. The above statement is exemplified by observing that when member 101 is severed (i.e., the leg of the structure between members 4 and 5 at level 1 shown in Figure 3.10), a 16.02% and 15.44% change resulted in the 1st bending mode of the prototype and model, respectively. Since this member greatly influences the motion of the structure during bending about the global y-axis (i.e., M_y), a 28.56% and 29.94% also resulted in the 2nd flexural mode (mode 4) of the prototype and model, respectively. To understand the effects of member removal on the natural frequencies further, computer generated mode shapes associated with the computed natural frequencies for the hydro-elastic model were computed.

Mode Shapes for the Intact and Damaged Model. The effects

of member removal can be visually seen by comparing the mode shapes of the intact and damaged hydro-elastic model depicted in Figures 7.11–7.30. Observe that, except for mode 4, all the other modes remain virtually unchanged, when member 70 was removed. More explicitly, for those modes which are unaffected by the removal of member 70, the global motion about their respective axes is the same. (That is, bending modes remain in bending and twisting remain in twisting.) However, for the 2nd flexural mode (mode 4), the global geometric configuration of the structure appears distorted—see Figure 7.18. The structure appears to twist towards the direction of the damaged member. This could have resulted because the removal of member 70 caused a change in the structural symmetry as far as stiffness is concerned. Slight variations also occur in modes 5, 8, 9 and 10. A re-examination of Table 7.4 also shows that percentages ranging 4.75% to 6.35% were computed for those modes. From these observations, it can also be concluded that the removal of member 70 may have slightly disrupted the structural symmetry regarding stiffness for these modes.

Similar trends to those discussed previously are observed when member 70 and 68 were removed. For example, notice in Figure 8.2 that the overall structural configuration appears less distorted compared with the case when member 70 was removed (Figure 8.1). This, therefore, suggests that the symmetry of the structure was restored. In other words, though the stiffness of the structure was reduced appreciably, the stiffness was more evenly distributed than when member 70 was inactivated. An examination of Figure 8.4 shows that when member 68 is removed, the global geometric configuration of the structure is opposite to that of the case when member 70 was severed. Therefore, the net result, when both members (70 and 68) are

ORIENTATION 

HORIZONTAL SCALE = 2.5112 FEET PER INCH
 VERTICAL SCALE = 2.5112 FEET PER INCH
 EQUIVALENT ROTATION X 0.0 Y 20.0 Z -40.0
 MEMBER 4 FEET 8.1047 ETC /SEC

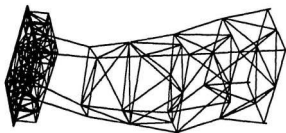
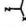


FIG. 8.1 DYNAMIC MODE # 4 (MEMBER 70 REMOVED).

ORIENTATION 

HORIZONTAL SCALE = 2.3044 FEET PER INCH
 VERTICAL SCALE = 2.3044 FEET PER INCH
 EQUIVALENT ROTATION X 0.0 Y 20.0 Z -40.0
 MEMBER 4 FEET 4.1048 ETC /SEC

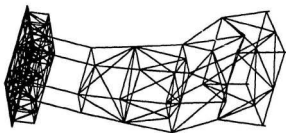


FIG. 8.2 DYNAMIC MODE # 4 (70 & 68 REMOVED).

ORIENTATION

 HORIZONTAL SCALE = 2.8112 FEET PER INCH
 VERTICAL SCALE = 2.8112 FEET PER INCH
 EQUIVALENT ROTATION X 0.0 Y 25.0 Z -40.0
 MODE 4 FROM 8.1047 CYC /SEC

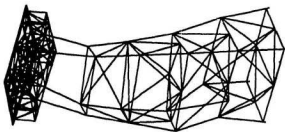


FIG. 8.3 THE EFFECT OF MEMBER 70 ON MODE # 4.

ORIENTATION

 HORIZONTAL SCALE = 2.3644 UNITS PER INCH
 VERTICAL SCALE = 2.3644 UNITS PER INCH
 EQUIVALENT ROTATION X 0.0 Y 25.0 Z -40.0
 MODE 4 FROM 8.1188 CYC /SEC

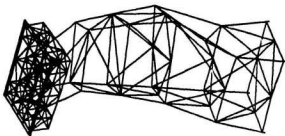


FIG. 8.4 THE EFFECT OF MEMBER 68 ON MODE # 4.

removed is a cancellation effect, and explains why the structure appears less distorted than in the cases where the members are severed independently. To examine the effects of the removal of members 70 and 68 on the other modes, refer to Figures D.1–D.18, Appendix D.

The observations noted above suggest that members 70 and 68 contributed to the stiffness of the 2nd bending mode, M_y . Thus, when the stiffness of the structure was reduced by the removal of these members, the frequency at which the mode could be excited was reduced.

This reduction in stiffness could be explained as follows: the deformation of the structure during bending results from shear displacements of the panels (i.e., the regions containing the damaged members). As a consequence, when member 70 or 68 is severed, the neighbouring k-brace member cannot transmit direct load without the horizontal brace, to which it is attached, undergoing bending. This implies that the companion brace is virtually inactive; so the shear stiffness of the panel is reduced.

It should be mentioned that the frequency reductions were mainly attributable to a reduction in stiffness rather than a reduction in mass, because the mass of the individual structural members is small (e.g., member 70 \approx 0.11 kg). So the influence from a reduction in mass would be minimal.

8.1.2 Response to a Train of Regular Waves

Displacement Response. Figure 7.31 shows the response of the idealized 3-D structures to a train of regular waves having wave parameters presented earlier in section 7.1.2. These graphs show that the behavior of the prototype and the hydro-elastic model is similar. Ten cycles of analyses are shown. Observe that in both the prototype and model, the transition from

the transient to the steady state motion is clearly seen. After approximately two time periods (i.e., 6 and 32 seconds for the model and prototype, respectively), both structures experience steady state motion. Moreover, the response levels for the non-linear analyses—using the non-linear form of the Morrison's wave force equation—are slightly lower than that obtained using the linear analyses.

For the stick model idealization, the results were depicted in Figure 7.35. The dynamic behavior is similar to that of the 3-D model idealization. After approximately two time periods, both idealizations experience steady state motion. Based on the levels of the response, it is valid to say that the stick model idealization of the hydro-elastic model slightly over estimates the dynamic response of the structure. (That is, when compared to the 3-D idealization.)

To compare the dynamic behavior of the prototype and model, the dynamic responses, discussed previously from the 3-D idealizations, were non-dimensionalized. An examination of the results presented in Figure 7.32 suggests there is good agreement between the prototype and model. Thus, it can be concluded that it is possible to predict, theoretically, the dynamic performance of the prototype based on the results attained from the theoretical hydro-elastic model. Because it was not possible to excite certain natural frequencies with the stick model in the free vibration analyses (Table 7.2), and the model slightly overestimated the dynamic response (refer to Figure 7.35), it is considered that the 3-D model idealization is probably better suited to simulate the physical hydro-elastic model for the wave tank tests. As a result, from this stage onwards, the analyses will be focussed on the 3-D idealization of the hydro-elastic model.

Force Variation Along the Jacket. Figures 7.33 and 7.34 show the non-dimensionalized force distribution for the idealized 3-D model and prototype. Note that in both cases (i.e., the forces resulting from the non-linearized and linearized form of Morrison's equation), there is good agreement between the prototype and model. As should be expected, the magnitude of the nodal forces increases with increasing distance from the sea bed to the mean water level. At node 23, there are regions of zero force which result at instances where the node is above the wave. The almost step-like functional distribution for the force at node 19 results, because of the method used to lump the nodal forces.² Each submerged structural member was sub-divided into ten sub-elements. At each sub-element, the water particle acceleration and velocity were computed, and were then used in the Morrison's wave force equation. At the surface, however, there are occasions when the water surface lies between the nodal points of a sub-element. So only the forces below the water level are computed. This phenomenon only occurs at the surface nodes. Intuitively, it would appear the solution to this problem would be to make the sub-elements smaller at the surface. Nevertheless, there would still be occasions when the problem would reoccur, probably to lesser extent. Considering the length of each structural member along the jacket, it seems that ten sub-elements per submerged member are appropriate. Besides, increasing the number of sub-elements would also increase the CPU time of the analyses.

By comparing the force variations for the non-linear and linear analyses (Figures 7.33 and 7.34), it is observed that the levels of the force for the non-linear case are slightly lower than that of the linear case. This explains why

²The theoretical justification is summarized in Figure 3.11, Chapter 3.

the response levels for the non-linear analyses, noted earlier, were slightly lower than that of the linear case.

Further examination of the force variations also shows that the curvature of the non-linear forces is slightly different from the forces predicted using linear analyses—i.e., using the linearized form of the Morrison's equation. For instance, at a time ratio of 0.5 (refer to Figure 7.33), an inflection point exists as the curves changes from positive to negative values. As seen in Figure 7.34, this inflection point is not present in the linear analyses. (The inflection point is a result of the non-linearity in the forces.)

8.1.3 Response to Irregular Waves

Computer simulated studies (using the measured irregular wave spectra from the wave tank facility) were carried out. The results for the white noise input wave spectrum were shown in Figures 7.36–7.39. Those for the JONSWAP input wave spectrum were presented in Figures 7.40–7.42.

White Noise Test Simulation. To extract the relevant modal parameters, the time domain signals (computed at nodes 12, 18, 23 and 78) were transformed to the frequency domain. These nodal responses corresponded to those measured with accelerometers A1, A2, A3 and A4 on the physical hydro-elastic model. Figure 7.36 shows a typical global x-direction spectral density function of the output acceleration at node 18. This graph was obtained using conventional FFT procedures. Four resonant peaks are noticeable. Because of the resolution, it would be difficult to locate the frequencies at which resonance exist. Figure 7.37 shows the same results using the MEM method mentioned presented in Chapter 5. Note the difference in resolution and precision. Based on the free vibration analysis results, the

first peak on the lower frequency end of the spectrum corresponds to the 1st flexural mode (mode 1); the second peak corresponds to the 2nd flexural mode; the 3rd is associated with mode 7; and the fourth peak represents mode 8.

JONSWAP Test Simulation. Computed acceleration spectral densities using the JONSWAP input wave spectrum were presented in Figures 7.40–7.42. Similar trends to the white noise tests simulations are observed.

Damage Simulation Studies. Like the free vibration analyses results presented earlier, Figures 7.38 and 7.41 show that when member 70 was severed to simulate damage of that member, the mode most affected is the 2nd flexural mode, M_y . Notice that when members 70 and 68 are inactivated, the 2nd bending mode is most affected—refer to Figures 7.39 and 7.42. To compare the effects of the damaged member(s) on the resonant frequencies visually, the results at node 23 are presented as an example. Results for the white noise test simulations are depicted in Figures 8.5–8.6.

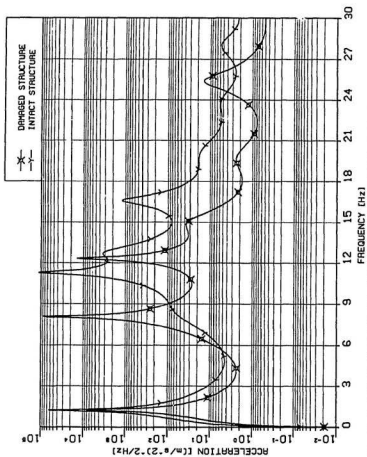


FIG. 8.5 A COMPARISON OF THE SHIFT IN RESONANT FREQUENCY AT NODE 23 DUE TO DAMAGE (MEMBER 70 REMOVED—WHITE NOISE TEST SIMULATION).

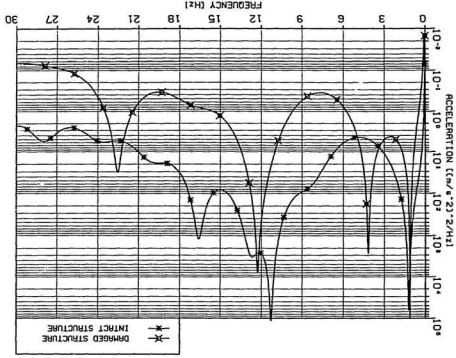


FIG. 8.6 A COMPARISON OF THE SHIFT IN RESONANT FREQUENCY AT NODE 23 DUE TO DAMAGE (MEMBERS 70 AND 68 REMOVED--WHITE NOISE TEST SIMULATION).

8.2 Experimental Results

8.2.1 Transient Decay Tests to Compute Damping

In-Air Tests. Average global x and y direction damping ratio variations (using the logarithmic decrement method) were shown in Figure 7.45. In both cases, the damping variation is more steady after eight cycles. Therefore, this region was used to determine the transient decay damping. For comparison, computed damping estimates using the above method and the average damping obtained from the curve fitting method (i.e., the Lavenberg-Marquardt and Finite difference Jacobian) are shown here:

Damping Estimates from In-Air Tests

	Logarithmic Decrement	Curve Fitting
$\zeta_{air,x}$	$0.9218 \pm 0.03\%$	$0.9112 \pm 0.02\%$
$\zeta_{air,y}$	$0.6334 \pm 0.02\%$	$0.6277 \pm 0.01\%$

In-Water Tests. Like the *in-air* tests, average global x and y direction damping ratio variations (using the logarithmic decrement method) were depicted in Figure 7.48. After six cycles, the variation in damping is more steady. The following are the damping estimates:

Damping Estimates from In-Water Tests

	Logarithmic Decrement	Curve Fitting
$\zeta_{water,x}$	$3.5756 \pm 0.15\%$	$3.6576 \pm 0.04\%$
$\zeta_{water,y}$	$1.7033 \pm 0.04\%$	$1.7221 \pm 0.02\%$

These damping factors are associated with the 1st global flexural modes in the global x and y directions. The values obtained from the *in-air* tests corre-

spond approximately to those which could be expected from steel structures vibrating in air and, therefore, are satisfactory. Damping of steel structures vibrating in water is very low, typically 1 to 3% [22]. Hence, the results obtained from the *in-water* tests also correspond, approximately, to those which could be expected from steel structures. As a result, the similitude condition imposed by equation (4.26), in Chapter 4 (i.e., $\zeta_m = \zeta_p$), is satisfied.

8.2.2 Wave Probe Results

Spectral Density Functions for the input signals from the white noise and JONSWAP input wave spectra were seen in Figures 7.50 and 7.52, respectively. When these functions are compared to those obtained using conventional FFT procedures (Figure 7.49 and 7.51), the superiority of the MEM technique over the use of conventional FFT methods is palpable. Further examination of the MEM functions shows that there is practically very little difference between the signals measured with the wave probes P1, P2 and P3 for the two distinct input wave spectra. This would, therefore, suggest that there were no cross tank oscillations capable of altering the global x-direction response of the physical hydro-elastic model during the wave structure interaction experiments.

8.2.3 Wave Tests Results

Response to a Train of Regular Waves

From the results of the experimental and theoretical model to a train of regular waves (Figure 7.54), it is seen that there is good agreement between experiment and theory. The transition from the transient to the steady state response is very apparent in all the cases. Observe, however, that the

theoretical results computed using the non-linear form of Morrison's wave force equation simulates the experimental values more closely than with that obtained with the linearized form. (The results from the linear analyses are slightly higher.) From these results, the workability of the experimental model with its associated instrumentation, and the computer model were ascertained.

Response to Irregular Waves

Resonant frequencies for the irregular wave induced vibration investigations for the white noise and JONSWAP tests are epitomized in Tables 8.1–8.8. These values were computed using equation (6.34), in Chapter 6 (i.e., the Maximum Entropy expression). It is not suggested that estimates of resonant frequencies could not be taken directly from the spectral density graphs. The major impediment, though, is that the accuracy would be very dependent on the sampling frequency, Δf , because all the spectral density ordinates will occur at intervals of Δf apart. Notwithstanding, when estimates of resonant frequencies are obtained by solving for the roots of equation (6.34), the accuracy is improved, for it depends on the tolerance (i.e., the maximum deviation of the function from zero) specified in Muller's algorithm³.

Results from White Noise Tests. Results of the structural response (acceleration) to the white noise input wave spectrum were presented in Figures 7.56–7.60. For the intact structure, resonant peaks are well defined. For accelerometers A1 and A2, relative extrema points occur at about 1.08 Hz.

³i.e., the *IMSL* numerical scheme noted earlier on page 132, Chapter 6, used to solve for the roots.

**Table 8.1 Measured Resonant Frequencies from Accelerometer A1
(Results for the Intact and Damaged Structure: White Noise Tests).**

Modes of Vibration	Measured Frequency [Hz]			
	Intact Structure	Damage Member(s)		
		70 Half-cut at Node 18	70 Severed at Node 18	70 Removed and 68 cut-off at node 16
Mode 1 (1st Flexure, M_y)	*	*	*	*
Mode 4 (2nd Flexure, M_y)	11.7381	11.6411	7.1308	4.0425
Mode 7 (3rd Flexure, M_y)	*	*	12.7603	10.7527
Mode 8 (3rd Flexure, M_z)	16.0648	16.0091	14.7363	13.3416
Mode 10 (4th Flexure, M_y)	25.2719	25.1690	*	*

**Table 8.2 Measured Resonant Frequencies from Accelerometer A1
(Results for the Intact and Damaged Structure: JONSWAP Tests).**

Modes of Vibration	Measured Frequency [Hz]			
	Intact Structure	Damage Member(s)		
		70 Half-cut at Node 18	70 Severed at Node 18	70 Removed and 68 cut-off at node 16
Mode 1 (1st Flexure, M_y)	*	*	*	1.2497
Mode 4 (2nd Flexure, M_y)	11.7382	11.6598	7.0714	4.014
Mode 7 (3rd Flexure, M_y)	*	13.7179	13.0767	10.1929
Mode 8 (3rd Flexure, M_x)	16.0622	16.0341	15.0058	13.1991
Mode 10 (4th Flexure, M_y)	25.3205	25.48	24.9917	*

NB: * indicates levels too low to be recorded.

**Table 8.3 Measured Resonant Frequencies from Accelerometer A2
(Results for the Intact and Damaged Structure: White Noise Tests).**

Modes of Vibration	Measured Frequency [Hz]			
	Intact Structure	Damage Member(s)		
		70 Half-cut at Node 18	70 Severed at Node 18	70 Removed and 68 cut-off at node 16
Mode 1 (1st Flexure, M_y)	1.2642	1.2409	1.2056	1.1503
Mode 4 (2nd Flexure, M_y)	11.7473	11.6411	7.1340	4.0375
Mode 7 (3rd Flexure, M_y)	*	*	*	10.7812
Mode 8 (3rd Flexure, M_x)	16.0349	16.0125	14.6231	*
Mode 10 (4th Flexure, M_y)	25.0654	25.1160	25.0363	*

**Table 8.4 Measured Resonant Frequencies from Accelerometer A2
(Results for the Intact and Damaged Structure: JONSWAP Tests).**

Modes of Vibration	Measured Frequency [Hz]			
	Intact Structure	Damage Member(s)		
		70 Half-cut at Node 18	70 Severed at Node 18	70 Removed and 68 cut-off at node 16
Mode 1 (1st Flexure, M_y)	1.2707	1.2663	1.2185	1.1685
Mode 4 (2nd Flexure, M_y)	11.7337	11.6392	7.1023	4.0143
Mode 7 (3rd Flexure, M_y)	*	*	14.7691	10.5841
Mode 8 (3rd Flexure, M_x)	16.0228	16.0526	*	*
Mode 10 (4th Flexure, M_y)	25.3239	25.0928	24.7716	22.8329

NB: * indicates levels too low to be recorded.

**Table 8.5 Measured Resonant Frequencies from Accelerometer A3
(Results for the Intact and Damaged Structure: White Noise Tests).**

Modes of Vibration	Measured Frequency [Hz]			
	Intact Structure	Damage Member(s)		
		70 Half-cut at Node 18	70 Severed at Node 18	70 Removed and 68 cut-off at node 16
Mode 1 (1st Flexure, M_y)	1.2669	1.2440	1.2268	1.1722
Mode 4 (2nd Flexure, M_y)	11.7228	11.6148	7.0890	4.0422
Mode 7 (3rd Flexure, M_y)	*	*	12.8047	10.7660
Mode 8 (3rd Flexure, M_x)	16.0102	15.9992	16.0074	13.3369
Mode 10 (4th Flexure, M_y)	25.4543	25.2505	25.0621	*

**Table 8.6 Measured Resonant Frequencies from Accelerometer A3
(Results for the Intact and Damaged Structure: JONSWAP Tests).**

Modes of Vibration	Measured Frequency [Hz]			
	Intact Structure	Damage Member(s)		
		70 Half-cut at Node 18	70 Severed at Node 18	70 Removed and 68 cut-off at node 16
Mode 1 (1st Flexure, M_y)	1.2752	1.2478	1.2091	1.2003
Mode 4 (2nd Flexure, M_y)	11.7395	11.6549	7.0556	4.0332
Mode 7 (3rd Flexure, M_y)	*	*	13.0872	10.7764
Mode 8 (3rd Flexure, M_x)	15.9904	16.0079	16.0743	13.3021
Mode 10 (4th Flexure, M_y)	25.3107	25.5429	24.7700	23.5912

NB: * indicates levels too low to be recorded.

**Table 8.7 Measured Resonant Frequencies from Accelerometer A4
(Results for the Intact and Damaged Structure: White Noise Tests).**

Modes of Vibration	Measured Frequency [Hz]			
	Intact Structure	Damage Member(s)		
		70 Half-cut at Node 18	70 Severed at Node 18	70 Removed and 68 cut-off at node 16
Mode 1 (1st Flexure, M_y)	1.2757	1.2718	1.2636	1.1690
Mode 4 (2nd Flexure, M_y)	11.7332	11.6331	7.2533	4.0355
Mode 7 (3rd Flexure, M_y)	*	13.6720	12.6360	
Mode 8 (3rd Flexure, M_x)	16.1025	*	14.8932	13.3073
Mode 10 (4th Flexure, M_y)	25.7214	*	*	23.1122

**Table 8.8 Measured Resonant Frequencies from Accelerometer A4
(Results for the Intact and Damaged Structure: JONSWAP Tests).**

Modes of Vibration	Measured Frequency [Hz]			
	Intact Structure	Damage Member(s)		
		70 Half-cut at Node 18	70 Severed at Node 18	70 Removed and 68 cut-off at node 16
Mode 1 (1st Flexure, M_y)	1.2718	1.2643	1.2682	1.1659
Mode 4 (2nd Flexure, M_y)	11.7350	11.6450	7.0010	4.0096
Mode 7 (3rd Flexure, M_y)	*	*	13.1079	*
Mode 8 (3rd Flexure, M_x)	15.9976	*	*	*
Mode 10 (4th Flexure, M_y)	25.3104	*	*	*

NB: * indicates levels too low to be recorded.

After a close look at the measured input wave spectra from wave probes P1, P2 and P3 (refer to Figure 7.50), it is observed that those relative extrema points (peaks) of concern occur in the region of the peak ordinates of the measured input wave spectra. From this observation, it is concluded that the relative maxima points or peaks seen on the spectra from accelerometers A1 and A2 are associated with the quasi-static stiffness controlled response at the peak of the wave spectrum. Four distinct peaks are seen on the results from accelerometers A2, A3 and A4. The first occurs at 1.27 Hz the second occurs at 11.7 Hz; the third occurs at 16 Hz and the fourth at 25 Hz.

Only three distinct damping-controlled response peaks are seen on the spectral density function in the results for accelerometer A1. The resonant peak associated with the lowest flexural mode of the structure is not present. This could be explained as follows: Accelerometer A1 is the most submerged sensor. As can be observed from the mode shape of the fundamental mode of the hydro-elastic model (refer to Figure 7.11), most of the oscillations occur in the deck region. A1 was installed at a joint located approximately 198.12 cm below the deck level. Thus, when the hydro-elastic model resonates at its fundamental mode, the level of the oscillations might have been below the measuring range of the accelerometer. This statement is justified by observing that as the structure underwent damage (refer to Figure 7.60), the amplitude of the oscillations increase. At this point, the oscillations are within the measuring range of accelerometer A1, as seen by the emergence of the peak associated with the fundamental mode. The percentage changes in resonant frequencies resulting from damaged members are presented in Tables 8.9–8.16.

**Table 8.9 Percent Changes in Resonant Frequencies Due to Damaged
(Results from Accelerometer A1: White Noise Tests).**

Modes of Vibration	Damage member(s)		
	70 Half Cut at Node 18	70 Severed at Node 18	70 Removed and 68 Severed at node 16
Mode 1 (1st Flexure, M_y)	*	*	*
Mode 4 (2nd Flexure, M_y)	-0.8264	-39.2508	-65.5609
Mode 8 (3rd Flexure, M_x)	-0.3467	-8.3033	-16.9514
Mode 10 (4th Flexure, M_y)	-0.4072	*	*

**Table 8.10 Percent Changes in Resonant Frequencies Due to Damaged
(Results from Accelerometer A1: JONSWAP Test).**

Modes of Vibration	Damage member(s)		
	70 Half Cut at Node 18	70 Severed at Node 18	70 Removed and 68 Severed at node 16
Mode 1 (1st Flexure, M_y)	*	*	*
Mode 4 (2nd Flexure, M_y)	-0.4134	-39.6030	-65.7385
Mode 8 (3rd Flexure, M_x)	-0.1749	-6.5769	-17.8251
Mode 10 (4th Flexure, M_y)	0.6299	-1.2986	*

NB: * indicates levels too low to be recorded.

**Table 8.11 Percent Changes in Resonant Frequencies Due to Damaged
(Results from Accelerometer A2: White Noise Tests).**

Modes of Vibration	Damage member(s)		
	70 Half Cut at Node 18	70 Severed at Node 18	70 Removed and 68 Severed at node 16
Mode 1 (1st Flexure, M_y)	-1.8431	-4.6353	-8.9938
Mode 4 (2nd Flexure, M_y)	-0.4805	-39.2711	-65.4835
Mode 8 (3rd Flexure, M_x)	-0.1397	-8.8046	*
Mode 10 (4th Flexure, M_y)	0.2019	-0.1161	*

**Table 8.12 Percent Changes in Resonant Frequencies Due to Damaged
(Results from Accelerometer A2: JONSWAP Test).**

Modes of Vibration	Damage member(s)		
	70 Half Cut at Node 18	70 Severed at Node 18	70 Removed and 68 Severed at node 16
Mode 1 (1st Flexure, M_y)	-0.3463	-4.1079	-8.0428
Mode 4 (2nd Flexure, M_y)	-0.6360	-39.4709	-64.8762
Mode 8 (3rd Flexure, M_x)	0.1859	*	*
Mode 10 (4th Flexure, M_y)	-0.9126	-2.4179	-9.8369

NB: * indicates levels too low to be recorded.

**Table 8.13 Percent Changes in Resonant Frequencies Due to Damaged
(Results from Accelerometer A3: White Noise Tests).**

Modes of Vibration	Damage member(s)		
	70 Half Cut at Node 18	70 Severed at Node 18	70 Removed and 68 Severed at node 16
Mode 1 (1st Flexure, M_y)	-1.8076	-3.1652	-7.4749
Mode 4 (2nd Flexure, M_y)	-0.4969	-39.5280	-65.3708
Mode 8 (3rd Flexure, M_x)	-0.0687	-0.0175	-16.6975
Mode 10 (4th Flexure, M_y)	-0.8007	-1.5408	*

**Table 8.14 Percent Changes in Resonant Frequencies Due to Damaged
(Results from Accelerometer A3: JONSWAP Test).**

Modes of Vibration	Damage member(s)		
	70 Half Cut at Node 18	70 Severed at Node 18	70 Removed and 68 Severed at node 16
Mode 1 (1st Flexure, M_y)	-2.1487	-5.1835	-5.8735
Mode 4 (2nd Flexure, M_y)	-0.4663	-39.7447	-65.5647
Mode 8 (3rd Flexure, M_x)	0.2348	0.6506	-16.7078
Mode 10 (4th Flexure, M_y)	0.9174	-2.1363	-6.7936

NB: * indicates levels too low to be recorded.

**Table 8.15 Percent Changes in Resonant Frequencies Due to Damaged
(Results from Accelerometer A4: White Noise Tests).**

Modes of Vibration	Damage member(s)		
	70 Half Cut at Node 18	70 Severed at Node 18	70 Removed and 68 Severed at node 16
Mode 1 (1st Flexure, M_y)	-0.3057	-0.9485	-6.0124
Mode 4 (2nd Flexure, M_y)	-1.0324	-37.6500	-65.3105
Mode 8 (3rd Flexure, M_x)	*	-7.5100	-17.3588
Mode 10 (4th Flexure, M_y)	*	*	-2.3685

**Table 8.16 Percent Changes in Resonant Frequencies Due to Damaged
(Results from Accelerometer A4: JONSWAP Test).**

Modes of Vibration	Damage member(s)		
	70 Half Cut at Node 18	70 Severed at Node 18	70 Removed and 68 Severed at node 16
Mode 1 (1st Flexure, M_y)	-0.5897	-5.0008	-8.3268
Mode 4 (2nd Flexure, M_y)	-0.6823	-40.2899	-65.8029
Mode 8 (3rd Flexure, M_x)	*	*	*
Mode 10 (4th Flexure, M_y)	*	*	*

NB: * indicates levels too low to be recorded.

Member 70 Severed. It may be recalled, from section 8.11, that it was verified, from the computer simulation studies, that the mode most affected after the hydro-elastic model underwent damage, was the 2nd flexural mode, M_y . From this verification, it seems palpable to assume that if this trend were repeated on the output spectral density functions, the frequency at that point (i.e., before any damage occurred) would be the 2nd flexural mode, M_y . As seen in Figures 7.59 and 7.64, the resonant peak most affected by the severance of member 70 occurs at 11.7 Hz. This, therefore, suggests that the frequency of the 2nd flexural mode of the structure is excited at that frequency (11.7 Hz). Accordingly, it can be inferred that the resonant peak at 1.27 Hz corresponds to the 1st Flexural mode, M_y ; the peak at 16 Hz corresponds to the 3rd flexural mode, M_x , and the peak at 25 Hz is compatible the 4th flexural mode, M_y .

When an incision was made half-way through member 70 at the joint corresponding to node 18 on the theoretical model (refer to Figure 5.13), only small changes in the resonant frequency of the 2nd flexural mode, M_y , resulted. For example, in the results from accelerometer A1, the 2nd flexural mode, M_y , only changed from 11.73 Hz to 11.64 Hz—a 0.82% decrease (Table 8.5). These small percentage shifts in the resonant frequency of the 2nd flexural mode suggest that the simulated crack did not influence the axial stiffness of the member significantly. No appreciable shifts occurred in the other resonant peaks, because the stiffness of the panel containing member 70 was only slightly reduced. However, by cutting off the member at node 18, the 2nd flexural mode, M_y , shifted to about 7.1 Hz, a decrease of 39%. (For example, Figure 8.7.) This significant change resulted because, at that failure stage, the shear stiffness of the panel containing member 70 was reduced

appreciably. Since the mass of the member is small compared with the total mass of the structure, there was no measurable change between that condition and when the member was removed entirely from the structure. Thus, the reduction in frequency was attributable to a reduction in stiffness.

Member 70 Severed and 68 Cut-off at Node 16. For this damaged condition, the most predominant change of 65% occurs in the excitation frequency of the 2nd flexural mode; that is, a reduction from 11.7 Hz to 4 Hz. This large shift in frequency could be explained as follows: Member 68 contributes to the shear stiffness for global bending of the hydro-elastic model in the x-x plane (refer to Figure 5.13). For this reason, when the member was cut-off at one end, a reduction in the shear stiffness occurred, and accounts for the increase in amplitude of the higher peaks. The independent contribution of members 70 and 68 to the shear stiffness can be visually seen in Figures 8.3 and 8.4. Observe how the shearing takes place in the panel containing the damaged members as the structure vibrates at its 2nd flexural mode. The combined effect of both members was shown in Figure 8.2. As in the theoretical results, to compare the influence of the damaged member(s) on the resonant frequencies visually, the results from accelerometer A3 (for the white noise tests) are shown as an example; refer to Figures 8.7-8.8.

Results from the JONSWAP Tests. Similar trends to that of the white noise test results are noticeable in the output spectral density functions of the JONSWAP tests. The only major differences are seen in the levels of the peaks as seen, for example, in Figure 8.9. These differences are due to differences in the energy content of the input wave spectra.

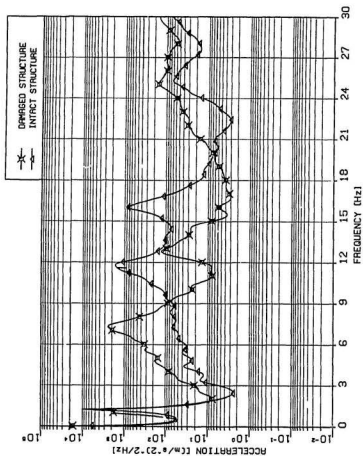


FIG. 8.7 A COMPARISON OF THE ACCELERATION SPECTRAL DENSITIES FROM A3 FOR THE INTACT AND DAMAGE STRUCTURE (MEMBER 70 REMOVED---WHITE NOISE TEST).

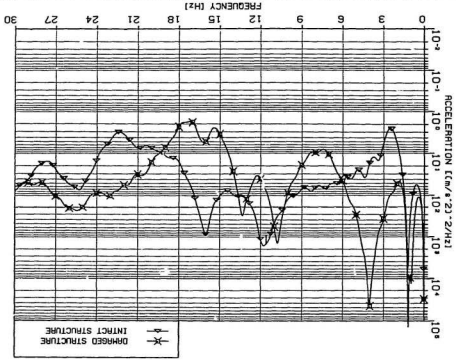


FIG. 8.8 A COMPARISON OF THE SPECTRAL DENSITIES FROM A3 FOR THE INTACT AND DAMAGED STRUCTURE (MEMBERS 70 AND 68 REMOVED--WHITE NOISE TEST).

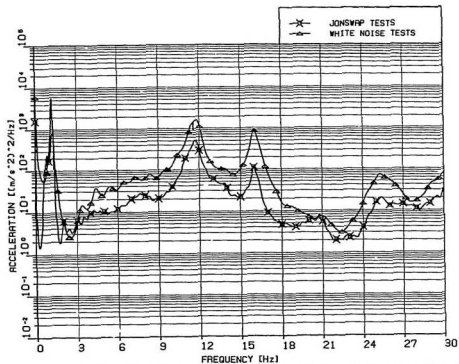


FIG. 8.9 A COMPARISON OF THE RESPONSE LEVELS OF THE WHITE NOISE AND JONSWAP TEST RESULTS MEASURED WITH ACCELEROMETER A3 (INTACT STRUCTURE).

Damping Estimates from the Force Response Data

Damping estimates predicted with the half-power bandwidth and MEM method for the intact and damage structural configurations—from the response measured with accelerometer A3 and A4—were shown in Tables 7.9–7.10. Results for the 1st flexural mode (M_y) are: 2.02% and 2.41% for the white noise and JONSWAP tests, respectively. These values represent the total damping of the structure. Therefore, since the hydro-dynamic component (which is water particle velocity and acceleration dependent) is included, the numbers could vary depending on the level of the response. The values are lower than that predicted with the transient decay test, where a value of $3.57 \pm 0.15\%$ was obtained. In both methods, the values suggest that the structure is lightly damped (i.e., $\zeta \leq 5.0\%$), and seem to reaffirm the assumption of lightly damped structures which is usually made in dynamic analyses—at least for the lower modes. (Damping estimates for the damaged structure are presented in Tables D.1–D.4.)

In both the transient and half-power methods, it was assumed that the modal frequencies are well separated. This assumption is justified if there is no co-ordinate coupling between modes, which depends on the relative positions of the center of mass and stiffness. Mass eccentricities will prohibit purely translational modes, and thus provide co-ordinate coupling. From the typical free decay graphs presented in Figures 5.10–5.11 in Chapter 5 and the well separated resonant peaks observed on the spectral density functions of the wave test results, the assumptions made regarding the separation of modal frequencies is justified.

8.2.4 Impact Test Results

The objective of the impact studies was to verify the locations of the resonant peaks obtained in the wave test results. Like the results presented earlier for the wave Tests (Figures 7.56-7.65), four peaks are observed on the spectral density and transfer function depicted in Figures 7.66-7.75 for the intact structure. Generally, there is a phase shift of approximately 180° as the response passes through resonance. An examination of the phase functions reveals that this condition is satisfied on the three higher peaks, and to a lesser extent the lower one located between 1 and 3 Hz. The coherence function ranges between 0.95 and 0.6—suggesting reasonable coherence for this type of experiment.

When member 70 was severed, the shift in the second peak (Figures 7.70-7.72) is analogous to that seen in the wave test results. Based on these observations and the computer generated free vibration analyses results reported earlier in the preceding chapter, it is concluded that the first peak seen in the results for the intact structure (between 1 and 3 Hz) is the 1st flexural mode (M_y); the second (between 9 and 12 Hz) is the 2nd flexural mode (M_y); the third (between 15 and 18 Hz) is mode 8 and the fourth (between 24 and 27) is mode 10.

Again when member 70 was severed and member 68 was cut-off at node 16, similar trends to those reported for the wave test results (refer to Figures 7.73 and 7.75) are observed. Similar results for the undamaged and damaged structural conditions were obtained, when the impact was initiated at the other designated impact locations shown in Figure 5.6. For the case when the impact was initiated at H6, refer to Figures D.19-D.30, Appendix D.

Based on the impact test results and the results from the free vibration analyses, it is concluded that the relative maxima points seen on the output response spectra of the wave test (Figures 7.57–7.65) results are attributable to resonance.

8.3 Comparison Between the Experimental and Theoretical Results

An examination of the results presented in Tables 8.17–8.20 shows that there is good agreement between the resonant frequencies obtained experimentally, and with those computed numerically using the Finite Element Method (FEM). This means that the techniques employed in the idealization and construction of the experimental hydro-elastic model, to carry out Structural Integrity Monitoring, is highly satisfactory.

In both the experimental and theoretical results, the mode most affected when a k-brace member was severed (member 70) was the 2nd flexural mode, M_y . A 29% shift in the resonant frequency of the 2nd flexural mode (M_y) was obtained from the theoretical results while, on the other hand, a 39% shift was computed from the experimental results. Moreover, when two members were damaged (members 70 and 68) a 65% decrease was observed in the experimental results for the 2nd flexural mode, compared to a 63% for the same mode in the theoretical results. Again, the mode most affected in both experimental and theoretical analyses, when two k-brace members were damaged, was the 2nd flexural mode, M_y .

Table 8.17 Comparison of the Resonant Frequencies from the Experimental and Theoretical Results (White Noise and JONSWAP Tests) at Location A1.

	MEM Estimates of Resonant Frequencies Intact Structure			
	Experimental Results		Theoretical Results	
	White Noise	JONSWAP	White Noise	JONSWAP
Mode 1 (1st Flexure, M_y)	†	†	1.2044	1.2032
Mode 4 (2nd Flexure, M_y)	11.7381	11.7382	11.3773	11.3600
Mode 8 (3rd Flexure, M_z)	16.0648	16.0622	16.1264	16.1201
Mode 10 (4th Flexure, M_y)	25.2719	25.3206	27.8285	27.8503

† indicates levels too low to be measured.

‡ indicates resonant peak not well defined.

Table 8.18 Comparison of the Resonant Frequencies from the Experimental and Theoretical Results (White Noise and JONSWAP Tests) at Location A2.

	MEM Estimates of Resonant Frequencies Intact Structure			
	Experimental Results		Theoretical Results	
	White Noise	JONSWAP	White Noise	JONSWAP
Mode 1 (1st Flexure, M_y)	1.2642	1.2707	1.2031	1.2046
Mode 4 (2nd Flexure, M_y)	11.7473	11.7337	11.3597	11.3619
Mode 8 (3rd Flexure, M_z)	16.0349	16.0228	16.1224	16.1294
Mode 10 (4th Flexure, M_y)	25.0654	25.3239	27.9868	27.9384

Table 8.19 Comparison of the Resonant Frequencies from the Experimental and Theoretical Results (White Noise and JONSWAP Tests) at Location A3.

	MEM Estimates of Resonant Frequencies Intact Structure			
	Experimental Results		Theoretical Results	
	White Noise	JONSWAP	White Noise	JONSWAP
Mode 1 (1st Flexure, M_y)	1.2669	1.2753	1.2022	1.2016
Mode 4 (2nd Flexure, M_y)	11.7228	11.7395	11.3787	11.3441
Mode 8 (3rd Flexure, M_z)	16.0103	15.9905	16.1240	16.1254
Mode 10 (4th Flexure, M_y)	25.4545	25.3107	27.9164	27.8888

Table 8.20 Comparison of the Resonant Frequencies from the Experimental and Theoretical Results (White Noise and JONSWAP Tests) at Location A4.

	MEM Estimates of Resonant Frequencies Intact Structure			
	Experimental Results		Theoretical Results	
	White Noise	JONSWAP	White Noise	JONSWAP
Mode 1 (1st Flexure, M_y)	1.2757	1.2718	1.2083	1.2083
Mode 4 (2nd Flexure, M_y)	11.7332	11.7251	11.3590	11.3590
Mode 8 (3rd Flexure, M_x)	16.1026	15.9976	16.1237	16.1230
Mode 10 (4th Flexure, M_y)	25.7214	27.5275	27.7801	27.7795

In all cases, the discrepancies between the experimental and theoretical (FEM) results are small. These discrepancies (which include (a) the resonant frequencies presented in Tables 8.17–8.20, and (b) the percentage shift in the resonant frequencies resulting from damaged members) are a result of the many approximations incorporated in the FEM computer model. They may be summarized as:

- In the computer generated FEM model, the elements themselves are idealizations of the individual structural members in the hydro-elastic physical model, and behave according to idealized material properties and approximate force-displacement theories.
- Element connections are either very rigid or perfectly flexible. In the experimental hydro-elastic model the connections between the members are neither rigid nor perfectly flexible.
- Structural masses are estimated and lumped at the nodes to conserve both storage and computer solution time. This can represent the global behaviour of structure very well, but eliminates all the individual member vibrations. (More details will be given later.)
- The response of the structure is represented as the linear sum of independent, uncoupled modal responses. Though this is a good approximation in the lower modes, higher order modes may not be entirely independent, for they may be coupled by non-proportional damping terms.

Subject to these limitations, the following statements can be made regarding the computer generated finite element results.

The invalidity of the lumped mass idealization of the structure can be explained as follows: For any dynamic system, the analysis is greatly complicated because the inertia forces result from structural displacements which, in turn, are affected by the magnitude of the inertia forces. This closed cycle of cause and effect can be approached directly only by formulating the problem in terms of differential equations. However, because the mass of each structural member is distributed continuously along its length, the displacements and accelerations must be defined for each point along the length of the member if the inertia forces are to be completely understood. In such a situation, the analysis must be formulated in terms of partial differential equations, since the position along the span of each member besides the time must be taken as independent variables.

On the other hand, when the lumped mass idealization is used (as in the computer analyses), the very complicated motion of the structure is greatly reduced, for the inertia forces can only be developed at the nodal points in the finite element model of the structure.

The discrepancies between the experimental results and theoretical results are larger for the damaged structural configuration. This may have resulted because, in the computer model, the rigidity of the connections at the joint was maintained even after the member(s) were removed. In reality, the removal of one or more members would result in an increase in the stress of the remaining members which, in turn, would be transmitted to the joints (nodes). The excess stress would have a weakening effect on the joints (particularly the neighbouring joints); the extent of which is proportional to the magnitude of the excess stress transferred. This weakening of the joints is not present in the theoretical model, because the change in flexibility results

from a removal of the stiffening contribution of the damaged member(s).

In the experimental hydro-elastic model, all the joints are neither perfectly rigid nor flexible. (Joints were fastened with **ABS** solvent glue.) Therefore, when the structure underwent damage, the excess stress transmitted to the remaining members, particularly the neighbouring ones, could have resulted in a weakening of some of the joints of the remaining member(s)—especially the joint(s) closest to the damaged member(s). The net effect on the total stiffness of the structure would be greater than that of the theoretical model. This, in turn, would result in larger shifts in frequencies of the modes in which the flexibility is greatly influenced by the removal of the particular member(s) (e.g., mode 4 and member 70).

From the overall structural geometry, it would seem that, in the theoretical results, the percentage shift in frequencies resulting from the removal of member 68 would be equal to that of member 70. An examination of Table 7.4 shows that there are discrepancies in the results for those similar structural damage configurations. This may have resulted from the iterative scheme used. The subspace iteration method was used to solve for the natural frequencies. There is an error associated with the method that is small for the first few modes, and becomes larger as the number of modes in the solution increases.

Chapter 9

Concluding Remarks and Recommendations

This treatise dealt with a detailed design and construction of a hydro-elastic model of a typical four-legged jacket offshore platform. Both an indepth theoretical and experimental analysis were carried out. Experiments were conducted in a wave tank equipped with a pseudo random wave making facility. To obtain the necessary modal parameters (e.g., resonant frequencies, and damping ratios) from the ambient response data, the recently developed Marple algorithm was used with the very powerful Maximum Entropy Method (MEM). Regarding structural integrity monitoring, structural damage was simulated by saw cutting the member(s) under consideration. In the theoretical analyses, this was done by making the member(s) inactive in the analyses. The detection of damage was based on the changes in resonant frequencies compared with the intact structure.

9.1 Concluding Remarks

Based on the reported results and evaluations, important conclusions can be reached. Among these are the following:

1. The methods used in the design, modelling and adjustments, construction, instrumentation and in processing the data are reliable and valid techniques to carry out structural integrity monitoring of offshore structures, through the analyses of reduced hydro-elastic models.
2. The Maximum Entropy Method (MEM) proved to be a very powerful means of obtaining high resolution smooth spectra from very short time series records. Since the spectral density results obtained from the time series data can be attained in functional form, resonant frequencies and damping ratios could be numerically computed. This inherent facet of MEM may have very important applications in experimental modal analysis—particularly in the area of system identification from ambient vibration data. (It is not suggested that the MEM technique is a replacement of the conventional FFT procedures.)
3. A predictable relationship exists between physical damage and changes in the modes of vibration of the structure. However, as illustrated in Table 7.4, the success of the structural integrity monitoring technique depends, to a major extent, on the position or location of the damaged member(s). This observation could not be verified experimentally, since once a member was severed, it could not be easily repaired under water.
4. When an inclined member in a k-braced panel was severed to simulate damage of that member, a 39% decrease in the resonant frequency of the 2nd flexural mode—seen on the spectral density of the response—was experimentally observed. (A 65% decrease in the same mode was observed when two similar k-brace members on opposite sides of the structure were severed). The theoretical, finite element, results were in

general agreement.

5. An investigation into the effect of a member cracking suggested that the *Structural Integrity Method* is limited because of the low sensitivity/resolution regarding resonant frequency versus cracks. This, therefore, implies that only major damages (i.e., primary structural element failure) can be detected.
6. At each resonant frequency, the structure deformed in a different manner. Hence, the relative magnitudes between the various resonant frequencies should provide an indication of the general location at which the structure had been weakened. The primary benefit of such a system is that any damaged member which has a large influence on the stiffness of a particular mode of the structure will, obviously, result in an analogous large change in the excitation frequency of that mode. Thus, it is imperative that the stiffness characteristics of the structure be completely understood; so any large changes in the resonant frequency of a specific mode may be localized.
7. From the theoretically computed mode shapes, it was possible to observe the effect of damage on the most affected mode(s) from the shearing of the panel containing the damaged member(s). This could not be shown experimentally, since it would require an array of transducers to compute the mode shapes from the experimental data.
8. Estimates of damping for the 1st mode (from the wave induced vibrations studies) are lower than that obtained with the transient decay tests. The values computed from the wave tests are: 2.02% and 2.47%,

for the white noise and JONSWAP tests, respectively; $3.57 \pm 0.15\%$ was obtained with the transient decay tests. In all the cases, however, the values are less than 5.0%, and seem to reaffirm the assumption of lightly damped structures which is usually made in dynamic analyses—at least for the lower modes.

9. The stick model idealization of the structure only gave partial results regarding frequencies and mode shapes; moreover, the dynamic response is slightly over estimated. A more realistic representation is a 3-D idealization, which incorporates all the degrees of freedom and gives a much better representation of the dynamic mode shapes of the structure.

9.2 Recommendations

It should be clearly understood that the structural integrity method should not be conceptualized as a panacea for solving the problem of early detection of subsurface damages with certainty, since certainty, in such a complex environment as the ocean, can rarely be assured. Notwithstanding, if applied with conventional detection procedures on a continuous basis, the usefulness of the technique should be enhanced.

From the experienced gained in this study, the following recommendations are made:

1. Experiments were carried out in a wave tank capable of producing only unidirectional waves. Thus, only the modes in the direction of the waves (i.e. the global x-direction) were excited to measurable amplitudes. Had these tests been conducted in a wave tank facility capable of producing multidirectional waves, such modes as the 1st torsional

mode, for example, might have been excited to measurable amplitudes. An alternative solution would have been to carry out tests with the structure oriented at various angles to the incoming waves. But, these tests could not be attempted, because of the time limitations set, for the experiments, at the wave tank facility.

2. The transient decay tests showed that the natural period and damping constant of the structure increase when it was submerged in water (refer to Table 7.5 and 7.7). It would, perhaps, have been advantageous to examine at what ratio of the mass of the submerged zone to that of the total mass does the water affects the natural period and damping. These tests could have been carried out by varying the water depth for each set of experiments. This would suggest at what water depth the added mass coefficient, used in the theoretical analyses, is important.
3. Throughout the experiments, the magnitude of the deck mass was fixed. The detection of structural damage was based solely on the changes in the resonant frequencies of the global modes. It might have been, presumably, beneficial to examine the effect of the frequency changes with varying magnitudes of the deck mass.
4. Some assessment of the mode shapes of the structure should be obtained, so a comparison to the theoretically computed eigenvectors can be made. However, this would require an array of accelerometers along the structure where the mode shapes are of interest. There is certainly a need for more laboratory work (in and out of water) in this area of study, besides more experiments on actual operating platforms in the ocean.

Finally, it should be mentioned that at the time of writing this dissertation, preliminary work is being done, at Memorial University, in the area of system identification on small beam elements with the hope of extending it to a model of a tripod offshore structure. It is hoped that the experience gained from this investigation (particularly the use of the Maple algorithm with the Maximum Entropy Method) will be very useful in those system identification studies.

References

- [1] R.G. Goward, *Development of Fire Protection of Offshore Structures-I*, Applied Science Publishers Ltd., London, cited by C. Jebaraj, "Dynamic Response of Pile-Supported Offshore Towers Subjected to Wave Forces: Considering Soil-Fluid Interaction," *Ph.D. thesis*, Dept. of Applied Mechanics, I.I.T., Madras—600 036, India, September 1982, p. 3.15.
- [2] K. Ponnuraj, "A Study of the Effects of Member Loss on Offshore Steel Jackets," *Master's thesis*, I.I.T., Madras, India, cited by C. Jebaraj, "Dynamic Response of Pile-Supported Offshore Towers Subjected to Wave Forces: Considering Soil-Fluid Interaction," *Ph.D. thesis*, Dept. of Applied Mechanics, I.I.T., Madras—600 036, India, September 1982, p. 3.15.
- [3] G. Sebastiani, "Development in Inspection and Monitoring of offshore Structures," *Case Histories in Offshore Structures*, Edited by G. Maier, pp. 356–365.
- [4] R.B. Blackman and J.W. Tukey, *The Measurements of Power Spectra*, Dover Publication, Inc., New York, 1958.
- [5] O. Loland and A.C. Mackenzie, "On The Natural Frequencies of Damped Offshore Platforms," *Mech. Res. Comm.*, Volume 1, Pergamon Press, Department of Mechanical Engineering, University of Glasgow G12 899, Scotland, 1974, pp. 352–354.
- [6] R.D. Begg, A.C. Mackenzie, C.J. Dodds and O. Loland, "Structural Integrity Monitoring Using Digital Processing of Vibration Signals," *8th Annual Offshore Technology Conference*, Houston, Texas, Paper No. 2551, May 3–6, 1976, pp. 313–317.
- [7] R.D. Begg and A.C. Mackenzie, "Monitoring Offshore Structures Using Vibration Analysis," *Proceedings of the IES Symposium, Integrity of Offshore Structures*, Glasgow, Scotland, April 1978.
- [8] O. Loland and C.J. Dodds, "Experiences in Developing and Operating Integrity Monitoring Systems in the North Sea," *8th Annual Offshore Technology Conference*, Houston, Texas, Paper Number 2551, May 3–6, 1976, pp. 313–317.

- [9] O. Loland, A.C. Mackenzie and R.D. Begg, "Integrity Monitoring of Fixed Steel Offshore Oil Platforms," *BSSM/RINA Joint Conference*, Measurements in the Offshore Industry, Edinburgh, September 1975.
- [10] R.D. Begg, "Analysis for Deep North Sea Installation," *Petroleum Engineer*, October 1977, pp. 108-116.
- [11] R.D. Begg and A.C. Mackenzie, "Monitoring of Offshore Structures Using Vibration Analysis," *Structural Monitoring Seminar on Structural Integrity Monitoring of Offshore Structures*, Glasgow, April 1978, pp. 1-7.
- [12] G.P.D. Lock and A.W. Jones, "The Detection of Failures in Offshore Structures by Vibration Analysis. A Feasibility Study," *Interpretation of Complex Signals from Mechanical Systems Symposium*, London, 1976, pp. 31-35.
- [13] L.R. Wooton, "Use of Vibration Monitoring on Offshore Structures," *Institution of Civil Engineers*, London, Proceedings of Conference, Paper Number 9, July 1977, pp. 95-102.
- [14] D. R. Brown, "Monitoring and Structural Response of Offshore Structures," *European Offshore Petroleum Conference and Exhibition*, London, October 14-27, 1978, p. 169.
- [15] J.K. Vandiver, "Detection of Structural Failure on Fixed Platforms by Measurement of Dynamic Response," *Seventh Annual Offshore Technology Conference*, Houston, Texas, Paper Number 2267, May 5-8, 1975, pp. 243-251.
- [16] R.F. Busby, "Underwater Inspection/Testing/Monitoring of Offshore Structures," *Ocean Engineering*, Volume 6, Pergamon Press Ltd., Britain, 1979, pp. 456-471.
- [17] S. Rubin, "Mode Extraction from Ambient Vibration of an Offshore Platform," *ASCE Spring Convention and Exhibit*, Boston, April 2-6, 1979.
- [18] J.K. Vandiver and R.B. Campbell, "Estimation Of Natural Frequencies and Damping Ratios of Three Similar Offshore Platforms using Maximum Entropy Spectral Analysis," *ASCE Spring Convention and Exhibit*, Boston, Mass., April 6, 1979.
- [19] A.W. Irwin, "Dynamic Tests on Small Scale Structures—Application and Analysis of Data," *Applied Science Publishers Ltd.*, England, 1975.
- [20] M.E. Wojnarowski, S.G. Stiansen and N.E. Reddy, "Structural Integrity Evaluation of a Fixed Platform Using Vibration Criteria," *9th Annual Offshore Technology Conference*, Paper No. OTC 2909, Houston, Texas, May 2-5, 1971, pp. 247-253.

- [21] J.K. Vandiver, "Structural Damage Detection by Measurement of Dynamic Response," *Spring Meeting/STAR Symposium*, Paper No. T4, San Francisco, California, May 25-27, 1977, pp. 173-181.
- [22] J.K. Vandiver, "The Effect of Liquid Storage Tanks on the Dynamic Response of Offshore Platforms," *Journal of Petroleum Technology*, October 1979, pp. 91-96.
- [23] D.M. Duggan, E.R. Wallace and S.R. Caldwell, "Measured and Predicted Vibrational Behavior of Gulf of Mexico Platforms," *Twelfth Annual Offshore Technology Conference*, Paper No. OTC 3864, Houston, Texas, May 5-8, 1980, pp. 91-96.
- [24] D.M. Duggan, E.R. Wallace and S.R. Caldwell, "Measured Vibrational Behavior of a Gulf of Mexico Platform," *Thirteenth Annual Offshore Technology Conference*, Paper No. OTC 4137, Houston, Texas, May 4-7, 1980, pp. 199-203.
- [25] R.B. Campbell and J.K. Vandiver, "The Estimation of Natural Frequencies and Damping Ratios of Offshore Structures," *Twelfth Annual Offshore Technology Conference*, Paper No. OTC 3851, Houston, Texas, May 5-8, 1980, pp. 53-57.
- [26] R.N. Coppolino and S. Rubin, "Detectability of Structural Failure in Offshore Platforms by Vibration Monitoring," *Twelfth Annual Offshore Technology Conference*, Paper No. OTC 3865, Houston, Texas, May 5-8, 1980, pp. 101-106.
- [27] P. Lepert, M. Chay, J.Y. Heas and P. Marzul, "Vibration Detection Applied to Offshore Platforms," *Twelfth Annual Offshore Technology Conference*, Paper No. OTC 3918, Houston, Texas, May 5-8, 1980, pp. 627-630.
- [28] B.G. Burke, C. Sundararajan and F.M. Lafaie, "Characterization of Ambient Vibration Data by Response Shape Vectors," *Thirteenth Annual Offshore Technology Conference*, Paper No. OTC 4137, Houston, Texas, May 4-7, 1981, pp. 199-203.
- [29] B.G. Burke and N.R. Sosdian, "Analysis of Ambient Vibration Data by Multiple Shape Vectors," *Fourteenth Annual Offshore Technology Conference*, Paper OTC 4284, Houston, Texas, May 3-6, 1982, pp. 625-635.
- [30] H. Crohas and P. Lepert, "Damage-Detection Monitoring Method for Offshore Platforms is Field-Tested," *Oil and Gas Journal*, February 22, 1982, pp. 94-103.
- [31] M.J. Briggs and J.K. Vandiver, "Multichannel Maximum Entropy Method of Spectral Analysis Applied to Offshore Platforms," *Fourteenth Annual Offshore Technology Conference*, Paper No. OTC 4286, Houston, Texas, May 3-6, 1982, pp. 647-652.

- [32] M.J. Briggs, "Multichannel Maximum Entropy Method of Spectral Analysis Applied to Offshore Structures," *OE thesis*, Massachusetts Institute of Technology/Woods Hole Oceanographic Institute Joint Program in Ocean Engineering, 1981.
- [33] M.F. Cook and J.K. Vandiver, "Measured and Predicted Dynamic Response of a Single Pile Platform to Random Wave Excitation," *Fourteenth Annual Offshore Technology Conference*, Paper No. 4285, Houston, Texas, May 3-6, 1982, pp. 637-643.
- [34] R. Nataraja, "Structural Integrity Monitoring in Real Seas," *Fifteenth Annual Offshore Technology Conference*, Paper No. 4538, Houston, Texas, May 2-5, 1983, pp. 221-224.
- [35] J.W. Jones, "Monitoring and Assessing Integrity/Stability of Offshore Arctic Structures," *35th Annual Technical Meeting of the Petroleum Society of CIM*, Calgary, Alberta, Canada, June 10-13, 1984, pp. 283-318.
- [36] J.C.S. Yang, T. Tsai, W.H. Tsai and R.Z. Chen, "Detection and Identification of Structural Damage from Dynamic Response Measurements," *Proceedings of the 4th International Offshore Mechanics and Arctic Engineering Symposium*, Volume 2, Dallas, Texas, Feb. 17-21, 1985, pp. 505-511.
- [37] T. Moan, J. Amdahl, A.G. Engseth and T. Granli, "Collapse Behavior of Trusswork Steel Platforms," *Proceedings of the 4th International Conference on Behavior of Offshore Structures (BOSS'85)*, Delft, The Netherlands, July 1-5, 1985, pp. 255-268.
- [38] F. Shahrivar and J.G. Bouwkamp, "Damage Detection in Offshore Platforms Using Vibration Information," *Journal of Energy Resources Technology*, Volume 108, Dallas, Texas, June 1986, pp. 97-106.
- [39] W.H. Tsai, D.N. Kung and J.C.S. Yang, "Application of System Identification Technique To Damage Detection and Location in Offshore Platforms," *7th International Conference on Offshore Mechanics and Arctic Engineering*, Houston, Texas, Feb. 7-12, 1988, pp. 77-84.
- [40] S.W. Chakrabarti, W.A. Tam and A.L. Wolbert, "Wave Forces on a Randomly Oriented Tube," *7th Annual Offshore Technology Conference*, Paper No. OTC 2190, Houston, Texas, May. 5-8, 1975, pp. 249-256.
- [41] G.I. Airy, "On Tides and Waves," *Encyclopedia Metropolitana*, Vol. 5, London, 1845, pp. 241-396, cited by K. Munaswamy, K., Subbaraj and A.S.J. Swamidass, *Development of Offshore Structural Analysis Program (OSAP)*, Technical Report No. 16, Ocean Engineering Center, Indian Institute of Technology, Madras, India, November 1980, p. 2.11.

- [42] G.G. Stokes, "On the Theory of Oscillatory Waves," *Trans. Cambridge Philosophical Society*, VIII, 1847, p. 441, cited by K. Munaswamy, K., Subbaraj and A.S.J. Swamidas, *Development of Offshore Structural Analysis Program (OSAP)*, Technical Report No. 16, Ocean Engineering Center, Indian Institute of Technology, Madras, India, November 1980, p. 2.12.
- [43] D.J. Korteweg and G. de-Vries, "On the Change of Form of Long Waves," *Philosophical Magazine*, Series 5, 39, 1895, pp. 442-443, cited by K. Munaswamy, K., Subbaraj and A.S.J. Swamidas, *Development of Offshore Structural Analysis Program (OSAP)*, Technical Report No. 16, Ocean Engineering Center, Indian Institute of Technology, Madras, India, November 1980, p. 2.12.
- [44] J. Boussinesque, "Theorie des ondes et des Remous qui se Propagent Le Long D'un Rectangulaire Horizontalen etc.," *J'L de Mathematique Pure et Applique*, Series 2, 17, 1872, pp. 55-108, cited by K. Munaswamy, K., Subbaraj and A.S.J. Swamidas, *Development of Offshore Structural Analysis Program (OSAP)*, Technical Report No. 16, Ocean Engineering Center, Indian Institute of Technology, Madras, India, November 1980, p. 2.12.
- [45] D.C. Nelson, "A Review of Sub-structure Analysis of Varying Systems," *The Shock and Vibration Digest*, Vol. 11, No. 11, Nov. 1979, pp. 1-9.
- [46] A.Y.T. Leung, "An Accurate Method of Dynamic Condensation in Structural Analysis," *International Journal of Numerical Methods in Engineering*, Vol. 12, 1978, pp. 1705-1715.
- [47] O.C. Zienkiewicz, *The Finite Element Method*, McGraw Hill Book Company (U.K.) Ltd., p. 304.
- [48] R.D. Cook, *Concepts and Application of Finite Element Analysis*, John Wiley and Sons, Inc., 1981.
- [49] R.W. Clough and J. Penzien, *Dynamics of Structures*, McGraw-Hill Book Company, 1975.
- [50] R.J. Guyan, "Reduction of Stiffness and Mass Matrices," *Journal of AIAA*, Vol. 11, No. 6, 1973, p. 892.
- [51] H.C. Houbolt, "A Recurrence Matrix Solution for Dynamic Response of Aircrafts," *Journal of Aeronautical Sciences*, Vol. 17, 1950, pp. 540-550.
- [52] J. Lamb, *Hydrodynamics*, Dover Publications, New York, 1945.
- [53] R.L. Wiegell, *Oceanographical Engineering*, Prentice-Hall, Inc., Englewood, Cliffs, N. J., 1964.

- [54] J. Penzien and S. Tseng, "Three-dimensional Dynamic Analysis of Offshore Platforms," *Numerical Methods in Offshore Engineering*, John Wiley and Sons, Inc., 1976.
- [55] L.E. Borgman, "Computations of the Ocean-wave Forces on Inclined Cylinders," *Journal of Geophysical Research*, Transaction AGU 39, No. 5, Oct. 1958, pp. 885-888.
- [56] D.I.H. Barr, "Method of Synthesis—basic procedures for the new approach to similitude," *Water Power*, in two parts, Vol. 21, pp. 148-158, 183-188, April-May 1969.
- [57] J.J. Sharp, *Hydraulic Modelling*, Butterworths, London, 1981.
- [58] J.J. Sharp, "Basic Applications of Similitude Theory," *Water and Water Engineering*, London, Vol. 77, No. 931, pp. 344-349, September 1973.
- [59] T. Sarpkaya and M. Isaacson, *Mechanics of Wave Forces on Offshore Structures*, Van Nostrand Reinhold Company New York, 1981.
- [60] F. Carneiro, "Some Aspects of the Dimensional Analysis Applied to the Theory and Experiment of Offshore Platforms," *Offshore Structures Engineering*, Volume 4: Proceedings of the 3rd International Symposium on Offshore Structures held at COPPE, Federal University of Rio de Janeiro, Brazil, September 1981, pp. 542-557.
- [61] W.J. Graff, *Introduction to Offshore Structures—Design, Fabrication, Installation*, Gulf Publishing, Texas, 1981, pp. 24, 92-134.
- [62] *General Design of Offshore Structures*, Notes from a Short Course Offered at the University of Texas, Austin, Texas, pp. 1.1-4.54, cited from Lecture Notes by D.V. Reddy for the Graduate Course, *Ocean Engineering Structures*, Memorial University, St. John's, Newfoundland, Spring 1981.
- [63] H.W.M. El-Tahan, "Dynamic Response of A Hydro-Elastic Model of a Typical Semi-Submersible to Waves and Bergy-Bit Impact," *Doctoral thesis*, Memorial University of Newfoundland, Canada, 1985.
- [64] J.P. Burg, "Maximum Entropy Spectral Analysis," *Ph.D. thesis*, Stanford University, U.S.A., 1975.
- [65] A. Van den Bos, "Alternative Interpretation of Maximum Entropy Spectral Analysis," *IEEE Transactions on Information Theory*, Vol. IT-17, July 1971.
- [66] L.M. Barrodale, R.E. Delves, R.E. Erickson and C.A. Zela, "Computational Experience with Marple's Algorithm for Autoregressive Spectrum Analysis," *Geophysics*, Volume 48, No. 9, September 1983, pp. 1274-1286.

- [67] L.S. Marple, "A New Autoregressive Spectrum Analysis Algorithm," *IEEE Transactions on Acoustics, Speech, and Signal Processing*, Vol. ASSP-28, No. 4, August 1980, pp. 441-454.
- [68] W.J. Vetter and M.J. Porsani, "Extended Matrix Formulation for the Marple Algorithm," *IEEE International Conference on Acoustics, Speech, and Signal Processing*, Vol. 1, 1987, pp. 340-343.
- [69] S. Haykin, "Nonlinear Methods in Spectral Analysis," *Topics in Applied Physics*, Vol. 34, Springer-Verlag, New York, 1979.
- [70] D.W. Bass and M.R. Haddara, "Nonlinear Models of Ship Roll Damping," *International Shipbuilding Progress*, Marine Technology Quarterly, Vol. 35, No. 40, April 1988, pp. 5-24.
- [71] W.G. Halvorsen and D.L. Brown, "Impulse Technique for Structural Frequency Response Testing," *Reprint from Sound and Vibration by PCB Piezotronics, Inc.*, Buffalo, N.Y., pp. 8-21, November 1977.
- [72] R.B. Campbell, "The Estimation of Natural Frequencies and Damping Ratios of Offshore Structures," *Ph.D. thesis*, Massachusetts Institute of Technology, 1980.
- [73] *Modern Plastics Encyclopedia*, Vol. 48: No. 10A, McGraw Hill, New York, October 1971, pp. 552-553.
- [74] J.R. Morrison, M.P. O'Brien, J.W. Johnson, and S.A. Schaaf, "The Force Exerted by Surface Waves on Piles," *Petroleum Trans.*, AIME 189, 1950, pp. 149-189.
- [75] N. Kryloff and Bogoliuboff, *Introduction to Nonlinear Mechanics: Approximate asymptotic methods*, Princeton Univ. Press, 1943.
- [76] Y.K. Lin, *Probabilistic Theory of Structural Dynamics*, McGraw Hill, N.Y., 1967.
- [77] R.W. Hornbec, *Numerical Methods*, Quantum Publishing, New York, 1975.

Bibliography

- [1] Z. Yin, Z. Chen and R. Ke, "Vibration Testing and Dynamic Analysis of Offshore Platform Models," *7th International Conference on Offshore Mechanics and Arctic Engineering*, Houston, Texas, Feb. 7-12, 1988, pp. 85-89.
- [2] K. Yoshida, H. Suzuki and N. Oka, "Control of Dynamic Response of Tower-Like Offshore Structures in Waves," *7th International Conference on Offshore Mechanics and Arctic Engineering*, Houston, Texas, Feb. 7-12, 1988, pp. 249-256.
- [3] O.N. Strand, "Multichannel Complex Maximum Entropy (Autoregressive) Spectral Analysis," *IEEE Trans. on Aut. Control*, Vol. AC-22, No. 4, August 1977, pp. 634-640.
- [4] D.W. Tuffs and R. Kumaresan, "Estimation of Frequencies from Multiple Sinusoids," *Proc. of IEEE*, Vol. 70, 1982, pp. 975-989.
- [5] H. Akaike, "A New Look at Statistical Model Identification," *IEEE Trans., Automatic Control*, AC-19,6, 1974, pp. 716-723.
- [6] H. Akaike, *On Entropy Maximization Principle*, in P.R. Krishniah (ed.), *Applications of Statistics*, Amsterdam, North-Holland, 1977, pp. 27-41.
- [7] R.G. Brown, *Smoothing, Forecasting and Prediction of Discrete Time Series*, Prentice-Hall, Englewood Cliffs, N.J., 1963.
- [8] M.A. Marshall, "Structural Integrity Monitoring of a Fixed-Bottom Frame Tower," *M.Eng. thesis*, Memorial University of Newfoundland, Canada, 1982, 134 p.
- [9] *GTSTRUDL Users' Manual*, GTICES Systems Laboratory, Georgia Institute of Technology, School of Civil Engineering, Atlanta, Georgia, Version 8701VAX, Sept. 1987.
- [10] H. El-Tahan, *IRWAF—A Computer Program for Irregular Wave Forces on Cylindrical Elements*, Faculty of Engineering, Memorial University of Newfoundland, Newfoundland, Canada, Sept. 1979, pp. 1-64.

- [11] J. Zhou, "Ocean Wave Simulation For Model Engineering Studies," *MTS Closed Loop*, The Magazine of Testing and Simulation Technology, Vol. 17, Summer 1988, pp. 19-23.
- [12] J.S. Bendat and A.G. Piersol, *Random Data Analysis and Measurements*, John Wiley and Sons, 1971.
- [13] L.E. Franks, *Signal Theory*, Prentice Hall, 1969.
- [14] L.H. Koopmans, *The Spectral Analysis of Time Series*, Academic Press, 1974.
- [15] S.K. Miller, *Complex Stochastic Processes*, Addison-Wesley Publishing company, Inc., 1978.
- [16] A.V. Appenheimer, *Application of Digital Signal Processing*, Prentice Hall, Inc., 1978.
- [17] M. Richardson, "Identification of the Modal Properties of an Elastic Structure from Measured Transfer Function Data," *20th I.S.A., International Symposium*, Albuquerque, M.M., May 1974.
- [18] M. Richardson, "Modal Analysis using Digital Test Systems," *Seminar on Understanding Digital Control and Analysis in Vibration Test Systems*, Shock and Vibration Information Center Publication, Naval Research Lab., Washington, D.C., May 1975.
- [19] M. Richardson and J. Kniskern, "Identifying Modes of Large Structures from Multiple Input and Response Measurements," *SAE Aerospace Engineering and Manufacturing Meeting Proceedings*, San Diego, 1976.
- [20] K.A. Ramsey, "Effective Measurements for Structural Dynamics Testing," *Sound and Vibration Magazine*, Part I, Nov. 1975, pp. 24-35, Part II, April 1976, pp. 18-31.
- [21] H. Edward, "Death in the North Sea," *Readers' Digest*, Montreal, November 1980, pp. 75-79.
- [22] W. McKinney, "Band Selectable Fourier Analysis," *Hewlett Packard Journal*, April 1975, pp. 20-24.
- [23] J.T. Broch, *Mechanical Vibration and Shock Measurements*, Bruel and Kjaer, June 1973.
- [24] M.H. Richardson, *Detection of Damage in Structures from Changes in their Dynamic (Modal) Properties—A Survey*, Structural Measurements, Inc., 1980.
- [25] S.H. Crandall and W.D. Mark, *Random Vibration in Mechanical Systems*, Academic Press, 1963.

- [26] D.E. Malen and E.A. Vaughan, "Digital Filtering for Analysis of Structural Vibration," *SAE*, Paper Number 730503, May 1973.
- [27] F.F. Lang, "Understanding Vibration Measurements," *Nicolet Scientific Corp.*, Appl. Note, June 1975.
- [28] P. Roth, "Effective Measurements using Digital Signal Analysis," *IEEE Spectrum*, April 1971, pp. 62-70.
- [29] S.A. Tretter, *Introduction to Discrete-Time Signal Processing*, John Wiley and Sons, Inc., 1976.
- [30] J.B. Thomas, *An Introduction to Applied Probability and Random Processing*, John Wiley and Sons Inc., 1971.
- [31] W.D. Stanley, *Digital Processing of Signals*, Reston Publishing Company, Inc., 1975.
- [32] K. Munaswamy, K., Subbaraj and A.S.J. Swamidas, *Development of Offshore Structural Analysis Program (OSAP)*, Technical Report No. 16, Ocean Engineering Center, Indian Institute of Technology, Madras, India, November 1980, pp. 1.1-14.7.
- [33] M. Arockiasamy, *et al.*, "Stochastic Response of Compliant Platforms to Random Waves," *2nd Pan American Congress on Ocean Engineering*, UPAD1-82, San Juan, Puerto Rico, W.I., August 1982, pp. 1-18.
- [34] G.M. Jenkins and D.G. Watts, *Spectral Analysis and Its Applications*, Holden-Day, San Francisco, 1969.
- [35] H.M. Tiedemann, "Shortcomings of Offshore Subsurface Engineering Inspection," *Marine Technology*, Volume 11, No. 1, January 1974, pp. 19-30.
- [36] R.M. Kenley and C.J. Dodds, "West Sole WE Platform: Detection of Damage by Structural Response Measurements," *Proceedings of 1980 OTC*, Paper No. 3866, Houston, Texas, May 1980.
- [37] D.V. Reddy, M. Arockiasamy and P.S. Cheema, "Response of Offshore Towers to Non-stationary Ice Forces," *Proc. POAC'81*, Quebec City, Quebec, Canada.
- [38] H. Schenck, *Introduction to Ocean Engineering*, McGraw-Hill Book Company, 1975.
- [39] B.J. Muga and J.F. Wilson, *Dynamic Analysis of Ocean Structures*, Plenum Press, New York-London, 1970.
- [40] L.E. Borgman, "Directional Spectra Models for Design Use for Surface Waves," *HEL Report 1-12*, University of California, June 1978.

- [41] M.G. Hallam, N.J. Heaf and L.R. Wooton, "Dynamics of Marine Structures Methods of Alleviating the Dynamic Response of Fixed Structures Subject to Wave and Current Action," *Report UR8 (Second Edition)*, CIRIA Underwater Engineering Group, London, England, October 1978.
- [42] I.M. Rapoport, *Dynamics of Elastic Containers Partially Filled with Liquid*, Springer-Verlag New York Inc., 1968.
- [43] F. Taylor and S.L. Smith, *Digital Signal Processing in Fortran*, Lexington Books, Lexington, Massachusetts, 1976.
- [44] C.T. Chen, *One-Dimensional Digital Processing*, Marcel Dekker, New York, 1979.
- [45] B. Nath, *Fundamentals of Finite Elements for Engineers*, The Athlone Press of the University of London, 1974.
- [46] J.C. Hancock, *An Introduction to the Principles of Communication Theory*, McGraw-Hill Book Company, Inc., 1961.
- [47] T.H. Dawson, *Offshore Structural Engineering*, Prentice-Hall Inc., Englewood Cliffs, New Jersey, 1983.
- [48] H. Matlock, W.P. Dawkins and J.J. Panak, "Analytical Model for Ice-Structure Interaction," *Proc. ASCE*, EMD, Vol. 97, 1971, pp. 1083-1092.
- [49] H.L. Langhaar, *Dimensional analysis and Theory of Models*, Robert E. Krieger Publishing Company, Huntington, New York, 1980.
- [50] E.D. Sotelino and J.L. Roehl, "Experimental Analysis of a Reduced Size Offshore Structure," *Offshore Structures Engineering*, Volume 4: Proceedings of the 3rd International Symposium on Offshore Engineering at COPPE, Federal University of Rio de Janeiro, Brazil, September 1981, pp. 559-569.
- [51] L.I. Sedov, *Similarity and Dimensional Analysis in Mechanics*, Academic Press, London, 1959.
- [52] W.E. Baker, P.S. Westine and F.T. Drodge, *Similarity Methods in Engineering Dynamics*, Hayden Book Co., N.J., 1973.
- [53] S.J. Kline, *Similitude and Approximation Theory*, McGraw-Hill, New York, 1965.
- [54] H.E. Huntley, *Dimensional Analysis*, Dover, New York, 1967.
- [55] S.P. Timoshenko, D.H. Young and W. Weaver, *Vibrations Problems in Engineering*, John Wiley and Sons, 1974.

- [56] C.G. Salmon and J.E. Johnson, *Steel Structures Design and Behavior*, International Textbook Company, 1971.
- [57] R. Rosen and M. Rubinstein, "Dynamic Analysis by Matrix Decomposition," *Journal of the Engineering Mechanics Division*, American Society of Civil Engineers, April 1968.
- [58] K.J. Bathe and E.L. Wilson, *Numerical Methods in Finite Element Analysis*, Prentice-Hall, 1976.
- [59] T.H.G. Megson, *Linear Analysis of Thin-walled Elastic Structures*, John Wiley and Sons, Inc., 1974.
- [60] *SIMQKE—A Computer Program for Artificial Motion Generation*, Dept. of Civil Eng., M.I.T., Nov. 1976.
- [61] J.W. Cooley and J.W. Tukey "An Algorithm for the Machine Calculation of Complex Fourier Series," *Mathematics of Computations*, Vol. 19, No. 90, 1965.
- [62] L.E. Borgman, "The Spectral Density for Ocean Wave Forces," *Hydraulic Eng. Lab., Univ. of Calif., Berkeley, Calif.* Dec. 1965.
- [63] C.L. Kirk, R. Nataraja and J.H. Teltow, "Deterministic and Random Wave Forces on Gravity Offshore Platforms," *ASME Paper N76-WA/FE-24*, ASME Meeting, Dec. 1976.
- [64] R.A. Fuchs, "On the Theory of Short-Crested Oscillatory Waves, Gravity Waves," *National Bureau of Standards Circular No. 521*, 1952, pp. 187-200.
- [65] J.F. Wilson, *Dynamics of Offshore Structures*, John Wiley and Sons, Inc., 1984.
- [66] L.S. Marple, "A Frequency Resolution of High Resolution Spectrum Analysis Techniques," *Proc. 1st RADC Spectrum Estimation Workshop*, 1978, pp. 19-35.
- [67] K.A. Ramsey, "Effective Measurements for Structural Dynamics Testing—Part 1," *Sound and Vibration*, Vol. 9, No. 11, 1977.

Appendix A

Selected Algorithms

Three algorithms are included in this appendix:

1. Cook's method for diagonalization of a consistent matrix,
2. Houbolt's algorithm, and
3. Longuet-Higgins and Cokelet smoothing algorithm.

A.1 Diagonalization of a Consistent Mass Matrix Using Cook's Method

Cook [48] recommends a procedure which applies to elements whose translational DOF are mutually parallel (e.g., beam and plate elements). The scheme is summarized as:

1. Compute only the diagonalized coefficients of the consistent mass matrix.
2. Compute \bar{M} , the total mass of the element.
3. Compute a number s by adding the diagonal coefficients m_{ij} associated with translation, but not rotation.
4. Compute the diagonal coefficients m_{ii}^* by multiplying them by the ratio $\frac{\bar{M}}{s}$; this preserves the translational mass of the element.

Thus, if the following $n \times n$ consistent mass matrix is available:

$$\begin{bmatrix} m_{11} & m_{12} & m_{13} & \dots & m_{1n} \\ m_{21} & m_{22} & m_{23} & \dots & m_{2n} \\ \vdots & \vdots & \vdots & \dots & \vdots \\ m_{n1} & m_{n2} & m_{n3} & \dots & m_{nn} \end{bmatrix} \quad (\text{A.1})$$

This matrix is diagonalized (using Cook's suggestions) as:

$$\begin{bmatrix} m_{11}^* & 0 & 0 & \dots & 0 \\ 0 & m_{22}^* & 0 & \dots & 0 \\ \vdots & \vdots & \vdots & \dots & \vdots \\ 0 & 0 & 0 & \dots & m_{nn}^* \end{bmatrix} \quad (\text{A.2})$$

where

$$m_{ii}^* = m_{ii} \left(\frac{\overline{M}}{s} \right),$$

$$s = (m_{11} + m_{22} + \cdots + m_{nn}),$$

\overline{M} = the total mass of the structure, and

$$i = 1, 2, 3, \dots, n.$$

A.2 Houbolt Algorithm

This algorithm solves a 3rd order equation, using a backward finite difference scheme.

The dynamic equation of motion (neglecting damping) is:

$$[M]\ddot{x} + [k]x = f(t). \quad (A.3)$$

... x is expressed in a backward finite difference scheme of 3rd order as:

$$\ddot{x}_i = \alpha x_i + \beta x_{i-1} + \gamma x_{i-2} + \delta x_{i-3} + \chi, \quad (A.4)$$

where i is the term step value of integration and α , β , γ , δ and χ are the coefficients to be computed at each time step.

The recurrence process is initiated with the following expressions:

$$\ddot{x}_i = \frac{1}{\Delta t^2}(x_{i+1} - 2x_i + x_{i-1}), \quad (A.5)$$

and

$$\dot{x}_i = \frac{1}{6\Delta t}(2x_{i+1} + 3x_i - 6x_{i-1} + x_{i-2}), \quad (A.6)$$

where Δt is the interval between two consecutive steps. The initial conditions are (when $i = 0$):

$$\begin{aligned} x_i &= 0, \\ \dot{x}_i &= 0, \\ \ddot{x}_i &= p(\tau), \end{aligned} \quad (A.7)$$

where $p(\tau)$ is the force per unit mass. Using the above conditions in equation (A.3) yields (when $i = 0$):

$$\begin{aligned} p(\tau) &= \frac{1}{\Delta t^2}(x_1 - 0 + x_{-1}), \\ x_1 + x_{-1} &= p(\tau)\Delta t^2, \\ x_{-1} &= p(\tau)\Delta t^2 - x_1. \end{aligned} \quad (A.8)$$

Substituting equation (A.5) in equation (A.4), the next relationship is:

$$\begin{aligned} 0 &= 2x_1 + 0 - 6x_{-1} + x_{-2}, \\ x_{-2} &= 6p(\tau)\Delta t^2 - 8x_1. \end{aligned} \quad (\text{A.9})$$

For $i \geq 1$, the recurrence relationship is:

$$\begin{aligned} \ddot{x}_i &= \frac{1}{\Delta t^2}(2x_i - 5x_0 + 4x_{-1} - x_{-2}), \\ &= \frac{1}{\Delta t^2}(2x_i + 4(p(\tau)\Delta t^2 - x_1) - 6p(\tau)\delta t^2 + 8x_1), \\ &= \frac{1}{\Delta t^2}(6x_i - 2p(\tau)\Delta t^2), \\ &= \frac{1}{\Delta t^2}(6x_i - 2p(\tau)). \end{aligned} \quad (\text{A.10})$$

When $i = 1$, the Houbolt's constants are:

$$\alpha = \frac{6}{\Delta t^2}, \chi = -2p(\tau), \beta = \gamma = \delta = 0. \quad (\text{A.11})$$

For $i \geq 1$, the recurrence relationships are:

$$\begin{aligned} \ddot{x}_i &\approx \frac{1}{\Delta t^2}(2x_i - 5x_{i-1} + 4x_{i-2} - x_{i-3}), \\ \dot{x}_i &\approx \frac{1}{\Delta t^2}(11x_i - 18x_{i-1} + 9x_{i-2} - 2x_{i-1}). \end{aligned} \quad (\text{A.12})$$

For $i \geq 2$, the recurrence relationship is:

$$\begin{aligned} \ddot{x}_i &= \frac{1}{\Delta t^2}(2x_i - 5x_1 + 4x_0 - x_{-1}), \\ &= \frac{1}{\Delta t^2}(2x_i + 5x_1 + (p(\tau)\Delta t^2 + x_1), \\ &= \frac{1}{\Delta t^2}(2x_i - 4x_1 + p(\tau)\Delta t^2). \end{aligned} \quad (\text{A.13})$$

... $i \geq 2$, the Houbolt's constants are:

$$\alpha = \frac{2}{\Delta t^2}, \beta = \frac{-4}{\Delta t^2}, \chi = -p(\tau), \gamma = \delta = 0. \quad (\text{A.14})$$

For $i = 3$

$$\begin{aligned}\ddot{x}_3 &= \frac{1}{\Delta t^2}(2x_3 - 5x_2 + 4x_1 + x_0), \\ &= \frac{1}{\Delta t^2}(2x_3 - 5x_2 + 4x_1).\end{aligned}\quad (\text{A.15})$$

... $i = 3$, the Houbolt's constants are:

$$\alpha = \frac{2}{\Delta t^2}, \beta = \frac{-5}{\Delta t^2}, \gamma = \frac{4}{\Delta t^2}, \delta = \chi = 0. \quad (\text{A.16})$$

For $i \geq 4$, the recurrence relationship is:

$$\ddot{x}_4 = \frac{1}{\Delta t^2}(2x_4 - 5x_3 + 4x_2 + x_1). \quad (\text{A.17})$$

... $i = 4$, the Houbolt's constants are:

$$\alpha = \frac{2}{\Delta t^2}, \beta = \frac{-5}{\Delta t^2}, \gamma = \frac{4}{\Delta t^2}, \delta = \frac{-1}{\Delta t^2}, \chi = 0. \quad (\text{A.18})$$

Finally, by substituting equation (A.2) into equation (A.1)—while knowing the values of the constants α, β, γ and χ —the equation of motion of the system is:

$$[[\alpha][M] + [K]] \underline{x}_i = \underline{p}(\tau)_i - [M][\beta x_{i-1} + \gamma x_{i-2} + \delta x_{i-3} + \chi]. \quad (\text{A.19})$$

So if the previous time step values are known, the present time step response can be computed.

A.3 Longuet-Higgins and Cokelet Smoothing Algorithm

In the smoothing algorithm attributable to Longuet-Higgins and Cokelet [77], a function $f(x)$ is defined at equally spaced points x_j , $j = 1, 2, 3, \dots, N$, and it is assumed that alternate points lie in a smooth curve. Thus, $f(x)$ can be locally approximated by two polynomials:

$$h(x) = (a_0 + a_1x + \dots + a_nx^n) + (-1)^j(b_0 + b_1x + \dots + b_{n-1}x^{n-1}). \quad (\text{A.20})$$

Here the first polynomial represents a smooth mean curve, while the second represents a quantity which oscillates with period 2 in j . Therefore, the smooth curve can be taken to be the first polynomial:

$$\bar{h}(x) = (a_0 + a_1x + a_2x^2 + \dots + a_nx^n). \quad (\text{A.21})$$

The coefficients $a_0, a_1, a_2, \dots, a_n$ and $b_0, b_1, b_2, \dots, b_{n-1}$ can be defined uniquely from the condition: $h(x_j) = f(x_j)$ at $(2n+1)$ consecutive points $(j-n)$ to $(j+n)$, inclusive. When $n = 2$, the five point formula for a central point becomes:

$$\bar{f}_j = \frac{1}{16}(-f_{j-2} + 4f_{j-1} + 10f_j + 4f_{j+1} - f_{j+2}), \quad (\text{A.22})$$

where $f_j \equiv f(x_j)$; $\bar{f}_j \equiv \bar{f}(x_j)$. For $j = 1, 2, N-1$ and N , the $(2n+1)$ consecutive points at which $h(x_j) = f(x_j)$ are to be considered are for the intervals: (j) to $(j+2n)$, $(j-1)$ to $(j+2n-1)$, $(j-2n+1)$ to $(j+1)$ and $(j-2n)$ to (j) , respectively. After carrying out the necessary algebraic operations, the resulting formulae are:

$$\begin{aligned} \bar{f}_j &= \frac{1}{16}(11f_j + 12f_{j+1} - 6f_{j+2} - 4f_{j+3} - 3f_{j+4}), \quad \text{for } j = 1 \\ \bar{f}_j &= \frac{1}{16}(3f_{j-1} + 8f_j + 6f_{j+1} - f_{j+3}), \quad \text{for } j = 2 \end{aligned}$$

$$\bar{f}_j = \frac{1}{16}(-f_{j-3} + 6f_{j-1} + 8f_j + 3f_{j+1}), \text{ for } j = N-1 \quad (\text{A.23})$$

$$\bar{f}_j = \frac{1}{16}(3f_{j-4} - 4f_{j-3} - 6f_{j-1} + 12f_{j-1} + 11f_j), \text{ for } j = N.$$

Least Square Smoothing Formulae. The smoothing formulae corresponding to a third-degree least square approximation over five points are given by:

$$\bar{f}_j = \frac{1}{35}(3f_{j-2} - 12f_{j-1} + 17f_j + 12f_{j+1} - 3f_{j+2}), \text{ for } 2 < j < N-1$$

$$\bar{f}_j = \frac{1}{70}(69f_j - 4f_{j+1} - 6f_{j+2} + 4f_{j+3} - f_{j+4}), \text{ for } j = 1$$

$$\bar{f}_j = \frac{1}{35}(2f_{j-1} + 27f_j + 12f_{j+1} - 8f_{j+2} + 2f_{j+3}), \text{ for } j = 2 \quad (\text{A.24})$$

$$\bar{f}_j = \frac{1}{35}(2f_{j-3} - 8f_{j-2} + 12f_{j-1} - 27f_j + 2f_{j+1}), \text{ for } j = N-1$$

$$\bar{f}_j = \frac{1}{70}(-f_{j-4} + 4f_{j-3} - 6f_{j-2} + 4f_{j-1} + 69f_j), \text{ for } j = N.$$

Appendix B

Sample Calculations

Typical calculations to select member section sizes for the experimental hydro-elastic model are included here.

B.1 Sample Calculations to Select Member Section Sizes

The following is a summary of sample calculations for the values depicted in Table 4.4.

To determine the geometric scale ratio:

$$\begin{aligned}\frac{L_m}{L_p} &= \frac{h_{w,m}}{h_{w,p}} \\ &= \frac{1.6 \text{ m}}{48.77 \text{ m}} \\ &= \frac{1}{30}\end{aligned}\quad (B.1)$$

To compute the wall thickness of the members in group 2:

$$\begin{aligned}\left(\frac{d_m}{d_p}\right) &= \left(\frac{L_m}{L_p}\right)^2 \left(\frac{E_p}{E_m}\right) \\ &= \left(\frac{1}{30}\right)^2 \left(\frac{206.896 \text{ kN/mm}^2}{1.83 \text{ kN/mm}^2}\right) \\ &= 0.1253 \\ \implies d_m &= 0.1253 d_p \\ &= 0.1253(12.7 \text{ mm}) \\ &= 0.1591 \text{ mm}(1/16 \text{ in}).\end{aligned}\quad (B.2)$$

To calculate the exterior diameter of the members in group 2:

$$\begin{aligned}\frac{D_m}{D_p} &= \frac{L_m}{L_p} \\ &= \left(\frac{1}{30}\right)(457.2) \text{ mm} \\ &= 15.25 \text{ mm}(0.60 \text{ in}).\end{aligned}\quad (B.3)$$

To determine the required density of the material of the model:

$$\rho_{s,m}^* = \rho_{s,p} \left(\frac{L_m}{L_p}\right) \left(\frac{d_p}{d_m}\right) \quad (B.4)$$

$$\begin{aligned}
&= 7.847 \times 10^{-3} \text{ kg/cm}^3 \left(\frac{1}{30} \right) \left(\frac{1}{0.1253} \right) \\
&= 2.087 \times 10^{-3} \text{ kg/cm}^3.
\end{aligned}$$

The density of **ABS** plastic ($\rho_{s,m}$) is equal to $1.107 \times 10^{-3} \text{ kg/cm}^3$; so,

$$\begin{aligned}
\Delta\rho_{s,m} &= \rho_{s,m}^* - \rho_{s,m} \\
&= 2.087 \times 10^{-3} - 1.107 \times 10^{-3} \\
&= 9.8 \times 10^{-4} \text{ kg/cm}^3.
\end{aligned} \tag{B.5}$$

Hence, lumped masses should be added to the experimental model, based on the above value, to compensate for the difference between the density of the **ABS** plastic (i.e., the material available), and the density required (i.e., $\rho_{s,m}^*$) in the following manner:

From computer analyses, the total volume of material required using the section sizes chosen is:

$$\begin{aligned}
Volume &= \sum (vol_{group\ 1} + vol_{group\ 2} + \dots + vol_{group\ 5}) \\
&= \sum (663.2356 + 933.9454 + 1355.9961 + 1024.1808 + 1388.4747) \\
&= 5365.853 \text{ cm}^3.
\end{aligned} \tag{B.6}$$

Consequently, the total mass required is computed as:

$$\begin{aligned}
Mass &= (Volume \times \Delta\rho_{s,m}) \\
&= 5.26 \text{ kg}.
\end{aligned} \tag{B.7}$$

As there are 20 nodes below the waterline, the total mass is distributed at 0.26 kg per node (i.e., $5.26/20$).

Appendix C

Calibration Curve and Instrumentation Settings

Included in this appendix are:

1. Calibration and instrumentation settings for the accelerometers, charge amplifiers, low pass filters, wave probes, and
2. Calibration curve for the impact hammer.

C.1 Calibration and Instrumentation Settings

The following are the calibration and instrumentation settings for the accelerometers, charge amplifiers, low-pass filters and wave probes used in the experiments:

Table C.1 Calibration Settings for Accelerometers

	Accelerometers				
	A1	A2	A3	A4	A5
B & K type	4339	4343	4379	4379	8306
Serial No.	293380	465255	1426469	1352502	1176627
Sensitivity	10.42 pC/g	10.14 pC/g	315 pC/g	310 pC/g	10 pC/g

Charge Amplifiers:

These were adjusted based on the charge sensitivity of each accelerometer.

L.L.F. = 0.3 Hz.

Low Pass Filters:

0 dB gain for all channels (i.e., A1–A5), and

maximum cut-off Frequency = 30 Hz.

Wave Probes:

Normal Sensitivity = 0.25 Volts/cm.

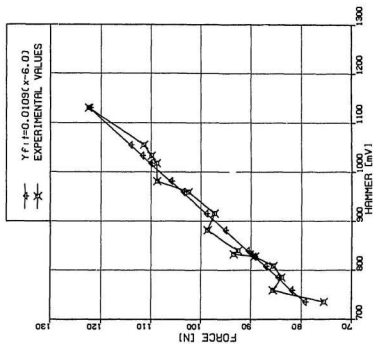


FIG. C.1 CALIBRATION CURVE FOR THE IMPULSE HAMMER.

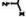
Appendix D

Miscellaneous

This appendix includes:

1. Computer generated mode shapes (Members 70 and 68 removed),
2. impact test results for an impact initiated at H6, and
3. MEM damping estimates from the response of the damaged structure.

D.1 Mode Shape (Members 70 and 68 Removed)

ORIENTATION

 HORIZONTAL SCALE = 2.3848 FEET PER INCH
 VERTICAL SCALE = 2.3848 FEET PER INCH
 EQUIVALENT ROTATION X 0.0 Y 20.0 Z -40.0
 MODE 1 FREQ 1.2529 CYC / SEC

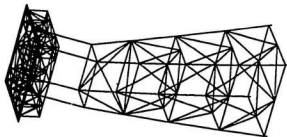


FIG. D.1 DYNAMIC MODE # 1 (CONTRACT MODEL).

ORIENTATION

 HORIZONTAL SCALE = 2.3862 FEET PER INCH
 VERTICAL SCALE = 2.3862 FEET PER INCH
 EQUIVALENT ROTATION X 0.0 Y 20.0 Z -40.0
 MODE 1 FREQ 1.1826 CYC / SEC

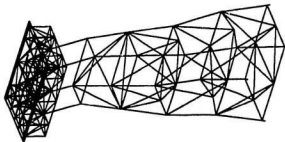
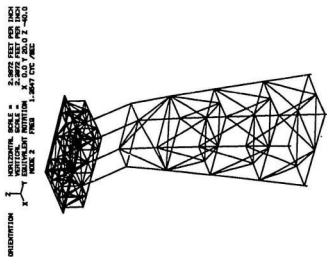


FIG. D.2 DYNAMIC MODE # 1 (70 & 68 REMOVED).

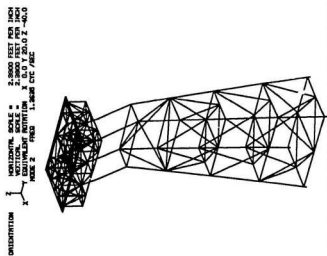
ORIENTATION



HORIZONTAL SCALE = 2.5972 FEET PER INCH
 VERTICAL SCALE = 2.5972 FEET PER INCH
 EQUIVALENT MOTION X 0.0 Y 20.0 Z -40.0
 MODE 2 FREQ 1.3647 CTC /SEC

FIG. D.3 DYNAMIC MODE # 2 (INTRAC MODEL).

ORIENTATION



HORIZONTAL SCALE = 2.5900 FEET PER INCH
 VERTICAL SCALE = 2.5900 FEET PER INCH
 EQUIVALENT MOTION X 0.0 Y 20.0 Z -40.0
 MODE 2 FREQ 1.3626 CTC /SEC

FIG. D.4 DYNAMIC MODE # 2 (70 & 68 REMOVED).

ORIENTATION

 HORIZONTAL SCALE = 2.3248 FEET PER INCH
 VERTICAL SCALE = 2.3248 FEET PER INCH
 EQUIVALENT ROTATION X 0.0 Y 20.0 Z -40.0
 MODE 3 FREQ 1.4278 CYC /SEC

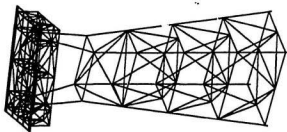
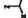


FIG. D.5 DYNAMIC MODE # 3 (CONTRACT MODEL).

ORIENTATION

 HORIZONTAL SCALE = 2.3248 FEET PER INCH
 VERTICAL SCALE = 2.3248 FEET PER INCH
 EQUIVALENT ROTATION X 0.0 Y 20.0 Z -40.0
 MODE 3 FREQ 1.4278 CYC /SEC

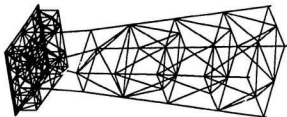
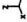


FIG. D.6 DYNAMIC MODE # 3 (70 & 68 REMOVED).

ORIENTATION 

HORIZONTAL SCALE = 2.4650 FEET PER INCH
 VERTICAL SCALE = 2.4650 FEET PER INCH
 DISPLACEMENT MOTION X 0.0 Y 0.0 Z -90.0
 MODE 8 FREQ 12.0468 C/C /SEC

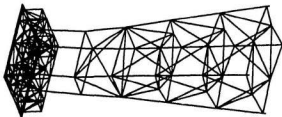


FIG. D.7 DYNAMIC MODE # 5 (INTRACT MODEL).

ORIENTATION 

HORIZONTAL SCALE = 2.8544 FEET PER INCH
 VERTICAL SCALE = 2.8544 FEET PER INCH
 DISPLACEMENT MOTION X 0.0 Y 0.0 Z -90.0
 MODE 8 FREQ 11.7708 C/C /SEC

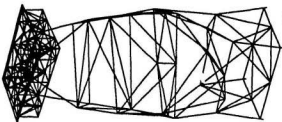


FIG. D.8 DYNAMIC MODE # 5 (70 & 68 REMOVED).

ORIENTATION 

HORIZONTAL SCALE = 2.3148 FEET PER INCH
 VERTICAL SCALE = 2.3148 FEET PER INCH
 EQUIVALENT MOTION X 0.0 Y 20.0 Z -40.0
 MODE 6 FREQ 11.1888 C/C /SEC

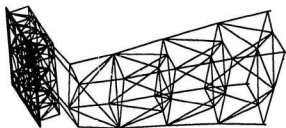
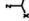


FIG. D.9 DYNAMIC MODE # 6 (INTACT MODEL).

ORIENTATION 

HORIZONTAL SCALE = 2.4082 FEET PER INCH
 VERTICAL SCALE = 2.4082 FEET PER INCH
 EQUIVALENT MOTION X 0.0 Y 20.0 Z -40.0
 MODE 6 FREQ 12.0867 C/C /SEC

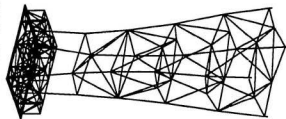


FIG. D.10 DYNAMIC MODE # 6 (70 & 68 REMOVED).

ORIENTATION

 HORIZONTAL SCALE = 2.07M FEET PER INCH
 VERTICAL SCALE = 2.000 FEET PER INCH
 EQUILIBRIUM POSITION X 0.0 Y 20.0 Z -40.0
 MODE 7 FREQ 11.4408 CYC /SEC

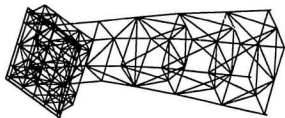
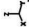


FIG. D.11 DYNAMIC MODE # 7 (INTRACT MODEL).

ORIENTATION

 HORIZONTAL SCALE = 2.000 FEET PER INCH
 VERTICAL SCALE = 2.000 FEET PER INCH
 EQUILIBRIUM POSITION X 0.0 Y 20.0 Z -40.0
 MODE 7 FREQ 12.9328 CYC /SEC

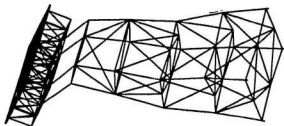


FIG. D.12 DYNAMIC MODE # 7 (70 & 68 REMOVED).

ORIENTATION

 HORIZONTAL SCALE = 2.3186 FEET PER INCH
 VERTICAL SCALE = 2.3186 FEET PER INCH
 EQUIVALENT ROTATION X 0.0 Y 20.0 Z -40.0
 MODE 8 FREQ 18.1228 CYC /SEC

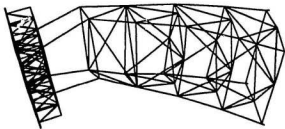
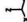


FIG. D.13 DYNAMIC MODE # 8 (CONTACT MODEL).

ORIENTATION

 HORIZONTAL SCALE = 2.2744 FEET PER INCH
 VERTICAL SCALE = 2.2744 FEET PER INCH
 EQUIVALENT ROTATION X 0.0 Y 20.0 Z -40.0
 MODE 8 FREQ 12.8825 CYC /SEC

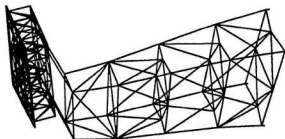


FIG. D.14 DYNAMIC MODE # 8 (70 & 68 REMOVED).

ORIENTATION 

HORIZONTAL SCALE = 2.3174 FEET PER INCH
 VERTICAL SCALE = 2.3174 FEET PER INCH
 EQUILIBRIUM POSITION X 0.0 Y 20.0 Z -40.0
 MODE 8 FREQ 17.2018 CYC /SEC

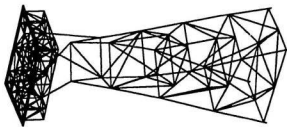


FIG. D.15 DYNAMIC MODE # 9 (INTRACT MODEL).

ORIENTATION 

HORIZONTAL SCALE = 2.2968 FEET PER INCH
 VERTICAL SCALE = 2.2968 FEET PER INCH
 EQUILIBRIUM POSITION X 0.0 Y 20.0 Z -40.0
 MODE 8 FREQ 15.8483 CYC /SEC

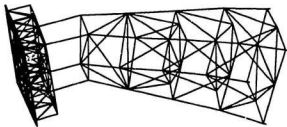


FIG. D.16 DYNAMIC MODE # 9 (70 & 68 REMOVED).

ORIENTATION 

HORIZONTAL SCALE = 2.8000 FEET PER INCH
 VERTICAL SCALE = 2.8000 FEET PER INCH
 DISPLACEMENT UNIT = 0.10 Y 20.0 Z -40.0
 MODE 10 FREQ 28.7658 CYS /SEC

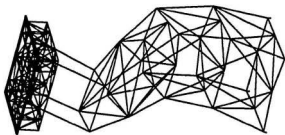


FIG. D.17 DYNAMIC MODE # 10 (INTRACT MODEL).

ORIENTATION 

HORIZONTAL SCALE = 2.4186 FEET PER INCH
 VERTICAL SCALE = 2.4186 FEET PER INCH
 DISPLACEMENT UNIT = 0.10 Y 20.0 Z -40.0
 MODE 10 FREQ 21.8610 CYS /SEC

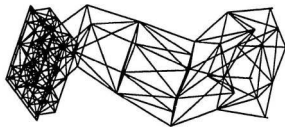


FIG.D.18 DYNAMIC MODE # 10 (70 & 68 REMOVED).

D.2 Results for an Impact Initiated at H6

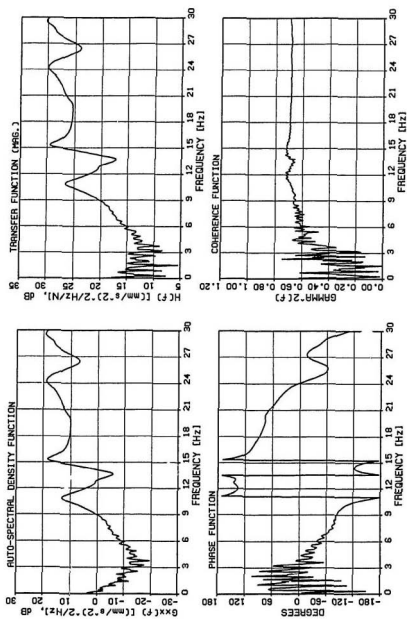


FIG. D.19 RESULTS FROM ACCELEROMETER A1 DUE TO AN IMPACT INITIATED AT H6 (INTACT STRUCTURE).

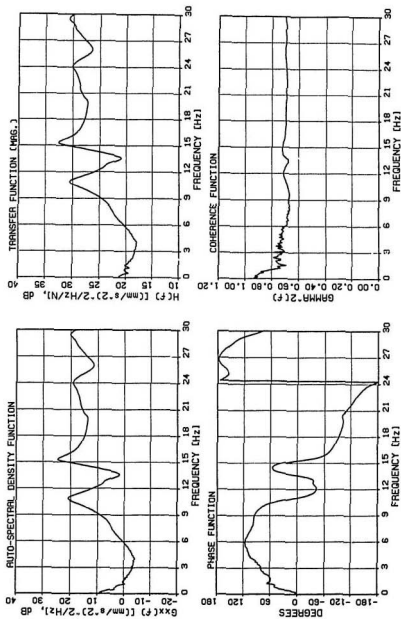


FIG. D-20 RESULTS FROM ACCELEROMETER A2 DUE TO AN IMPACT INITIATED AT H6
(INTACT STRUCTURE).

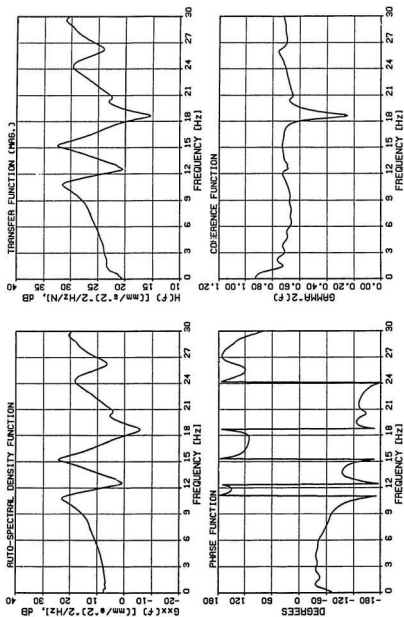


FIG. D.21 RESULTS FROM ACCELEROMETER A3 DUE TO AN IMPACT INITIATED AT H8 (INTACT STRUCTURE).

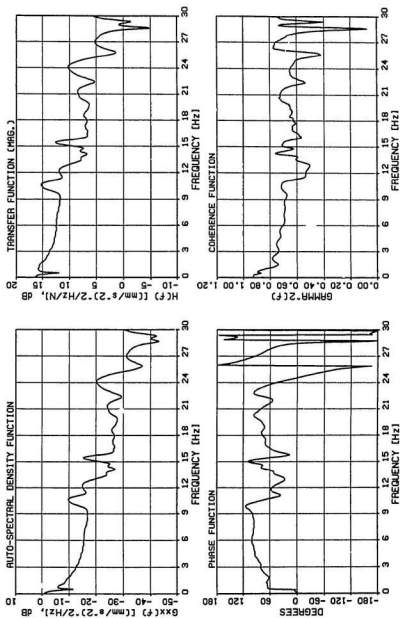


FIG. D.22 RESULTS FROM ACCELEROMETER A4 DUE TO AN IMPACT INITIATED AT H6 (INTACT STRUCTURE).

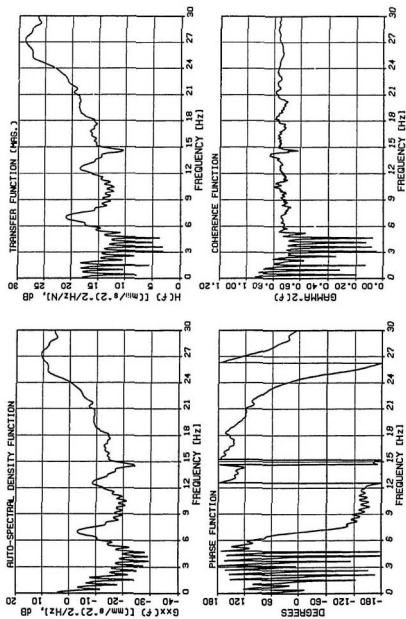


FIG. D.23 RESULTS FROM ACCELEROMETER A1 DUE TO AN IMPACT INITIATED AT H6
(DAMAGED STRUCTURE: MEMBER 70 SEVERED AT NODE 18).

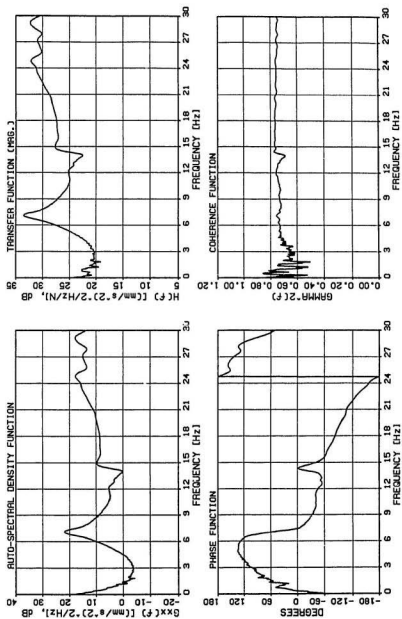


FIG. D.24 RESULTS FROM ACCELEROMETER A2 DUE TO AN IMPACT INITIATED AT H6
(DAMAGED STRUCTURE: MEMBER 70 SEVERED AT NODE 18).

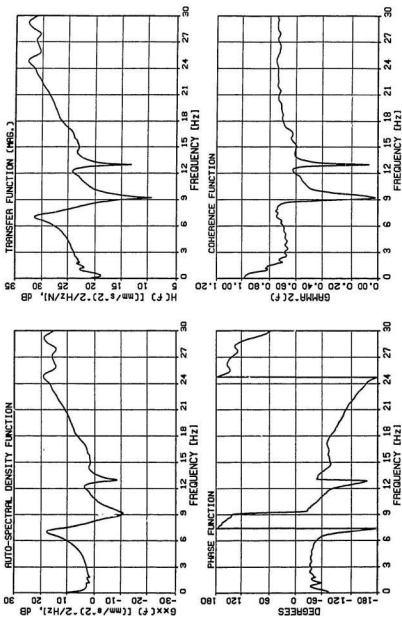


FIG. D.25 RESULTS FROM ACCELEROMETER A3 DUE TO AN IMPACT INITIATED AT H6
 (DAMAGED STRUCTURE: MEMBER 70 SEVERED AT NODE 18).

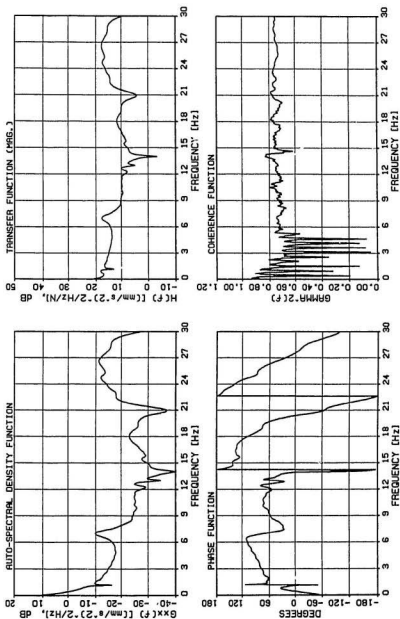


FIG. D.26 RESULTS FROM ACCELEROMETER A4 DUE TO AN IMPACT INITIATED AT H8
(DAMAGED STRUCTURE: MEMBER 70 SEVERED AT NODE 18).

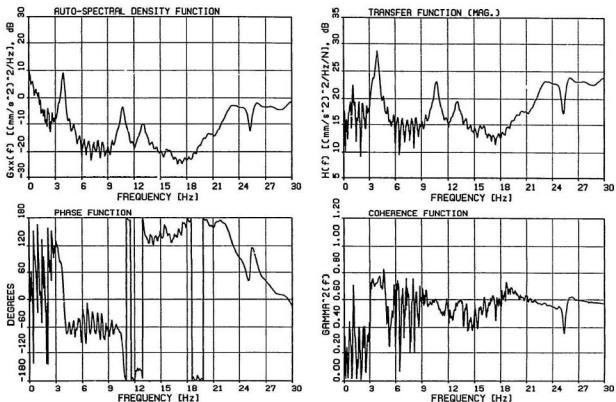


FIG. D.27 RESULTS AT ACCELEROMETER A1 DUE TO AN IMPACT INITIATED AT H6
 (DAMAGED STRUCTURE: MEMBER 70 SEVERED, AND MEMBER 68 CUT-OFF AT NODE 18).

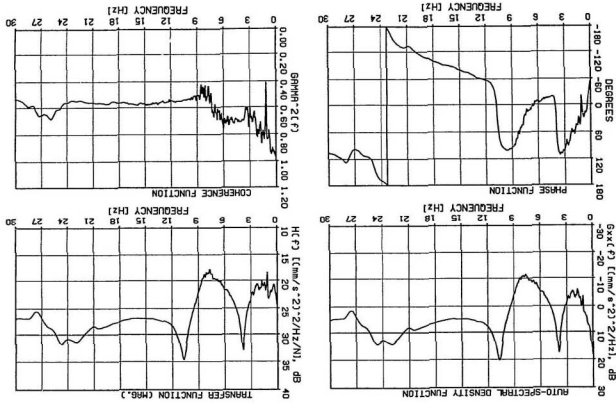


FIG. D.28 RESULTS AT ACCELEROMETER A2 DUE TO AN IMPACT INITIATED AT H6
 (DAMAGED STRUCTURE: MEMBER 70 SEVERED, AND MEMBER 68 CUT-OFF AT NODE 18).

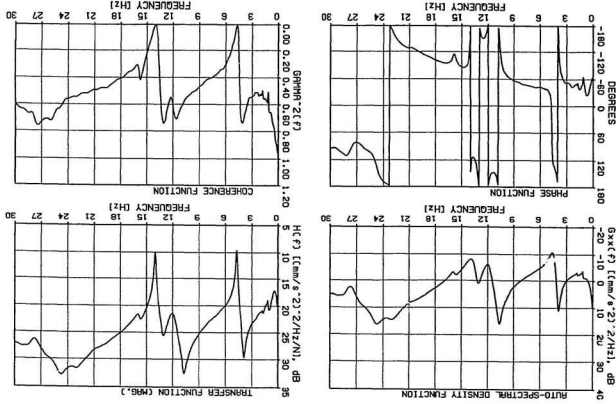


FIG. D.29 RESULTS AT ACCELEROMETER A3 DUE TO AN IMPACT INITIATED AT H6
(DAMAGED STRUCTURE; MEMBER 70 SEVERED, AND MEMBER 68 CUT-OFF AT NODE 18).

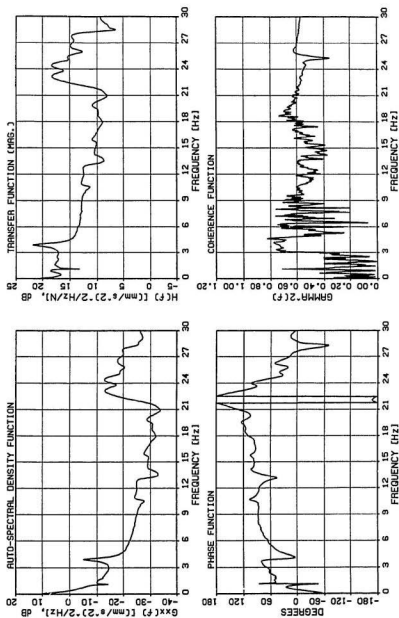


FIG. D.30 RESULTS AT ACCELEROMETER R4 DUE TO AN IMPACT INITIATED AT H6 (DAMAGED STRUCTURE: MEMBER 70 SEVERED, AND MEMBER 68 CUT-OFF AT NODE 18).

D.3 MEM Damping Estimates for the Damaged Structure

Table D.1 MEM Damping Estimates from the Response Measured with Accelerometer A3
(Damaged Structure: Member 70 Severed).

	Modal Damping Ratios at each Resonant Frequency			
	White Noise Tests		JONSWAP Tests	
	Frequency [Hz]	Damping Ratio, ζ	Frequency [Hz]	Damping Ratio, ζ
Mode 1 (1st Flexure, M_x)	1.2268	0.0305	1.2091	0.0491
Mode 4 (2nd Flexure, M_y)	7.0890	0.0554	7.0556	0.0540
Mode 8 (3rd Flexure, M_z)	16.0074	†	16.0743	†
Mode 10 (4th Flexure, M_y)	25.0621	0.0654	24.7700	0.0585

† indicates resonant peak not well defined.

**Table D.2 MEM Damping Estimates from the Response Measured with Accelerometer A3
(Damaged Structure: Members 70 and 68 Severed).**

	Modal Damping Ratios at each Resonant Frequency			
	White Noise Tests		JONSWAP Tests	
	Frequency [Hz]	Damping Ratio, ζ	Frequency [Hz]	Damping Ratio, ζ
Mode 1 (1st Flexure, M_y)	1.1722	0.0151	1.2003	0.0149
Mode 4 (2nd Flexure, M_y)	4.0422	0.0216	4.0322	0.0209
Mode 8 (3rd Flexure, M_z)	13.3369	0.0171	13.3021	0.0878
Mode 10 (4th Flexure, M_y)	†	0.0410	23.5912	0.0735

† indicates levels too low to be measured.

Table D.3 MEM Damping Estimates from the Response Measured with Accelerometer A4
(Damaged Structure: Member 70 Severed).

Modal Damping Ratios at each Resonant Frequency				
	White Noise Tests		JONSWAP Tests	
	Frequency [Hz]	Damping Ratio, ζ	Frequency [Hz]	Damping Ratio, ζ
Mode 1 (1st Flexure, M_y)	1.2636	0.0367	1.2682	0.0496
Mode 4 (2nd Flexure, M_y)	7.2533	0.0826	7.0010	0.0728
Mode 8 (3rd Flexure, M_x)	12.6360	0.0306	13.1079	0.0318
Mode 10 (4th Flexure, M_y)	23.5014	0.0220	24.1527	0.0179

**Table D.4 MEM Damping Estimates from the Response Measured with Accelerometer A4
(Damaged Structure: Members 70 and 68 Severed).**

	Modal Damping Ratios at each Resonant Frequency			
	White Noise Tests		JONSWAP Tests	
	Frequency [Hz]	Damping Ratio, ζ	Frequency [Hz]	Damping Ratio, ζ
Mode 1 (1st Flexure, M_y)	1.1690	0.0604	1.1659	0.0736
Mode 4 (2nd Flexure, M_y)	4.0355	0.0238	4.0096	0.0173
Mode 8 (3rd Flexure, M_x)	13.3073	0.0518	†	‡
Mode 10 (4th Flexure, M_y)	25.1122	0.0339	†	‡

† indicates levels too low to be measured.

‡ indicates resonant peak not well defined.

